School of Chemical and Petroleum Engineering

Department of Chemical Engineering

An Investigation on the Top-of-the-line Corrosion Using Novel Methods

Md Mayeedul Islam

This thesis is presented for the Degree of

Doctor of Philosophy

of

Curtin University

September 2017

Declaration

To the best of my knowledge and belief this thesis contains no material previously published by any other person except where due acknowledgment has been made.

This thesis contains no material which has been accepted for the award of any other academic degree or diploma in any university.

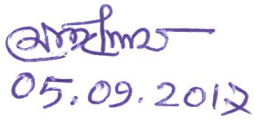

05.09.2012

Md Mayeedul Islam

Abstract

Corrosion at the inner wall of wet gas transportation pipelines due to the condensation of water vapour, referred to as top-of-the-line corrosion (TLC), is one of the major concerns in the oil and gas industry. Primary challenges associated with TLC are relevant to its control and monitoring. The research presented in this thesis involved the design and development of monitoring techniques for TLC that allows *in-situ* monitoring of inner wall surface temperature and collection of the condensed liquid and measurement of droplet retention time (DRT). Additionally, a novel electrochemical probe, that enables the use of electrochemical techniques under continuously condensing water, has been designed and applied in the research presented. With the new setup and the novel measurement technique, the influences of various parameters on the TLC behaviour have been revisited. These parameters include the inner wall surface temperature, gas temperature, water condensation rate (WCR) and monoethylene glycol (MEG) content on TLC in CO_2 environment.

This study demonstrates that there is a critical surface temperature below which the TLC rate is independent of the WCR. This is due to the slow corrosion kinetics at low surface temperatures. The role of the WCR on TLC has been emphasized and quantified through the droplet retention time, which is shown to be directly proportional to the supersaturation of Fe^{2+} and $FeCO_3$ formation at the top of the line (TOL). The $FeCO_3$ precipitation kinetics at TOL differ from that at the bottom of the line (BOL) due to the different hydrodynamic conditions at these locations.

Three electrochemical techniques namely; linear polarization resistance (LPR), electrochemical impedance spectroscopy (EIS) and electrochemical frequency modulation (EFM) have been applied in this study for *in-situ* monitoring of TLC rate as well as for studying $FeCO_3$ precipitation mechanism at TOL. The electrochemical results have been verified and validated with non-electrochemical methods, such as weight loss and Fe^{2+} concentration measurements in the absence and presence of $FeCO_3$ precipitation. The application of electrochemical methods revealed that $FeCO_3$ formation at the TOL proceeds in 3 stages; i) active state, ii) formation of a porous layer, and iii), formation of protective $FeCO_3$ layers consisting of inner (mixture of $FeCO_3$ and Fe_3C) and outer layer ($FeCO_3$). The $FeCO_3$ precipitation process is of

similar nature compared to the process under total immersion conditions despite different kinetic parameters of $FeCO_3$ precipitation at the TOL.

The study also revealed that the addition of MEG into the system reduces WCR at the TOL and corrosion rates at both the TOL and BOL, respectively. The concentration of co-condensed MEG at the TOL increases with increasing BOL MEG concentrations as well as decreasing condensation rates. The reduction in the condensation rates in the presence of MEG and the adsorption of MEG on active sites is resulting in a retardation of the galvanic effect between ferrite and cementite, have been identified as the cause of a reduction in the uniform corrosion rate. However, localized corrosion is found at the TOL in the presence of MEG within the water droplet area, where corrosion products were found to be porous and less thick compared to areas outside the droplet. Based on these results, a new mechanism for localized corrosion at the TOL in the presence of MEG has been proposed.

The influence of MEG on the dissociation constant of acetic acid has also been investigated in order to predict the likelihood of acetic acid to be co-condensed on TOL. The results reveal that MEG increases the dissociation constant of acetic acid which allows larger quantities of acetic acid to be co-condensed at the TOL.

Acknowledgements

First and foremost, I wish to thank almighty Allah for immeasurable blessings, protection and affection. I would like to express my sincere appreciation to my principal supervisor Prof. Rolf Gubner for his constructive guidance, internal motivation and giving me the opportunity of this study with a great freedom and care. My heartfelt gratitude should go to my co-supervisor Dr. Kod Pojtanabuntoeng for her unlimited support and guidance throughout the study. Her consistent patience in teaching with detail depth of knowledge helped me completing the study. I would also like to thank Prof. Brian Kinsella, a wonderful and caring person, who helped me to explore myself in different areas of corrosion.

I would like to acknowledge the help and contribution from the staff and students of CCEIC at different stage in this study. Special thanks to Dr. Kateřina Lepková, and Dr. Laura Machuca for their advice during this study. Thanks to all my friends and well-wishers who helped me from different orientation for completing a wonderful journey.

Finally, I am indebted to my family and in particular my parents, my wife Dr. Mst. Jannatul Ferdoush and my lovely daughter Sidratul Muntaha for their sacrifice, mental support and caring. Especial thanks to my sweet daughter whom I deprived a lot from my care during this study.

List of publications included as part of the thesis

This thesis is assembled as a hybrid consisting of published papers, submitted manuscripts and manuscripts in preparation, which form the individual chapters listed below:

Chapter 2

M.M. Islam, T. Pojtanabuntoeng, R. Gubner, Condensation corrosion of carbon steel at low to moderate surface temperature and iron carbonate precipitation kinetics, Corros. Sci. 111 (2016) 139–150.

Chapter 3

M.M. Islam, T. Pojtanabuntoeng, R. Gubner, Influence of monoethylene glycol on the condensation rate and corrosion rate of carbon steel under condensing condition, under review in Corrosion Science (submitted: 01.03.2017).

Cahpter 4

M.M. Islam, R. Gubner, T. Pojtanabuntoeng, Study of the top-of-the-line corrosion using a novel electrochemical probe, accepted in Corrosion – The Journal of Science and Engineering.

Chapter 5

M.M. Islam, T. Pojtanabuntoeng, R. Gubner, B. Kinsella, Electrochemical investigation into the dynamic mechanism of CO_2 corrosion product film formation on the carbon steel under water condensation condition, under review in Corrosion Science.

Appendix I

M.M. Islam, R. Gubner, T. Pojtanabuntoeng, Are corrosion rates and condensation rates proportional in TLC?, CORSYM-2015, NACE International and Gateway India Section, Paper No. 3, 2015.

Appendix II

M.M. Islam, R. Gubner, T. Pojtanabuntoeng, Electrochemical investigation into the influence of monoethylene glycol on CO_2 corrosion in the presence of acetic acid, manuscript in preparation.

I assure that I have obtained, where necessary, permission from all the copyright owners to use any third-party copyright material reproduced in the thesis or to use any of my own published work in which copyright is held by another party.

Conference presentations

- M. M. Islam, T. Pojtanabuntoeng, R. Gubner, “Are condensation rate and corrosion rates proportional in TLC?” Top-of-the-line Corrosion Conference - 2015, 26 - 28 July, 2015, Jakarta, Indonesia.
- M. M. Islam, T. Pojtanabuntoeng, R. Gubner, “Development of an electrochemical method to study top-of-the-line corrosion”, CORROSION – 2017, 26 – 30 March, 2017, New Orleans, USA, Paper No. 9106.

Statement of contribution of others

I, Md Mayeedul Islam, as the first author of the individual publications comprising each chapter of this thesis, was primarily involved in planning and conducting the experiments, data analysis and interpretation of the findings and manuscript preparations. Contributions by the co-authors are mentioned below and the written statements from the co-authors are included in Appendix IV.

Chapter 2-4 and Appendix I & II

Thunyaluk Pojtanabuntoeng significantly contributed to the conception of experiments, data interpretation, and evaluation of the manuscripts. Rolf Gubner actively participated in the preparation and critical revision of the manuscripts.

Chapter 5

Thunyaluk Pojtanabuntoeng significantly contributed to the conception of experiments, data interpretation, and evaluation of the manuscripts. Rolf Gubner and Brian Kinsella also provided input to the experimental concepts and actively participated in the preparation and critical revision of the manuscript.

Curtin Corrosion Engineering Industry Centre (CCEIC) under the School of Chemical and Petroleum Engineering provided all the facilities for the project to conduct all experiments. International Postgraduate Research Scholarship (IPRS) assisted financially to conduct the project.

Table of content

List of figures

List of tables

List of abbreviations

TLC	Top-of-the-line corrosion
BOL	Bottom-of-the-line
TOL	Top-of-the-line
WCR	Water condensation rate
pCO_2	Partial pressure of carbon dioxide
DRT	Droplet retention time
HAc	Acetic acid
PET	polyethylene terephthalate
SEM	Scanning electron microscope
EDS	Energy dispersive X-Ray spectroscopy
DI	Deionized
SS	Stainless stell
ER	Electrical resistance
QCM	Quartz crystal microbalance
EC	Equivalent circuit
LPR	Linear polarization resistance
EIS	Electrochemical impedance spectroscopy
EFM	Electrochemical frequency modulation

Chapter 1: Introduction and overview

Corrosion is the deterioration of metal by interactions with its surrounding environment [1]. Principally, corrosion is an electrochemical reaction where anodic oxidation and cathodic reduction reactions are taking place simultaneously at discrete locations on the metallic surface. Corrosion causes enormous economic losses and has impacts on a global scale. The estimated global economic loss due to corrosion is about 2.5 trillion USD in 2013, which is equivalent to 3.4% of the global gross domestic product [2]. Corrosion takes place almost on all metallic structures. Carbon steel pipelines, widely used for transportation of fluids and gases, because of their comparatively low cost, good mechanical strength and availability, are vulnerable to corrosion. In the USA, about 15% to 20% of all leading pipeline failures are caused by corrosion [2]. The present study focusses on an internal corrosion problem of subsea pipelines.

This chapter provides an overview of the full dissertation. After a critical literature survey, the gaps in the current understanding of top-of-the-line corrosion are identified, based on which the objectives of this study have been set and significance and contribution of this study have been stated. The dissertation outline includes introductions to each chapter explaining how the objectives have been met. Last, but not least, a summary and discussion section outlines the major findings from each of the following chapters (publications).

1.1 Literature Review

1.1.1 Introduction to top-of-the-line corrosion (TLC)

For the oil and gas industry, transportation of production fluids and gases from offshore platforms to onshore processing plants can be challenging. The product fluids and gases coming from the reservoir contain hydrocarbons, solids, organic acids, carbon dioxide, water, etc., which form a multiphase complex mixture [3]. An economic and convenient way to transport the fluids and gases over long distances is through carbon steel pipelines. The presence of water, dissolved salts, solids, carbon dioxide and organic acids in the carbon steel pipelines is detrimental as it causes internal corrosion problems [4,5]. Top-of-the-line corrosion (TLC) is an internal corrosion phenomenon occurring at the upper portion of the inner wall of gas

transmission pipelines due to condensation of water vapour. The pipelines prone to TLC are typically operated in the stratified and wavy-stratified flow regime [5–9]. TLC is considered dangerous since effective mitigation strategies have not been found. Conventional corrosion inhibitors injected into the bottom of the pipeline cannot reach to the top of the line (TOL) due to their non-volatile nature. Further, the use of volatile corrosion inhibitor to mitigate TLC still has issues with persistency as water continuously condenses on TOL and dilutes the inhibitor concentration. Similarly, conventional batch treatment is not cost effective to mitigate the TLC, as it requires frequent treatment and production interruptions [10].

TLC can be sub-divided as 'sweet' corrosion and 'sour' corrosion depending on the corrosive constituents. The former occurs in CO_2 dominated environments and the latter takes place in H_2S containing environments [11]. Only sweet TLC will be considered throughout the entire dissertation.

1.1.2 Mechanism of sweet TLC

Figure 1.1 illustrates the schematic of a cross sectional view of a wet-gas transportation pipeline where TLC occurs. When water saturated gas is transported from the wellhead to the processing plant, water condensation takes place at the inner wall of the pipeline due to temperature gradient between the warm (or hot) production fluids and the colder outside environment [5]. CO_2 present in the gas phase dissolves in the condensed liquid and the organic acid vapour co-condenses, which lowers the pH of the condensed water [12]. Hence, the condensed water becomes corrosive and corrodes the upper portion of the inner wall of the pipeline [13].

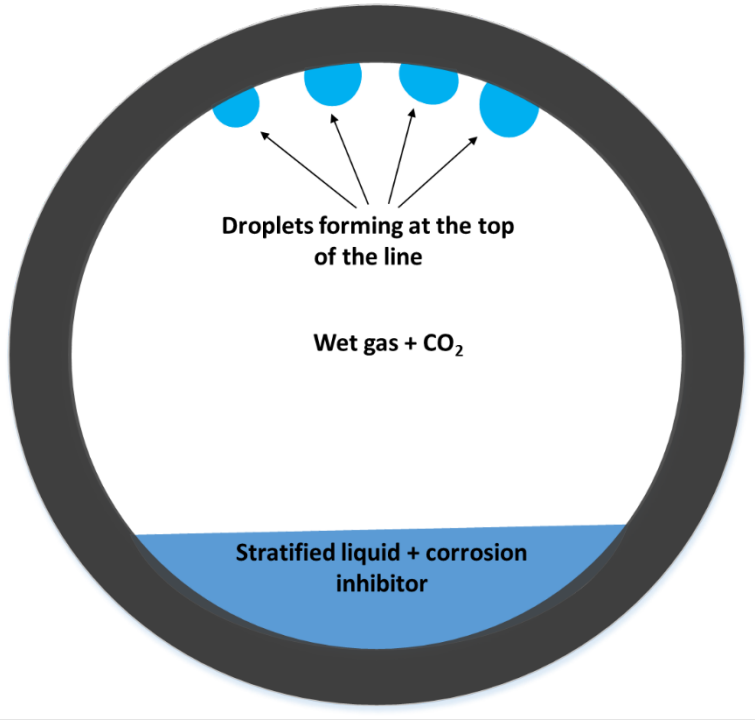

Figure 1.1: Schematic diagram showing a cross sectional view of a wet gas pipeline. Condensation of water vapour leads to top of the line corrosion.

In sweet CO_2 environments, the principle corrosion reactions occurring at the bottom of the line (BOL) and TOL are identical. The following series of reactions are proposed to occur in CO_2 corrosion of carbon steel [14–16]:

$$CO_{2(g)} \leftrightarrow CO_{2(aq)} \tag{1.1}$$

$$CO_{2(aq)} + H_2O_{(aq)} \leftrightarrow H_2CO_{3(aq)} \tag{1.2}$$

$$H_2CO_{3(aq)} \leftrightarrow H^+_{(aq)} + HCO^-_{3(aq)} \tag{1.3}$$

$$HCO^-_{3(aq)} \leftrightarrow H^+_{(aq)} + CO^{2-}_{3(aq)} \tag{1.4}$$

$$Fe_{(s)} \longrightarrow Fe^{2+}_{(aq)} + 2e^- \tag{1.5}$$

$$2H^+_{(aq)} + 2e^- \longrightarrow H_{2(g)} \tag{1.6}$$

$$Fe^{2+}_{(aq)} + CO^{2-}_{3(aq)} \leftrightarrow FeCO_{3(s)} \tag{1.7}$$

However, an insight into the TLC mechanism can be provided by discussing the influential factors. Several empirical, semi-empirical, mechanistic models and experimental works have identified factors affecting TLC. The important parameters are outlined below:

1.1.2.1 Water condensation rate

The water condensation rate (WCR) plays a critical role on TLC and this factor is also influenced by many parameters including gas temperature, sub-cooling temperature, non-condensable gas concentration, gas velocity, system pressure and internal pipe diameter [17]. Vitse et al. proposed a semi-empirical model for the TLC rate calculation considering that condensation takes place either as film that drains down to the bottom of the pipe or as droplets that stay at the TOL before falling due to gravity [18]. However, the morphology of the corroded steel surfaces at the TOL reported from field cases [5,13], and visual observation of the condensing pattern in a recent study [17] indicate that dropwise condensation is more likely to occur as opposed to filmwise condensation.

A proportional relationship between WCR and TLC rate has been reported and is generally accepted [10,19–21]. At high condensation rates, condensed water is quickly renewed, which impedes the condensed water to become saturated for $FeCO_3$ to precipitate. In contrast, a low condensation rate helps to establish saturation of $FeCO_3$ within the droplet and/or within a thin condensed film, which in turn favours the formation of $FeCO_3$ film on the surface to reduce the TLC [22]. The investigated range of WCRs found in the literature varied from 0.001 mL m^{-2} s^{-1} to 2.25 mL m^{-2} s^{-1} [13,19,23–28]. The critical WCR was estimated to be between 0.15 mL m^{-2} s^{-1} to 0.25 mL m^{-2} s^{-1} in low organic acid containing environments above which severe TLC can be expected [10]. However, other critical factors, such as the presence of organic acids, temperature and complexing anions, can influence iron carbonate precipitation and can further reduce the value of the critical WCR [29].

The overall effect of condensation rates, summarised by Olsen and Dugstad [30], indicated that at very high condensation rates, the pipeline experienced very high corrosion rates of up to several mm y^{-1}. In such conditions, only a negligible amount of protective corrosion products remained on the surfaces, which had no influence on

corrosion rates. When condensation rates decreased to just above the critical value, a reduction in corrosion rate occurs because of the accumulation of corrosion products on the surface. A further decrease in condensation rates, just below the critical value and low operating temperature, a non-protective scale formed on the steel surface. In such situations, the condensation rate did not influence the corrosion rate. Finally, at condensation rates well below the critical value and at high operating temperatures, a protective corrosion product film was formed and the corrosion rates were significantly decreased [30].

A further insight into the influences of WCR on TLC have been revisited in this study and the results are discussed in Chapter 2 and Appendix I.

1.1.2.2 Bulk gas temperature

The gas temperature is another critical parameter in TLC as it influences the condensation rates by changing vapour pressure of water, thickness of the condensed film/droplets and temperature of the inner wall surface [31]. Vitse et al. studied the effect of a wide range of gas temperature from 40 ℃ to 90 ℃ on TLC [22]. TLC increased with increasing temperature up to values between 70 ℃ to 80 ºC. Afterwards, the trend of corrosion rate reversed with a further rise of temperature to 90 ºC. The initial increase of TLC rate with increasing gas temperature (<70 ºC) was due to the increase of reaction rate. However, at higher temperatures (>80 ℃), additional mechanisms were proposed such as: i) the increased condensation rate makes the condensed liquid film thicker and thereby limits the mass transfer of corrosive species, ii) precipitation of $FeCO_3$ takes place on the surface protecting the surface partially, and iii) higher corrosion rate may enrich the concentration of ferrous ion which in turn increases the pH and alters the mechanism of electrochemical reaction [22].

Singer et al. correlated the gas temperature with the nature of corrosion product formed. Their study reported that the corrosion product formed at low temperature (40 ℃) was mostly porous $FeCO_3$ and less protective. Therefore, corrosion rates increased for the first couple of days and remained constant afterwards at this temperature. On the contrary, a dense and protective $FeCO_3$ film formed at higher

temperature (> 70 °C). Thus, a higher corrosion rate was found in the initial stage, which declined over time due to the formation of the protective $FeCO_3$ film [25,32].

An empirical model developed by Nyborg and Dugstad predicted an increase of TLC from 0.03 to 0.14 mm y^{-1} with increasing gas temperature from 30 °C to 90 °C as a result of increasing condensation rates [21]. However, protection against corrosion due to the $FeCO_3$ formation was not considered in their model.

Based on the above discussion, it can be argued that a variation of the gas temperature ultimately changes the condensation rates and temperature of the inner wall of the pipeline, which in turn ultimately affects the mechanism of TLC and nature and properties of the corrosion products that formed. To validate this hypothesis, the influences of gas temperature on TLC rates have been revisited in this study and discussed in Chapter 2 and Appendix I.

1.1.2.3 Wall temperature

Asher et al. predicted a decreasing trend of the TLC rates with rising wall temperature from 25 °C to 90 °C based on CorrCast™ mechanistic model that was compared with their experimental results [24]. Their study focused on comparing their results with the findings of other prediction models and the authors did not include mechanistic information.

Qin et al. illustrated the effect of low pipe wall temperatures on TLC at constant gas temperature of 25 °C [33]. The study reported a slight change of TLC with increasing wall temperature from 5 to 15 °C followed by a sharp decrease of TLC rates when the wall temperature was raised to 20 °C. The authors proposed that slow reaction kinetics at low temperature do not significantly increase the corrosion rates. However, at higher temperature (20 °C), low condensation rates reduce the TLC sharply. It should be noted that the experimental design used in this study might have produced an unrealistic pattern of water condensation whereby the condensed liquid glided vertically from top to bottom instead of forming droplets on the steel surfaces.

A relatively better understanding of the effect of wall temperature on TLC was described by Ojifinni et al. [19] where a constant decrease in normalized corrosion rates were found with increasing wall temperature from 25 to 65 °C at a water

condensation rate between 0.17 to 0.2 mL m^{-2} s^{-1}. The formation of a protective $FeCO_3$ film at higher temperatures was identified as the cause in the TLC rate reduction.

However, the wall temperatures reported in the literature are outer wall temperatures, which were maintained by circulation of a cooling liquid. It is worth mentioning that the inner and outer wall temperatures are not identical due to the temperature gradient between the warmer gas temperature and the outer cooling water temperature. Since water condensation, iron dissolution and $FeCO_3$ formation take place at the inner surface and are affected by temperature, therefore, the inner wall surface temperatures have been measured in this study and its influences on TLC and $FeCO_3$ film formation are discussed in Chapter 2.

1.1.2.4 Partial pressure of CO_2 (pCO_2)

A proportional relationship between the partial pressure of carbon dioxide (pCO_2) and the average TLC rates were proposed by Singer and co-workers [25]. The study also correlated the pCO_2 with the nature of the corrosion products formed on the surface. The author demonstrated that a lower pCO_2 (0.13 bar) is not favourable for the formation of protective $FeCO_3$ layers due to the low supersaturation leading to a low but constant corrosion rate with time. Whereas at high pCO_2 (> 2 bar), the initial attack was more aggressive but the average corrosion rate decreased over time. This was attributed to the formation of protective $FeCO_3$ layers since higher supersaturation in the condensed liquid was attained.

Vitse and co-workers investigated the influence of pCO_2 over a range from 1 bar to 8 bar on TLC. pCO_2 was found to influence the TLC process at high water condensation rates, but it remained indifferent at low condensation rates. At higher condensation rates, supersaturation cannot be reached due to the high rate of renewal of condensed liquid. In this situation, increase in partial pressure of CO_2 decreased the pH of the condensed liquid making the environment more corrosive. Conversely, at low condensation rates, the condensed liquid attains saturation or even supersaturation with the corrosion product resulting in increasing the pH and decreasing the kinetic of corrosion reaction by CO_2 [22].

Ojifinni and Li identified the pCO_2 as a less influential parameter on TLC by conducting experiments at a constant condensation rate (~ 0.18 mL m^{-2} s^{-1}) and at

25 °C and 55 °C wall temperatures [19]. It was found that a minor increase of TLC rates was observed at both temperatures when increasing pCO_2 from 50 psi (3.45 bar) to 261 psi (18 bar). The low influence of the pCO_2 was explained by the competitive role of CO_2 and corroded Fe^{2+} to change the pH and supersaturation of the condensed liquid [19]. A similar explanation was also given by Oehler et al. who reported slight increased TLC rates with increasing pCO_2 from 5 to 20 bar at constant condensation rates and in absence of acetic acid [34].

In summary, the pCO_2 has both positive and negative influences on TLC. On one side it helps to form $FeCO_3$ film that reduces corrosion rates, on the other side it decreases the pH of the condensed liquid and, therefore, increases the corrosivity of the medium. However, its ultimate effect largely depends on other environmental conditions such as WCR at the TOL.

The present investigation did not revisit the influence of pCO_2 because of time constrain and limitation of the existing setup. However, the concept of the electrochemical setup used in this study could be adapted to high-pressure arrangements and would provide valuable new insight into the underlying corrosion mechanisms.

1.1.2.5 Monoethylene glycol (MEG) content

Monoethylene glycol (MEG) is predominantly used as a hydrate inhibitor in wet gas pipelines because of its less toxicity compared to methanol, low vapour density, and recyclability [35,36]. Typically, 80-90 wt% MEG in water (lean MEG) is injected at the wellhead and the MEG concentration decreases to almost 30-60 wt% (rich MEG) at the outlet as a result of dilution by condensed water and/or produced water [23,41,42]. Numerous studies suggested that glycol inhibits CO_2 corrosion at the bottom of the line (BOL) [39–42]. Generally, the inhibiting action increases with increasing the MEG concentration.

When MEG is used as a hydrate inhibitor in gas transportation pipelines, MEG evaporates and co-condenses at the TOL along with water when a temperature gradient is present [27]. Mendez et al. found a slight reduction in TLC rates when 50 wt.% of MEG presented in the BOL along with the brine solution [20]. The study proposed that a decrease in the water content in the vapour phase causes the reduction in TLC since

almost no MEG was present in the condensed liquid. Ehsani et al. traced the presence of MEG in the condensed liquid but did not investigate its influence on TLC [42]. It has been reported that the condensing phase would contain almost the same MEG content as the aqueous phase at the BOL when a complete chemical equilibrium is achieved [23]. Since the reactions of CO_2 corrosion in TOL is similar to BOL conditions, it is possible that MEG reduces the corrosion rate for TLC as well. But, most of the investigations relating to MEG were conducted under BOL conditions. The effects of MEG on the TLC have rarely been studied to-date. Therefore, a part of this dissertation studied the influences of MEG on TLC and BOL corrosion which have been discussed in Chapter 3 and Appendix II.

1.1.2.6 Organic acid content

Organic acids originating from either the natural gas reservoir or from regenerated glycol, which causes some degradation, are present in most wet gas transportation pipelines. Typical organic acid concentrations ranges from 100 ppm to 3000 ppm among which acetic acid is (HAc) dominant constituting 50 to 90% of the total organic acids [13,43]. It has been reported that the concentration of organic acids in the condensed liquid decreases with increasing condensation rates [12,44]. High condensation rates reduce the TOL organic acid concentration to approximately 75% of the BOL organic acid concentration [45]. It is well agreed upon in the literature that the presence of HAc aggravates both the uniform and localized TLC rates and reduces the integrity of the pipeline [12,13,32,34]. It was proposed that acetic acid promotes the corrosion rate by either facilitating the cathodic reaction or by changing the solubility and protectiveness of the corrosion product [12].

The likelihood of HAc to be co-condensed at the TOL also depends on the dissociation constant (*pK*a) of HAc present in the BOL. Higher the *pK*a, larger amount of HAc will remain as undissociated which could evaporate and co-condense at the TOL. It has been stated in the previous section that pipelines contain larger amount of MEG at the BOL, which might influence the *pK*a of HAc as other organic solvent does. However, the *pK*a of HAc in presence of MEG has not been reported. Therefore, in this study the likely hood of HAc to be co-condensed at the TOL in presence of MEG has been predicted by estimating the *pK*a of HAc in MEG solution and are discussed in detail in Appendix II.

1.1.3 $FeCO_3$ precipitation at the top of the line

Iron carbonate ($FeCO_3$) is a predominant corrosion product in CO_2 corrosion of carbon steel, which provides physical barrier between the electrolyte and the solid metallic surface and thereby reducing the corrosion rate [46–48]. Investigations conducted under BOL conditions identified several environmental conditions, such as iron concentration [14,49], solution pH [50], temperature [14,50,51], pCO_2 [15], microstructure of the carbon steel [47,52], and exposure time [47] that affect the protectiveness of the layer. The scaling tendency model was proposed to predict the protectiveness of the $FeCO_3$ scale formation [53]. A mechanistic model proposed by Nesic et al. described the growth of the $FeCO_3$ film on a mild steel surface and the model anticipates that the precipitation kinetic is dependent on temperature and local species concentration [54]. Protective $FeCO_3$ is formed at high temperature (> 60 °C), even with low supersaturation, whereas, porous and loosely adhered films forms at low temperature (< 40 °C) with high supersaturation [55].

The mechanisms of $FeCO_3$ film formation and film growth in CO_2 environment under immersion condition have been widely reported [53,54,56–60]. However, those mechanisms at TOL conditions have rarely been studied. A number of investigations reported the presence of $FeCO_3$ films at TOL under water condensation conditions in a CO_2 environment [22,28,61]. Sharp edged crystals were found in the area covered by the water droplet [62]. The nature of the $FeCO_3$ film formation was correlated with the temperature, pCO_2, and condensation rates [22,25]. Generally, a high temperature, high pCO_2 and low condensation rate lead to the formation of a very dense and protective $FeCO_3$ layer. In this dissertation, the formation mechanism of $FeCO_3$ at the TOL has been examined using the new set-up and the results are discussed in detail in Chapter 2 and Chapter 5.

I.1.4 Nature of TLC

TLC is inherently identified as localized corrosion in several field investigations [5,6]. However, in the field the corrosion features appeared is so large that the corrosion process is sometimes referred to as “localized uniform corrosion” instead of just

"localized corrosion"[44]. The first reported case of TLC described the corrosion profile as "sharp-edged pits which join together to form large areas of corrosion" [6]. Singer discussed in detail the localized nature of TLC and proposed a prediction model for localized TLC [44,62]. The study reported that extent of localized corrosion increased with increasing condensation rates, presence of acetic acid in the condensed water and gas temperature. Local breakdown of the $FeCO_3$ film due to the constant replenishment of the condensed water was thought to initiate the localized corrosion. The location of the droplet did not link directly to the area of localized attack. Gou et al. reported pitting corrosion on TOL in MEG co-condensation system [61]. However, the authors did not conclude any role of MEG on localized corrosion. In this study (Chapter 3), a correlation has been made between the location of droplet and area of localized attack and the role of MEG on localized corrosion has been described.

1.1.5 Top of the line corrosion monitoring techniques

1.1.5.1 Field monitoring

In the field, monitoring of TLC requires inline inspection (ILI) tools equipped with sensors, such as eddy current measurement, magnetic flux leakage or ultrasonic metal loss [8,63,64]. Weight loss coupons and electrical resistance probes are also used in different locations of the pipeline to monitor TLC [65].

1.1.5.2 Laboratory monitoring

In case of laboratory-oriented TLC monitoring devices, a wide variety of setups were proposed and employed to improve an understanding of TLC. A brief summary of these devices is given in Table 1.1.

A review of the laboratory monitoring techniques reveals that the TLC rates were measured either by weight loss, electrical resistance (ER) probes or by measuring the Fe^{2+} concentration in the bulk or condensed liquids. However, the systematic study into the design, development and validation of electrochemical probe for TLC application has not been reported. Therefore, the present study develops and validates a new electrochemical probe for TLC study, which is discussed in Chapter 4 and Chapter 5.

Table 1.1: Different approaches used in TLC monitoring.

No.	Configuration	Total pressure (bar)	Gas Temp. (°C)	Wall Temp. (°C)	WCR[1] range ($g\ m^{-2}\ s^{-1}$)	Method of TLC rate determination	Notes	Ref.
1	Horizontal cooled carbon steel tube	1	30-70	NR[2]	0.10-1.50	Fe^{2+} measurement in the condensed liquid	Condensation took place on the outside surface of the carbon steel tube.	[66]
2	Horizontal cooled carbon steel U-tube	20	91-115	30-80	0.40	Weight loss, and Fe^{2+} measurement in the bulk liquid	Condensation took place on the outside surface of the carbon steel tube.	[34,67]
3	Vertical cooled tube	NR[2]	68	NR[2]	NR[2]	Fe^{2+} measurement in the condensed liquid	Condensation took place on the inner circumference where condensed liquid glide through the vertical tube from upward to downward instead of forming droplet.	[12,45]
4	Cold finger probe	1	NR[2]	NR[2]	0.25-0.40	LPR, and Fe^{2+} measurement in the condensed liquid	Particular design of the probe cannot differentiate the influence of environmental parameters such as condensation rate and temperature.	[67]
5	Quartz crystal microbalance (QCM)	6.89	30	5	NR[2]	Change in frequency of a quartz crystal gives the corrosion rate.	Technical difficulties to use in real field	[68,69]
6	Glass cell apparatus	1	35-50	25-30	0.023-0.092	Weight loss	No provision of collecting the condensed liquid.	[70]

No.	Configuration	Total pressure (bar)	Gas Temp. (°C)	Wall Temp. (°C)	WCR[1] range ($g\ m^{-2}\ s^{-1}$)	Method of TLC rate determination	Notes	Ref.
7	Glass cell apparatus	1	70	NR[2]	0.25	Weight loss and electrical resistance (ER) probe	No provision of collecting the condensed liquid.	[71,72]
8	Flow loop	3-8	40-90	NR[2]	0.05-1	ER probe	Representative to field condition Only one method for corrosion rate measurement	[17,22, 73]
9	Flow loop	3-8	40-90	33.5-70	0.05-1	Weight loss	Representative to field condition Only one method for corrosion rate measurement	[25,74, 75]

[1] WCR = water condensation rate
[2] NR = not reported

1.2 Research gaps

In order to improve on the existing knowledge of TLC, it is essential to develop a setup with multiple capabilities, such as, the measurement of inner wall temperature (where all chemical processes are taking place), *in-situ* collection and analysis of condensed liquid (to understand its chemistry and accurate measurement of condensation rates), and provision of post experimental analysis of the corrosion products. Chapter 2 in this dissertation addresses this gap by developing a new TLC setup with combination of all the listed capabilities missing in the current literature. Moreover, most of the monitoring techniques for TLC are still confined within the use of weight loss coupons or ER probes. Weight loss coupons only provide integrated corrosion rates over long periods of exposure. ER probes provide instantaneous corrosion rates but not information on the corrosion mechanisms. Besides, the presence of conductive corrosion products and temperature can influence the result of ER probe.

Electrochemical corrosion testing will be of great interest in studying TLC because it is not only instantaneous but also able to measure the corrosion rates without isolating the specimen from the environment or even significantly disturbing it. In addition, mechanistic information on the corrosion process can be unveiled using electrochemical techniques. However, the *in-situ* monitoring of TLC rates using electrochemical techniques is still a challenge for researchers and in the field because of small volume of electrolyte at the TOL in conjunction with the high resistivity of the condensed liquid. Therefore, in Chapter 4 and Chapter 5, new electrochemical probe has been designed and developed to meet the current needs.

Based on the literature review above, this study emphasizes on the development of the electrochemical monitoring techniques of TLC and revisits some of the important areas, where gaps have been identified to get a better understanding of TLC mechanism; i.e. influence of surface temperature (Chapter 2 and Appendix I), WCR (Chapter 2 and Appendix I), and MEG (Chapter 3 and Appendix II) on TLC and precipitation mechanism of $FeCO_3$ on TOL (Chapter 5).

1.3 Objectives of the study

Based on the gaps in the current understanding (section 1.2), this study aimed to:

- ✓ Design and develop experimental setup capable of measuring real inner surface temperature, droplet retention time (DRT) and *in-situ* collection of condensed liquid for its analysis (Chapter 2 and Appendix I).
- ✓ Incorporate electrochemical methods for instantaneous monitoring of TLC and understanding the interfacial process occurring on TOL (Chapter 4 and Chapter 5).
- ✓ Revisit the mechanism of TLC using the new setup (Chapter 2 and Chapter 5).
- ✓ Study the influence of bulk MEG concentration on condensation rate, co-condensation, TLC rate and BOL corrosion rate (Chapter 3 and Appendix II).

1.4 Significance and contribution of the thesis on the understanding of TLC

This thesis outlines the development of a unique TLC monitoring technique by incorporating electrochemical methods (Chapter 4 and 5), which can open up a new window in the real-time field monitoring of TLC and investigating the efficiency of inhibition methods. The mechanisms of TLC have been revisited in this study and some previously hidden facts of TLC are revealed. For instance, proportional relationship between condensation rate and TLC rate are not valid at low surface temperature (~15 °C) and in the absence of $FeCO_3$ film (Chapter 2). Furthermore, this study highlighted the importance of the inner wall surface temperature to get an improved insight into the TLC mechanisms. At surface temperatures below 30 °C, WCR does not influence corrosion rate, which is identified as critical surface temperature for atmospheric condition (Chapter 2). This study also found that iron carbonate precipitation mechanism on TOL is similar to total immersion condition, which was identified using electrochemical impedance spectroscopy (EIS) at the TOL (Chapter 5). All these findings advance the current understanding of TLC which could be utilised when planning for TLC inhibition, inspection, and prediction.

In addition, the role of MEG on TLC has been identified. MEG prevents uniform corrosion but causes localised corrosion on the TOL (Chapter 3 and Appendix II). The findings are useful for many gas development projects using MEG as hydrate inhibitor.

1.5 Dissertation outline

This dissertation is assembled as a hybrid consisting of published papers and submitted manuscripts (in various stages of submission and review) that constitute a chapter each.

Chapter 2 describes the development of a new TLC setup that is capable of measuring the surface temperature *in-situ* and collecting the condensed water as it is produced. As a result, the critical inner wall surface temperature (below which WCR does not influence TLC rate) and droplet retention time (DRT) were identified.

Using the above design, Chapter 3 presents the influence of bulk MEG concentration on condensation rates, co-condensation of MEG and TLC rates. Localized corrosion found in the presence of MEG is discussed by correlating droplet locations with the surface morphology and chemistry of corrosion products formed.

Chapter 4 describes in further detail the experimental setup and introduces the electrochemical methods used to study TLC and validates these with non-electrochemical methods.

Chapter 5 utilises the electrochemical methods under $FeCO_3$ film forming condition to investigate the mechanism of $FeCO_3$ formation at the TOL.

Appendix I distinguishes the influence of interrelated parameters, such as, surface temperature, gas temperature and condensation rates on TLC rates.

Appendix II describes the influence of MEG and acetic acid (HAc) on carbon steel corrosion mechanisms under CO_2 conditions at constant pH and temperature under BOL condition. A particular emphasis is given on the dissociation constant of acetic acid in MEG solutions.

1.6 Thesis summary and discussion

TLC is one of the major concerns in the oil and gas industry. Due emphasis has been given in this study to develop an improved TLC monitoring technique, based on electrochemical methods, and to revisit those influential parameters , such as, inner wall temperature, gas temperature and WCR, as well as MEG content in the BOL.

This study has been conducted in two stages. During the first stage, a new TLC experimental setup has been designed, which is capable of monitoring real inner wall surface temperature, *in-situ* collection of the condensed liquid, and measurement of the droplet retention time (DRT) (Chapter 2 and Appendix I). Using the new setup, the DRT has been quantified for the first time (Section 2.4.1) and correlated with supersaturation and scale formation (Section 2.5.2). For instance, under TOL conditions, high supersaturation may not favour the formation of protective iron carbonate films if the DRT is low. Conversely, low supersaturation with long DRT allows the formation of a protective $FeCO_3$ scale at the TOL (Section 2.5.3). Similarly, the measurement of the actual surface temperature at the inner wall determines the critical surface temperature (30 °C) below which the TLC rate is independent on WCR (Section 2.4.2). However, the WCR plays a role in TLC when the surface temperature increases to and above 30 °C and when the precipitation of $FeCO_3$ is thermodynamically and kinetically favourable (Sections 2.4.2 and 2.5.4). The analysis of the condensed liquids allows the calculation of the species concentrations, accurate measurement of *in-situ* pHs of the condensed liquids, $FeCO_3$ supersaturation and the scaling tendency (Section 2.5.1). In this investigation, the pH of the condensed liquid was between 5 to 6. This study also revealed that the kinetic parameters of iron carbonate formation at TOL and BOL are different. Hence, a new kinetic constant has been proposed to calculate the $FeCO_3$ formation rate at the TOL (Section 2.5.3.2).

The new setup was also used to study the influences of MEG on TLC (Chapter 3). It was found that an increase in MEG concentrations in the bottom liquid decreases the condensation rates and uniform corrosion rates but increases the amount of co-condensed MEG at the TOL (Sections 3.4.1 and 3.4.2). However, severe localized corrosion was shown to develop in the areas underneath the droplet when MEG co-condenses (Section3.4.3 and Figure 3.15). Surface and cross sectional analysis reveals that corrosion product formed within the droplet boundary is more porous and thinner compared to that formed outside of the droplet (Figure 3.17 and Figure 3.18). Corrosive liquid penetrates through the pores and attributes to localized corrosion.

The influence of MEG on CO_2 corrosion of carbon steel in the presence of HAc has been investigated under BOL conditions (Appendix II). The results show that an increase in MEG concentration reduces the dissociation constant of HAc and increases the amount of undissociated, volatile HAc (Section II.4.1). This amount of undissociated HAc is pH dependent and can be significant at pH 5 and above (Figure II.2). This study makes the important prediction that a higher HAc concentration will result in increased co-condensation with water at the TOL in the presence of MEG in the BOL. This study also finds that under BOL condition HAc aggravates the CO_2 corrosion of carbon steel but this effect diminishes significantly with increasing MEG concentration (Table II.1).

In the second stage, an electrochemical TLC probe has been designed to include electrochemical methods namely: linear polarization resistance (LPR), electrochemical impedance spectroscopy (EIS) and electrochemical frequency modulation (EFM) for TLC study (Chapter 4). The results from electrochemical techniques have been verified with non-electrochemical techniques, such as weight loss and Fe^{2+} concentration measurements, in the absence and presence of $FeCO_3$ film (Sections 4.4.3 and 5.4.1). The electrochemical techniques are also used to understand the interfacial processes and $FeCO_3$ formation mechanism on TOL (Chapter 5). The trend of the *in-situ* corrosion rates and EIS study reveals that the formation $FeCO_3$ film at TOL has 3 stages: i.) active state when corrosion rates initially increase due to the galvanic coupling effect between ferrite and cementite, ii.) formation of porous layer when corrosion rates start to decline, and iii.) formation of protective $FeCO_3$ layer consisting of inner (mixture of $FeCO_3$ and Fe_3C) and outer layer ($FeCO_3$) when corrosion rates reach to minimum stable values (Section 5.4.4). The outcomes of this study indicate that the newly designed electrochemical probe is capable of not only monitoring *in-situ* TLC rates but also to provide information of interfacial processes occurring at the TOL.

In summary, this thesis describes the development of a novel TLC monitoring technique and presents new mechanistic information associated with the corrosion processes under CO_2 conditions. All experiments in this investigation were conducted in glass cells which limits its use in high temperature and high pressure conditions. However, the design and

concept could be adopted for use in high temperature and high-pressure autoclaves, flow loops and even in real field monitoring of TLC. In addition, the new setup with the electrochemical probe could be used effectively in more complex environments, such as the presence of corrosion inhibitors, MEG, and in flowing conditions. The new technique also opens up opportunity for TLC inhibition to be studied systematically, which in turn will contribute to safer production in the oil and gas industry.

1.7 References

[1] H.H. Uhlig, The corrosion handbook, John Willey and Sons Inc., New York, 1948: pp. 3-4.

[2] J.R. Scully, Corrosion is a Global Issue, Corrosion. (n.d.). http://corrosionjournal.org/page/specialfeatures?code=nace-prem-site (accessed July 19, 2017).

[3] J. Villarreal, D. Laverde, C. Fuentes, Carbon-steel corrosion in multiphase slug flow and CO_2, Corros. Sci. 48 (2006) 2363–2379.

[4] Y.H. Sun, T. Hong, W.P. Jepson, Corrosion under wet gas conditions, CORROSION/2001, Paper No. 1034, NACE, Houston, Texas, 2001.

[5] Y.M. Gunaltun, D. Supriyatman, J. Achmad, Top of line corrosion in multiphase gas lines. A case history, CORROSION/99, Paper No. 36, NACE, Houston, Texas, 1999.

[6] M. Estavoyer, Corrosion problems at Lack sour gas field, in: H_2S Corros. Oil Gas Prod., NACE, Houston, Texas, 1981: p. 905.

[7] J. Oddo, M. Tomson, Simplified calculation of $CaCO_3$ saturation at high temperatures and pressures in brine solutions, J. Pet. Technol. 34 (1982) 1583–1590.

[8] J.R. Piccardino, M. Stuvik, Y. Gunaltun, T. Pornthep, Internal inspection of wet gas lines subject to top of line corrosion, CORROSION/2004, Paper No. 04354, NACE, Houston, Texas, 2004.

[9] U. Kaewpradap, Top of the line corrosion field case, Top Line Corros. Conf./2015, NACE, Jakarta, Indonesia, July 27-29, 2015.

[10] Y. Gunaltun, A. Belghazi, Control of top of the line corrosion by chemical treatment, CORROSION/2001, Paper No. 01033, NACE, Houston, Texas, 2001.

[11] M. Singer, A. Camacho, B. Brown, S. Nesic, Sour top-of-the-line corrosion in the presence of acetic acid, CORROSION/2010, Paper No. 10100, NACE, Houston, Texas , 2010.

[12] D. Hinkson, Z. Zhang, M. Singer, S. Nesic, Chemical composition and corrosiveness of the condensate in top-of-the-line corrosion, Corrosion. 66 (2010) 045002–045008.

[13] Y.M. Gunaltun, D. Larrey, Correlation of cases of top of line corrosion with calculated water condensation rates, CORROSION/2000, Paper No.00071, NACE, Houston, Texas, 2000.

[14] S. Nesic, Key issues related to modelling of internal corrosion of oil and gas pipelines - A review, Corros. Sci. 49 (2007) 4308–4338.

[15] S. Nesic, W. Sun, Corrosion in acid gas solutions, in: T.J.A. Richardson (Ed.), Shreir's Corros., Oxford, Elsevier, 2010: pp. 1270–1298.

[16] S. Nesic, J. Postlethwaite, S. Olsen, An electrochemical model for prediction of corrosion of mild steel in aqueous carbon dioxide solutions, Corrosion. 52 (1996) 280–294.

[17] Z. Zhang, D. Hinkson, M. Singer, H. Wang, S. Nesic, A Mechanistic model of top-of-the-line corrosion, Corrosion. 63 (2007) 1051–1062.

[18] F. Vitse, K. Alam, Y. Gunaltun, Semi-empirical model for prediction of the top of the line corrosion risk, CORROSION/2002, Paper No. 02245, NACE, Houston, Texas, 2002.

[19] R.A. Ojifinni, C. Li, A parametric study of sweet top-of-line corrosion in wet gas pipelines, CORROSION/2011, Paper No. 11331, NACE, Houston, Texas, 2011.

[20] C. Mendez, M. Singer, A. Camacho, S. Hernandez, S. Nesic, Y. Gunaltun, et al., Effect of acetic acid, pH and MEG on the CO_2 top of the line corrosion, CORROSION/2005, Paper No. 05278, NACE, Houston, Texas, 2005.

[21] R. Nyborg, A. Dugstad, Top of line corrosion and water condensation rates in wet gas pipelines, CORROSION/2007, Paper No. 07555, NACE, Houston, Texas, 2007.

[22] F. Vitse, S. Nesic, Y. Gunaltun, D.L. de Torreben, P. Duchet-Suchaux, Mechanistic model for the prediction of top-of-the-line corrosion risk, Corrosion. 59 (2003) 1075–1084.

[23] G. Svenningsen, R. Nyborg, Modeling of top of line corrosion with organic acid and glycol, CORROSION/2014, Paper No. 4057, NACE, Houston, Texas, 2014.

[24] S. Asher, W. Sun, R. Ojifinni, J. Pacheco, C. Li, J. Nelson, et al., Top of the line corrosion prediction in wet gas pipelines, CORROSION/2012, Paper No. C2012-0001303, NACE, Houston, Texas, 2012.

[25] M. Singer, D. Hinkson, Z. Zhang, H. Wang, S. Nesic, CO_2 top of the line corrosion in presence of acetic acid: A parametric study, Corrosion. 69 (2013) 719–735.

[26] G. Svenningsen, F. Martin, N. Rolf, H. Fukagawa, I. Kurniawan, Top of line corrosion with high CO_2 and organic acid, CORROSION/2013, Paper No. 2591, NACE, Houston, Texas, 2013.

[27] A. Dugstad, Top of Line Corrosion- impact of MEG and organic acid in the gas phase, CORROSION/2014, Paper No. 4382, NACE, Houston, Texas, 2014.

[28] T. Pojtanabuntoeng, M. Singer, S. Nesic, Top-of-the-line corrosion in the presence of hydrocarbon co-condensation in flowing condition, Corrosion/2012, Paper No. C2012-0001534, NACE, Houston, Texas, 2012.

[29] D. John, L. Capelli, B. Kinsella, S. Bailey, Top of the line corrosion control by chemical treatment, CORROSION/2009, Paper No. 09286, NACE, Houston, 2009.

[30] S. Olsen, A. Dugstad, Corrosion under dewing condition, CORROSION/91, Paper No 472, NACE, Houston, Texas, 1991.

[31] Y. Chen, L. Zhang, H. Qin, L. Xu, M. Lu, Effects of temperature on CO_2 top of line corrosion of pipeline steel, CORROSION/2011, Paper No. 11327, NACE, Houston, Texas, 2011.

[32] M. Singer, S. Nesic, Y. Gunaltun, Top of the line corrosion in presence of acetic acid and carbon dioxide, CORROSION/2004, Paper No. 04377, NACE, Houston, Texas, 2004.

[33] H. Qin, L. Xu, W. Chang, M. Lu, L. Zhang, Top of the line corrosion under low temperature and high condensation rate conditions, CORROSION/2011, Paper No. 11328, NACE, Houston, Texas, 2011.

[34] M. Oehler, Top-of-the-line corrosion control by continuous chemical treatment, PhD desertation, Curtin University, Perth, Australia, 2012.

[35] M.N. Lehmann, A. Lamm, H.M. Nguyen, C.W. Bowman, W.Y. Mok, B. Hughes, et al., Corrosion inhibitor and oxygen scavenger for use as MEG additives in the inhibition of wet gas pipelines, OFFSHORE TECHNOLOGY CONFERENCE/2014, Kuala Lumpur, 2014..

[36] E. Gulbrandsen, J. Morard, Why does glycol inhibit co_2 corrosion?, CORROSION/98, Paper No. 98221, NACE, Houston, Texas, 1998.

[37] P. Fosbøl, K. Thomsen, E. Stenby, Improving mechanistic CO_2 corrosion models, CORROSION/2009, Paper No. 09561, NACE, Houston, Texas, 2009.

[38] B.A. Stefl, S.F. Bosen, Buffering and inhibition of glycol in gas dehydration applications: an alternative to amines, Corrosion. 53 (1997) 163–168.

[39] S. Ramachandran, S. Mancuso, K.A. Bartrip, P. Hammonds, Inhibition of acid gas corrosion in pipelines using glycol for hydrate inhibition, CORROSION/2006, Paper No. 06447, NACE, Houston, Texas, 2006.

[40] I. Ivonye, C. Wang, X. Hu, A. Neville, Corrosion study of carbon steel in the

presence of monoethylene glycol (MEG) and corrosion inhibitors in acid, CORROSION/2013, Paper No. 2349, NACE, Houston, Texas, 2013.

[41] J. Kvarekvål, A. Pedersen, An electrochemical study of corrosion inhibition of carbon steel in sour glycol solutions, CORROSION/2013, Paper No. 2447, NACE, Houston, Texas, 2013.

[42] H. Ehsani, Influence of monoethylene glycol (MEG) on the corrosion inhibition of wet-gas flow lines, M Phil. desertation, Curtin University, Perth, Australia 2013.

[43] T. Tran, B. Brown, S. Nesic, B. Tribollet, Investigation of the electrochemical mechanisms for acetic acid corrosion of mild steel, Corrosion. 70 (2013) 223–229.

[44] M. Singer, Study of the localized nature of top of the line corrosion in sweet environment, Corrosion. 73 (2017) 1030–1055.

[45] D. Hinkson, M. Singer, Z. Zhang, S. Nesic, A study of the chemical composition and corrosivity of the condensate in top of the line corrosion, Corrosion/2008, Paper No. 08466, NACE, Houston, Texas, 2008.

[46] B.R. Linter, G.T. Burstein, Reactions of pipeline steels in carbon dioxide solutions, Corros. Sci. 41 (1999) 117–139.

[47] D.A. López, S.N. Simison, S.R. de Sánchez, The influence of steel microstructure on CO_2 corrosion. EIS studies on the inhibition efficiency of benzimidazole, Electrochim. Acta. 48 (2003) 845–854.

[48] J.B. Sun, G.A. Zhang, W. Liu, M.X. Lu, The formation mechanism of corrosion scale and electrochemical characteristic of low alloy steel in carbon dioxide-saturated solution, Corros. Sci. 57 (2012) 131–138.

[49] M. Rogowska, J. Gudme, A. Rubin, K. Pantleon, R. Ambat, Effect of Fe ion concentration on corrosion of carbon steel in CO_2 environment, Corros. Eng. J. 51 (2016) 25–36.

[50] A.S. Yaro, K.R. Abdul-Khalik, A.A. Khadom, Effect of CO_2 corrosion behavior of mild steel in oilfield produced water, J. Loss Prev. Process Ind. 38 (2015) 24–38.

[51] W. Sun, S. Nesic, R.C. Woollam, The effect of temperature and ionic strength on iron carbonate ($FeCO_3$) solubility limit, Corros. Sci. 51 (2009) 1273–1276.

[52] J.L. Mora-Mendoza, S. Turgoose, Fe_3C influence on the corrosion rate of mild steel in aqueous CO_2 systems under turbulent flow conditions, Corros. Sci. 44 (2002) 1223–1246.

[53] E.W.J. van Hunnik, B.F.M. Pots, E.L.J.A. Hendriksen, The formation of protective $FeCO_3$ corrosion product layer in CO_2 corrosion, CORROSION/1996, Paper No. 6, NACE, Houston, Texas, 1996.

[54] S. Nesic, K.L.J. Lee, A mechanistic model for carbon dioxide corrosion of mild steel in the presence of protective iron carbonate films - Part 3: Film growth model, Corrosion. 59 (2003) 616–628.

[55] A. Dugstad, Mechanism of protective film formation during CO_2 corrosion of carbon steel, CORROSION/98, Paper No. 31, NACE, Houston, Texas, 1998.

[56] L. Wei, X. Pang, C. Liu, K. Gao, Formation mechanism and protective property of corrosion product scale on X70 steel under supercritical CO_2 environment, Corros. Sci. 100 (2015) 404–420.

[57] M. Nordsveen, S. Nešić, R. Nyborg, A. Stangeland, A mechanistic model for carbon dioxide corrosion of mild steel in the presence of protective iron carbonate films - Part 1: Theory and verification, Corrosion. 59 (2003) 443–456.

[58] S. Nesic, M. Nordsveen, R. Nyborg, A. Stangeland, A mechanistic model for carbon dioxide corrosion of mild steel in the presence of protective iron carbonate films - Part 2: A numerical experiment, Corrosion. 59 (2003) 489–497.

[59] M. Gao, X. Pang, K. Gao, The growth mechanism of CO_2 corrosion product films, Corros. Sci. 53 (2011) 557–568.

[60] F. Farelas, M. Galicia, B. Brown, S. Nesic, H. Castaneda, Evolution of dissolution processes at the interface of carbon steel corroding in a CO_2 environment studied by EIS, Corros. Sci. 52 (2010) 509–517.

[61] S. Guo, F. Farelas, M. Singer, A glycol/water co-condensation model to investigate the influence of monoethylene glycol on top-of-the-line corrosion, Corrosion. 73 (2017) 742–755.

[62] M. Singer, Study and modeling of the localized nature of top of the line corrosion, PhD desertation, Ohio University, Ohio, USA, 2013.

[63] N.I. Uzelac, M. Beller, K. Reber, O.A. Barbian, New generation of ultrasonic in-line inspection tools, CORROSION/2004, Paper No. 4162, NACE, Houston, Texas, 2004.

[64] O. Stawicki, T. Beuker, R. Ahlbrink, B. Brown, Monitoring of top of line corrosion with eddy current technology combined with magnetic flux leakage method, CORROSION/2010, Paper No. 10094, NACE, Houston, Texas, 2010.

[65] S. Punpruk, M. Thammachart, Y. Gunaltun, Field testing of volatile corrosion inhibitors and evaluation of batch treatment efficiency by cooled probe, CORROSION/2010, Paper No. 10096, NACE, Houston, Texas, 2010.

[66] B.F.M. Pots, E.L.J.A. Hendriksen, CO_2 Corrosion under scaling conditions - the special case of top-of-line corrosion in wet gas pipelines, CORROSION/2000, Paper No. 00031, NACE, Houston, Texas, 2000.

[67] M. Oehler, S. Bailey, R. Gubner, M. Gough, Testing of generic volatile inhibitor compounds in different top-of-the-line corrosion laboratory test methods, CORROSION/2012, Paper No. 1483, NACE, Houston, Texas, 2012.

[68] S. Ramachandran, V. Jovancicevic, P. Rodgers, I. Ahmed, M. Al-Waranbi, A new top-of-the-line corrosion inhibitor to mitigate carbon dioxide corrosion in wet gas systems, CORROSION/2013, Paper No. 2274, NACE, Houston, Texas, 2013.

[69] K. Cattanach, S. Ramachandran, V. Jovancicevic, A new methodology for monitoring corrosion under sales gas conditions using the quartz crystal microbalance, CORROSION/2011, Paper No 11085, NACE, Houston, Texas, 2011.

[70] T. Pojtanabuntoeng, M. Singer, S. Nesic, Water/hydrocarbon co-condensation and the influence on top-of-the-line corrosion, CORROSION/2011, Paper No. 11330, NACE, Houston, Texas, 2011.

[71] Y. Gunaltun, T.E. Pou, M. Singer, C. Duret, S. Espitalier, Laboratory testing of volatile corrosion inhibitors, CORROSION/2010, Paper No. 10095, NACE, Houston, Texas, 2010..

[72] I. Jevremovic, M. Singer, M. Achour, D. Blumer, T. Baugh, V. Miskovic-Stankovic, et al., A novel method to mitigate the top-of-the-line corrosion in wet gas pipelines by corrosion inhibitor within a foam matrix, Corrosion. 69 (2012) 186–192.

[73] I. Jevremović, M. Singer, M. Achour, V. Mišković-Stanković, S. Nesic, Evaluation of a novel top-of-the-line corrosion (TLC) mitigation method in a large-scale flow loop, Corrosion. 71 (2015) 389–397.

[74] M. Singer, A. Camacho, B. Brown, S. Nesic, Sour top-of-the-line corrosion in the presence of acetic acid, Corrosion. 67 (2011) 85003–16.

[75] M. Singer, J. Al-Khamis, S. Nesic, Experimental study of sour top-of-the-line corrosion using a novel experimental setup, Corrosion. 69 (2013) 624–638.

[76] W. Sun, S. Nesic, Kinetics of corrosion layer formation: Part 1 - Iron carbonate layers in carbon dioxide corrosion, Corrosion. 64 (2008) 334–346.

.

Chapter 2: Condensation corrosion of carbon steel at low to moderate surface temperature and iron carbonate precipitation kinetics*

2.1 Abstract

This study investigates the influence of surface temperature and droplet retention time (DRT) on the corrosion rate, $FeCO_3$ supersaturation, and scaling tendency of carbon steel exposed to water condensation. This corrosion phenomenon is also known as top of the line corrosion (TLC). TLC is found to be governed by surface temperature irrespective of water condensation rates (WCR) at low surface temperature (15 °C). The results also demonstrate that the DRT directly influences $FeCO_3$ supersaturation and scale formation. A new kinetic constant for the calculation of $FeCO_3$ precipitation rate under condensing condition at the top of the line is proposed.

Keywords: Carbon steel; SEM; Weight loss; CO_2 corrosion; Kinetic parameters

2.2 Introduction

Corrosion due to water condensation commonly called top-of-the-line corrosion (TLC) occurs in wet gas transportation pipelines operating in stratified flow. Internal corrosion occurs at the upper portion (between 10 to 2 o'clock positions) where water condenses as a result of temperature difference between the outside environment and the process fluid [1-3]. Dissolved gases such as CO_2, H_2S and volatile organic acids are the prime corrosive constituents of the condensed liquid corroding the inner steel surface due to their acidic nature [4]. Since its discovery in 1960s, extensive laboratory studies and field data identified water condensation rate (WCR), gas temperature (T_g), gas flow rate, partial pressure of CO_2 and the presence of organic acids as the controlling factors of sweet TLC [4-9]. However, the most influential and interrelated factors in TLC are WCR, T_g and inner wall temperature or surface temperature (T_s) [10]. It can be anticipated that

* This chapter is reproduced from 'M.M. Islam, T. Pojtanabuntoeng, R. Gubner, Condensation corrosion of carbon steel at low to moderate surface temperature and iron carbonate precipitation kinetics, Corros. Sci. 111 (2016) 139–150'.

distinguishing the roles of each parameter could lead to a better understanding and an improved prediction model.

Literature has been focusing on the effect of WCR as it is considered to be the dominant parameter determining TLC severity. The critical WCR was estimated to be between 0.15 mL m^{-2} s^{-1} to 0.25 mL m^{-2} s^{-1} in low organic acid environment [10]. Wide ranges of WCR from 0.001 mL m^{-2} s^{-1} to 2.25 mL m^{-2} s^{-1} have been studied [8,10-16]. The direct proportional relationship between WCR and TLC rates has been reported. This is due to the constant replenishment of freshly condensed water prevents the condensed film to be saturated with $FeCO_3$.

It is apparent that WCR determines the droplet retention time (DRT) ─ the time at which a water droplet remains in contact with a steel surface before detaching due to gravity. Though the DRT is inversely proportional to WCR, the WCR only provides hypothetical droplet longevity instead of the exact duration. Hence, DRT is important information and may explain TLC mechanism since the water chemistry of a droplet continuously changes with time. Pojtanabuntoeng et al. observed the condensation pattern in water-hydrocarbon co-condensation system using a borescope but the longevity of droplet at different condensation rate was not reported [17].

Two dominant reactions; i.e. iron dissolution and iron carbonate precipitation, occur adjacent to the steel surface while undergo corrosion in CO_2 environment [18,19]. Therefore, the thermodynamic and kinetic of both reactions would be governed by T_s rather than T_g. Yet, most studies as well as prediction models addressed the TLC phenomenon as a function of T_g with little attention to T_s [7,20,21]. This is because WCR is assumed to be the governing parameter controlled by T_g.

For example, Nyborg and Dugstad developed an empirical model to calculate sweet TLC rate based on T_g, partial pressure of CO_2, and WCR excluding the effect of T_s [7]. According to the model, TLC rate increased from 0.03 mm y^{-1} to 0.14 mm y^{-1} when T_g increased from 30 °C to 90 °C as a result of an increasing condensation rate. A more advanced TLC prediction model determines TLC rate by taking into account the effect of T_g, CO_2 partial pressure, gas velocity, condensation rate, and acetic acid (HAc)

concentration. T_s is calculated implicitly through heat and mass transfer across the pipe wall [9].

The effect of the outer pipe wall temperature on TLC ranging from 5 °C to 90 °C has been investigated [10,14,20,22]. For instance, Asher et al. reported the effect of pipe wall temperature on TLC based on the mechanistic model and compared it with experimental results at a constant condensation rate of 0.1 mL m^{-2} s^{-1}. The study reported a declining trend of TLC rate with increasing wall temperature from 25 °C to 90 °C [10]. However, TLC scenario at low pipe wall temperature was reported by Qin et al. [22]. In this study, at a constant T_g of 25 °C, TLC rates only decreased slightly with an increasing wall temperature from 5 °C to 15 °C. The authors attributed their results to the slow electrochemical reaction kinetics at low temperature. With increasing temperature to 20 °C, corrosion rate decreased sharply due to low condensation rate combined with higher tendency of scale formation. It should be noted also that the experimental design applied in this study might produce an unrealistic condensation pattern where the condensed liquids glided vertically from top to bottom on a rotating flat samples instead of forming droplets.

Additionally, limited electrolyte at the top of the line (TOL) challenges the use of conventional electrochemical measurements and it has not been reported in an open literature. The measurement of TLC rate has been relied on weight loss method. This method provides an integrated corrosion rate over a long period of exposure and may not capture the continuous changes due to corrosion and scale formation processes at TOL surface. The competitive effect of these two phenomena can be best understood by an instantaneous monitoring of TLC rates and the water chemistry of the condensed water.

This study presents a new design of the TLC setup that is capable of direct measurement of T_s and *in-situ* collection and analysis of condensed water for its chemistry. With this new setup, the influences of the two interrelated parameters on sweet TLC; i.e. WCR and T_s, are differentiated at low to moderate surface temperatures. Additionally, the thermodynamic and kinetic of $FeCO_3$ scale formation at TOL are discussed based on DRT and water chemistry of the condensed liquid.

2.3 Experimental

2.3.5 Test material

A 1030 carbon steel rod (carbon 0.30 %, manganese 0.75 %, silicon 0.25 %, phosphorous 0.04 %, sulphur 0.04 % and iron balance) was used as a sample in this study. The 20 mm diameter steel rod was cut into 16 mm long cylindrical samples. After an initial polishing with 600 grit silicon carbide paper and rinsing with deionized (DI) water and ethanol, the samples were electro-coated with cationic epoxy (Powercron^{TM} 6000 CX) leaving one circular surface exposed for experiments. A 1.5 mm diameter hole was drilled 10 mm deep from the side of the sample just 1 mm above the exposed surface for inserting the surface temperature probe.

2.3.6 Experimental procedure

A schematic diagram of TLC set-up is shown in Figure 2.1. The exposed surface was polished with silicon carbide paper to 1200 grit surface finish, cleaned with DI water and ethanol, and dried with oil-free compressed air. The prepared carbon steel sample was weighed in an analytical balance which has a resolution of 0.1 mg. It was then inserted into the polyethylene terephthalate (PET) lid in such a way that the top coated portion was suspended into the cooling chamber and the bared portion was exposed to the corrosive environment. The bottom portion of the PET lid was machined at an angle of around 20° to allow any water droplets condensing on the lid to slide away and not mix into the collection cup. This was done to avoid an artificially high water condensation rate and potentially inaccurate assessment of the water chemistry. The temperature probe was inserted into the sample to measure surface temperature (T_s) and the other thermocouple was positioned in the gas phase near the sample to record gas temperature (T_g). The TLC lid was then placed onto a glass cell of 2 L volume assembled with CO_2 inlet and outlet, a thermocouple (to control bulk liquid temperature), and a condensed liquid collection cup. The whole assembly was deoxygenated by sparging with high purity CO_2 gas (99.99 %) for 10 min. The cooling chamber was connected to a water bath to maintain the desired T_s.

In a separate container, 1400 mL of high purity water (18.2 MΩ.cm), pre-sparged with high purity CO_2 overnight and preheated to a predefined temperature, was transferred to the TLC cell using a peristaltic pump to avoid oxygen contamination. T_g and T_s were controlled by adjusting the bulk liquid temperature and the cooling water temperature, respectively. As soon as T_g and T_s reached the desired value, the experiment started.

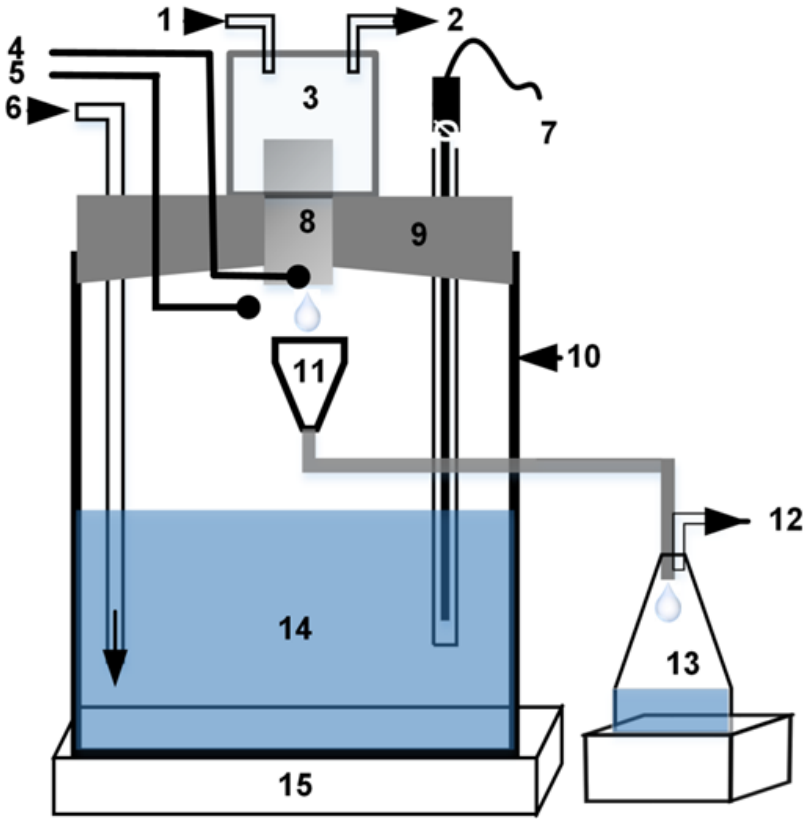

Figure 2.1: Schematic of top-of-the-line corrosion (TLC) setup; 1. Cooling water inlet, 2. Cooling water outlet, 3. Stainless steel cooling chamber, 4. Surface temperature probe, 5. Gas temperature probe, 6. CO_2 inlet, 7. Thermocouple, 8. Carbon steel sample, 9. Polyethylene terephthalate lid, 10. Glass vessel of 2 L volume, 11. Condensate collector, 12. CO_2 outlet, 13. Condensate reservoir, 14. High purity water, 15. Heater.

The condensed liquid, dropped into a condensate collector placed directly beneath the sample, was transferred immediately into the condensate reservoir at room temperature to avoid any re-evaporation. The liquid was then collected periodically from the reservoir to determine its mass, pH, and ferrous ion concentration. The water condensation rate was

calculated by dividing the collected condensed water with surface area and time. The *in-situ* corrosion rate was calculated based on dissolved iron (Fe^{2+}) presenting in the condensed liquid for a certain exposure time according to Eq. (2.1) [23,24]. The integrated corrosion rate was determined by summarising Fe^{2+} in the condensed liquid during the entire experiment.

$$R_{corr} = \frac{87600W}{At\rho} \tag{2.1}$$

where R_{corr} is the corrosion rate, mm y^{-1}; W is the dissolved iron measured in the condensed liquid, g; t is the test duration, h; A is the surface area, cm^2; ρ is the density of specimen, g cm^{-3}; 87600 is the unit conversion constant.

At the end of the experiment, the sample was removed from the lid, rinsed with ethanol and dried with high purity N_2 (99.99%). The sample surface was then examined with scanning electron microscope (SEM) and energy dispersive X-Ray spectroscopy (EDS). Several samples were also characterized with Raman Spectroscopy. Afterwards, corrosion products were removed following ASTM G1-03 using Clarke's solution (1000 mL of hydrochloric acid, 20 g of antimony trioxide and 50 g of stannous chloride) [24]. For each cleaning cycle, the specimen was pickled in Clarke's solution for 30 s with constant stirring, subsequently rinsed in DI water, acetone, and dried. The mass loss was plotted against cleaning cycles in which the change in slope indicates the complete removal of corrosion product. Finally, the weight loss corrosion rate was calculated using Eq. (2.1) but substituting W with the mass loss obtained from the chemical cleaning procedure.

2.3.7 Calculation of scaling tendency

The $FeCO_3$ scaling tendency was determined experimentally in a similar approach as described by Yaakob [25]. Accordingly, the corrosion products formed during the experiment was assumed to be comprised of solely $FeCO_3$.

Therefore, the difference between the mass loss obtained from chemical cleaning (W_1) and the total Fe^{2+} presenting the condensed water integrated over the entire test duration (W_2)

was assumed to deposit on the surface as $FeCO_3$ which was confirmed by performing a mass balance of Fe^{2+}. The scale formation rate (R_{SF}) and scaling tendency (S_T) were then calculated according to Eq. (2.2) [25] and Eq. (2.3) [15] respectively:

$$R_{SF} = \frac{(W_1 - W_2)M_1}{1000 M_2 A t} \tag{2.2}$$

$$S_{T(exp)} = \frac{R_{SF}}{R_{corr}} \tag{2.3}$$

where R_{SF} is the scale formation rate, kmol m^{-2} s^{-1}; W_1 is the mass loss obtained from chemical cleaning, g; W_2 is the total amount of Fe^{2+} measured in the condensed liquid, g; M_1 is the molecular weight of $FeCO_3$, 115.8 g mol^{-1}; M_2 is the molecular weight of Fe, 55.85 $gmol^{-1}$; A is the surface area of the steel sample, m^2; t is time, s; R_{corr} is corrosion rate, kmol m^{-2} s^{-1}; $S_{T(exp)}$ is the experimentally measured scaling tendency, dimensionless. Because scaling tendency ($S_{T(exp)}$) is a relative quantity between the rates of $FeCO_3$ formation and corrosion, it is dimensionless. Therefore, corrosion rate R_{corr} from Eq. (2.1) expressed in mm y^{-1} was converted to kmol m^{-2} s^{-1} in Eq. (2.3).

2.3.8 Measurement of droplet retention time (DRT)

Figure 2.2 depicts the arrangement of 3 thermocouples for DRT determination. In addition to the 2 thermocouples measuring the surface and gas temperatures, the third temperature probe was positioned just beneath the sample surface to measure the droplet temperature. The temperatures were recorded every 1 min. DRT determination experiments were carried out separately from corrosion experiments but at the same conditions. DRT was measured from the fluctuation of droplet temperature at a given T_s and T_g.

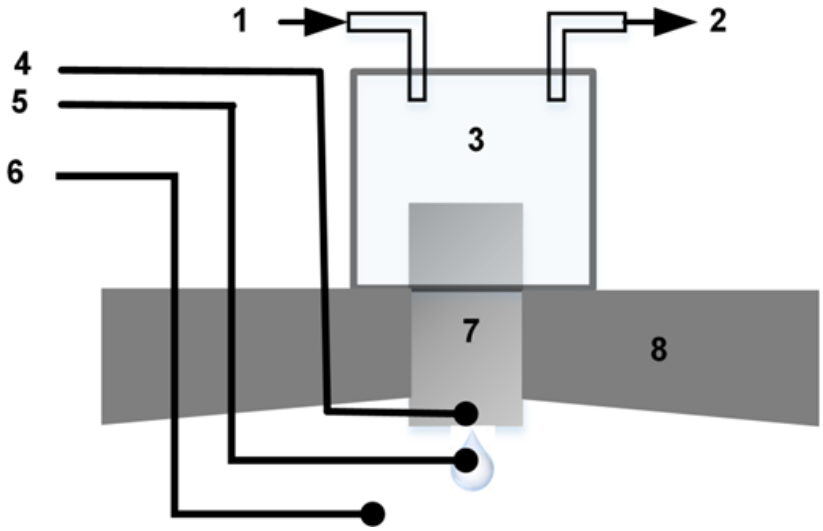

Figure 2.2: Schematic of measurement of droplet retention time (DRT); 1. Cooling water inlet, 2. Cooling water outlet, 3. Stainless steel cooling chamber, 4. Surface temperature probe, 5. Droplet temperature probe, 6. Gas temperature probe, 7. Carbon steel sample, 8. Polyethylene terephthalate lid.

2.4 Results

2.4.5 Droplet retention time (DRT) and water condensation rate (WCR)

Figure 2.3 illustrates the temperature fluctuation from the thermocouple dedicated for measuring the droplet temperature with time at gas temperature (T_g) = 40 °C and surface temperature (T_s) = 15 °C. Initially, this thermocouple read gas temperature and the reading decreased as the water droplet grew closer to this thermocouple. The lowest temperature reading was obtained when the droplet reached its maximum size and came into contact with the thermocouple. As soon as it detached from the surface, the reading reached back to the gas temperature denoting the initiation of the new droplet. In other word, for each cycle of a droplet, there was the maximum temperature indicating the initiation of a droplet and the minimum temperature representing when it fell. The interval between the two minimum readings indicated the DRT. For each condition, several intervals were recorded and the average value is reported with standard deviation. DRT for other conditions were measured in the same way.

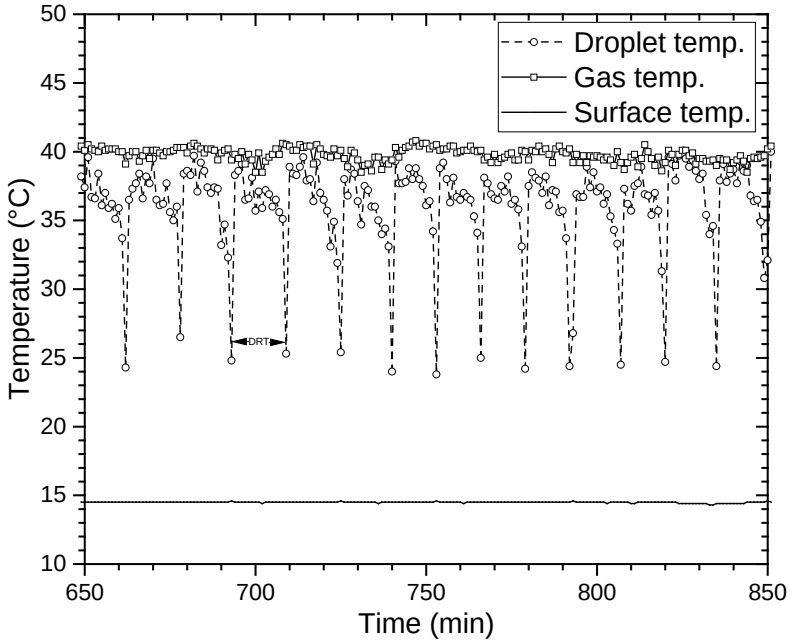

Figure 2.3: General fluctuation of surface, gas, and droplet temperature profile with time. Time interval between 2 minimum readings of droplet temperature show droplet retention time (DRT).

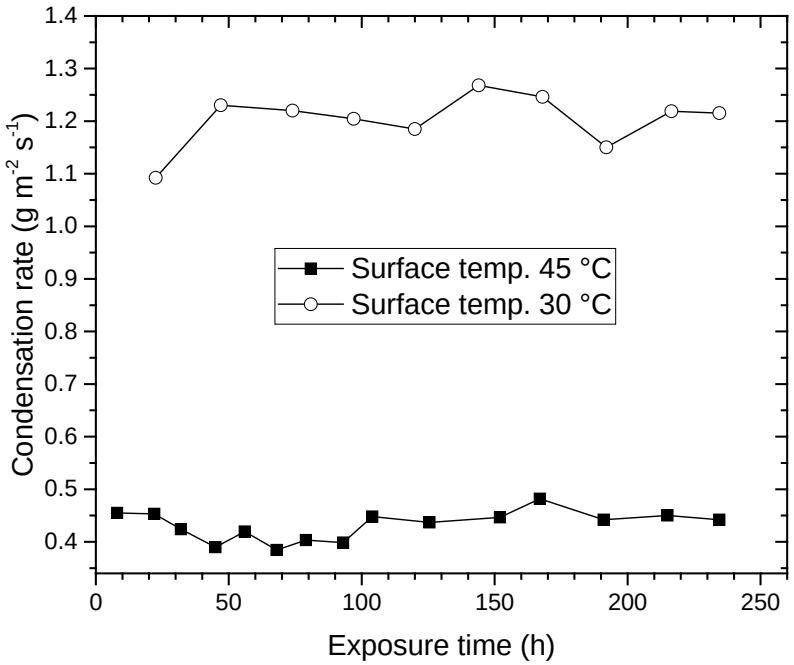

Figure 2.4: In-situ water condensation rate (WCR) at 55 °C gas temperature and different surface temperatures.

The *in-situ* WCR at T_g = 55 °C and at T_s = 30 °C and 45 °C are shown in Figure 2.4 illustrating that relatively constant WCR was maintained throughout the experiments.

Table 2.1 summarises the DRT and WCR at different experimental conditions. As expected, the shortest DRT of 6 min was recorded at the highest WCR of 1.55 g m^{-2} s^{-1} at T_g = 55 °C and T_s = 15 °C. The lowest WCR was 0.17 g m^{-2} s^{-1} at T_g = 41 °C and T_s = 40 °C. At this condition, it was not possible to identify the variation in droplet temperature due to the marginal difference between T_g and T_s. Hence, the DRT at low WCR was extrapolated and was found to be approximately 50 min (Figure 2.5).

Table 2.1: Water condensation rate (WCR) and droplet retention time (DRT) at different experimental conditions.

Condition		WCR ($g\ m^{-2}s^{-1}$)	DRT (min)
T_g (°C)	T_g (°C)		
55 ± 1	15 ± 0.5	1.55 ± 0.16	6.0 ±1
55 ± 1	30 ± 0.5	1.20 ± 0.05	7.5 ±1
55 ± 1	45 ± 0.5	0.43 ± 0.03	20.0 ±1
40 ± 1	15 ± 0.5	0.63 ± 0.02	14.0 ±1
40 ± 1	30 ± 0.5	0.34 ± 0.01	26.0 ±1
41 ± 1	40 ± 0.5	0.17 ± 0.02	50.0 ±1

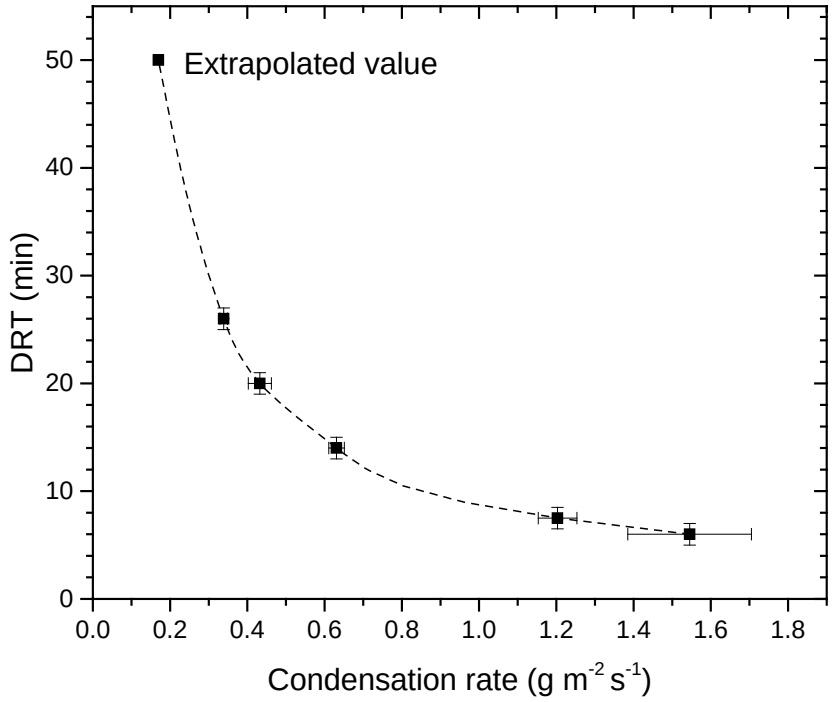

Figure 2.5: Droplet retention time (DRT) as a function of water condensation rate.

2.4.6 Top of the line corrosion (TLC) rates

Figure 2.6 depicts the *in-situ* corrosion rates calculated from Fe^{2+} in the condensed liquid at T_g = 55°C and varying T_s; i.e. 15 °C, 30 °C, and 45 °C. Two distinctive scenarios can be observed; namely i) an increasing corrosion rate with time (at 15 °C and 30 °C temperature) and ii) a relatively constant corrosion rate followed by a slight decline (at 45 °C temperature). At T_s = 15 °C, TLC rate gradually increased throughout the experiments to 0.95 mm y^{-1} which was approximately double compared to its initial value. Similar trend was also observed at T_s = 30 °C but the corrosion rate increased faster compared to the results obtained at 15 °C.

A different trend was observed at T_s = 45 °C. The TLC rates initially fluctuated within 0.55 mm y^{-1} to 0.67 mm y^{-1} with time up to approximately 160 h then consistently decrease for the next 80 h until the end of the experiment. Furthermore, after 240 h exposure, this condition exhibited the lowest corrosion rate of 0.51 mm y^{-1} despite its higher initial corrosion rate as compared to the experiment carried out at T_s = 15 °C.

Another set of experiments were conducted at lower T_g (40 °C) and different T_s and the *in-situ* TLC rates are depicted in Figure 2.7. The results revealed similar TLC rates and an increasing trend at T_s = 15 °C and 30 °C. The final corrosion rates were almost double compared to their initial values at both conditions. On the contrary, corrosion rates at T_s = 40 °C remained constantly low throughout the experiment.

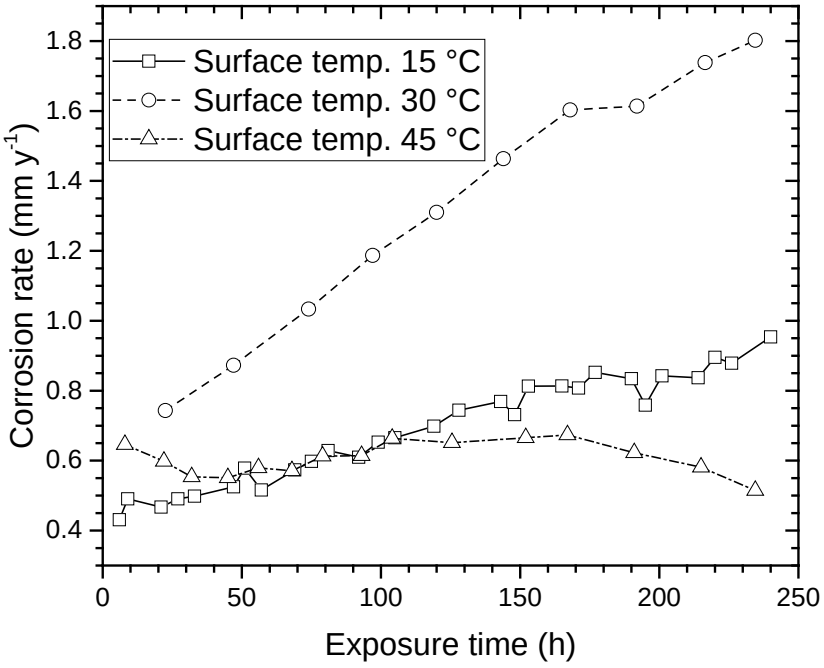

Figure 2.6: In-situ top of the line corrosion rates at 55 °C gas temperature and different surface temperatures.

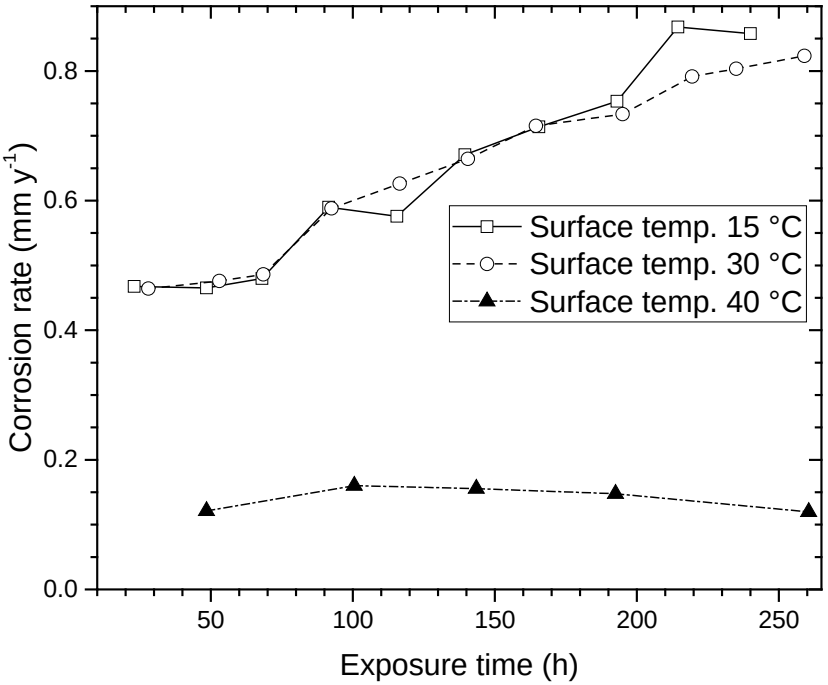

Figure 2.7: In-situ top of the line corrosion rates at 40 °C gas temperature and different surface temperatures.

The integrated TLC rates obtained from mass loss of the test coupons and also from the total Fe^{2+} in the condensed water are compared in Figure 2.8. The solid lines and dashed lines represent data obtained at T_g = 55 °C and 40 °C, respectively. Mass loss corrosion rate are slightly higher than that measured from Fe^{2+} measurement in the condensed liquid. This may be due to the fact that a portion of dissolved iron was retained on the surface as corrosion product and was not detected in the condensed liquid.

Figure 2.8 illustrates the dominant role of T_s on TLC rate. As T_s increased from 15 °C to 30 °C with a constant T_g = 55 °C, corrosion rates from both methods almost doubled, despite the slight decrease in condensation rate from 1.55 g m^{-2} s^{-1} to 1.20 g m^{-2} s^{-1} (Table 2.1). Similarly, at T_g = 40 °C, increasing T_s from 15 °C to 30 °C caused a slight increase in corrosion rate (0.73 mm y^{-1} to 0.81 mm y^{-1} from mass loss) despite the 2-fold decrease in the WCR. Figure 2.8 also demonstrates that at low T_s (15 °C), corrosion rate remained constant when T_g was increased from 40 °C to 55 °C even though WCR increased more than double (0.63 g m^{-2} s^{-1} to 1.55 g m^{-2} s^{-1}).

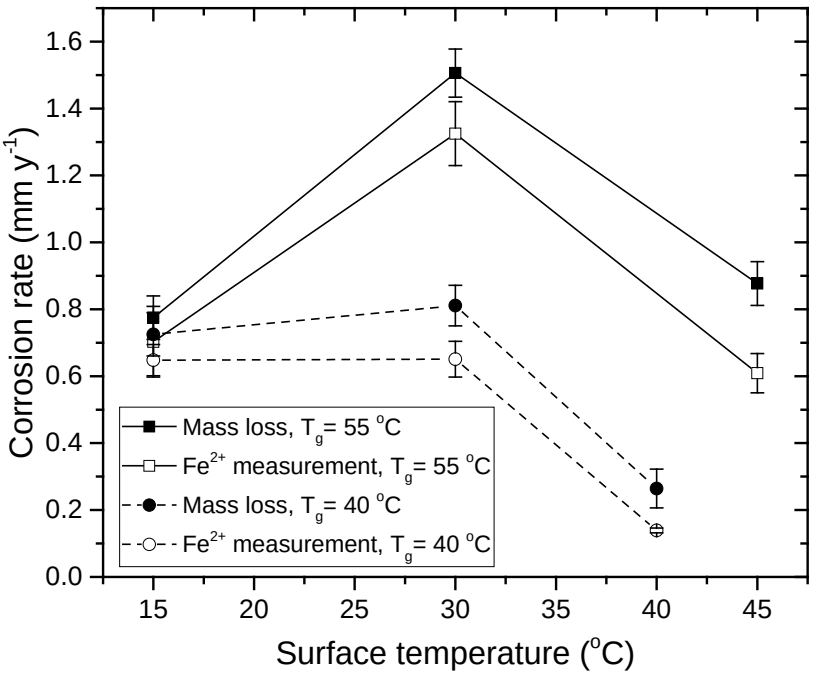

Figure 2.8: Top of the line corrosion rates obtained from mass loss and dissolved iron (Fe^{2+}) measurement at 55 °C and 40 °C gas temperature (T_g) and different surface temperature (T_s).

However, WCR still exhibited direct correlation with TLC rate and governed the corrosion process in a number of conditions. For instance, further increase of T_s from 30 °C to 45 °C reduced WCR from 1.20 g m^{-2} s^{-1} to 0.43 g m^{-2} s^{-1} and the corrosion rate from 1.5 mm y^{-1} to 0.88 mm y^{-1}. Another example can be seen at T_g = 41 °C and T_s = 40 °C where WCR was significantly low; i.e. 0.17 g m^{-2} s^{-1}. At this condition, low corrosion rates of 0.26 mm y^{-1} and 0.14 mm y^{-1} were obtained from mass loss and iron concentration measurement, respectively.

In short, it appears that WCR begins to play a significant role in determining the TLC rates when T_s is above 30 °C.

Furthermore, Figure 2.8 shows comparable integrated corrosion rates between T_s of 15 °C and 45 °C at T_g = 55 °C. However, the *in-situ* corrosion rates at these conditions show different trend as shown earlier in Figure 2.6. At 15 °C there is an increase in corrosion rate whereas at 45 °C the corrosion rate is declined. This signifies that without the *in-situ* corrosion rates, the corrosiveness of the situation at hand may be misinterpreted.

2.4.7 Surface analysis

Figure 2.9 shows the SEM images and EDS spectra of samples after exposing to T_g = 55 °C and different T_s for 240 h. Non-adherent corrosion product was observed on the surfaces at T_s = 15 °C and 30 °C [Figure 2.9(a) and (b)]. Iron carbonate crystal was not found from the SEM images under these conditions. EDS reveals low intensity peaks of carbon and oxygen in relation to that of iron which may indicate the presence of iron carbide and iron oxide. On the contrary, at T_s = 45 °C, well defined crystals are clearly visible in the SEM image shown in Figure 2.9(c) and the strong peak of oxygen in the EDS spectra might indicate the presence of $FeCO_3$ [27-29].

SEM images and EDS spectra of samples exposed to T_g = 40 °C and different T_s are shown in Figure 2.10(a) to (e). At low T_s of 15 °C, no $FeCO_3$ was observed in the SEM image shown in Figure 2.10(a). Increasing T_s slightly to 30 °C resulted in a different scenario. Though not uniformly distributed, $FeCO_3$ is visible in some areas as shown in the SEM images and EDS spectra [Figure 2.10(b) to (d)]. Increasing the T_s to 40 °C, closer to T_g, is more favourable for $FeCO_3$ precipitation. The entire surface was covered with $FeCO_3$ as indicated by SEM image and high intensity peak of oxygen from EDS [Figure 2.10(e)]. Figure 2.11 displays Raman spectra obtained from different areas on this sample. The peaks shown at 287 cm^{-1}, 731 cm^{-1}, 1090 cm^{-1} are the characteristics band of $FeCO_3$ [30].

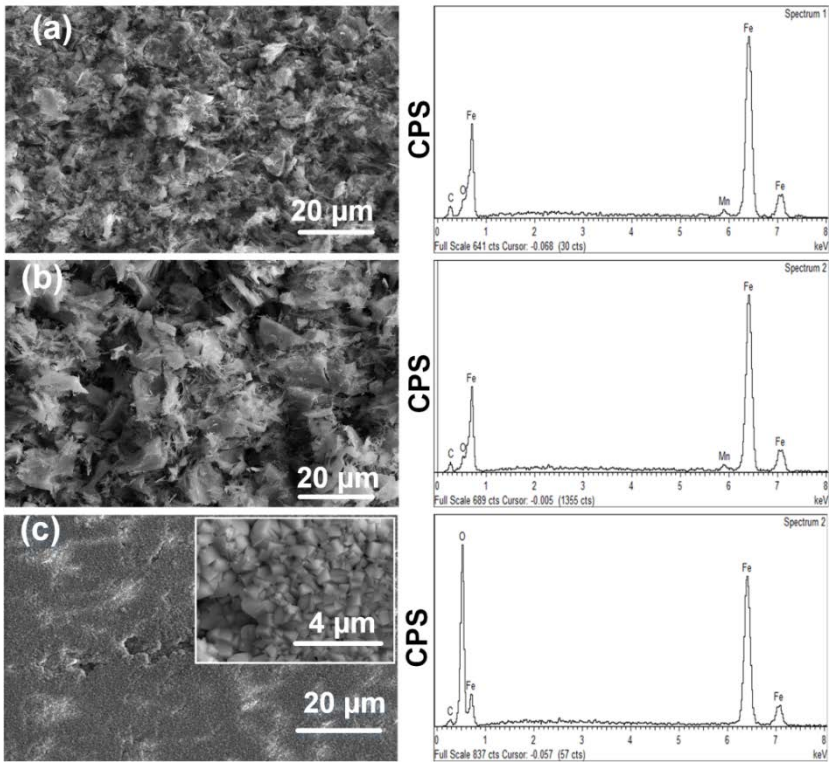

Figure 2.9: SEM images and EDS spectra of the samples after 240 hours of exposure at 55 °C gas temperature and (a) 15 °C, (b) 30 °C and (c) 45 °C surface temperature. $FeCO_3$ fully covered the underlying steel only at 45 °C surface temperature.

2.5 Discussion

The difference in TLC behaviour shown in the results section could be explained by the formation of $FeCO_3$ which is correlated with the water chemistry of condensed water, the supersaturation values, and the scaling tendencies. It can be assumed that the chemical reactions and corrosion mechanism at the TOL are identical to that at the bottom because of the same nature of electrochemical reactions and the aggressive species at the metal surface [9]. Therefore, the concentration of each species in the droplet can be calculated from the knowledge of water chemistry equilibrium in the condensed water in CO_2 environment.

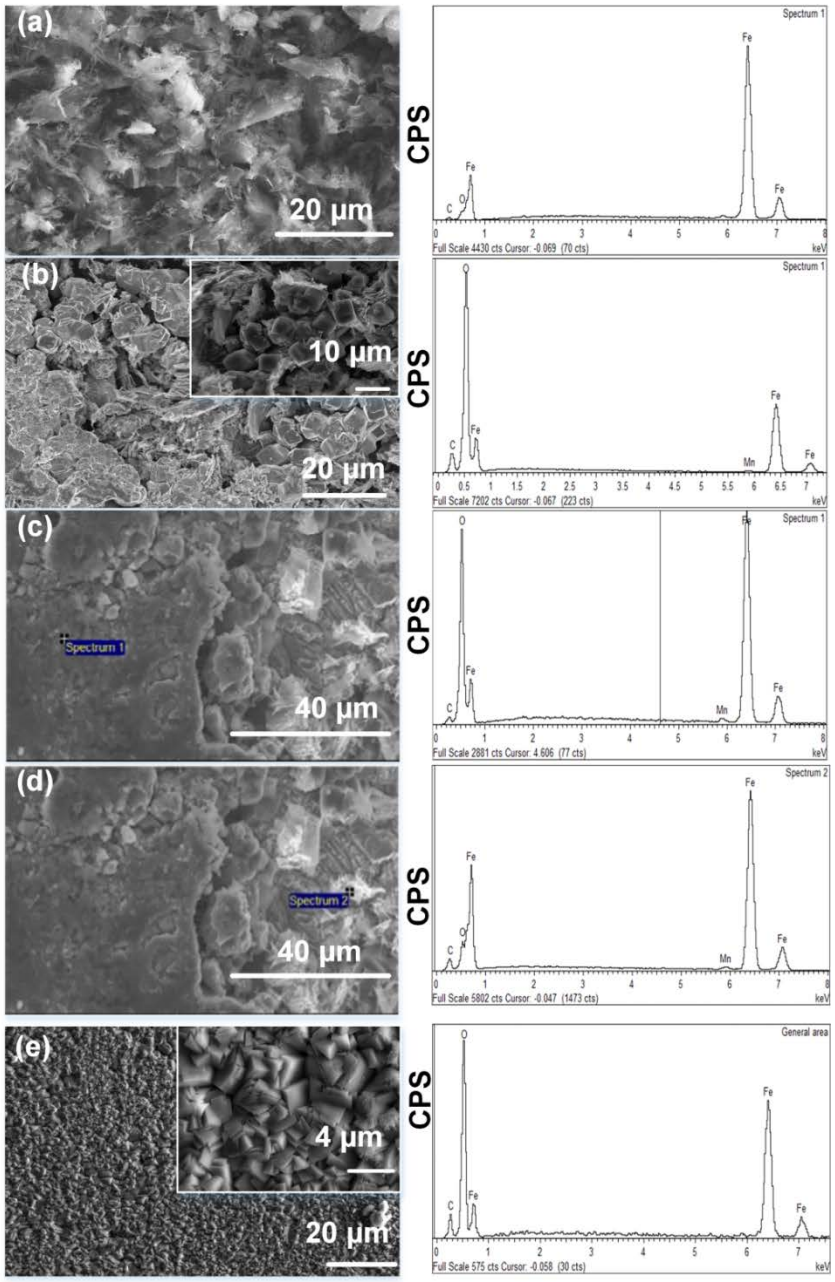

Figure 2.10: SEM images and EDS spectra of TLC the samples after 240 hours of exposure at 40 °C gas temperature and (a) 15 °C, b to d) 30 °C and (e) 40 °C surface temperature. Partial and full coverage of $FeCO_3$ were observed at 30 °C and 40 °C surface temperature, respectively.

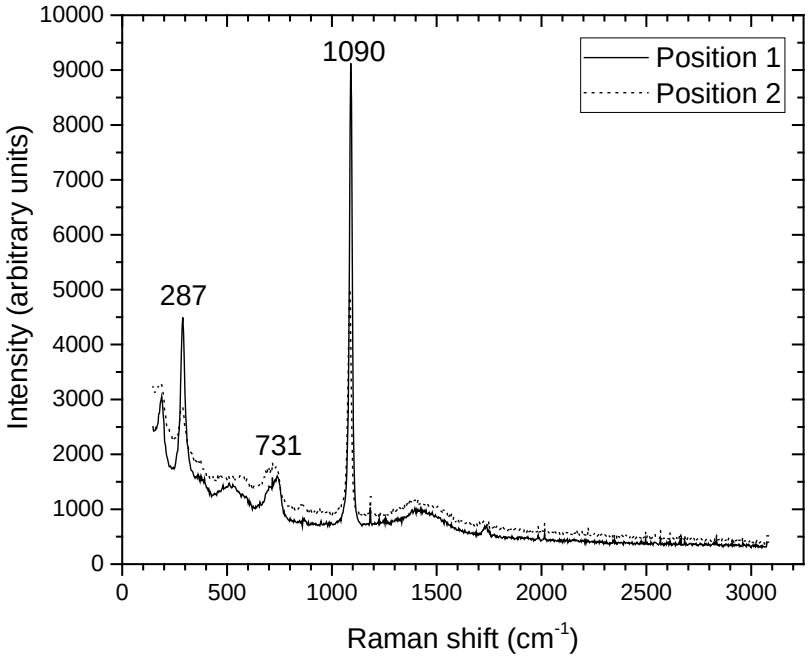

Figure 2.11: Raman shift of the sample after 240 hours of exposure at 41 °C gas temperature and 40 °C surface temperature confirming the presence of $FeCO_3$.

Below lists chemical reactions considered in this calculation [19,23,26,31,32]:

$$CO_{2(g)} \leftrightarrow CO_{2(aq)} \tag{2.4}$$

$$CO_{2(g)} + H_2O_{(aq)} \leftrightarrow H_2CO_{3(aq)} \tag{2.5}$$

$$H_2CO_{3(aq)} \leftrightarrow H^+_{(aq)} + HCO^-_{3(aq)} \tag{2.6}$$

$$HCO^-_{3(aq)} \leftrightarrow H^+_{(aq)} + CO^{2-}_{3(aq)} \tag{2.7}$$

$$H_2O_{(aq)} \leftrightarrow H^+_{(aq)} + OH^-_{(aq)} \tag{2.8}$$

where K_1, K_2, K_3, K_4, and K_5 are the equilibrium constants of reactions (2.4) to (2.8), respectively. The equilibrium constants are function of temperature, pressure and ionic strength (*I*) which can be found easily in the open literature [19,26]. *I* can be calculated from Eq. (2.9) as follows:

$$I = \frac{1}{2}\sum_i c_i z_i^2 \tag{2.9}$$

where I is ionic strength, in kmol m^{-3}; c_i is the concentration of the ith ion, kmol m^{-3}; z_i is its charge.

In the condensed liquid, dissolved iron (Fe^{2+}) is also present that needs to be taken into account to maintain the electro-neutrality. According to the electro-neutrality theory, the sum of positive charge is equal to that of negative charge which can be written as follows:

$$2c_{\mathrm{Fe^{2+}}} + c_{\mathrm{H^+}} = c_{\mathrm{HCO_3^-}} + 2c_{\mathrm{CO_3^{2-}}} + c_{\mathrm{OH^-}} \tag{2.10}$$

where $c_{\mathrm{Fe^{2+}}}$ is concentration of Fe^{2+} in the condensed liquid, kmol m^{-3}; $c_{\mathrm{H^+}}$, $c_{\mathrm{HCO_3^-}}$, $c_{CO_3^{2-}}$, and $c_{\mathrm{OH^-}}$ are the equilibrium concentration of H^+, HCO_3^-, CO_3^{2-} and OH^-, respectively in kmol m^{-3}. By combining the equilibrium constant formulas with Eq. (2.10), a mathematical equation with respect to $c_{\mathrm{H^+}}$ can be derived:

$$c_{H^+}^3 + 2c_{H^+}^2 - \left(K_5 + K_1K_2K_3p_{CO_2}\right)c_{H^+} - 2K_1K_2K_3K_4p_{CO_2} = 0 \tag{2.11}$$

where p_{CO_2} is partial pressure of CO_2 calculated using Antoine equation [33], bar.

2.5.5 pH of the condensed water

Because of the difficulty in measuring the pH of the condensed water *in-situ*, the pH was measured at room temperature in the condensate reservoir. Afterwards, *in-situ* pH of the condensed water was calculated using Eq. (2.11).

Figure 2.12 shows the comparison between the measured and calculated pH of the condensed water at T_g = 55 °C and T_s = 30 °C. The dotted line shows the pH measured at 25 °C temperature whereas the solid line is the calculated pH at the same temperature. Both the experimental and calculated data are in good agreement indicating the accuracy of the calculations.

The *in-situ* surface pH of the condensed water droplet at different experimental conditions calculated using Eq. (2.11) is depicted in Figure 2.13. In this case, T_s and partial pressure of CO_2 inside the test vessel were used in the calculation. Generally, pH of the condensed water varies from 5 to 6 based on experimental conditions. The figure reveals that the pH of the condensed water follows an identical trend with the *in-situ* corrosion rate as the concentration of Fe^{2+} governs the pH of the condensed water to balance the charge neutrality. Even though pH in some conditions increases with time, its influence on corrosion rate is negligible compared to other predominant factors such as T_s and condensation rates.

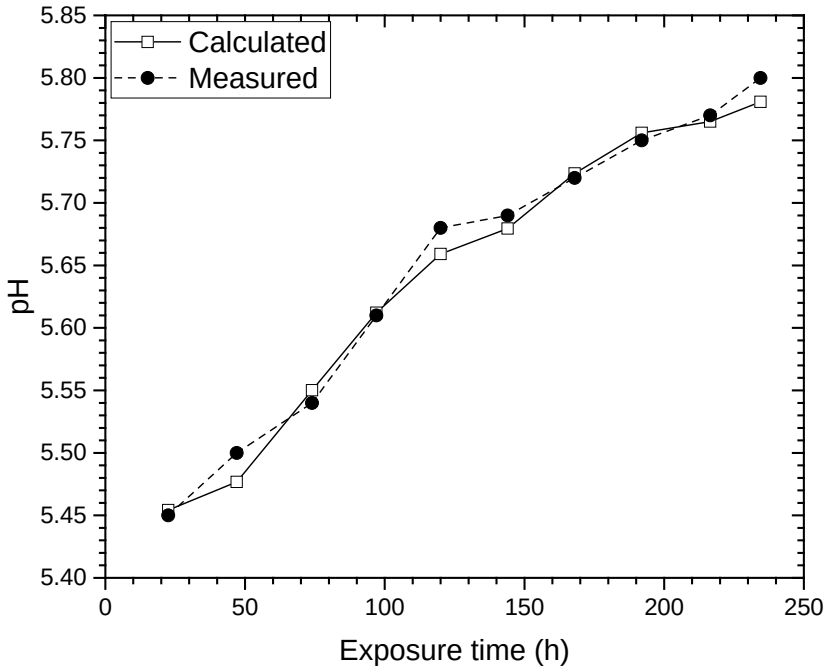

Figure 2.12: Comparison of calculated and experimentally measured pH of condensed water collected in the condensate reservoir at 25 °C. The condensation took place at 55 °C gas temperature and 30°C surface temperature.

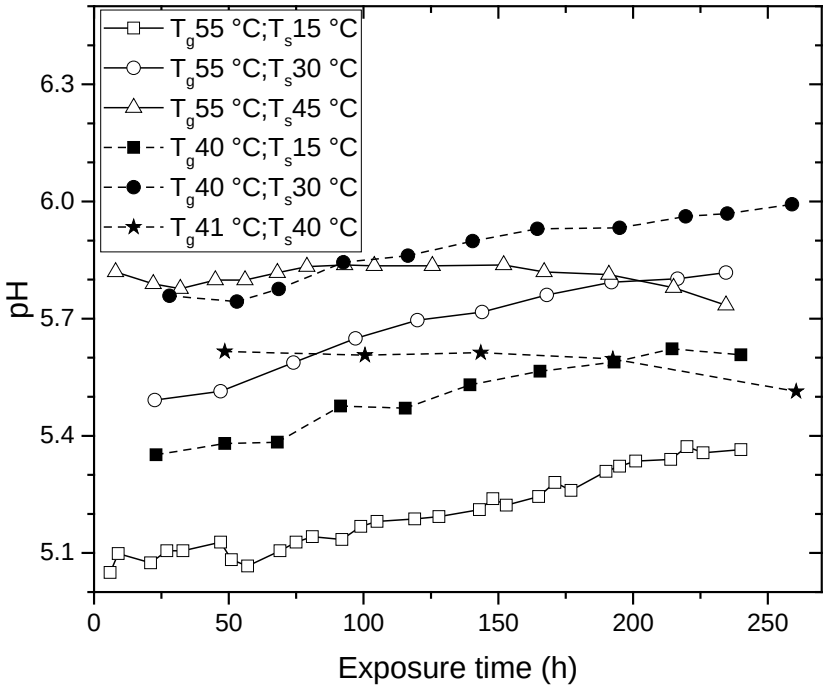

Figure 2.13: In-situ surface pH of the condensed water at different gas temperature (T_g) and surface temperature (T_s).

2.5.6 Iron carbonate supersaturation

As corrosion proceeds, concentration of Fe^{2+} in the water droplet increases favouring the formation of $FeCO_3$ according to Eq. (2.12) depending on the supersaturation and kinetics at the surface condition [8,34]:

$$Fe^{2+}_{(aq)} + CO^{2-}_{3(aq)} \overset{K_{sp}}{\longleftrightarrow} FeCO_{3(s)} \tag{2.12}$$

It is known that the presence of $FeCO_3$ can provide corrosion protection and may reduce corrosion rate [27]. The results showed that all test conditions do not favour $FeCO_3$ formation as it is controlled by T_s and WCR. To demonstrate this, the supersaturation and scaling tendency for each test conditions are required. The $FeCO_3$ supersaturation in the condensed water was calculated using Eq. (2.13) [26]:

$$S_S = \frac{c_{Fe^{2+}}\, c_{CO_3^{2-}}}{K_{sp}} \tag{2.13}$$

where S_S is the $FeCO_3$ supersaturation, dimensionless; $c_{Fe^{2+}}$ is ferrous ion concentration, kmol m^{-3}; $c_{CO_3^{2-}}$ is the concentration of carbonate ion obtained from calculation of chemical equilibrium, kmol m^{-3}; K_{sp} is the $FeCO_3$ solubility constant in (kmol m^{-3})^2. K_{sp} can be calculated using the Eq. (2.14) provided by Sun and Nesic [35]:

$$\log K_{sp} = -59.3498 - 0.041377T_k - \frac{2.1963}{T_k} + 24.5724\log(T_k) + 2.518I^{0.5} - 0.657I \quad (2.14)$$

where T_k is temperature, kelvin; and I is ionic strength, kmol m^{-3}.

$FeCO_3$ supersaturation of the condensed liquid with time at T_g = 55 °C and 40 °C with different T_s are presented in Figure 2.14(a) and 2.14(b), respectively. At T_s = 15 °C and T_g = 55 °C, the initial supersaturation was low but gradually increased to approximately 5 at the end of the experiment. However, it drastically increased overtime when the T_s was increased to 30 °C. On the contrary, supersaturation at T_s = 45 °C was the highest initially but relatively constant especially from 90 h to 160 h, after which it sharply decreased.

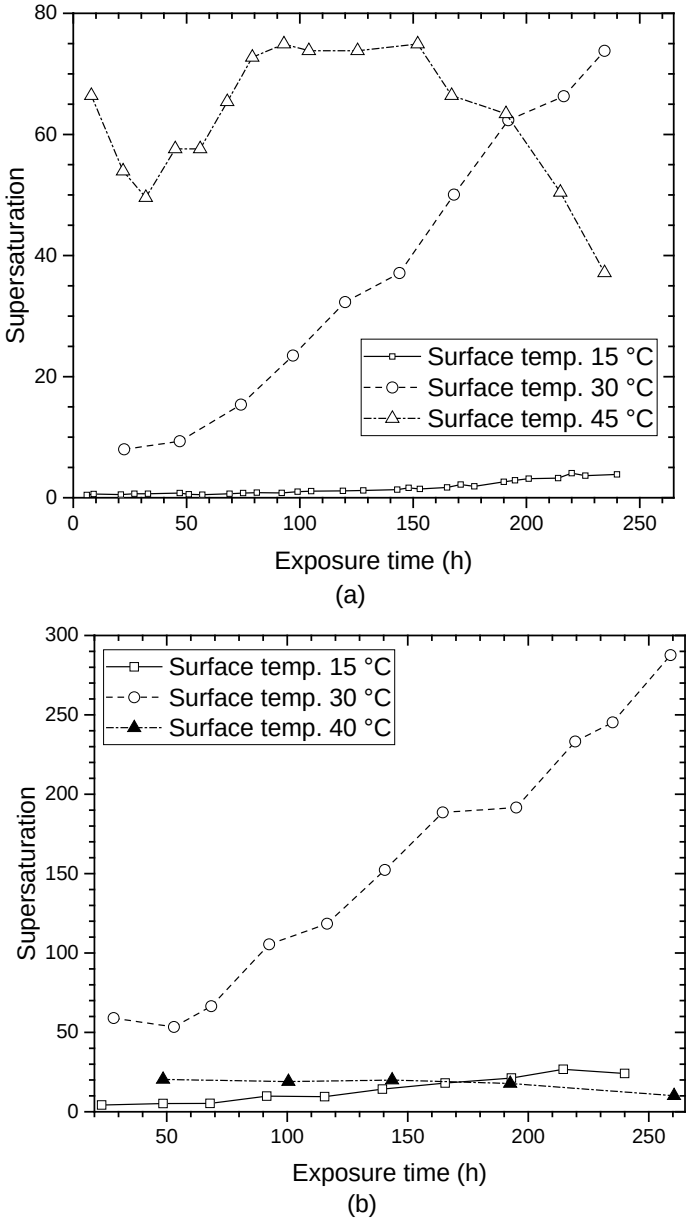

Figure 2.14: Iron carbonate supersaturation at a) 55 °C and b) 40 °C gas temperature and different surface temperature.

Similarly, at T_g = 40 °C as shown in Figure 2.14(b), the initial $FeCO_3$ supersaturation was the lowest at T_s = 15 °C which then gradually increased to 25 at the end of the experiment. At higher T_s of 30 °C, a drastic increase in the supersaturation value was observed; i.e. the highest initial supersaturation which also increased with time. Conversely, at T_s = 40 °C

and T_g = 41 °C, a relatively low supersaturation was observed which was constant up to around 200 h after which it gradually decreased.

Generally, the supersaturation of iron carbonate depends on the availability of ferrous ions, which originates from the corrosion process, the concentration of CO_3^{2-}, and the surface temperature where the reactions take place [36]. At T_g = 55 °C, supersaturation at T_s = 15 °C is significantly lower than that at T_s = 45 °C despite similar overall corrosion rates. This result emphasizes that iron carbonate formation is more favourable at a higher surface temperature due to the decrease in its solubility. In addition, the short DRT at T_s = 15 °C (6 min) did not allow sufficient contact time for $FeCO_3$ to precipitate. Conversely, high surface temperature along with comparatively long DRT creates supersaturation condition within condensed water droplet with iron carbonate at T_s = 45 °C. The latter condition favours the formation of iron carbonate scale on the sample surface thermodynamically and kinetically. When the protective iron carbonate scale forms and hinders the corrosion process, less iron dissolves into the condensed water which explains the decrease in supersaturation after around 160 h of exposure.

Meanwhile at T_s = 30 °C and T_g = 55 °C where corrosion rate was the highest, more iron dissolved into the condensed liquid raising supersaturation value and the precipitation of $FeCO_3$ became more thermodynamically favourable. However, no $FeCO_3$ was formed on the sample surface since $FeCO_3$ precipitation remains kinetically unfavourable at T_s = 30 ^oC due to short DRT (7.5 min).

A similar explanation is also applicable at T_g = 41 °C and T_s = 40 °C. This condition exhibited low supersaturation as a result of small amount of iron released from corrosion. Yet, $FeCO_3$ precipitated because of the long DRT of around 50 min. As a result, there was sufficient time to produce iron carbonate scale on the surface reducing further corrosion. This may explain the decline in supersaturation towards the end of the experiment. Similarly, Dugstad and Dronen reported the formation of $FeCO_3$ at 20 °C temperature and low precipitation rates at stagnant or semi-dry period for a long exposure time [37]. The authors suggested that the stagnant or semi-dry condition restricted the movement of

reactants or corrosion products which favoured the precipitation kinetics and improved the adherence of corrosion films.

From the above discussion, it can be concluded that the $FeCO_3$ precipitation at TOL is different from that at the bottom of the line (BOL). In case of BOL, high supersaturation generally favours the precipitation of iron carbonate [38]. But in case of TOL, high supersaturation may not always lead to the $FeCO_3$ formation if the droplets fall immediately. Conversely, $FeCO_3$ formation is possible at low supersaturation if enough time is given. This finding emphasizes that DRT is an important factor to be considered while investigating the TLC phenomena.

2.5.7 Scaling tendency of top of the line (TOL) specimen

2.5.7.1 Scaling tendency and iron content in the corrosion product

Scaling tendency is the measure of protectiveness of the surface by corrosion product. Scaling tendency was calculated based on experimental data using Eq. (2.3) and are reported in Table 2.2. It varies from 0.09 where no $FeCO_3$ precipitates to 0.47 where a protective $FeCO_3$ is observed.

To explain further, the effect of T_s on the experimental scaling tendency calculated using Eq. (2.3) and percentage of corroded iron forming the corrosion product at T_g = 55 °C and 40 °C are shown in Figure 2.15(a) and 2.15(b), respectively. At low T_s (15 °C), low scaling tendency of 0.1 was found at both T_g. Increasing T_s to 30 °C but maintaining T_g at 55 °C resulted in a slight increase of scaling tendency to 0.12. A significant increase in scaling tendency from 0.12 to 0.3 was observed once T_s was increased to 45 °C. Likewise, at T_g = 40 °C, it marginally increased to 0.2 with increasing T_s from 15 to 30 °C. Afterwards, a sharp rise of scaling tendency was found when the T_s was raised to 40 °C to reach a value of about 0.5.

The rise in scaling tendency is also supported by Figure 2.15(b) which demonstrates a profound increase in the precipitation of corrosion product on the surface. It is found that at T_s below 30 °C, less than 20% of the corroded iron was retained on the surface while the remaining dissolved into the condensed water. The conditions resulting in the lack of

protective corrosion product formation can be correlated to those conditions where corrosion rate increased with time. On the contrary, at 45 °C T_s, almost 33% of the corroded iron was retained on the surface contributing to high scale formation tendency. Around 48% of the corroded iron remained on the surface as a corrosion product when T_s and T_g were maintained at 40 °C and 41 °C, respectively, producing the highest scaling tendency among the experiments conducted.

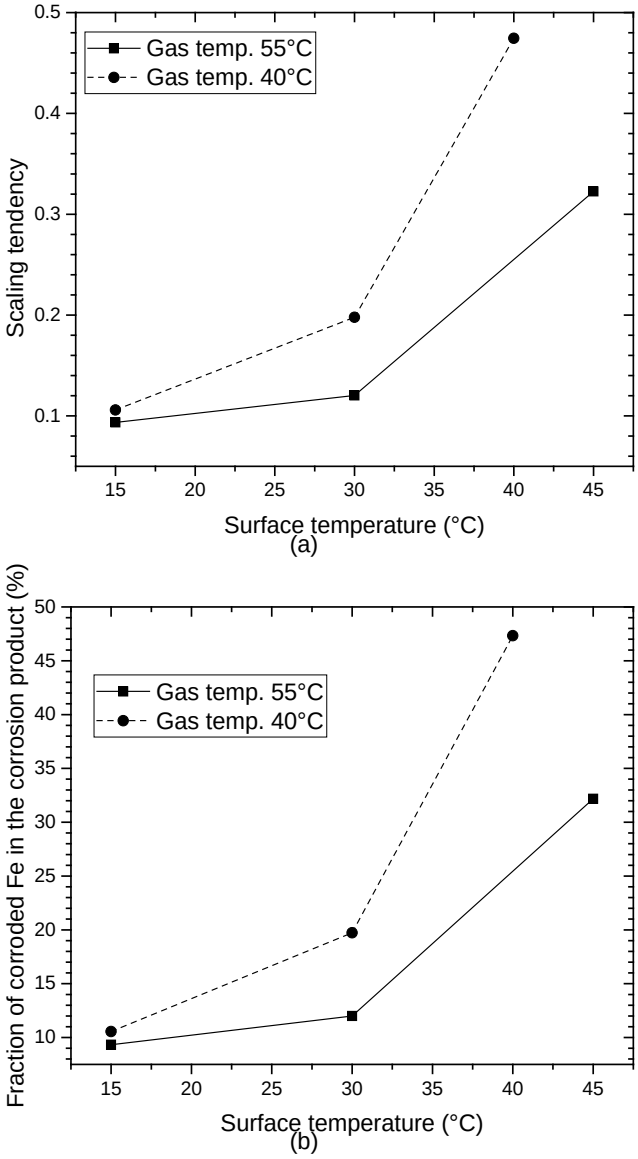

Figure 2.15: Effect of surface temperature on (a) experimental scaling tendency from Eq. (2.3) and (b) % of corroded iron retained on the surface at 55 °C and 40 °C gas temperature.

2.5.7.2 Comparison with existing scaling tendency correlation – New kinetic constant

To elucidate the observed TLC behaviour, scaling tendency values from the measurements were compared with previously proposed calculations. According to Nesic and Sun, scaling tendency is defined as the ratio of precipitation rate (R_P) to the corrosion rate (R_{corr}) expressed in same unit as shown in Eq. (2.15) [26]:

$$S_T = \frac{R_P}{R_{corr}} \tag{2.15}$$

Johnson and Thomson first proposed Eq. (2.16) to calculate the precipitation of $FeCO_3$ (R_P) at low level of supersaturation [39]:

$$R_P = K_r \frac{S}{V} K_{sp}[(S_S)^{0.5} - 1]^2 \tag{2.16}$$

where R_P is the iron carbonate precipitation rate, kmol m^{-3} s^{-1}; K_r is the kinetic constant, m^4 $kmol^{-1}$ s^{-1}; S/V is the surface to volume ratio, m^{-1}. But this equation overestimated R_P at high supersaturation level as stated by Van Hunnik et al. [40]. Consequently, they proposed another equation based on their experimental results as shown in Eq. (2.17) [40]:

$$R_P = K_r \frac{S}{V} K_{sp}(S_S - 1)(1 - {S_S}^{-1}) \tag{2.17}$$

However, R_P calculated from Eq. (2.17) was based on the decrease in Fe^{2+} concentration in the bulk solution. Van Hunnik et al. asserted that the total "lost" of Fe^{2+} ion in the solution was equivalent to the $FeCO_3$ precipitation rate on the steel surface assuming all the precipitation occurred on the steel surface [40].

Sun and Nesic discovered that $FeCO_3$ not only precipitated on the steel surface but also deposited elsewhere in the test system [38]. To determine the actual tendency of $FeCO_3$ precipitation, only precipitates on the steel surface should be considered. Subsequently, Sun and Nesic proposed the weight-change method to calculate "corrosion layer accumulation rate (R_{CLA})" as presented in Eq. (2.18) in order to distinguish it from the homogeneous precipitation [41]:

$$R_{CLA} = K_r K_{sp}(S_S - 1) \tag{2.18}$$

where R_{CLA} is the corrosion layer accumulation rate, kmol m^{-2} s^{-1}; K_r is the kinetic constant in m^4 kmol^{-1} s^{-1} calculated from Eq. (2.19):

$$K_r = e^{A-\frac{B}{RT_k}} \tag{2.19}$$

where A = 28.2 and B = 64851 J mol^{-1}; R = 8.314 J mol^{-1} K^{-1}.

Therefore, the scaling tendency at different conditions was calculated using R_{CLA} instead of R_P as shown in Eq. (2.20) [76] and the results are tabulated in Table 2.2.

$$S_{T(cal)} = \frac{R_{CLA}}{R_{corr}} \tag{2.20}$$

where $S_{T(cal)}$ is the calculated scaling tendency, dimensionless; R_{CLA} is corrosion product layer accumulation rate calculated from Eq. (2.18), kmol m^{-2} s^{-1}; R_{corr} is corrosion rate from dissolved iron measurement, kmol m^{-2} s^{-1}.

Table 2.2: Comparison of experimentally measured scaling tendency ($S_{T(exp)}$) and calculated scaling tendency ($S_{T(cal)}$) at different conditions.

Condition		$S_{T(exp)}$	$S_{T(cal)}$		$FeCO_3$ formation
T_g (°C)	T_s (°C)		Kinetic constant 28.2	Kinetic constant 24.6	
55	15	0.09	0.00-0.04	0.00	Not formed
55	30	0.12	0.46-2.40	0.00-0.07	Not formed
55	45	0.32	9.69-17.74	0.26-0.48	Formed
40	15	0.10	0.10-0.53	0.00-0.01	Not formed
40	30	0.20	6.38-24.91	0.20-0.68	Formed
41	40	0.47	7.16-15.82	0.20-0.43	Formed

Generally, it has been postulated that S_T<<1 produces porous and non-protective films, whereas, dense and protective $FeCO_3$ films are formed if S_T becomes greater or equals to one [26]. However, the critical S_T, at which effective corrosion reduction by $FeCO_3$ starts, can vary between 0.4 to 1 depending on carbon content in the steel [40].

Literature has reported good agreement between the scaling tendency criteria mentioned above and the observation of protective $FeCO_3$ in the bottom of the line condition. However, it appears that such criteria cannot be applied at TOL as shown in Table 2.2. For instance, calculated scaling tendency, $S_{T(cal)}$ using Eq. (2.20) at T_g = 55 °C and T_s = 30 °C was 0.46 to 2.4. But, no $FeCO_3$ precipitation was found on the sample surface at this condition. The over estimation of scaling tendency is observed for other conditions as well.

It can be postulated that the water droplets do not attach on the surface for constant period of time. As corrosion proceeds, Fe^{2+} concentration and temperature within the droplet varies from its initiation to termination. On the contrary, the larger volume of liquid in the BOL prevents the fluctuation of iron concentration due to corrosion. This highlights the significance of the difference in precipitation kinetics at TOL and BOL though similar reactions are taking place in CO_2 environment. Hence, the arbitrary kinetic constant '*A*' presented in Eq. (2.19) is not suitable for TOL condition.

A new value of '*A*' has been recalculated to 24.6 instead of 28.2 to match the calculated scaling tendency with experimental value as shown in Table 2.2.

The comparisons of scaling tendency using the new kinetic constant in general are in good agreement with the experimental value and theoretical concept. A minor discrepancy was found at T_s = 15 °C. At this temperature, no iron carbonate formation was identified on the surface as confirmed by SEM and EDS. So, the corrosion product retained on the surface might be iron carbide or iron oxide. But, during the calculation of scale formation rate using Eq. (2.2), the corrosion product was entirely assumed to be iron carbonate which makes the experimental scaling tendency slightly higher than the calculated value. In other cases, where iron carbonate precipitation was confirmed, the scaling tendencies obtained from both methods are comparable.

From the above discussion it can be concluded that a scaling tendency of around 0.5 is sufficient to form an iron carbonate layer in TOL and the proposed kinetic constant can be applied for the calculation of scaling tendency in the TOL.

2.5.8 Corrosion behaviour and $FeCO_3$ formation at the top of the line

Three important processes are assumed to take place simultaneously at the TOL: chemical reactions both homogeneous (dissociation, dissolution, etc.) and heterogeneous (precipitation of corrosion product scales); electrochemical reactions at the metal surface; and transport of species in the liquid droplet mainly by diffusion [9]. Depending on the conditions, the slowest step is the rate determining step.

The results have demonstrated that WCR alone simply cannot explain the TLC behaviour; TLC rates were independent of WCR in few occasions. For example, referring to Figure 2.8, it was found that at T_g = 55 °C, an increase of T_s from 15 °C to 30 °C increased the corrosion rates although the condensation rate decreased. Similarly, at T_s = 15 °C, an increase of T_g from 40 °C to 55 °C significantly increased the condensation rate but there was no significant change in TLC rates observed. Therefore, T_s is the governing factor and not the WCR. It is evident that the kinetic of any chemical reaction slows down at low temperature including iron dissolution process and $FeCO_3$ precipitation. Because of slow iron dissolution, the Fe^{2+} concentration in the condensed liquid remains low resulting in very low supersaturation and virtually very low or no accumulation of corrosion product on the surface.

It appears that the TLC rates increased with time throughout the entire period for those conditions where no or partially formed iron carbonate scale was found on the metal surface. It has been hypothesised that cementite (Fe_3C) and ferrite (α-Fe) are two important components of carbon steel microstructure in a corroding system [34,42,43]. As corrosion proceeds, ferrite, which has higher energy and electric potential, corrodes and dissolves into the condensed liquid while the cementite phase remains on the surface [27,44]. The latter being electrically conductive forms galvanic coupling with the remaining ferrite and acts as cathode; thereby increasing corrosion rate with time [45,46].

In addition, the local acidification of the solution imprisoned within the undissolved cementite layer could be another plausible explanation for the increasing of the corrosion rate over time [47].

The role of WCR becomes more prominent at higher T_s when $FeCO_3$ formation becomes thermodynamically favourable. For instance, the initial supersaturation at T_s = 45 °C and T_g = 55 °C was the highest among other T_s. Higher T_s may increase the iron dissolution rate but more importantly favours the thermodynamic of $FeCO_3$ precipitation as indicated by the highest initial supersaturation. In addition, the relatively low condensation rate (0.4 g m^{-2} s^{-1}) allows the droplet to retain at the surface for a longer period of time (approximately 20 min). The high temperature complimented by the long retention time promoted the formation of iron carbonate on the surface. Because of the reduction in TLC observed in Figure 2.6, this scale formation is considered protective as it provides a barrier to the underlying surface keeping it away from corrosive constituents. Therefore, the TLC at this condition is no longer governed by T_s (iron dissolution) alone but also by WCR (the iron carbonate scale formation). A similar explanation can be used for T_g = 40 °C when the T_s increased from 30 °C and 40 °C.

2.6 Conclusions

- A new technique has been developed to calculate the droplet retention time (DRT). It has been found that the droplets stay on the surface at the top of the line (TOL) from about 6 min to 50 min depending on water condensation rates under the chosen experimental conditions.
- At low surface temperatures (T_s = 15 °C), top of the line corrosion (TLC) is mainly governed by the surface temperature irrespective of the water condensation rate (WCR). But at moderate surface temperatures (T_s greater than 30 °C), both the surface temperature and water condensation rate influence TLC.
- The study reveals that iron carbonate supersaturation and DRT are the important parameters controlling iron carbonate precipitation. High supersaturation with low retention time may not favour the protective iron carbonate formation. Conversely,

low supersaturation with long retention time would be able to provide adequate protection on the TOL by forming the scale of iron carbonate.

- Based on the water chemistry calculation and experimental data, it has been found that the kinetic behaviour of iron carbonate formation at TOL is different from that at the bottom of the line. A new kinetic constant has been proposed for the calculation of iron carbonate formation rate at the TOL.

Acknowledgements

The authors would like to acknowledge the Microscopy & Microanalysis Facility (MMF), Curtin University for the access of SEM and EDS. One of us (M.M.I.) thanks the Curtin University for International Postgraduate Research Scholarship (IPRS).

2.7 References

[1] J.R. Piccardino, M. Stuvik, Y. Gunaltun, T. Pornthep, Internal Inspection of Wet Gas Lines Subject to Top of Line Corrosion, CORROSION/2004, Paper No. 04354, NACE, Houston, TX, 2004.

[2] Y.M. Gunaltun, D. Supriyatman, J. Achmad, Top of Line Corrosion in Multiphase Gas Lines. A Case History, CORROSION/99, Paper No. 36, NACE, Houston, TX, 1999.

[3] S. Nesic, Key issues related to modelling of internal corrosion of oil and gas pipelines - A review, Corros. Sci. 49 (2007) 4308–4338.

[4] D. Hinkson, Z. Zhang, M. Singer, S. Nesic, Chemical composition and corrosiveness of the condensate in top-of-the-line corrosion, Corrosion. 66 (2010) A1–8.

[5] M. Singer, J. Al-Khamis, S. Nesic, Experimental study of sour top-of-the-line corrosion using a novel experimental setup, Corrosion. 69 (2013) 624–638.

[6] M. Singer, S. Nesic, Y. Gunaltun, Top of the Line Corrosion in Presence of Acetic Acid and Carbon Dioxide, CORROSION/2004, Paper No. 04377, NACE, Houston, TX, 2004.

[7] R. Nyborg, A. Dugstad, Top of Line Corrosion and Water Condensation Rates in Wet Gas Pipelines, CORROSION/2007, Paper No. 07555, NACE, Houston, TX, 2007.

[8] G. Svenningsen, R. Nyborg, Modeling of Top of Line Corrosion with Organic Acid and Glycol, CORROSION/2014, Paper No. 4057, NACE, Houston, TX, 2014.

[9] Z. Zhang, D. Hinkson, M. Singer, H. Wang, S. Nesic, A mechanistic model of top-of-the-line corrosion, Corrosion. 63 (2007) 1051–1062.

[10] S.L. Asher, W. Sun, R. Ojifinni, J. Pacheco, C. Li, J. Nelson, S. Ling, Top of the Line Corrosion Prediction in Wet Gas Pipelines, CORROSION/2012, Paper No. 01303, NACE, Houston, TX, 2012.

[11] Y.M. Gunaltun, D. Larrey, Correlation of Cases of Top of Line Corrosion with Calculated Water Condensation Rates, CORROSION/2000, Paper No. 00071, NACE, Houston, TX, 2000.

[12] M. Singer, D. Hinkson, Z. Zhang, H. Wang, S. Nesic, CO_2 top of the line corrosion in presence of acetic acid: A parametric study, Corrosion. 69 (2013) 719–735.

[13] G. Svenningsen, M. Foss, R. Nyborg, H. Fukagawa, I. Kurniawan, Top of Line Corrosion with High CO_2 and Organic Acid, CORROSION/2013, Paper No. 2591, NACE, Houston, TX, 2013.

[14] R.A. Ojifinni, C. Li, A Parametric Study of Sweet Top-of-Line Corrosion in Wet Gas Pipelines, CORROSION/2011, Paper No. 11331, NACE, Houston, TX, 2011.

[15] A. Dugstad, Top of Line Corrosion- Impact of MEG and Organic Acid in the Gas Phase, CORROSION/2014, Paper No. 4382, NACE, Houston, TX, 2014.

[16] T. Pojtanabuntoeng, M. Singer, S. Nesic, Top-of-the-Line Corrosion in the Presence of Hydrocarbon Co-Condensation in Flowing Condition, CORROSION/2012, Paper No. 01534, NACE, Houston, TX, 2012.

[17] T. Pojtanabuntoeng, M. Singer, S. Nesic, Water/Hydrocarbon Co-Condensation and the Influence on Top-of-the-Line Corrosion, CORROSION/2011, Paper No. 11330, NACE, Houston, TX, 2011.

[18] B.R. Linter, G.T. Burstein, Reactions of pipeline steels in carbon dioxide solutions, Corros. Sci. 41 (1999) 117–139.

[19] G.A. Zhang, Y.F. Cheng, On the fundamentals of electrochemical corrosion of X65 steel in CO_2-containing formation water in the presence of acetic acid in petroleum production, Corros. Sci. 51 (2009) 87–94.

[20] Y. Chen, L. Zhang, H. Qin, L. Xu, M. Lu, Effects of Temperature on CO_2 Top of Line Corrosion of Pipeline Steel, CORROSION/2011, Paper No. 11327, NACE, Houston, TX, 2011.

[21] F. Vitse, S. Nesic, Y. Gunaltun, D.L. de Torreben, P. Duchet-Suchaux, Mechanistic model for the prediction of top-of-the-line corrosion risk, Corrosion. 59 (2003) 1075–1084.

[22] H. Qin, L. Xu, W. Chang, M. Lu, L. Zhang, Top of the Line Corrosion Under Low Temperature and High Condensation Rate Conditions, CORROSION/2011, Paper No. 11328, NACE, Houston, TX, 2011.

[23] L. Wei, X. Pang, C. Liu, K. Gao, Formation mechanism and protective property of corrosion product scale on X70 steel under supercritical CO_2 environment, Corros. Sci. 100 (2015) 404–420.

[24] ASTM Standard G1 − 03, Standard Practice for Preparing, Cleaning, and Evaluating Corrosion Test, in: Annu. B. ASTM Stand., vol. 03. 02, ASTM International, 2011.

[25] N. Yaakob, Top of the Line Corrosion in CO_2/H_2S Environments, PhD desertation, Ohio University, Ohio, USA, 2015.

[26] S. Nesic, W. Sun, Corrosion in acid gas solutions, in: T.J.A. Richardson (Ed.), Shreir's Corros., Oxford, Elsevier, 2010: pp. 1270–1298.

[27] M. Gao, X. Pang, K. Gao, The growth mechanism of CO_2 corrosion product films, Corros. Sci. 53 (2011) 557–568.

[28] Y. Zhang, X. Pang, S. Qu, X. Li, K. Gao, Discussion of the CO_2 corrosion mechanism between low partial pressure and supercritical condition, Corros. Sci. 59 (2012) 186–197.

[29] A.S. Yaro, K.R. Abdul-Khalik, A. A. Khadom, Effect of CO_2 corrosion behavior of mild steel in oilfield produced water, J. Loss Prev. Process Ind. 38 (2015) 24–38.

[30] M. Hanesch, Raman spectroscopy of iron oxides and (oxy)hydroxides at low laser power and possible applications in environmental magnetic studies, Geophys. J. Int. 177 (2009) 941–948.

[31] J. Oddo, M. Tomson, Simplified calculation of $CaCO_3$ saturation at high temperatures and pressures in brine solutions, J. Pet. Technol. 34 (1982) 1583 – 1590.

[32] M. Nordsveen, S. Nesic, R. Nyborg, A. Stangeland, A mechanistic model for carbon dioxide corrosion of mild steel in the presence of protective iron carbonate films—part 1: theory and verification, Corrosion. 59 (2003) 443–456.

[33] G.W. Thomson, The Antoine equation for vapor-pressure data., Chem. Rev. 38 (1946) 1–39.

[34] J.B. Sun, G.A. Zhang, W. Liu, M.X. Lu, The formation mechanism of corrosion scale and electrochemical characteristic of low alloy steel in carbon dioxide-saturated solution, Corros. Sci. 57 (2012) 131–138.

[35] W. Sun, S. Nesic, R.C. Woollam, The effect of temperature and ionic strength on iron carbonate ($FeCO_3$) solubility limit, Corros. Sci. 51 (2009) 1273–1276.

[36] T. Berntsen, M. Seiersten, T. Hemmingsen, Effect of $FeCO_3$ supersaturation and carbide exposure on the CO_2 corrosion rate of carbon steel, Corrosion. 69 (2013) 601–613.

[37] A. Dugstad, P.-E. Dronen, Efficient Corrosion Control of Gas Condensate Pipelines by pH-Stabilisation, CORROSION/99, Paper No. 20, NACE, Houston, TX, 1999.

[38] W. Sun, S. Nesic, Basics Revisited: Kinetics of Iron Carbonate Scale Precipitation in CO_2 Corrosion, CORROSION/2006, Paper No.06365, NACE, Houston, TX, 2006.

[39] M.L. Johnson, M.B. Tomson, Ferrous Carbonate Precipitation Kinetics and its Impact on CO_2 Corrosion, CORROSION/91, Paper No. 268, NACE, Houston, TX, 1991.

[40] E.W.J. van Hunnik, B.F.M. Pots, E.L.J.A. Hendriksen, The Formation of Protective $FeCO_3$ Corrosion Product Layer in CO_2 Corrosion, CORROSION/1996, Paper No. 6, NACE, Houston, TX, 1996.

[41] W. Sun, S. Nesic, Kinetics of corrosion layer formation: Part 1 - Iron carbonate layers in carbon dioxide corrosion, Corrosion. 64 (2008) 334–346.

[42] D.A. López, S.N. Simison, S.R. de Sánchez, The influence of steel microstructure on CO_2 corrosion. EIS studies on the inhibition efficiency of benzimidazole, Electrochim. Acta. 48 (2003) 845–854.

[43] F.F. Eliyan, A. Alfantazi, On the theory of CO_2 corrosion reactions - investigating their interrelation with the corrosion products and API-X100 steel microstructure, Corros. Sci. 85 (2014) 380–393.

[44] J.L. Mora-Mendoza, S. Turgoose, Fe_3C influence on the corrosion rate of mild steel in aqueous CO_2 systems under turbulent flow conditions, Corros. Sci. 44 (2002) 1223–1246.

[45] F. Farelas, M. Galicia, B. Brown, S. Nesic, H. Castaneda, Evolution of dissolution processes at the interface of carbon steel corroding in a CO_2 environment studied by EIS, Corros. Sci. 52 (2010) 509–517.

[46] J.L. Crolet, N. Thevenot, S. Nesic, Role of Conductive Corrosion Products in the Protectiveness of Corrosion Layers, Corrosion. 54 (1998) 194–203.

[47] J.L. Crolet, Protictiveness of Corrosion Layers, in: K.R. Trethewey, P.R. Roberge (Eds.), Model. Aqueous Corros. From Individ. Pits to Syst. Manag., Kluwer Academic Publishers, London, 1993: pp. 1–28.

Chapter 3: Influence of monoethylene glycol on the condensation rate and corrosion rate of carbon steel under condensing condition*

3.1 Abstract

This study investigates the influences of monoethylene glycol (MEG) on the condensation process and corrosion behaviour of carbon steel under condensing conditions. The results show that increasing bulk MEG concentration reduces condensation rates, uniform corrosion rates, and increases MEG concentration in the condensed liquid. However, localized corrosion occurs and pits aggregate within the droplet boundary when MEG co-condenses. Corrosion product comprises of $FeCO_3$ which is embedded in Fe_3C matrix and its thickness in the areas outside the droplet boundary is greater than that of the inside. Localized corrosion mechanism is proposed based on the nature of the corrosion product film.

Keywords: Carbon steel, SEM, Raman Spectroscopy, Weight loss, CO_2 corrosion

3.2 Introduction

During the transportation of unprocessed wet gas from offshore platforms to onshore processing plants, the water vapour in the gas phase condenses on the internal pipeline surface because of the temperature difference between wet gas stream and outside environment [1]. CO_2 and H_2S dissolve into the condensed water and organic acids, especially acetic acid, co-condense making the condensed liquid highly corrosive [2]. This leads to corrosion at the inner wall between 10 to 2 o'clock position of the pipeline which is called top-of-the-line corrosion (TLC) [1,3,4]. TLC is of serious concern in oil and gas industry due to its limited mitigation strategies. Conventional corrosion inhibitors injection in the liquid phase at the bottom of the pipeline is ineffective because it cannot reach the upper section due to their non-volatile nature.

Another flow assurance concern in operating wet gas transportation pipelines is hydrate formation, which could cause production reduction, interruption, and even physical

* This chapter is reproduced from 'M.M. Islam, T. Pojtanabuntoeng, R. Gubner, Influence of monoethylene glycol on the condensation rate and corrosion rate of carbon steel under condensing condition, under review in Corrosion Science (submitted: 01.03.2017)'.

damage to the pipelines [5]. Pipelines operating at high pressure and low temperature have potential risk of gas hydrate formation [6]. Monoethylene glycol (MEG) has been widely used as a hydrate inhibitor due to its reduced toxicity and recycling ability compared to other fluids, such as methanol [7]. The concentration of MEG injected at, or near, the well-head could be as high as 80-90 wt.% (referred to as lean MEG). Once it travels along the pipelines and is diluted with condensed water and/or formation water, its concentration typically reduces to 35-50 wt.% (referred to as rich MEG) [8]. However, in addition to hydrate inhibition, MEG decreases the general corrosion in various environments; e.g. sweet CO_2 [9,10] and sour corrosion [11], oxygen contaminated system [12–14] by affecting the physico-chemical properties of water in the pipeline; such as density, viscosity, CO_2 solubility, and solution conductivity [15]. Gulbrandsen and Morard reported that MEG adsorbs at the steel surface and thus limits the access of water and CO_2 molecule [15]. Furthermore, MEG also plays a complicated role in $FeCO_3$ precipitation. It promotes the precipitation by reducing $FeCO_3$ solubility yet it increases the induction time for precipitation [8,16].

Numerous studies have been conducted on the influence of temperature, condensation rate, CO_2 and H_2S partial pressure as well as acetic acid concentrations on TLC [17–19]. In a recent study, inner surface temperature has been identified as the influential parameter governing the severity of TLC at low surface temperature [3]. The condensation rate plays a role at moderate to high surface temperatures when $FeCO_3$ formation is favourable. Extensive discussion on the localised nature of TLC has been reported by Singer [20]. The author found that the extent of localised corrosion is controlled predominately by water condensation rate. The onset of localised corrosion was attributed to the breakdown and the non-uniformity of corrosion product ($FeCO_3$) under which pit propagated. The condensed water droplet size and location did not appear to correlate with the penetration rate of localised features.

In addition, effects of flow velocity, gas pressure and temperature of both bulk gas and pipe wall were also studied experimentally and prediction models have been proposed [4,21,22]. Yet, to date, little attention has been focussed on the influence of MEG on TLC.

Since the vapour pressure of MEG is much lower than that of water, the water vapour pressure decreases if appreciable amount of MEG is present in the liquid phase [23]. Consequently, the water condensation rate decreases and, at the same time, a portion of MEG co-condenses at the top of the line (TOL).

Guo et al. recently proposed a mathematical model that predicts condensation rates and concentrations of MEG in the condensed liquid. The authors validated the prediction results with flow loop experiments [24]. The model predictions agreed reasonably well (within 50% deviation) with experimental data up to 70% MEG in the bulk. The authors found that condensation rate decreased with increasing MEG concentrations. Discrepancy occurred between the model and experiments grew larger at higher MEG concentrations. In addition, the study reported the occurrence of localized corrosion at the TOL in presence of MEG in the bulk liquid. However, the location of droplet and the development of localized corrosion were not correlated. Therefore, it can be seen that the influence of MEG on TLC is not negligible and appears to be much more complicated than simply the change in condensation rates.

The present investigation systematically studied the effect of MEG on condensation rates and TLC rates at various MEG concentrations in the bottom of the line at different surface temperatures. Localized corrosion was evaluated by analysing the surface morphology and chemistry of corrosion products using scanning electron microscopy (SEM), Raman spectroscopy and 3D surface profilometry.

3.3 Experimental

3.3.1 Preparation of TLC test probe

Two test probes; i.e., carbon steel 1030 grade (carbon 0.30 %, manganese 0.75 %, silicon 0.25 %, phosphorous 0.04 %, sulphur 0.04 % and iron balance) for TLC study and 316L stainless steel (SS) for condensation rate study were made following the procedure outlined previously [3]. 20 mm-diameter and 16 mm-long samples were electro-coated with cationic epoxy (Powercron^{TM} 6000CX). The exposed surface, which was circular,

was wet ground with SiC paper to 600 grit, rinsed with DI water, ethanol, and dried with N_2 prior to the experiments.

3.3.2 Condensation rate and co-condensation of MEG experiments

The setup used in this study is schematically illustrated in Figure 3.1 and detail was described previously [3]. To avoid the interference of Fe^{2+} and Fe^{3+} in the subsequent analysis of MEG concentration in the condensed liquid, a 316L SS probe was used instead of a carbon steel sample. The prepared 316L SS probe was inserted into the polyethylene terephthalate (PET) lid so that the polished portion faced downward to the condensing vapour. The upper portion extruded above the lid and was inserted into a chamber where cooling liquid was circulated to maintain the surface temperature. The lid was then mounted onto a 2 L glass cell creating an air-tight environment. The whole assembly was deoxygenated by continuously sparging with high purity CO_2 gas (99.99%) for 10 min.

1400 g of solution containing different concentrations of MEG by weight percentage (wt.%) were introduced into the glass cell under exclusion of oxygen. Water vapour condensed on the carbon steel surface due to a temperature gradient created between the gas phase and probe surface. In this study, gas temperature (T_g) was maintained constant at 55 °C by controlling the liquid temperature at 65 ± 2 °C and surface temperatures (T_s) were set to 30 °C and 45 °C, respectively.

The condensed liquid was collected in-situ into the condensate reservoir placed out of the glass cell at room temperature to avoid any re-evaporation. The amount of MEG co-condensed with water was estimated by Mettler Toledo V30 Volumetric Karl Fischer titrator and cross-checked with the ethylene glycol refractometer (ATAGO PAL-91S). The condensation rate was calculated by dividing the collected condensed liquid with the exposed surface area of the probe and time.

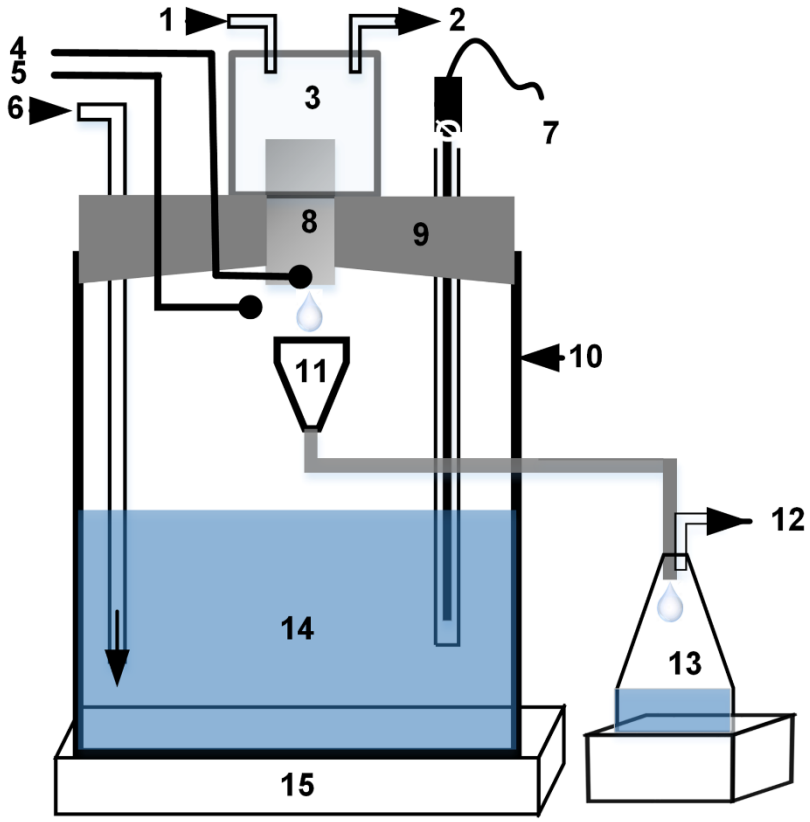

Figure 3.1: Schematic of top-of-the-line corrosion (TLC) setup; 1. Cooling water inlet, 2. Cooling water outlet, 3. Stainless steel cooling chamber, 4. Surface temperature probe, 5. Gas temperature probe, 6. CO_2 inlet, 7. Thermocouple, 8. Sample, 9. Polyethylene terephthalate lid, 10. 2-L glass vessel, 11. Condensate collector, 12. CO_2 outlet, 13. Condensate reservoir, 14. Test solution, 15. Heater.

3.3.3 TLC experiments

TLC experiments were conducted separately from the condensation experiments using the carbon steel sample. The condensed liquid collection cup was removed from glass vessel to allow the droplet to fall back into the bulk liquid maintaining the bulk liquid composition throughout the experiment. TLC rates were determined by 2 approaches; i.e. weight loss method and iron count. For the latter, dissolved iron (Fe^{2+}) concentration in the bulk liquid was measured periodically by a spectrophotometer. The in-situ corrosion rate was calculated based on Fe^{2+} presenting in the bulk liquid for a certain period. After finishing the experiment, corrosion product was removed and corrosion rate was calculated from the loss of weight of the whole probe as described elsewhere [3,25].

3.3.4 Immersion tests

For comparison, additional immersion experiments were conducted using 0% and 10% wt.% of MEG in order to estimate the influence of co-condensed MEG on TLC. The samples were circular shape (15 mm diameter × 4 mm thick) carbon steel 1030 prepared in a similar way as the TLC test specimens except the absence of a temperature couple insert. Three coupons were placed in the glass cell facing the non-coated area upwards. The glass cell was equipped with a thermocouple for controlling the liquid temperature; as well as, CO_2 inlet and outlet. 500 mL of test solutions were CO_2 saturated before transferring under oxygen exclusion into the glass cell and pH of the test solution was adjusted to 5.6 using 0.1M $NaHCO_3$ solution, similar to pH of the condensed liquid [3]. The temperature was maintained at 45 ˚C, similar to the surface temperature of the TLC experiment. After 30 d, 2 samples were cleaned for weight loss corrosion rates and the remaining sample was used for surface morphology and cross section analysis.

3.3.5 Surface characterization

An optical light microscope was used for identification and measurement of localized corrosion rates. Field emission scanning electron microscopy (FE-SEM) accompanied with energy dispersive X-ray spectroscopy (EDS) were used for morphological study and elemental identification of the corrosion product. Focus ion beam scanning electron microscopy (FIB-SEM) was used to measure the thickness of corrosion product film in and outside of the water droplet. The corrosion product was also characterized with confocal Raman spectroscopy at an excitation energy of 532 nm laser at ×100 magnification. Low laser power was used to prevent thermal transformation of the corrosion product.

3.4 Results and discussion

3.4.1 Influence of bulk MEG concentration on condensation rate and MEG co-condensation

Figure 3.2 presents the influence of the bulk MEG content on the condensation rates at surface temperature (T_s) = 30 °C and 45 °C and at constant gas temperature (T_g) = 55 °C. MEG concentration of 50% or less marginally decreased the condensation rates. However, once bulk MEG concentration was greater than 50%, condensation rate decreased drastically. For instance, at 50% bulk MEG concentration and T_s = 45 ˚C, condensation rate was 0.45 g m^{-2}s that reduced to below 0.2 g m^{-2}s when bulk MEG was increased to 80 %. The decreasing trend of condensation rates with increasing bulk MEG concentration is similar to the observation by Guo et al.[24]. The reduction in condensation rates with increasing bulk MEG content can be explained by the decrease in vapour pressure of MEG-water mixtures according to Raoult's law and Antoine equation [26]. The calculation at the temperature of the bulk liquid, 65 °C, shown in Figure 3.3 demonstrates that the vapour pressure of the MEG-water mixture decreases with increasing MEG content correlating with the observed decrease in condensation rates.

Figure 3.4 demonstrates the concentration of MEG in the condensed liquid as a function of bulk MEG content. A proportional relationship between MEG concentration in the bulk and at the top is found at both T_s. At T_s = 30 °C, MEG content at the TOL varied from 0% to 5% when the bulk contained 30% to 80%, respectively. When surface temperature was increased to 45 °C, higher concentrations of MEG at the top section was measured (1% to 10%).

Figure 3.4 also shows that at the same bulk MEG concentration, the concentration of MEG in the condensed liquid increases with T_s . This is attributed due to the higher vapour pressure of water compared to MEG as shown in Figure 3.5. The effect was more pronounced at higher bulk MEG concentration (low condensation rates) because of longer droplet retention time.

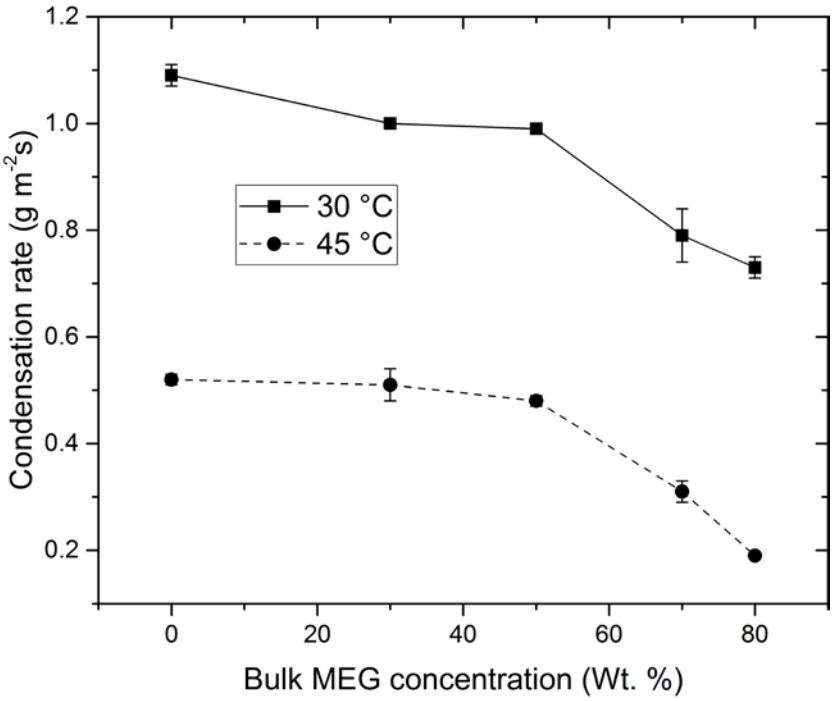

Figure 3.2: Influence of bulk MEG concentration on condensation rate at 55 °C gas temperature and different surface temperature; error bar is the standard deviation of multiple measurements.

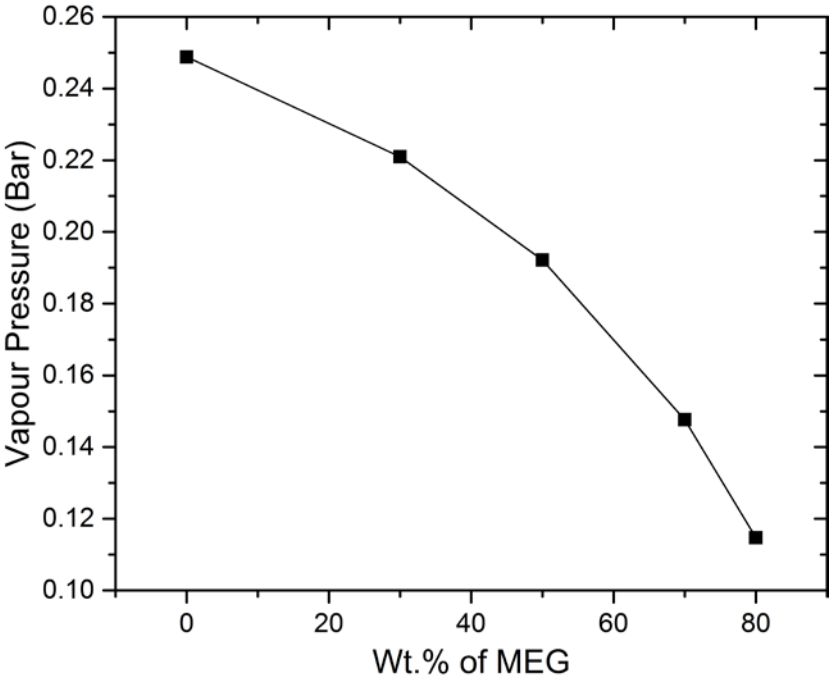

Figure 3.3: Vapour pressure of monoethylene glycol (MEG)-water mixture at 65 °C.

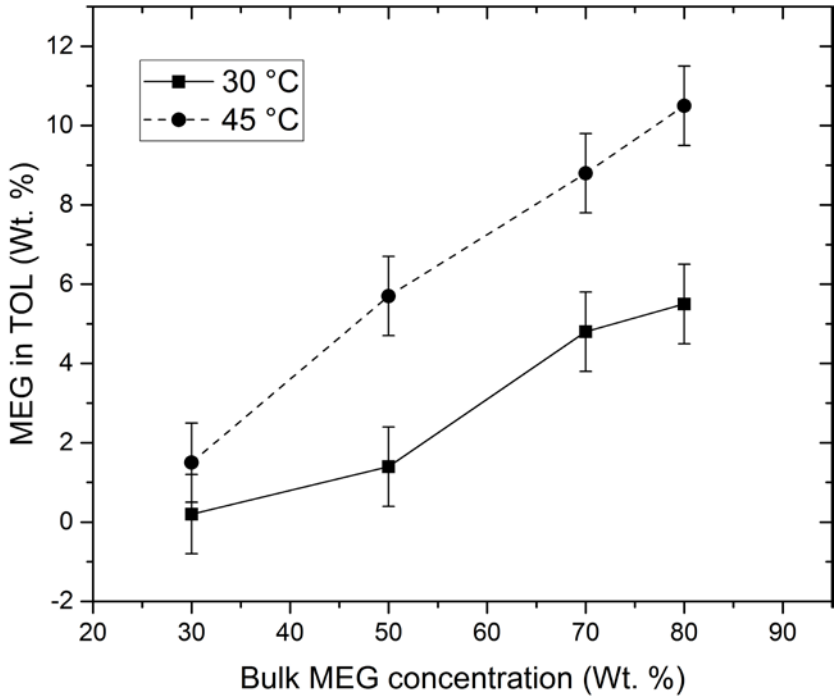

Figure 3.4: Influence of bulk MEG concentration on co-condensation of MEG in Top of the line (TOL). Bulk gas temperature 55 °C. Error bar is the standard deviation of multiple measurements.

3.4.2 Influence of MEG on top of the line corrosion (TLC)

The influence of MEG on TLC was investigated under two conditions; namely, T_s of 30 °C and 45 °C at constant T_g of 55 °C. Lower surface temperature conditions resulted in higher condensation rates are less favourable for iron carbonate formation, and vice versa.

3.4.2.1 Influence of MEG on TLC at 30 °C surface temperature

Figure 3.6 shows the in-situ TLC rates obtained from Fe^{2+} concentration in the bulk liquid at T_s = 30 °C and T_g = 55 °C for 10 d exposure. TLC rates constantly increased for 0% and 50% MEG throughout the experiments, whereas the corrosion rates initially increased but remained constant after 6 d of exposure for 80% MEG. The integrated corrosion rates obtained from weight loss and total Fe^{2+} measurement are depicted in Figure 3.7. Corrosion rate reduced in the presence of MEG due to the small reduction in condensation rate and increase in co-condensation of MEG. Corrosion rates calculated from Fe^{2+}

measurement is slightly (8% to 12%) lower than that found from weight loss. The small reduction indicates no considerable amount of corrosion product was formed on the surface [3].

SEM images of the corroded surface and the corresponding EDS spectra are depicted in Figure 3.8. Irregular morphology of the steel surface with network-like structure due to the selective dissolution of ferrite can be deduced from the SEM images. The small oxygen peak in the corresponding EDS spectra did not indicate the presence of $FeCO_3$. Because of the high condensation rates, resulting in a low droplet retention time, $FeCO_3$ formation was not kinetically favourable [3].

The increase of corrosion rates with time in the CO_2 environment, particularly in the absence of $FeCO_3$, has been observed before [3,27]. Galvanic coupling of ferrite (α-Fe) and cementite (Fe_3C) has been proposed to be one of the causes explaining of this observation. Ferrite, having higher electrochemical potential, corrodes preferentially and dissolves in the condensed liquid [28,29]. The electrically conductive cementite phase remains on the surface and acts as a cathode accelerating the dissolution of the remaining ferrite [30]. In addition, local acidification of solution confined within the cementite layer may also contribute to the rising corrosion rate with time [31].

As mentioned, corrosion rates were found to reach plateau after 6 d of exposure with 80% bulk MEG concentration. At this condition, approximately 5% of MEG co-condenses with water, which may be significant to reduce the effect of galvanic coupling by adsorbing at the active sites.

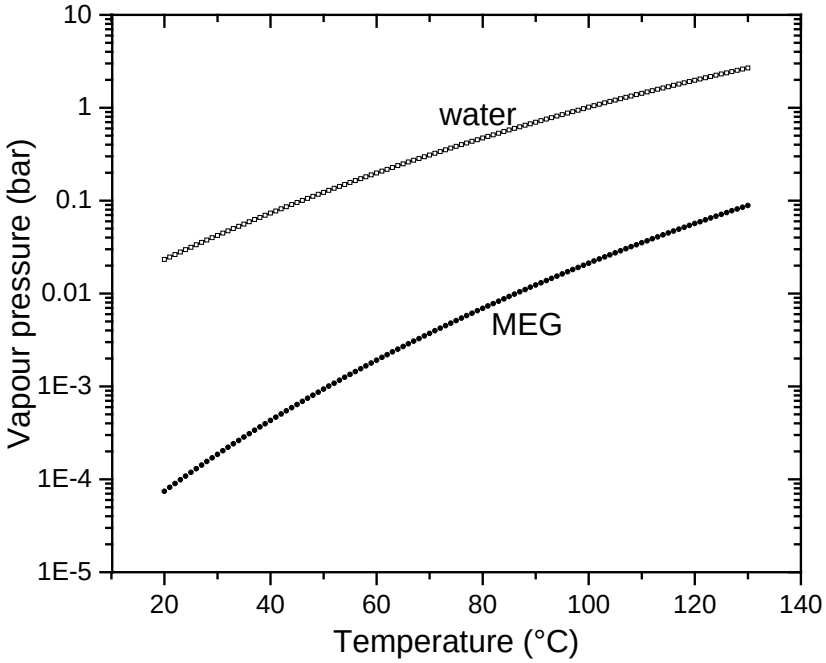

Figure 3.5: Pressure-temperature curve of MEG and water calculated from [24].

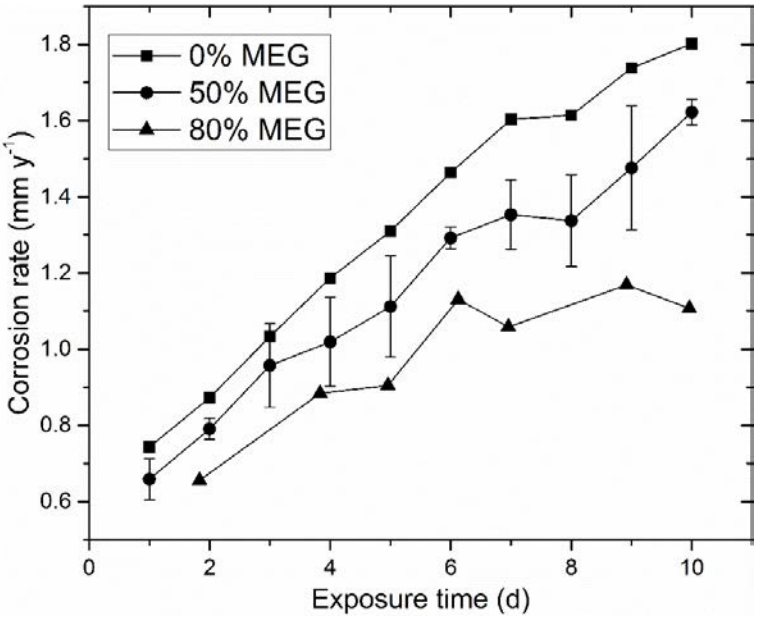

Figure 3.6: In-situ TLC rates for 10 days exposure at 30 °C surface temperature and 55 °C gas temperature at different bulk MEG content; error bar is the standard deviation of duplicate tests.

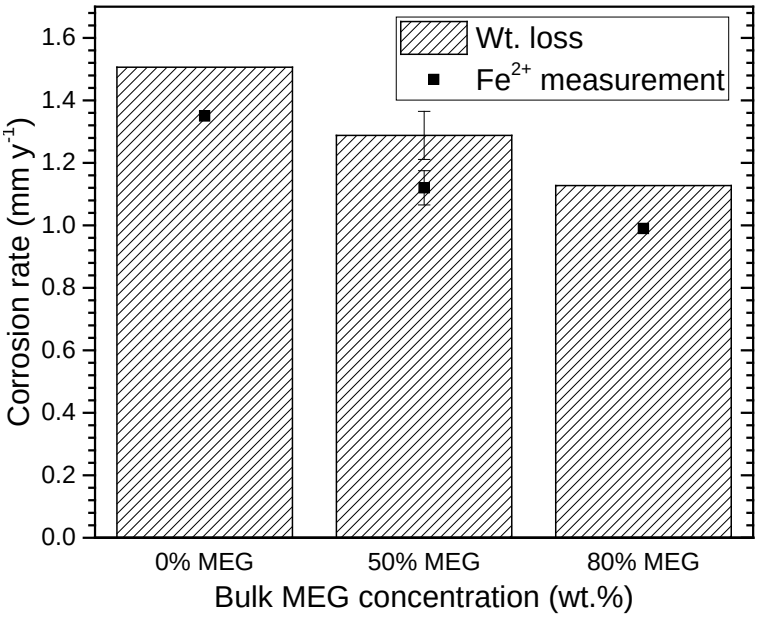

Figure 3.7: TLC rates obtained from weight loss method after 10 days of exposure at 30 °C surface temperature and 55 °C gas temperature at different MEG concentration in the bulk. Error bar is the standard deviation of duplicate tests.

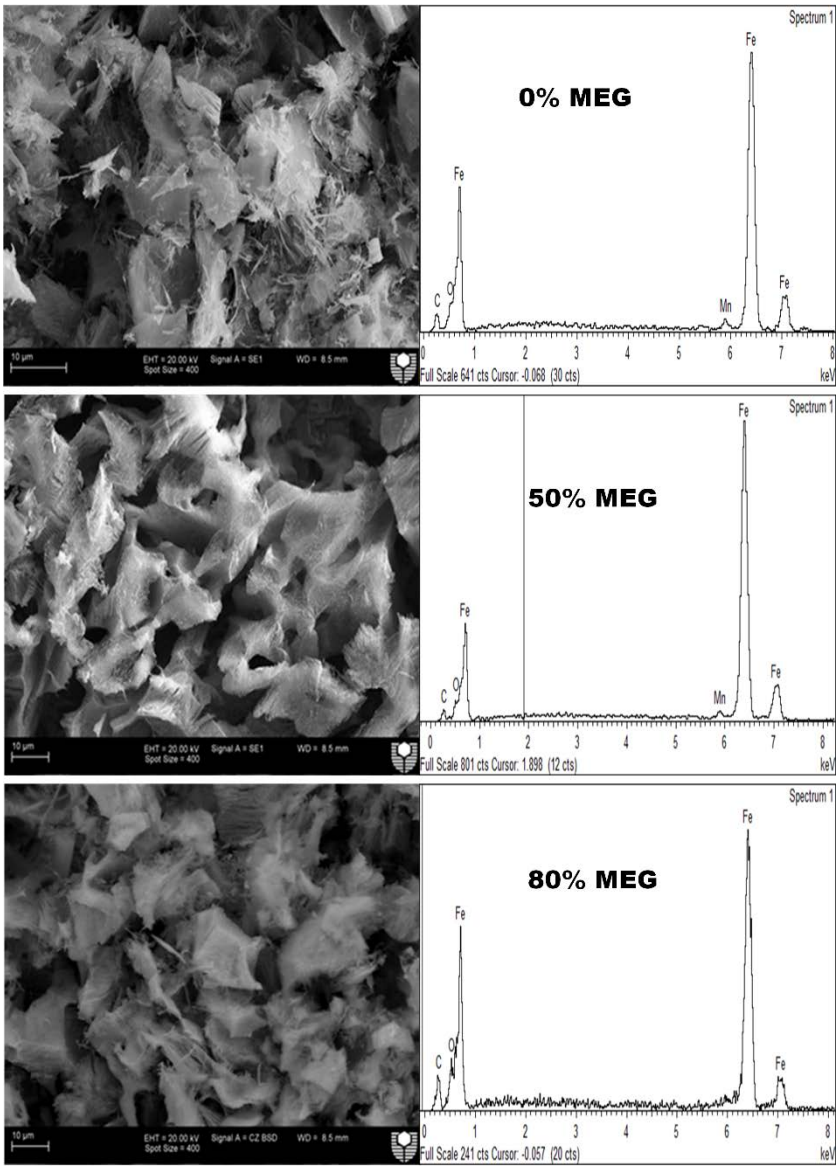

Figure 3.8: SEM images and corresponding EDS spectra of corrosion products after 10 days of exposure at 55 °C gas temperature and 30 °C surface temperature at different bulk MEG content showing no evidence of $FeCO_3$ formation.

3.4.2.2 Influence of MEG on TLC at 45 °C surface temperature

Experiments were conducted at T_s = 45 °C and T_g = 55 °C at 2 exposure times; i.e. 10 d and 17 d. Since in-situ corrosion rates obtained from the short-term tests eventually declined towards the end of the tests, particularly at 0% MEG, the experiments were repeated in duplicate by extending the test duration to attain a steady state corrosion rate;

i.e. 17 d. The reproducibility of the experiments is evident in Figure 3.9 where the results from 10 d lies within the error bar of those obtained from the 17 d tests.

Figure 3.9 also demonstrates the decrease in corrosion rates with increasing bulk MEG content. With 0 % bulk MEG, in-situ corrosion rates increases up to 5 d then constantly decline until 13 d before it becomes more or less constant. However, in the presence of MEG, the initial increase in the corrosion rates was not observed. Constant corrosion rates were monitored for up to 8 d and 10 d of exposure before the decline occurred in 50 % MEG and 80 % MEG, respectively.

Corrosion rates obtained from weight loss and total Fe^{2+} measurement after 10 d and 17 d of exposure at T_s = 45 °C and T_g = 55 °C at different bulk MEG content is shown in Figure 3.10. The error bar shown with 50% MEG concentration denotes the standard deviation of the duplicate test. Corrosion rates calculated from Fe^{2+} measurement is considerably lower (30% to 38%) compared to that obtained from weight loss measurement indicating the formation of corrosion product on the surface. At any given MEG concentrations in the bulk, the TLC rate after 10 d exposure is higher than for 17 d. The corrosion rates with respect to MEG concentration is consistent with that from in-situ measurements where an increasing bulk MEG reduces the TLC rates.

The decrease in uniform corrosion rates can be attributed to the reduction in condensation rates and increase in co-condensed MEG. Around 5% and 10% MEG co-condensed at 50% and 80% bulk MEG, respectively. This co-condensed MEG may adsorb on the surface and block the active sites for corrosion [9]. The galvanic effect between ferrite and cementite phase may be hindered resulting in a constant corrosion rate in 50% and 80% bulk MEG. Subsequent corrosion rate reduction with time as observed in all cases can be linked to the initiation and complete formation of protective iron carbonate layer [27,28,32].

A delay in the decline of corrosion rate at 50% and 80% MEG concentration; i.e. 8 d vs 10 d, was noted. MEG is reported to decrease the solubility of $FeCO_3$ but prolongs the induction time for $FeCO_3$ precipitation [8,16]. At 80% MEG in the bulk, the condensed liquid contained 10% MEG whereas only 5% was measured at 50% MEG. The difference

in MEG content within the condensed liquid could explain the observed differences in the induction time for $FeCO_3$ precipitation prolonging the period during which it is not protective.

SEM images and the representative EDS spectrum of the corrosion product after 10 d of exposure at T_s = 45 °C and at different bulk MEG contents are shown in Figure 3.11. In contrast to 30 °C surface temperature, crystals are visible at 45 °C and the high oxygen peak in the EDS spectrum indicates the presence of $FeCO_3$. After the removal of the corrosion product, no localized corrosion was identified in short-term tests but was observed on samples after longer exposure to MEG co-condensation. Comprehensive surface analysis was carried out to understand the mechanism of localised corrosion, which will be discussed in the section 3.3 in detail.

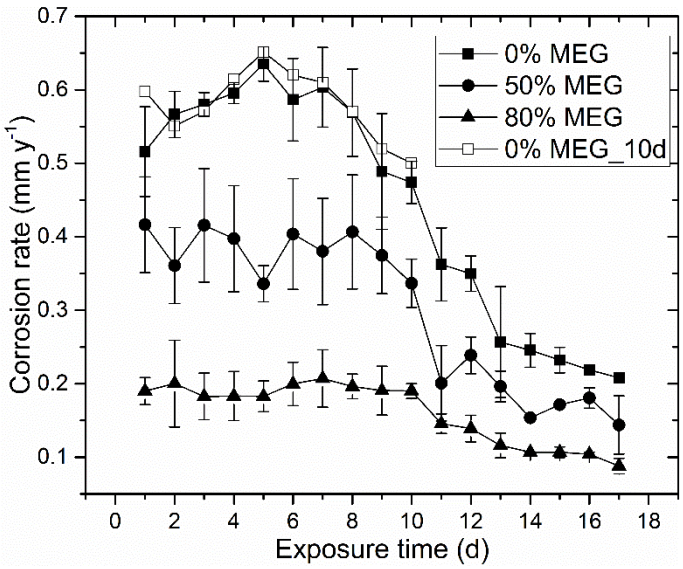

Figure 3.9: In-situ TLC rates at 45 °C surface temperature and 55 °C gas temperature at different bulk MEG contents; error bar is the standard deviation of duplicate tests.

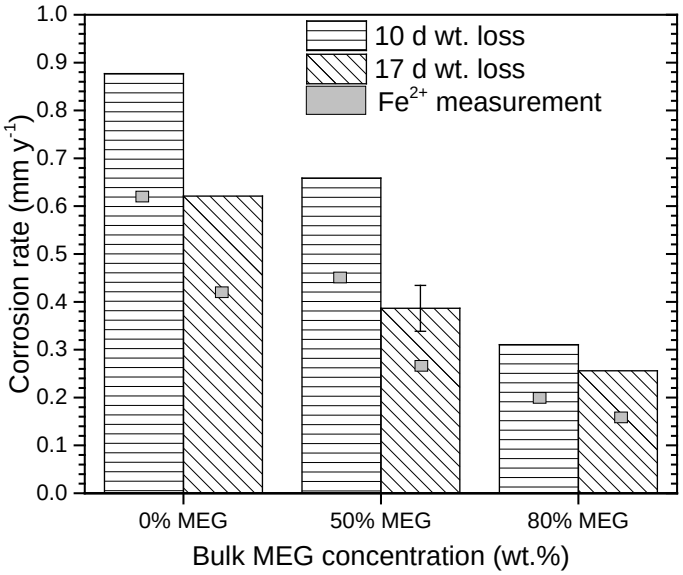

Figure 3.10: TLC rates obtained from weight loss of the coupon at 45 °C surface temperature and 55 °C gas temperature at different MEG content in the bottom of the line (BOL); error bar is the standard deviation of duplicate tests.

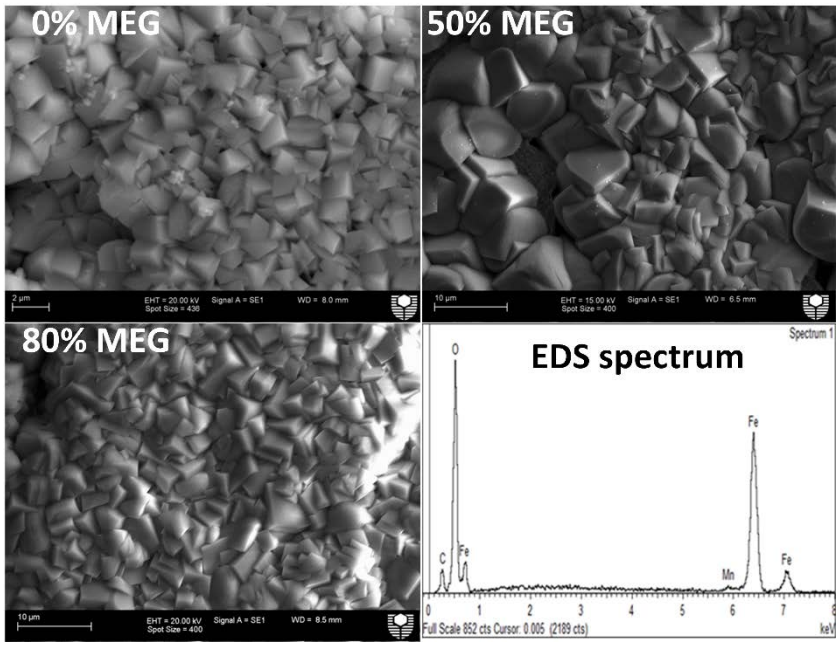

Figure 3.11: SEM images and EDS spectrum of corrosion products after 10 days of exposure at 55 °C gas temperature and 45 °C surface temperature at different bulk MEG content showing evidence of $FeCO_3$ crystal formation.

The reduction of TLC rates in the presence of MEG can be a result of i) the decrease in condensation rates and ii) the increase in MEG concentration in condensed liquid. To

identify and distinguish the relative contribution of each effect, immersion tests were conducted to exclude the influence of condensation rates using 10% MEG, which resembled the highest concentration at which MEG co-condensed. Corrosion rates of carbon steel immersing in 0% MEG and 10% MEG at 45 °C is shown in Figure 3.12. The inhibition efficiency offered by 10% MEG was approximately 22% as corrosion rate decreased from 1.43 mm y^{-1} to 1.11 mm y^{-1}. When compared with TLC experiments at similar water chemistry, the inhibition efficiency was estimated to be 59%. It should be noted that $FeCO_3$ precipitated (0.088 g in 0% MEG vs 0.075 g in 10% MEG) and expected to provide similar level of corrosion protection in both solutions; i.e. without MEG and with 10% MEG. This indicates that both influences; i.e. condensation rate reduction and MEG co-condensation, strongly contribute to the decrease in corrosion rate but the former is slightly more dominant. It should be noted also that no localised corrosion was observed under immersion conditions highlighting the adverse effect of condensation process on TLC.

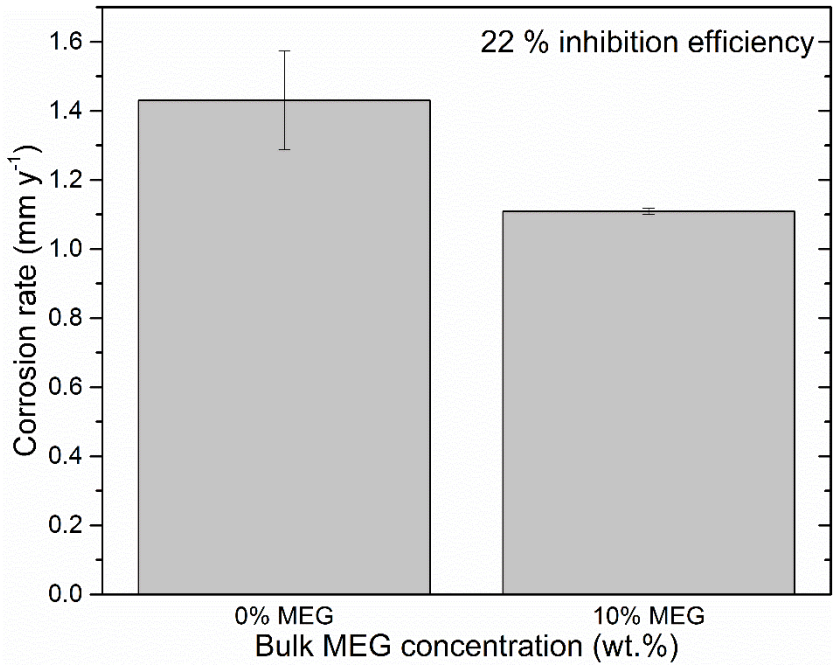

Figure 3.12: Corrosion rate under immersion condition at 45 °C temperature after 30 days of exposure. pH 5.6; error bar is the standard deviation of corrosion rates of two samples.

3.4.3 Localized corrosion on top of the line in the presence of MEG

Localized corrosion under CO_2 condition generally occurs when a protective film breaks down forming a galvanic cell between bare metal and $FeCO_3$ covered area [33]. A partially protective film may be considered as a prerequisite for initiating localized attack. Therefore, analysis on localised corrosion was done at T_s = 45 °C where $FeCO_3$ formation was favourable.

Extent of localised corrosion rate

Figure 3.13 and Figure 3.14 present the optical images of the surface of the corroded samples exposed for 10 d and 17 d, respectively. Clear evidence of water droplet formation is visible on the samples, especially in the presence of MEG, before removing the corrosion products. After cleaning the surface with Clarke's solution, no sign of localized corrosion was observed in short-term test but was evident in long-term test. In the absence of MEG, minor localized attack was found as depicted by few pits. On the contrary, in the presence of MEG, localized attack became more severe as number of pits significantly increased. It is also visible that pits aggregated inside the droplet. Because the pits were only visible after removing the corrosion products, it is reasonable to conclude that localized corrosion propagated underneath the corrosion product film [20], which was pervious to the corrosive environment.

The surface profilometry shown in Figure 3.15 illustrates the severity of the localized attack. Larger number of pits were found inside the droplet in the experiment with 50% bulk MEG as compared to that with 80%. However, the maximum pitting rate and pitting ratio were larger at 80 % MEG; i.e. 1.64 mm y^{-1} and pitting ratio of 4.24 in 50% bulk MEG as compared to 1.89 mm y^{-1} and pitting ratio of 7.89 in 80% bulk MEG. It should be noted that the pitting corrosion rate was calculated based on total exposure time. Since no evidence of localized corrosion was found up to 10 d of exposure, it is reasonable to believe that pit initiated at 10^{th} or subsequent d. In that sense, the actual pitting corrosion rate could be more than double of the reported values.

It was reasonable to question if a low concentration of MEG could cause an adverse effect under immersion condition. However, immersion tests conducted at 0% and 10% of MEG at 45 °C did not show any localised corrosion (Figure 3.16). This implies that MEG does not behave in same way under BOL and TOL conditions potentially due to the constant change of water droplet both physically and chemically during the condensation.

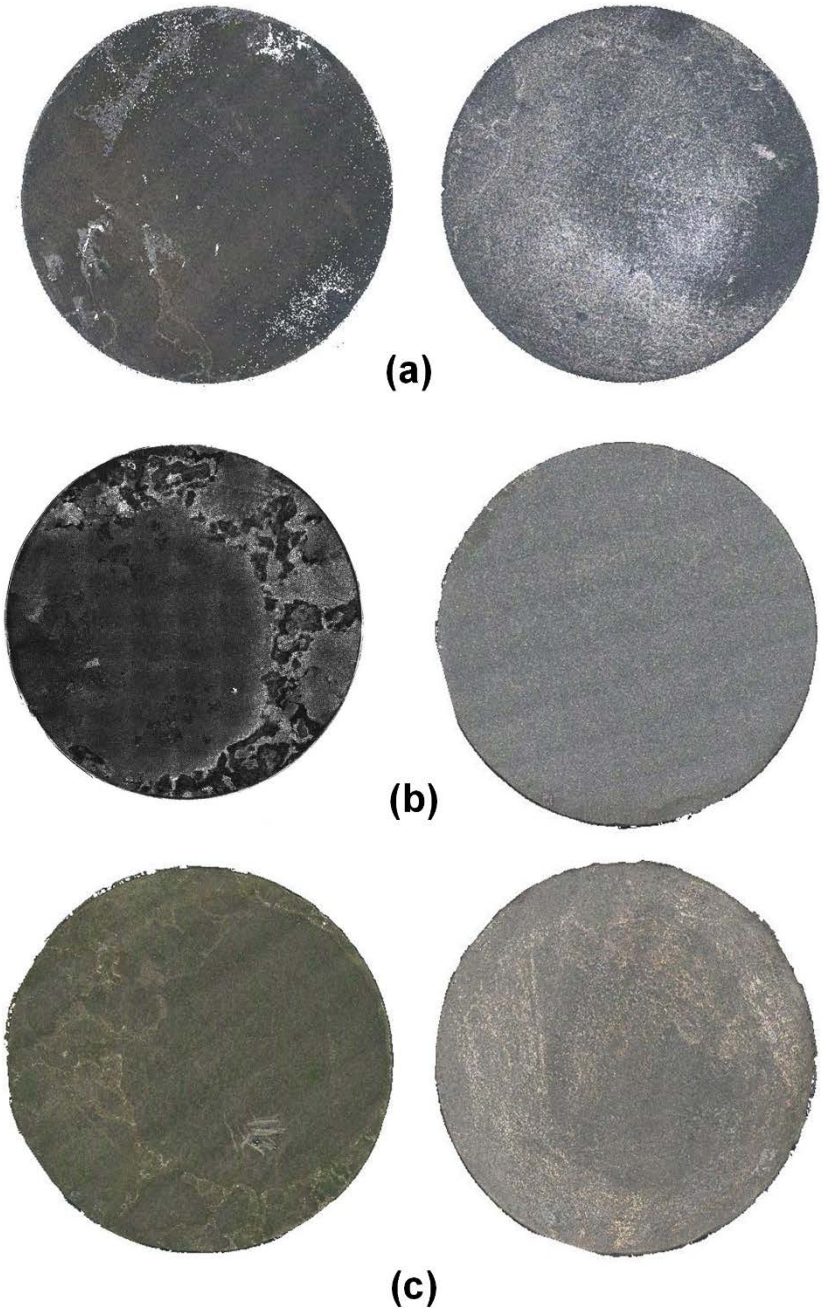

Figure 3.13: Optical images of the surface before removing the corrosion products (left side) and after removing the corrosion products (right side) after 10 days of exposure showing no initiations of pitting; (a) 0% MEG; (b) 50% MEG and (c) 80% MEG.

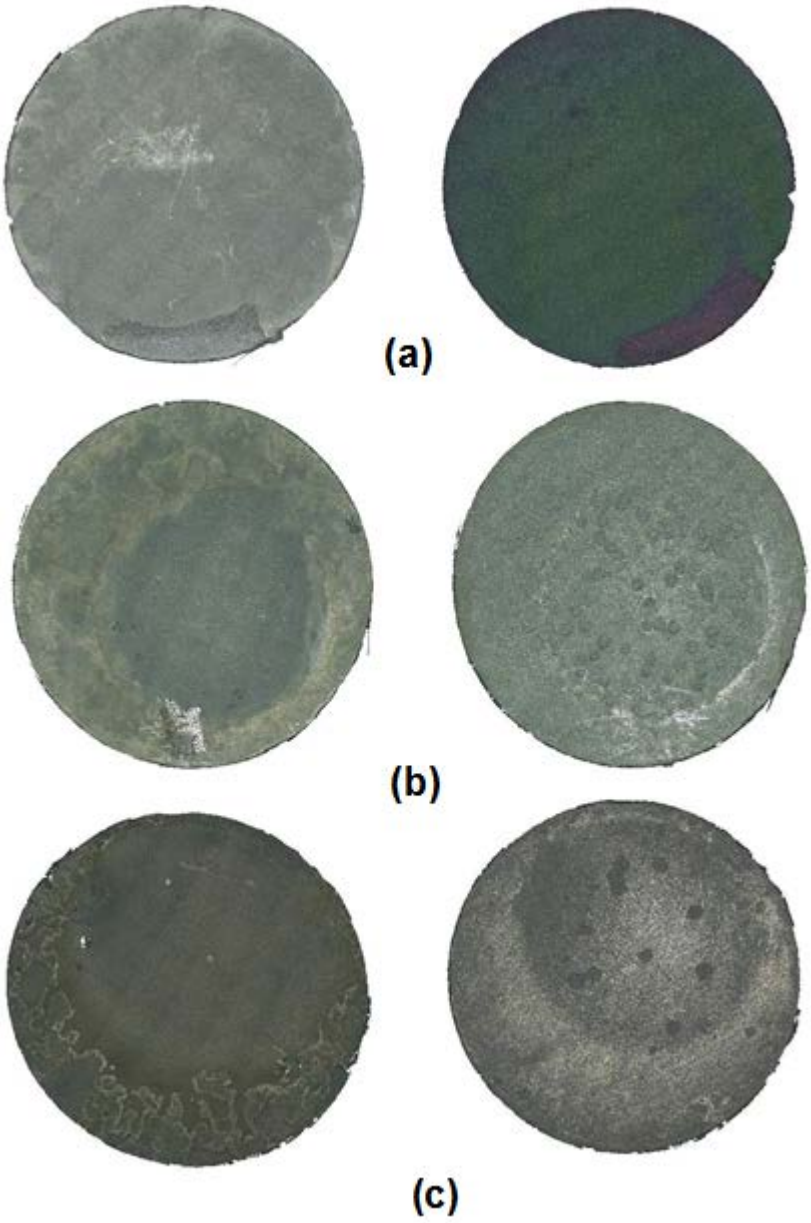

Figure 3.14: Optical images of the surface before removing the corrosion products (left side) and after removing the corrosion products (right side) after 17 days of exposure showing initiation of pitting; (a) 0% MEG; (b) 50% MEG and (c) 80% MEG.

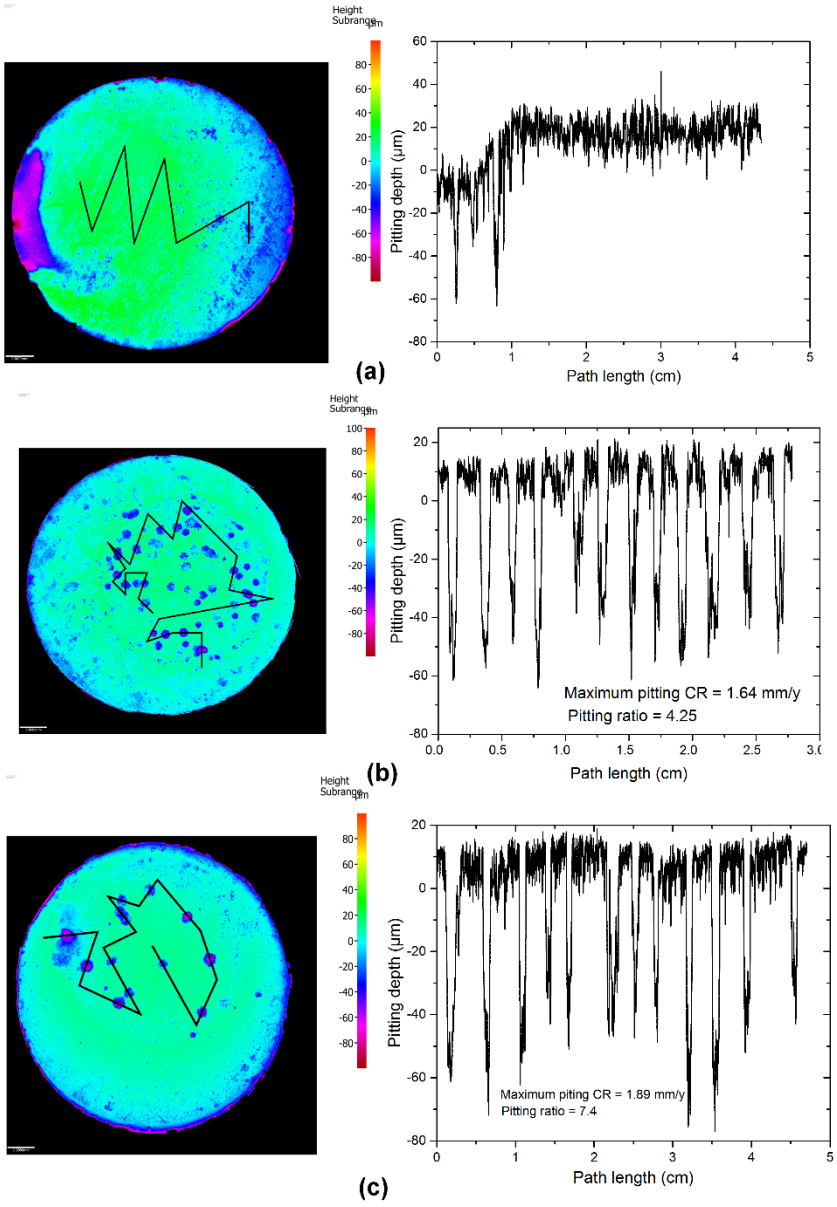

Figure 3.15: Surface profilometry of the corroded specimens after removing the corrosion product; (a) 0% MEG; (b) 50% MEG and (c) 80 % MEG.

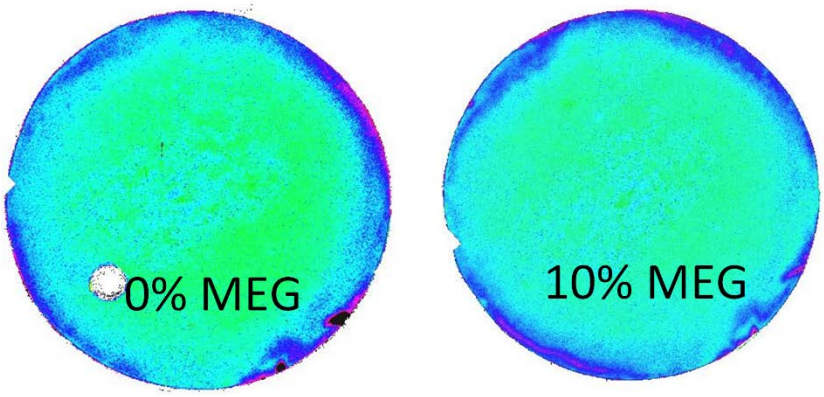

Figure 3.16: Surface images after the removal of corrosion product; 30 days immersion in 10% MEG at 45 °C.

3.4.3.1 Morphology and thickness of $FeCO_3$ and its role on localized corrosion

To explain the localized corrosion behaviour within the droplet, the variation in surface morphology was investigated. In TLC experiments containing 80% bulk MEG, the SEM images at different locations of the corroded samples are shown in Figure 3.17. Distinct $FeCO_3$ morphologies in and outside the droplet can be identified. Crystals of the corrosion products within the droplet have sharp edges and are randomly oriented and relatively large. Other investigators also reported formation of sharp edge crystal underneath the droplet area [20]. Conversely, crystals of corrosion product outside the droplet seem to have multiple layers potentially yielding additional corrosion protection. A similar morphology was observed in the experiments with 50% bulk MEG concentration.

The thickness of corrosion product film at these two selected different locations was measured by Focus Ion Beam-Scanning Electron Microscope (FIB-SEM). Figure 3.18(a) presents the thickness of corrosion product of a sample containing 0% MEG in the bulk after 17 days of exposure obtained from FIB-SEM. Thickness of $FeCO_3$ formed underneath the droplet was about 17 µm whereas that at the outside of the droplet was estimated to be 28 µm. Since FIB-SEM provides information of small area, a cross sectional analysis of the corrosion product has also been carried out to confirm the measurements. Figure 3.18(b) presents cross sectional images of the same sample, which is the panorama of multiple images covering the area of in- and outside the droplet. It is

apparent that the thickness of corrosion product outside the droplet is almost double compare to that of inside the droplet. A similar observation was also found for 50% and 80% bulk MEG.

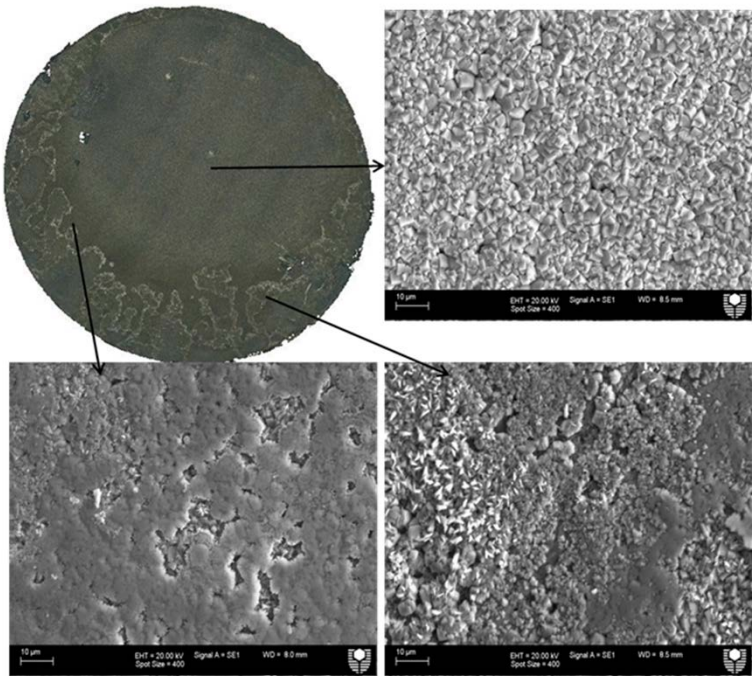

Figure 3.17:SEM images taken from different locations of the sample after 17 days exposed to condensation at 45 °C surface temperature and 55°C gas temperature with 80% MEG in the bulk.

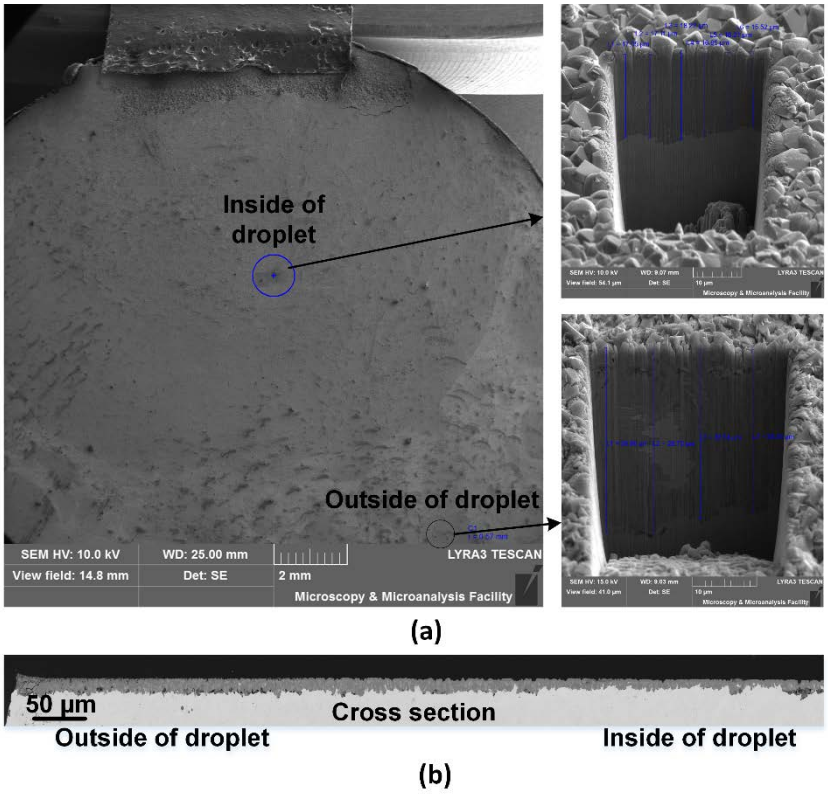

Figure 3.18: FIB-SEM image and cross section of corrosion product showing the difference of thickness of corrosion product inside (around 17 µm) and outside (around 28 µm) of the droplet on a sample containing 0% MEG in the bulk.

The average thickness of corrosion product at different MEG concentrations was also estimated from the weight of the corrosion product using the following formula:

$$T = \frac{M \times 10^4}{A \times \rho} \tag{3.1}$$

where, T is the thickness of corrosion product film, µm; M is the mass of the corrosion product, g; A is the exposed area, cm^2 and ρ is the density of iron carbonate, 3.9 g cm^{-3}.

Table 3.1 shows the comparison of thickness of corrosion product films at different bulk MEG content. The calculated values agree well with the measured ones. The thickness of the corrosion product film decreases with increasing bulk MEG concentration. It can be postulated that lower corrosion rate in higher MEG concentration produces less amount

of Fe^{2+} ions in the condensed liquid. Hence, less $FeCO_3$ precipitates that could contribute to localized corrosion.

Table 3.1: Thickness of corrosion product film at different bulk monoethylene glycol (MEG) content

Weight % of MEG in bulk	Thickness of corrosion product measured from SEM images (μm)		Average thickness of corrosion product from weight loss method (μm)
	Inside the droplet	Outside the droplet	
0	17 ± 2	28 ± 2	24
50	13 ± 2	22 ± 2	16
80	11 ± 2	18 ± 2	12

The difference in morphology and thickness of corrosion product films within and outside the droplet may be correlated with the condensation process, which is dynamic because of constant renewal and detachment of droplets on and from the TOL surface. As a droplet detaches, a new droplet often forms and propagates at the same location. During this transition, it is reasonable to expect continuous fluctuation in water chemistry, particularly pH and Fe^{2+} which may be diluted with freshly condensed water, and as a result, lowering $FeCO_3$ supersaturation within the droplet. On the contrary, the thickness of condensed liquid layer beyond the circumference of the droplet appears to remain constant. Hence, the condensation process hardly affects its water chemistry. If that is the case, it can be hypothesised that there is distinction between $FeCO_3$ supersaturation between that in- and outside the droplet; i.e. the former being continuously fluctuating while the latter being relatively constant.

During droplet renewal, $FeCO_3$ supersaturation within the droplet can be relatively low. At low supersaturation, crystal growth is more dominant than nucleation [32], which has been associated with porous and loose corrosion products [26]. The growth of nearby nucleus forms larger grains creating large interstitial space. The voids between grains allow corrosive species to penetrate through causing localised corrosion.

For the area outside the circumference of the droplet, the continuous and relatively stagnant film of condensed liquid ensures constant level of $FeCO_3$ supersaturation, which

is likely to be higher than that inside the droplet. Therefore, higher nucleation rate could be expected resulting in a smaller grains [33], which are more compact and provides additional protection. Hence, localised corrosion is hardly observed outside the droplet.

Comparison of Figure 3.19 and Figure 3.20 highlights the influence of hydrodynamic condition on the corrosion product film under TOL condition and immersion condition, respectively. Figure 3.19 shows the non-uniformity of the cross section of corrosion product film within a droplet under TOL condition at different bulk MEG content with a large extent of localized corrosion in presence of MEG (Figure 3.19(b) and (c)). Whereas uniform and thick (80 µm) layer of corrosion product can be observed when the sample immersed in 10% MEG at 45 °C for 30 days as shown in Figure 3.20. It is clear that the difference in the thickness and uniformity of the corrosion product, which contributes to the occurrence of localised corrosion, is due primarily to the hydrodynamic conditions.

3.4.3.2 Nature of corrosion products

The corrosion product film formed at 80 % bulk MEG after 17 d of exposure was analysed by Confocal-Raman spectroscopy (Figure 3.21) and EDS mapping (Figure 3.22) to identify its constituents. Corrosion product consisted mainly of $FeCO_3$ which integrates into the Fe_3C matrix as shown in Figure 3.21a. Two intense peaks at 1087 cm^{-1} and 287 cm^{-1} are typical signature of $FeCO_3$ [3,36]. On the other hand, there are areas with significant amount of Fe_3C present, as seen in the broad Fe_3C peak visible at 1322-1376 cm^{-1} and 1560-1600 cm^{-1} [37,38]. Raman mapping reveals that the bright area having lamellar structure in the optical micrograph (Figure 3.21b) corresponds well to areas depicted in blue (Figure 3.21c) indicating the presence of Fe_3C.

The existence of Fe_3C was also confirmed by EDS mapping which shows distribution of element of corrosion product within a pit (Figure 3.22). In the grey scale back-scattered image, a corrosion pit is visible underneath a single layer of crystalline particles. The pit is hollow with lamellar structure that appears to extend from the bottom of the pit to the particles. Major components of the film are O, Fe and C. Colour images show areas corresponding to the intensity of these elements. Area with high intensity of O could be

related to $FeCO_3$ whereas within the pit with visible lamellar type structure produced fainted amount of Fe and C, which can be correlated to Fe_3C.

Overall, the combined analysis of Raman, EDS and SEM confirm that the corrosion product film is duplex in nature constituting outer layer and inner layer. The outer layer is mainly composed of $FeCO_3$ whereas the inner layer is $FeCO_3$ embedded in the lamellar Fe_3C matrix. In addition, the localized areas are depleted of $FeCO_3$.

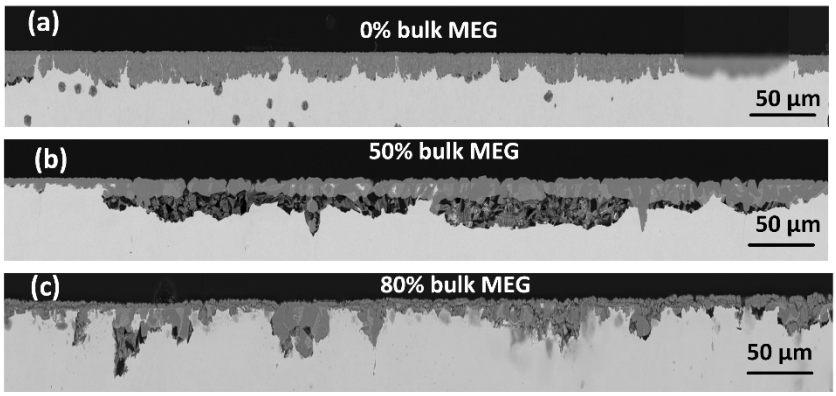

Figure 3.19: Comparison of cross section of corrosion product film inside the droplet at different bulk MEG concentration for 17 days exposure at 45 °C surface temperature and 55 °C gas temperature.

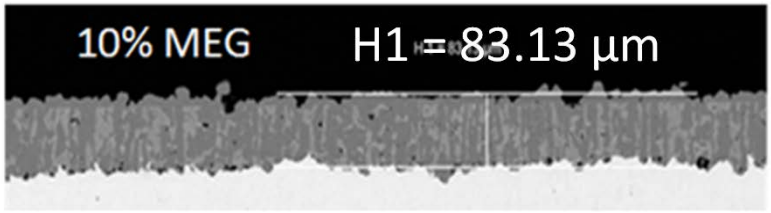

Figure 3.20: Cross section of corrosion product film formed under immersion condition; 30 days immersion in 10% MEG at 45 °C.

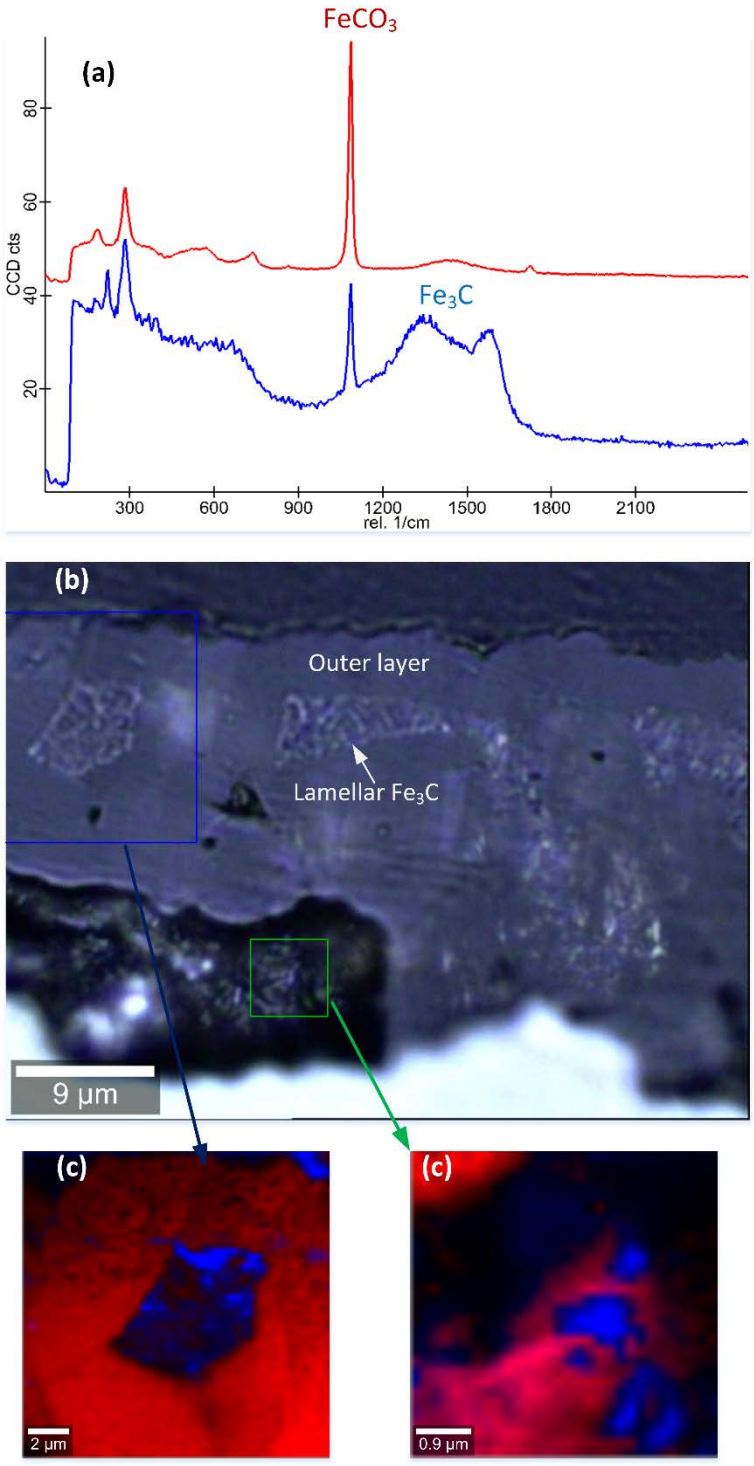

Figure 3.21: Raman analysis of corrosion product film formed at 80% bulk MEG after 17 days of exposure; a) spectra, b) optical images showing areas for analysis, and c) Raman mapping showing areas with distinct composition. Red represents $FeCO_3$ and blue represents areas containing Fe_3C.

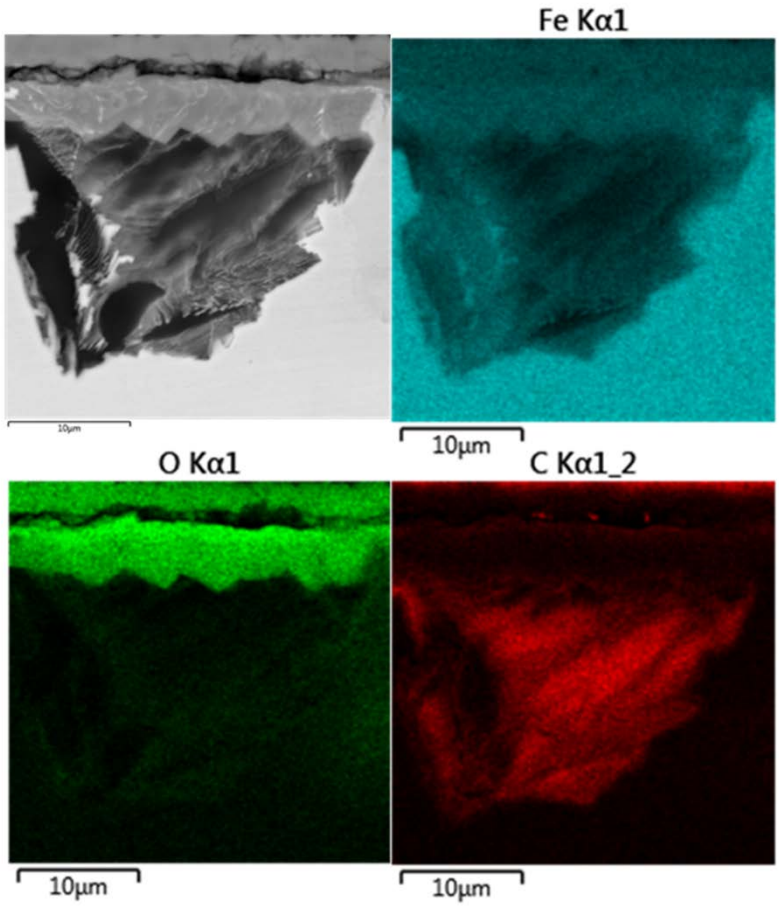

Figure 3.22: EDS mapping of cross section including a pit generated on the sample containing 80% bulk MEG.

3.4.3.3 Mechanism of localized corrosion

In the presence of 50% and 80% of MEG in bulk, uniform corrosion rates were significantly reduced but localized corrosion occurs on TOL within the droplet. Singer reported a greater localized corrosion with increasing condensation rates in sweet environment [20]. In this study, condensation rates decreased in the presence of MEG but the extent of localized corrosion increased. This highlights the role of MEG on localized corrosion; possibly how it influences the chemistry within the droplet.

Due to low corrosion rates in presence of MEG, a low supersaturation of $FeCO_3$ is expected since corrosion of steel is the only source of Fe^{2+} within a droplet. As stated earlier, crystal growth dominates over nucleation at low supersaturation forming larger

grains with large interstices (Figure 3.19 (b) and (c)) through which co-condensed MEG solution saturated with corrosive species can penetrate. Once that occurs, the nucleation of $FeCO_3$ is limited since MEG prolongs the induction time of $FeCO_3$ precipitation resulting in formation of cavity. It was hypothesised [33,39] and later on experimentally confirmed [40] that the localized corrosion of carbon steel in CO_2 environment occurs when a galvanic cell established between $FeCO_3$ covered surface which acts as cathode against a bare steel surface anode. Accordingly, the cavity exposes bare carbon steel surface and a potential difference is generated between areas with and without $FeCO_3$ creating an environment that initiates pitting corrosion.

Not all pits initiated due to galvanic cell formation propagates. Han et al. proposed that propagation of localized corrosion of mild steel in CO_2 conditions would continue only when the solution is near the saturation point with respect to $FeCO_3$ and the condition is called 'grey zone', where no significant $FeCO_3$ dissolution or additional precipitation is expected and the galvanic cell is established [40]. In TOL conditions, since supersaturation level remains low in presence of MEG and fluctuates during the initiation and termination of a droplet, the grey zone might be achieved inside the pit area and stabilize the galvanic cell to continue the pit propagation.

3.5 Conclusions

This study investigates the condensation process of monoethylene glycol (MEG) and water and how it influences corrosion of carbon steel. Main findings are summarised below:

- Condensation rate remarkably reduces when MEG concentration in the bulk is greater than 50% wt.%.
- Co-condensation of MEG in top of the line (TOL) increases with increasing bulk MEG concentration and decreasing condensation rate.
- Uniform corrosion rates decrease with increasing bulk MEG concentration primarily due to the decrease in condensation rate. In addition, MEG co-condensation plays a secondary role in reducing corrosion rates.

- MEG enhances localized corrosion in TOL and pits aggregate within the water droplet where corrosion product was more porous and less thick.
- Under condensing droplet, $FeCO_3$ supersaturation fluctuates and, with the presence of MEG, is relatively low. The combined effects lead to the formation of porous and non-protective $FeCO_3$ resulting in the propagation of localized corrosion.

Acknowledgements

The authors would like to acknowledge the Microscopy & Microanalysis Facility (MMF), Curtin University for the access of SEM and EDS. We would like to thank Dr. Thomas Becker, Department of Chemistry, Curtin University for analysing Raman data. The work was supported by International Postgraduate Research Scholarship (IPRS) provided by Curtin University.

3.6 References

[1] S. Nesic, Key issues related to modelling of internal corrosion of oil and gas pipelines - A review, Corros. Sci. 49 (2007) 4308–4338.

[2] D. Hinkson, Z. Zhang, M. Singer, S. Nesic, Chemical composition and corrosiveness of the condensate in top-of-the-line corrosion, Corrosion. 66 (2010) 045002–045008.

[3] M.M. Islam, T. Pojtanabuntoeng, R. Gubner, Condensation corrosion of carbon steel at low to moderate surface temperature and iron carbonate precipitation kinetics, Corros. Sci. 111 (2016) 139–150.

[4] Z. Zhang, D. Hinkson, M. Singer, H. Wang, S. Nesic, A mechanistic model of top-of-the-line corrosion, Corrosion. 63 (2007) 1051–1062.

[5] M. Wu, S. Wang, H. Liu, A study on inhibitors for the prevention of hydrate formation in gas transmission pipeline, J. Nat. Gas Chem. 16 (2007) 81–85.

[6] K.S. Pedersen, M.L. Michelsen, A.O. Fredheim, Phase equilibrium calculations for unprocessed well streams containing hydrate inhibitors, Fluid Phase Equilib.

126 (1996) 13–28.

[7] F. Ning, L. Zhang, Y. Tu, G. Jiang, M. Shi, Gas-hydrate formation, agglomeration and inhibition in oil-based drilling fluids for deep-water drilling, J. Nat. Gas Chem. 19 (2010) 234–240.

[8] G. Svenningsen, R. Nyborg, Modeling of top of line corrosion with organic acid and glycol, Corrosion/2014, Paper No. 4057, NACE, Houston, TX.

[9] M. Javidi, M. Khodaparast, Inhibitive performance of monoethylene glycol on CO_2 corrosion of API 5L X52 steel, J. Mater. Eng. Perform. 24 (2015) 1417–1427.

[10] T. Pojtanabuntoeng, M. Salasi, R. Gubner, The influence of mono ethylene glycol on CO_2 corrosion of carbon steel at elevated temperature (80-120 °C), Corrosion/2014, Paper No. 4176, NACE, Houston, TX.

[11] J. Kvarekvål, A. Pedersen, An electrochemical study of corrosion inhibition of carbon steel in sour glycol solutions, Corrosion/2013, Paper No. 2447, NACE, Houston, TX.

[12] A. Sherik, A. Lewis, A. Rasheed, A. Jabran, Effect of triethylene glycol on corrosion of carbon steel in H_2S, CO_2, and O_2 environments, Corrosion/2010, Paper No. 10188, NACE, Houston, TX.

[13] E. Samiento-Bustos, J.G. González-Rodriguez, J. Uruchurtu, V.M. Salinas-Bravo, Corrosion behavior of iron-based alloys in the LiBr+ethylene glycol+H_2O mixture, Corros. Sci. 51 (2009) 1107–1114.

[14] M.N. Khomami, I. Danaee, A.A. Attar, M. Peykari, Kinetic and thermodynamic studies of AISI 4130 steel alloy corrosion in ethylene glycol-water mixture in presence of inhibitors, Met. Mater. Int. 19 (2013) 453–464.

[15] E. Gulbrandsen, J. Morard, Why does glycol inhibit CO_2 corrosion?, Corrosion/98, Paper No. 98221, NACE, Houston, TX.

[16] E. Flaten, G. Watterud, J.-P. Andreassen, M. Seiersten, Precipitation of iron and calcium carbonate in pipelines at varying MEG contents, Int. Oilf. Scale

Conf./2008, Paper No. SPE 114089, Society of Petroleum Engineers, Aberdeen, UK.

[17] M. Singer, D. Hinkson, Z. Zhang, H. Wang, S. Nesic, CO_2 top of the line corrosion in presence of acetic acid: A parametric study, Corrosion. 69 (2013) 719–735.

[18] M. Singer, J. Al-Khamis, S. Nesic, Experimental study of sour top-of-the-line corrosion using a novel experimental setup, Corrosion. 69 (2013) 624–638.

[19] M. Singer, A. Camacho, B. Brown, S. Nesic, Sour top-of-the-line corrosion in the presence of acetic acid, Corrosion. 67 (2011) 85003–16.

[20] M. Singer, Study of the localized nature of top of the line corrosion in sweet environment, Corrosion. 73 (2017) 1030–1055.

[21] F. Vitse, K. Alam, Y. Gunaltun, Semi-empirical model for prediction of the top of the line corrosion risk, Corrosion/2002, Paper No. 02245, NACE, Houston, TX.

[22] F. Vitse, S. Nessic, Y. Gunaltun, D.L. de Torreben, P. Duchet-Suchaux, Mechanistic model for the prediction of top-of-the-line corrosion risk, Corrosion. 59 (2003) 1075–1084.

[23] A. Dugstad, Top of line corrosion- impact of MEG and organic acid in the gas phase, Corrosion/2014, Paper No. 4382, NACE, Houston, TX.

[24] S. Guo, F. Farelas, M. Singer, A glycol/water co-condensation model to investigate the influence of monoethylene glycol on top-of-the-line corrosion, Corrosion. 73 (2017) 742–755.

[25] ASTM G1 − 03, 2011, Standard practice for preparing, cleaning, and evaluating corrosion test, ASTM International.

[26] G.W. Thomson, The Antoine equation for vapor-pressure data., Chem. Rev. 38 (1946) 1–39.

[27] F. Farelas, M. Galicia, B. Brown, S. Nesic, H. Castaneda, Evolution of dissolution processes at the interface of carbon steel corroding in a CO_2 environment studied by EIS, Corros. Sci. 52 (2010) 509–517.

[28] M. Gao, X. Pang, K. Gao, The growth mechanism of CO_2 corrosion product films, Corros. Sci. 53 (2011) 557–568.

[29] J.L. Mora-Mendoza, S. Turgoose, Fe_3C influence on the corrosion rate of mild steel in aqueous CO_2 systems under turbulent flow conditions, Corros. Sci. 44 (2002) 1223–1246.

[30] J.L. Crolet, N. Thevenot, S. Nesic, Role of conductive corrosion products in the protectiveness of corrosion layers, Corrosion. 54 (1998) 194–203.

[31] J.-L. Crolet, Protrctiveness of Corrosion Layers, in: K.R. Trethewey, P.R. Roberge (Eds.), Model. Aqueous Corros. From Individ. Pits to Syst. Manag., Kluwer Academic Publishers, London, 1993: pp. 1–28.

[32] Y. Zhang, X. Pang, S. Qu, X. Li, K. Gao, Discussion of the CO_2 corrosion mechanism between low partial pressure and supercritical condition, Corros. Sci. 59 (2012) 186–197.

[33] R. Nyborg, A. Dugstad, Mesa corrosion altack in carbon steel and 0.5 % chromium steel, Corrosion/98, Paper No. 29, NACE, Houston, TX.

[34] S. Guo, L. Xu, L. Zhang, W. Chang, M. Lu, Corrosion of alloy steels containing 2% chromium in CO_2 environments, Corros. Sci. 63 (2012) 246–258.

[35] L. Wei, X. Pang, C. Liu, K. Gao, Formation mechanism and protective property of corrosion product scale on X70 steel under supercritical CO_2 environment, Corros. Sci. 100 (2015) 404–420.

[36] M. Hanesch, Raman spectroscopy of iron oxides and (oxy)hydroxides at low laser power and possible applications in environmental magnetic studies, Geophys. J. Int. 177 (2009) 941–948.

[37] C.T. Lee, M.S. Odziemkowski, D.W. Shoesmith, An in situ Raman-electrochemical investigation of carbon steel corrosion in $Na_2CO_3/NaHCO_3$, Na_2SO_4, and NaCl solutions, J. Electrochem. Soc. 153 (2006) B33–B41.

[38] X.-X. Bi, B. Ganguly, G.P. Huffman, F.E. Huggins, M. Endo, P.C. Eklund,

Nanocrystalline α–Fe, Fe_3C, and Fe_7C_3 produced by CO_2 laser pyrolysis, J. Mater. Res. 8 (1993) 1666–1674.

[39] R. Nyborg, Initiation and growth of mesa corrosion altack during CO_2 corrosion of carbon steel, Corrosion/98, Paper No. 48, NACE, Houston, TX.

[40] J. Han, B.N. Brown, S. Nesic, Investigation of the galvanic mechanism for localized carbon dioxide corrosion propagation using the artificial pit technique, Corrosion. 66 (2010) 95003–12.

Chapter 4: Study of the top-of-the-line-corrosion using a novel electrochemical probe[*]

4.3 Abstract

Top-of-the-line corrosion (TLC) is a concern for subsea wet-gas transportation pipelines operating in a stratified flow regime. The insufficient volume of electrolyte at the top-of-the-line combined with the low electrical conductivity of the condensed liquid has confined the majority of TLC studies to the weight loss method which only provides integrated corrosion rate over long period of exposure. The instantaneous monitoring of TLC rates using electrochemical methods is still a challenge for researchers and in the field.

To overcome this limitation, this study presents a novel TLC monitoring cell capable of measuring *in-situ* corrosion rates of carbon steel under condensing condition by electrochemical methods such as linear polarization resistance (LPR), electrochemical impedance spectroscopy (EIS) and electrochemical frequency modulation (EFM). The data presented in this paper have been conducted over 5 days at varying condensation rates to evaluate the feasibility and accuracy of the methods applied. In addition, TLC rates have also been measured by weight loss and monitored *in-situ* by measuring the iron concentration in the condensed liquids in order to compare these results with those from electrochemical methods. Both the electrochemical and non-electrochemical methods provide comparable results, which validates the design and efficacy of the probe. Therefore, the probe appears as a promising tool for further investigation into the TLC process and its inhibition.

4.4 Introduction

Top-of-the-line corrosion (TLC) is caused by the condensed water as a consequence of temperature gradient between the pipe wall and its external environment [1]. To date, TLC has accounted for numerous pipeline failures [2-5]. Its mitigation has been a challenge since conventional inhibitors cannot be effectively delivered to the corroding areas [6].

---

[*] This chapter is reproduced from 'M.M. Islam, T. Pojtanabuntoeng, R. Gubner, Study of the top-of-the-line corrosion using a novel electrochemical probe, accepted in Corrosion – The Journal of Science and Engineering'.

Over the last 25 years, a variety of TLC experimental setups have been utilized to unravel its mechanism and to develop effective prevention strategies and prediction tools. The most used method for TLC monitoring in the laboratory is weight loss. The coupon is flush-mounted on a lid and the coupon temperature is controlled externally. Condensation and corrosion takes place on the inner surface of the coupon which faces downward. The corrosion rate is measured from the weight loss of the coupon after removing the corrosion product [1,7-10]. The method is suitable for measuring uniform as well as localized corrosion rate over a period of time. This form of corrosion monitoring provides cumulative damage at the end of the exposure period.

Electrical resistance (ER) probes, flush-mounted into the vapour phase, have also been used in several experimental setups and in field monitoring in order to estimate corrosion rates and to determine the efficiency of inhibition techniques [11-14]. A metallic element of the ER probe is exposed to corrosive environment while a separate one is sealed within the probe as a reference material. Variations in the electrical resistance occurs due to thickness and/or net metal loss of the metallic element from corrosion process [15]. The ER technique has shown to be appropriate for TLC rate determinations. Besides, the formation of conductive corrosion products and even $FeCO_3$ on the surface can affect the performance of this probe. However, the method does not provide insight into the TLC mechanism. Furthermore, the sensing element needs to be completely covered by aqueous solutions for an accurate estimation of the corrosion rate [16].

Recently, the quartz crystal microbalance (QCM), was introduced to measure TLC and condensation rates [17]. QCM calculates a small variation in mass of deposited iron on a quartz crystal resonator by measuring its change in frequency. Nonetheless, this special device still faces many technical difficulties to become effective in real conditions.

Oehler et al. proposed a “cold finger probe” for monitoring the efficiency of volatile corrosion inhibitors (VCI) using the linear polarization resistance (LPR) technique [18]. Their design involved a sample holder mounted with carbon steel pins exposed

to the corrosive vapour phase. Water condensation took place onto the vertical pins because of external cooling of the holder. The condensed water dripped and was collected in a condensed liquid container. After collecting a certain volume of condensed liquid, the probe is pushed to immerse the pins into the condensed liquid for LPR measurements. Nevertheless, the particular design of the probe and the way of measuring the corrosion rates are unable to distinguish the influence of environmental parameters such as condensation rate and temperature.

Ajayi and Lyon utilized an electrochemical approach to investigate the efficiency of VCI [19]. The electrode system consisting of two identical narrow mild steel sheets were embedded in an acrylic mould of 30 mm in diameter where one was used as working electrode with an exposed area 0.0721 cm^2 separated by 0.5 mm silicon rubber sheet as insulating materials from the other which was used as a counter electrode. The difference in hydrophobicity and thermal conductivity of acrylic and metal surface may have effects on condensation pattern and, consequently, droplet retention time. In addition, comparison with non-electrochemical techniques is necessary to provide confidence in the accuracy of the results.

In a previous study, we presented a new experimental setup for *in-situ* measurement of corrosion rate by measuring the iron concentration in the condensed liquid [7]. The design provided accurate measurements of TLC rate in the absence of iron carbonate. If iron carbonate is formed, this method underestimates the TLC rate as compared to weight loss data because Fe^{2+} partially precipitates and is not entirely available in the condensed liquid. In addition, the method may not be adopted in the field due to challenges in collecting condensed liquid samples.

Therefore, this paper presents the design of a new electrochemical probe to measure the TLC rate of carbon steel using electrochemical methods. A series of experiments at different water condensation rates were conducted to verify the accuracy and limitations of this new probe. It is anticipated that successful development of TLC electrochemical monitoring could lead to further understanding of TLC mechanism, localised corrosion in particular, and efficient mitigation plans.

4.5 Experimental Procedures

4.5.1 Fabrication of TLC probe

The TLC probe, shown in Figure 4.1, was comprised of 2 carbon steel rods having the same chemical composition (carbon 0.30%, manganese 0.75%, silicon 0.25%, phosphorous 0.04%, sulphur 0.04% and iron balance). The larger rod with a diameter of 20 mm (0.79 in) and length of 30 mm (1.18 in) was drilled creating a 3 mm (0.12 in) in diameter hole at the center. The second carbon steel rod was machined to 2 mm (0.08 in) in diameter and 40 mm (1.57 in) in length. Both rods were sand-blasted and subsequently cleaned with deionized water and acetone and air dried before electrodeposited with cationic epoxy (Powercron^{TM} 6000CX) and cured in the oven for 20 minutes at 150 °C. The small rod was then inserted into the 3 mm hole and the annular space were filled with liquid epoxy (a mixture of resin and hardener). The small diameter electrode acted as a working electrode whereas the larger one acted as a counter/reference electrode. Both were electrically insulated by the cationic epoxy and liquid epoxy. The SEM image of working electrode separating from the counter electrode with resin is given in Figure 4.2.

Prior to experiments, the flat face of the probe was wet ground with silicon carbide paper down to 1200 grit. It was then cleaned with water, ethanol and dried with nitrogen. The dried probe was weighed with an analytical balance (resolution 0.1 mg) before fitting into the TLC lid.

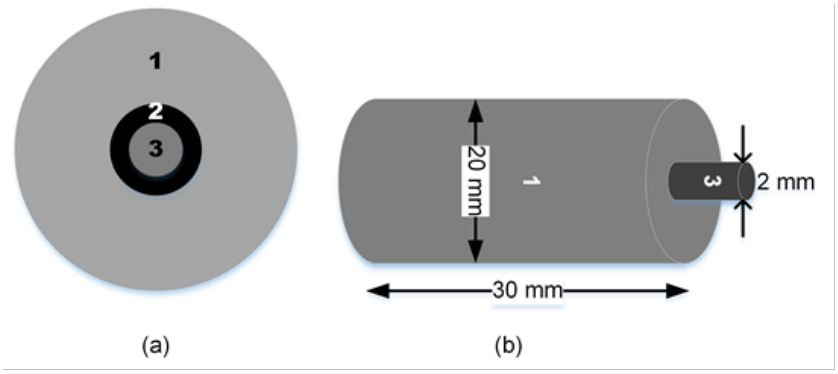

Figure 4.1: Schematic of top of the line corrosion (TLC) probe (drawing not in scale); (a) cross sectional view, (b) longitudinal view; 1. Carbon steel counter/reference electrode, 2. Epoxy resin separating two electrodes, 3. Carbon steel working electrode.

4.5.2 Cell setup for TLC

The schematic of the TLC setup is illustrated in Figure 4.3 and the detail was previously explained [7]. The prepared TLC probe was inserted into the polyethylene terephthalate (PET) lid so that the polished portion faced downward to the corrosive environment and the remaining part stayed above the lid. The lid was assembled with temperature probes for measuring gas temperature and surface temperature, thermocouple for controlling bulk liquid temperature, CO_2 inlet and outlet, and a condensed liquid collection cup. A copper tube was coiled around the upper portion of the probe through which cooling liquid was circulated to maintain the surface temperature. The surface temperature was measured by a temperature probe inserted into the hole just above the polished face of the TLC probe. Another temperature probe was suspended into the vapour phase to measure the gas temperature. The lid was mounted onto a 2 L glass cell creating an air-tight environment. The whole assembly was deoxygenated by continuously sparging with high purity CO_2 gas (99.99%) for 10 min.

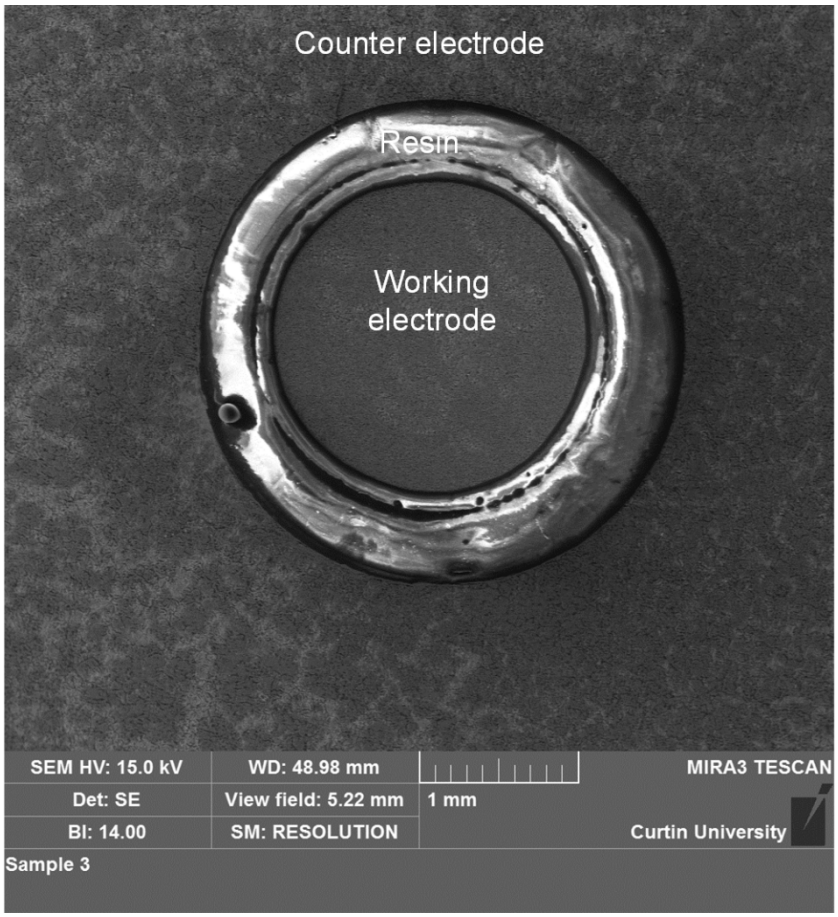

Figure 4.2: SEM image of the surface of TLC probe showing working electrode separated from counter electrode with resin.

1400 mL of high purity water (18.2 MΩ.cm), pre-sparged in a separate container with high purity CO_2 overnight and pre-heated to a predefined temperature, was transferred to the TLC cell using a peristaltic pump to avoid oxygen contamination. The bulk liquid temperature and the cooling water temperature were controlled to achieve the desired gas temperature and surface temperature. In this study, gas temperature was maintained constant at 55 °C and surface temperature was varied to 20 °C, 30 °C and 40 °C.

Water condensation took place on the surface of the TLC probe, which dripped and was transferred immediately into the condensate reservoir at room temperature to avoid any re-evaporation. Mass, pH, and ferrous ion concentration of the condensed liquid was measured periodically after collecting it from the reservoir. The ferrous ion

concentration was measured using a spectrophotometer. The water condensation rate was calculated by dividing the collected condensed water with exposed surface area of probe and time [7]. Because hot vapour can also condense along the tubing and the internal wall of the condensate reservoir, water condensation rates might be overestimated. Therefore, additional experiments were conducted when the surface temperature was slightly higher (1-2 °C) than the gas temperature which was kept at 55 °C. Condensed liquid collected in these preliminary experiments were then used to compensate when calculating for water condensation rates in subsequent tests. The *in-situ* corrosion rate was estimated from the dissolved iron (Fe^{2+}) presenting in the condensed liquid for a given exposure time [7]. After finishing the experiment, selected samples were characterised using SEM and EDS to investigate the surface morphology. Then the corrosion product was removed from the sample surface and corrosion rate was calculated from the loss of weight of the whole probe as described elsewhere [7,20]. Each test was repeated at least twice and the average and standard deviation were reported.

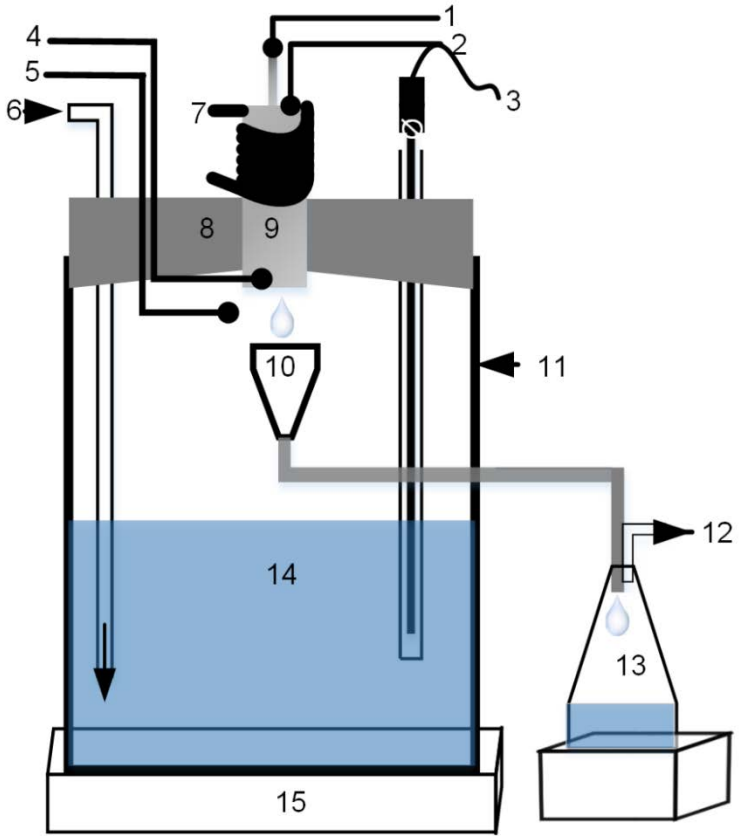

Figure 4.3: Schematic of top-of-the-line corrosion (TLC) setup reproduced from reference [7] with addition of TLC probe and cooling coil; 1. Working electrode connection, 2. Counter/reference connection, 3. Thermocouple, 4. Surface temperature probe, 5. Gas temperature probe, 6. CO_2 inlet, 7. Cooling coil for maintaining surface temperature, 8. Polyethylene terephthalate lid, 9. TLC probe, 10. Condensate collector, 11. 2-L glass vessel, 12. CO_2 outlet, 13. Condensate reservoir, 14. Milli-Q water, 15. Heater.

4.5.3 Electrochemical Measurements

All the electrochemical measurements were carried out in a 2-electrode arrangement. Measurements were performed with a Gamry Potentiostat/Galvanostat/ZRA (Reference 600). Echem Analyst Software (version 6.25) was used for analysing data. The following three electrochemical techniques were performed:

Electrochemical frequency modulation (EFM) was conducted at two frequencies of 0.02 Hz and 0.05 Hz. A perturbation signal with an amplitude of 5 mV for both perturbation frequencies were used. Stern-Geary constant (*B*) and corrosion rate were

calculated under diffusion mode. It should be noted that *B* obtained from EFM was divided by 2 and was subsequently used for corrosion rate calculation. This approach was compared with the results from weight loss (WL). In addition, a separate investigation was conducted under immersion condition to verify this approach and the results are described in the Appendix of this chapter.

Linear polarization resistance (LPR) was conducted within ±5 mV with respect to open circuit potential (OCP) at a scan rate of 10 mV/min. The polarization resistance was corrected by compensating the solution resistance at each condition and converted to corrosion rates using β obtained from EFM.

Electrochemical Impedance Spectroscopy (EIS) was carried out within a frequency range from 10 kHz to 0.1 Hz with an amplitude of 5 mV peak-to-peak at OCP. Corrosion rate was calculated from the charge transfer resistance using *B* obtained from EFM.

4.6 Results and discussion

4.6.1 TLC rate obtained from non-electrochemical techniques

Two non-electrochemical techniques; i.e. weight loss and Fe^{2+} concentration measurement, were performed and results were used as the basis to compare with those obtained from electrochemical techniques.

Figure 4.4 presents TLC rates obtained from weight loss measurements after 5 days and the corresponding condensation rates. The gas temperature was 55 °C and the surface temperatures were varied at 20 °C, 30 °C to 40 °C, respectively. The results showed that by increasing surface temperature from 20 °C to 30 °C, TLC rates increased from 0.75 mm y^{-1} to 0.86 mm y^{-1} despite the slight decrease in water condensation rates. A further increase of surface temperature from 30 °C to 40 °C while maintaining the gas temperature reduced water condensation rate from 1.10 g $m^{-2}s^{-1}$ to 0.76 g $m^{-2}s^{-1}$, whereas TLC rates are not statically different.

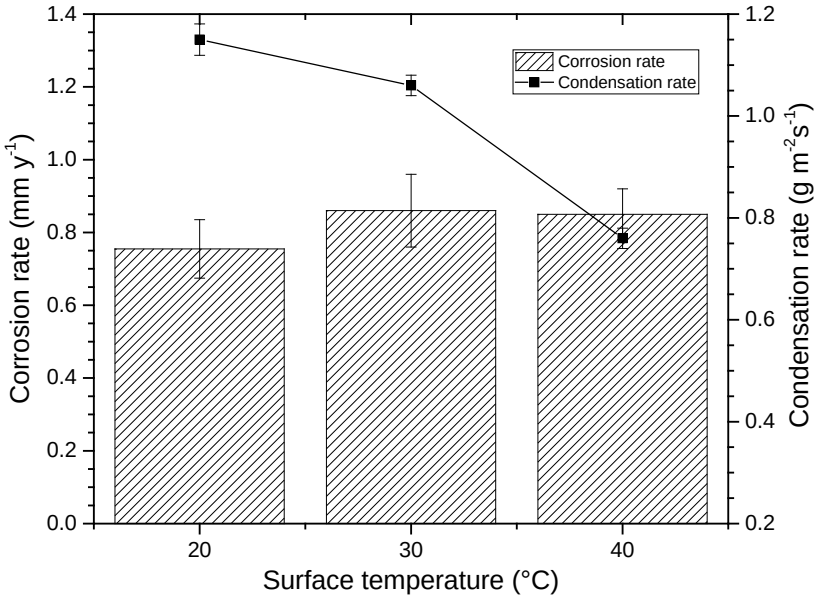

Figure 4.4: TLC rates obtained from weight loss of the coupon and corresponding condensation rates at different surface temperature and 55 °C gas temperature.

At 30 °C surface temperature and 55 °C gas temperature, no $FeCO_3$ was formed as confirmed in a previous study [7]. In the absence of iron carbonate scale, surface temperature was the governing parameter over condensation rate [7]. Hence, TLC rate increased while increasing surface temperature from 20 °C to 30 °C despite the reduction in the condensation rates. However, different scenario occurred at 40 °C surface temperature. At this temperature, $FeCO_3$ began to form specially on the surface outside the big water droplet, as shown in SEM image and EDS spectrum (Figure 4.5). This area was covered with a continuous liquid film which may be less disturbed by the condensation process. Hence, this area achieved $FeCO_3$ more readily compared to that under the droplet. Crystalline particles in SEM image shows high intensity of oxygen, iron, and carbon indicating the presence of $FeCO_3$ [7,21]. Therefore, decreasing condensation rate and increasing surface temperature assist the formation of $FeCO_3$ and obstructed the iron dissolution rate at 40 °C surface temperature [7].

The *in-situ* TLC rates measured by the iron concentration in the condensed liquid are shown in Figure 4.6. It is apparent that corrosion rates increased with time at all test temperatures. Galvanic effects between ferrite and pearlite of the carbon steel have

been reported to increase corrosion rates with time [7,22,23]. At 30 °C surface temperature, the iron concentration measurement also gives the highest corrosion rate. However, *in-situ* TLC rates at 40 °C is almost similar to that obtained at 20 °C surface temperature. The contradicting trend in corrosion rates at 40 °C surface temperature reported by WL (in Figure 4.5) and iron measurement was simply because all the corroded iron did not present in the condensed liquid as the surface temperature was favourable for $FeCO_3$ formation.

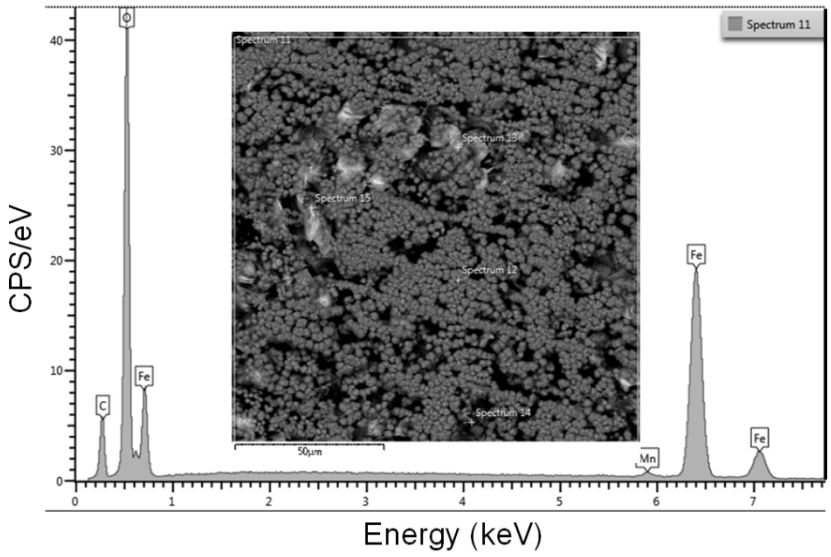

Figure 4.5: SEM and EDS of corrosion product obtained at 40 °C surface temperature and 55 °C gas temperature showing initiation of $FeCO_3$ scale.

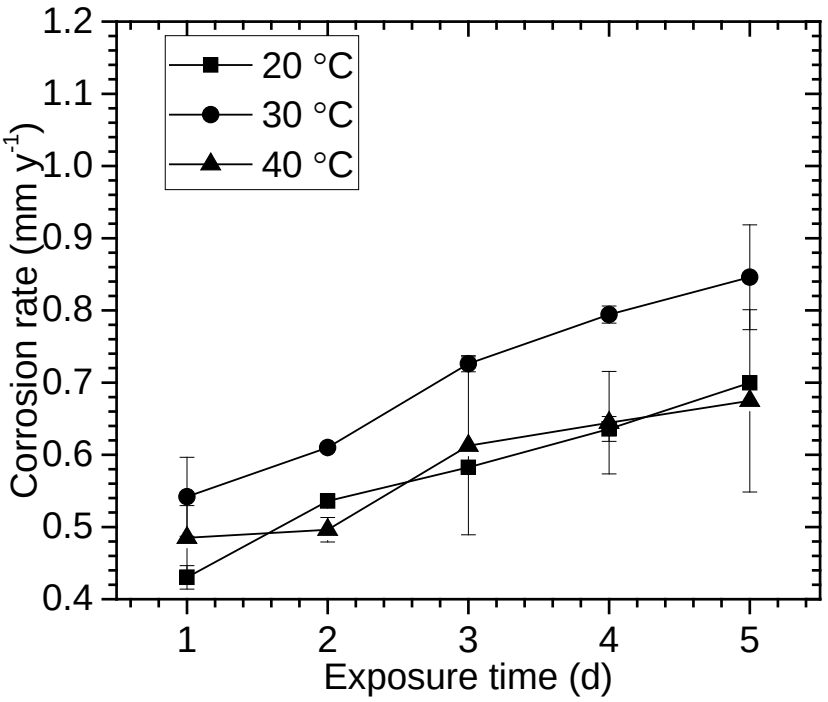

Figure 4.6: In-situ TLC rates obtained from Fe^{2+} concentration measurement in the condensed liquid at different surface temperature and 55 °C gas temperature.

4.6.2 TLC rate obtained from electrochemical techniques

Electrochemical frequency modulation (EFM)

Electrochemical frequency modulation (EFM) was selected for this study because of its ability to measure corrosion current density without prior knowledge of *B*. EFM is an AC technique where two sine waves at 2 different frequencies are applied simultaneously. The nonlinear nature of the corrosion process produces current responses at zero, harmonic, and intermodulation frequencies with respect to the applied signal [24,25]. In spite of its inherent ability to measure the corrosion rate, the EFM technique requires a preliminary understanding of whether the corrosion process under investigation is an active, diffusion, or passivating system. In addition, appropriate frequencies needs to be selected to avoid the influence of the capacitance double layer and the overestimation of corrosion current [26].

Table 4.1 presents the TLC rate and *B* obtained from EFM technique calculated using active mode and diffusion mode. It is found that the active mode of calculation gives an unexpected trend of corrosion rates (0.53-1.52 mm y^{-1}) and *B* value (12-33 mV) with respect to minor change in amplitude (5-7 mV). Therefore, it can be concluded that the active mode is not suitable for this application because of inconsistent results as shown in Table 4.1. In contrast, under diffusion mode of calculation, corrosion rate (0.59-0.65 mm y^{-1}) and *B* value (13-14 mV) are independent of the applied amplitude which provided fundamentally correct results (Table 4.1). When compared to existing literature, *B* values of 13 mV to 20 mV has been reported for carbon steel corrosion in CO_2 containing environment [27,28]. In addition, the cathodic reaction under CO_2 condition at pH above 5 (pH of the condensing liquid) has been reported to be either mass transfer/diffusion controlled or a mixed control depending on condition [29-31]. Pure charge transfer control has not been reported at conditions that would resemble that of condensed water (pH around 5-6 and at stagnant condition) [7]. For TLC, because of the formation of very thin condensed film of liquid, the mass transport might be the controlling factor [32]. Consequently, diffusion mode of calculation has been chosen for calculating the *B* value as well as TLC rates.

To illustrate the effect of frequency range on EFM measurements, the frequency and impedance plots obtained at 40 °C surface temperature and 55 °C gas temperature are illustrated in Figure 4.7. It can be seen that at a frequency below 0.3 Hz the impedance is independent of frequency, which is a characteristic of charge transfer resistance. If a frequency greater than 0.3 Hz is applied, the impedance starts to decrease as influenced by the capacitance double layer which in turns overestimate the corrosion rate [26]. This is demonstrated in Table 4.2 where EFM measurements were performed at a various range of frequencies and extremely high corrosion rates were obtained at high frequencies. Hence, frequencies of 0.02 Hz and 0.05 Hz were chosen for this study to avoid the influence of capacitance as well as to achieve a comparable result with weight loss measurement.

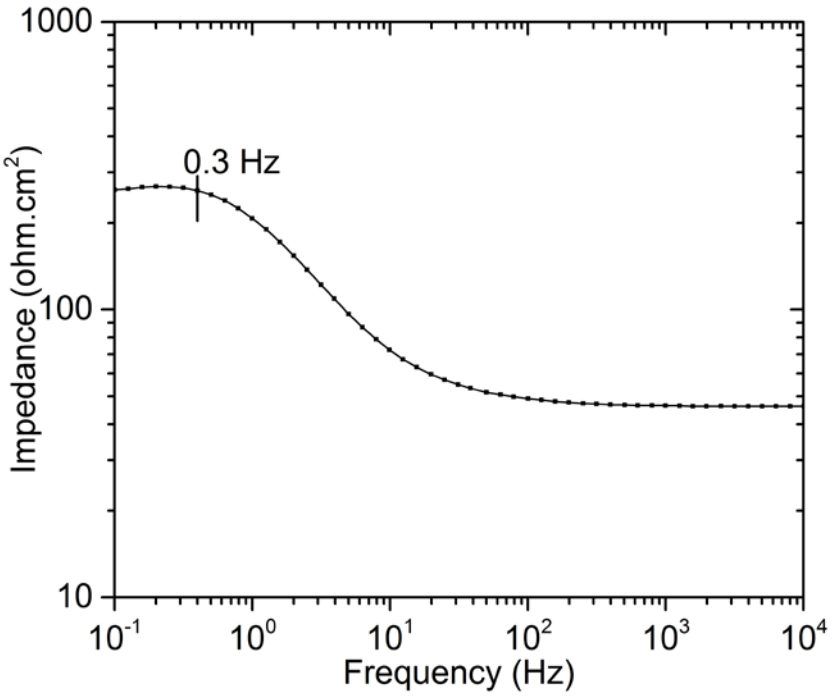

Figure 4.7: Frequency vs impedance curve under TLC condition at 40 °C surface temperature and 55 °C gas temperature for selection of base frequency of electrochemical frequency modulation technique.

Table 4.1: Comparison of Stern-Geary constant (B) and corrosion rate (CR) obtained from active mode and diffusion mode of calculation within the frequency range from 0.02 to 0.05 Hz at different amplitude at 40 °C surface temperature and 55 °C gas temperature.

Amplitude, mV	Active mode		Diffusion mode	
	B, mV	CR, mm/y	*B*, mV	CR, mm/y
5	12	0.53	13	0.59
6	26	1.12	13	0.59
7	33	1.52	14	0.65

Table 4.2: Influence of base frequency on Stern-Geary constant (B) and corrosion rate (CR) under TLC condition at 40 °C surface temperature and 55 °C gas temperature.

Amplitude, mV	Frequency, Hz	*B*, mV	CR, mm/y
5	0.02 to 0.05	14	0.61
5	0.2 to 0.5	19	0.86
5	2 to 5	55	4.26

The *in-situ* TLC rates obtained from EFM technique are given in Figure 4.8. Similar to the results obtained from the weight loss method, a temperature of 20 °C results in lower corrosion rate whereas TLC rates at 30 °C and 40 °C are almost similar. However, at all temperatures, the *in-situ* corrosion rates tend to increase throughout the entire experiment, which is in good agreement with the trend obtained from Fe^{2+} concentration measurement, as shown previously in Figure 4.6.

Figure 4.9 presents *B* values obtained from EFM technique at different surface temperatures for 5 days. The *B* value tends to increase with time at all temperatures tested but decreases with increasing surface temperatures. However, the *B* values found within the range from 15 to 20 are in agreement with literature values reported for CO_2 corrosion conditions [31-33].

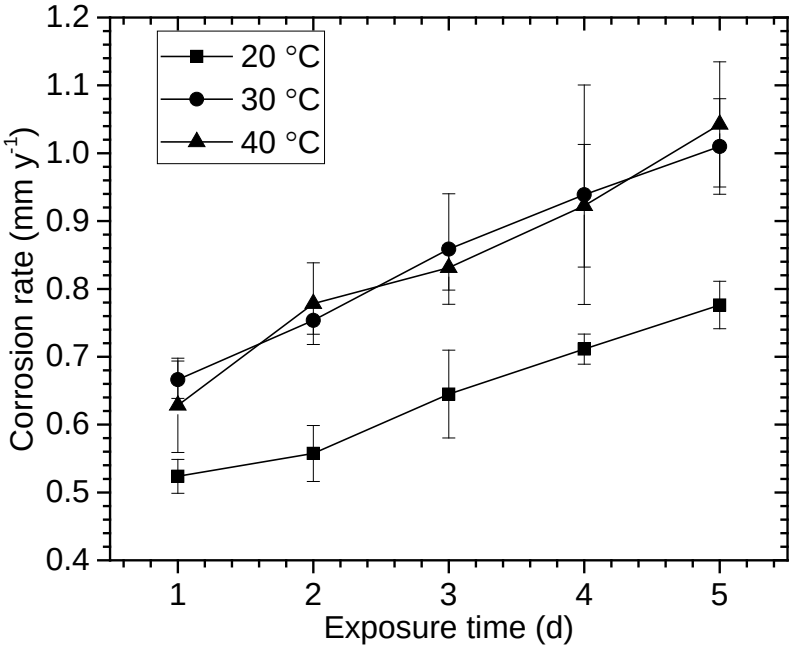

Figure 4.8: In-situ TLC rates obtained from EFM technique at different surface temperature and 55 °C gas temperature.

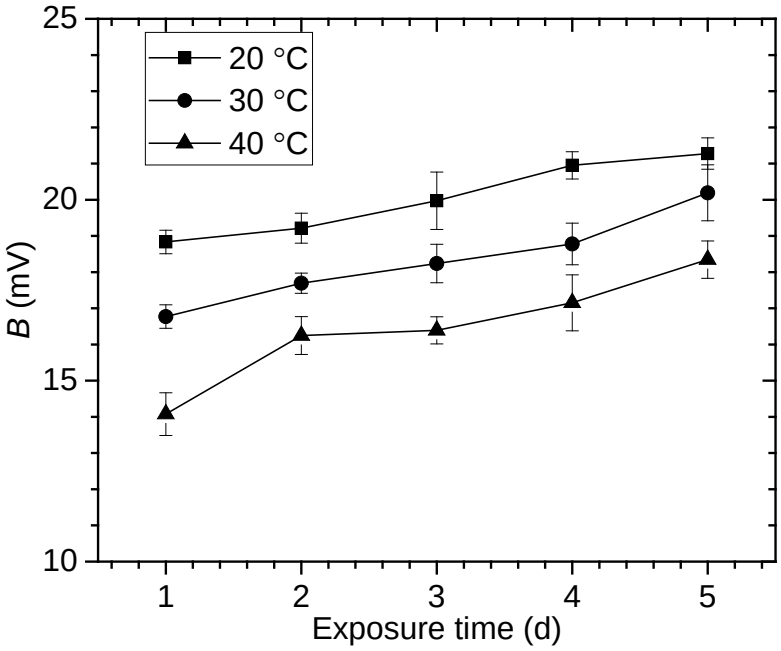

Figure 4.9: Stern-Geary constant (B) obtained from EFM technique at different surface temperatures and 55 °C gas temperature.

Linear polarization resistance measurement

Figure 4.10 shows the *in-situ* TLC rates calculated from linear polarization resistance (LPR) over 5 days at different surface temperatures employing *B* value obtained from EFM technique, as described above. LPR corrosion rates increase throughout the entire period at all surface temperatures. The lowest TLC rates were measured at 20 °C surface temperature whereas comparable TLC rates were seen at 30 °C and 40 °C. The results are also in good agreement with those obtained from the weight loss method.

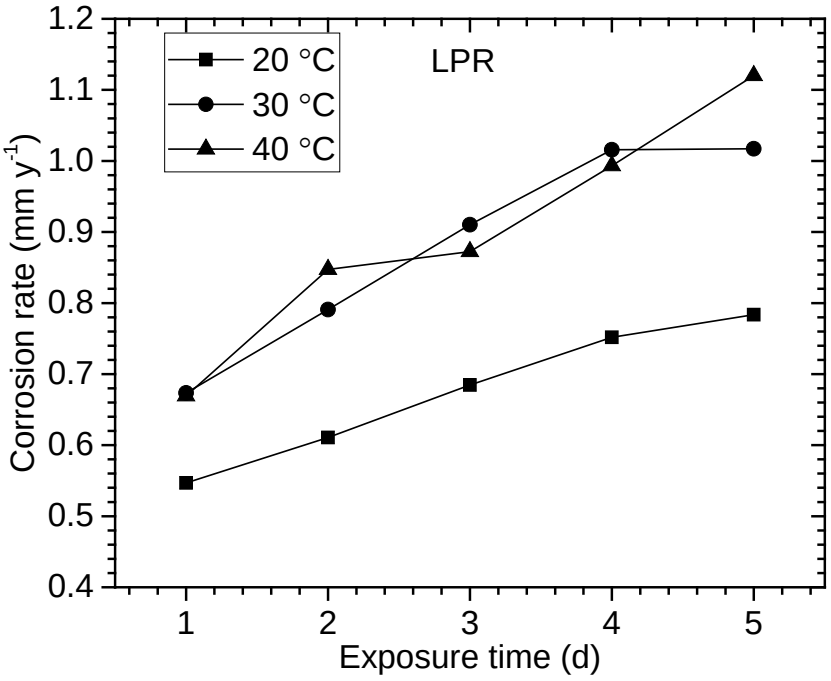

Figure 4.10: In-situ TLC rates obtained from LPR technique at different surface temperature and 55 °C gas temperature.

Electrochemical impedance spectroscopy (EIS) for TLC study

EIS has been widely employed in various complex corrosion phenomena as the results can be fitted through equivalent circuits allowing surface/electrolyte reactions to be explained. For instance, in addition to charge transfer resistance, EIS can distinguish solution resistance of the condensed droplets. The shape of the Nyquist and Bode plot can provide information about the properties of corrosion product film [19,35].

The Nyquist plots and corresponding fitting curves of the TLC coupon at 20 °C, 30 °C and 40 °C surface temperature are shown in Figure 4.11a, 4.11b and 4.11c respectively. Their similar shape is apparent; i.e., a depressed semicircle and an inductive loop in the low frequency range. The magnitude of semicircles decreases suggesting an increasing corrosion rate over time, which is in agreement with the Fe^{2+} measurement, EFM and LPR. Such behaviour has been reported as active surface state due to the frequent exposure of the cementite phase and subsequent galvanic coupling with ferrite in the absence of corrosion product scale [22,23,36]. The inductive loop at low frequencies is originated due to the adsorption of the intermediate species [37]. The extent of inductive loop decreases with time indicating the change in the corrosion mechanism.

EIS results were fitted with the equivalent circuit shown in Figure 4.12 which has been widely used for modelling the steel–CO_2 interface involving an adsorbed intermediate product [38]. The variation of resistances of the condensed liquid (R_s) derived from the fitting parameters are shown in Figure 4.13. At 20 and 30 °C, R_s decreased with time because of increasing corrosion rate and, subsequently, Fe^{2+} concentration in the condensed liquid. However, in spite of higher Fe^{2+} at 30 °C compared to 40 °C surface temperature, R_s was the lowest at 40 °C. Therefore, surface temperature is the dominant parameter controlling R_s. The charge transfer resistance obtained from EIS measurement after fitting with the equivalent circuit was converted to the corrosion rate using the *B* value obtained from EFM in the same condition. Figure 4.14 shows the change in corrosion rate up to 5 days at different surface temperatures. Similar to results obtained by the other electrochemical methods employed in this study, the TLC rates increased with time at all temperatures and the 20 °C provided lowest corrosion rate compared to the other surface temperatures.

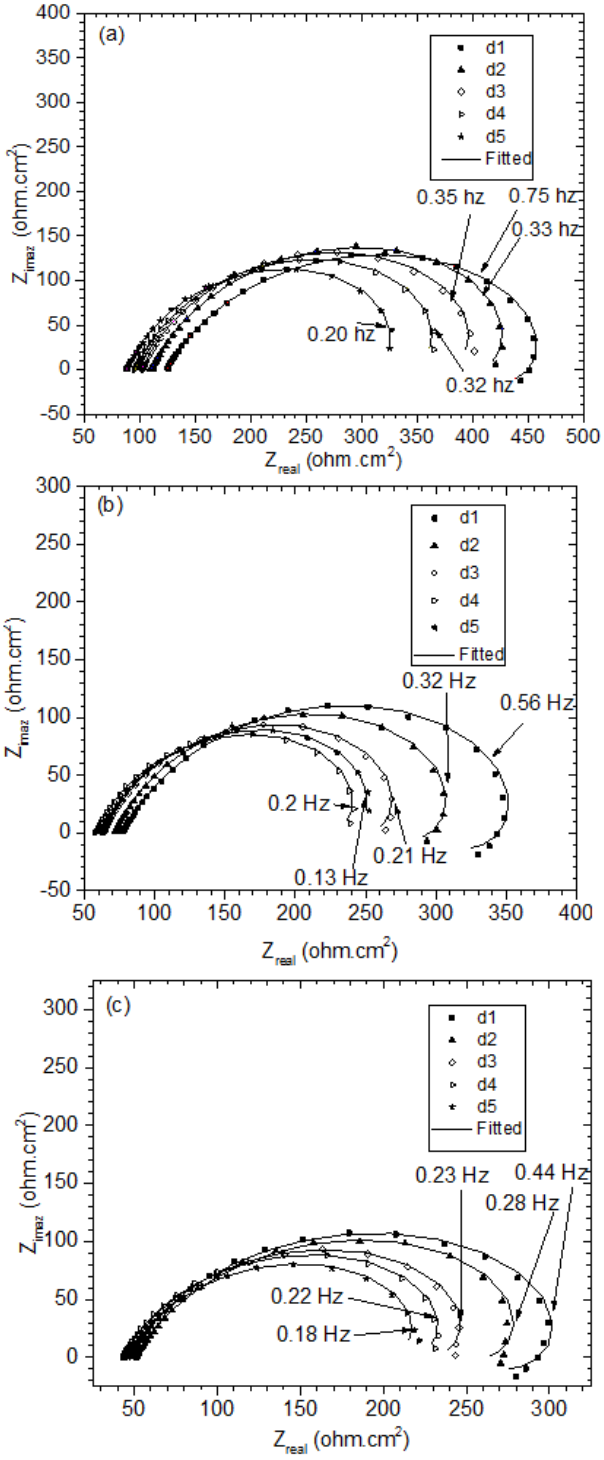

Figure 4.11: Nyquist plot of TLC sample surface at 55 °C gas temperature and (a) 20 °C, (b) 30 °C and (c) 40 °C surface temperature.

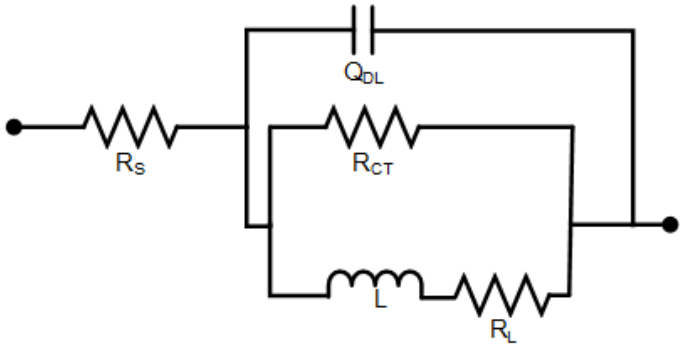

Figure 4.12: Equivalent circuit used to fit the EIS data; R_S is the solution resistance, Q_{DL} is the capacitance of the double layer, R_{CT} is the charge transfer resistance, L is the inductance and R_L is the resistance of an inductor.

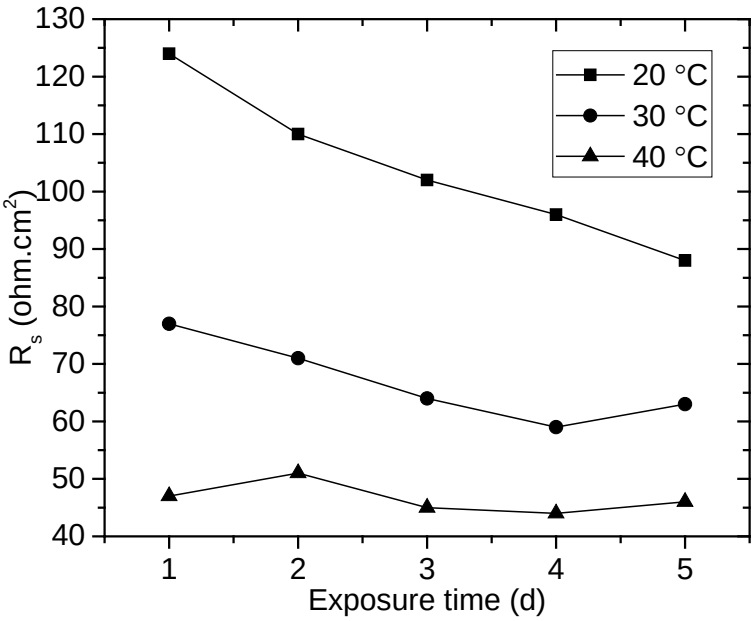

Figure 4.13: Variation of resistance of condensed water (Rs) with time at different experimental condition.

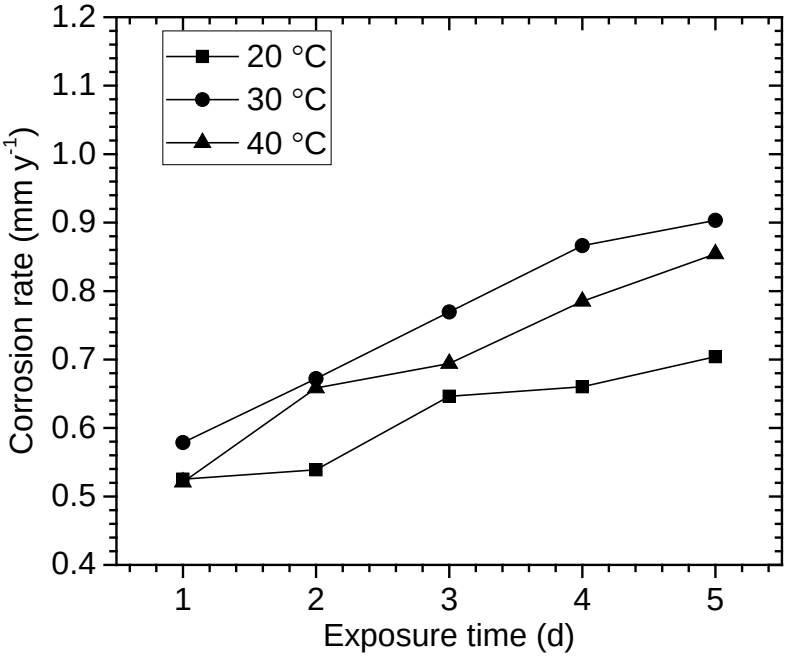

Figure 4.14: In-situ TLC rates obtained from EIS technique at different surface temperature and 55 °C gas temperature.

4.6.3 Comparison of TLC rates obtained from different techniques

The comparison of (integrated) TLC rates obtained from non-electrochemical techniques (weight loss and Fe^{2+} concentration) and the electrochemical techniques (LPR, EIS and EFM) at 20 °C, 30 °C and 40 °C surface temperatures and 55 °C gas temperature are shown in Figure 4.15. Overall, comparable corrosion rates are found between weight loss and the electrochemical techniques employed. LPR results (after taken into account the solution resistance) were approximately 20-30% greater than those from WL while EFM and EIS provided closer estimation. Regardless of electrochemical methods, *B* values used were obtained from EFM under diffusion mode and were subject to factor of 0.5 (as explained in the Appendix) which provided reasonable comparison in the conditions within this study. More importantly, it also shows that small volumes of condensed liquid on the surface of the electrode do not interfere with the electrochemical measurements and the setup successfully

differentiates the influences of environmental parameters (condensation rates and temperature) on TLC.

Some of the limitations should also be noted. For instance, the conditions selected in the current study exhibited only uniform corrosion. The localized nature of TLC may prevail at other conditions (e.g. longer term study, the presence of organic acids, etc.) and has not been addressed using this new monitoring device. Further study is also needed to understand a factor applied to *B*. Nonetheless, the study demonstrated the forward step in the development of the probe for electrochemical study of TLC.

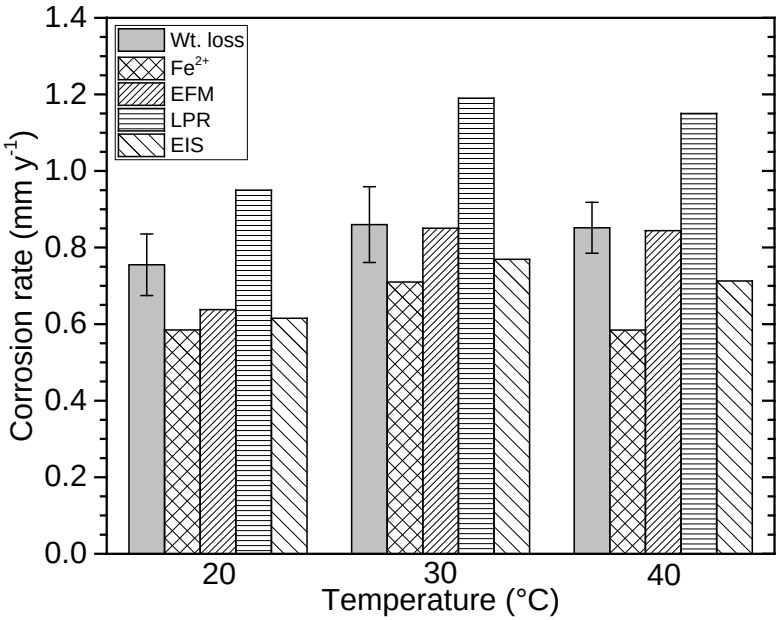

Figure 4.15: Comparison of TLC rates obtained from weight loss with line average corrosion rates obtained from Fe^{2+} measurement, electrochemical frequency modulation (EFM), linear polarization resistance (LPR), and electrochemical impedance spectroscopy (EIS) technique.

4.7 Conclusions

A new electrochemical setup for the investigation into top of the line corrosion (TLC) has been developed and verified. The following conclusions can be made from the study:

- The electrochemical methods selected for this study (EFM, LPR and EIS) are able to overcome the incompatibilities associated with the small volume of condensed water at the top of the line and provide good agreement with results obtained from non-electrochemical methods, particularly weight loss. More importantly, the new set-up in conjunction with EIS technique enables mechanistic studies on TLC process in addition to TLC rates.
- *In-situ* corrosion rates obtained by Fe^{2+} measurement provide lower values compared to weight loss technique and other electrochemical techniques. The difference is more pronounced at higher surface temperatures when iron carbonate may precipitate. This emphasizes that electrochemical techniques are more accurate compared to Fe^{2+} measurements for *in-situ* monitoring of TLC rate especially when $FeCO_3$ precipitation is likely.
- EFM could be a powerful technique for TLC monitoring as, in theory, it can provide the Stern-Geary constant (*B*) and corrosion rate directly. However, the present study demonstrated that an arbitrary factor is required. Therefore, a detail theoretical analysis is necessary to improve understanding and confidence in using this technique.

Acknowledgements

The authors would like to thank Curtin University for providing International Postgraduate Research Scholarship (IPRS) to conduct the study. We would like to thank Professor Brian Kinsella, Curtin Corrosion Engineering Industry Centre, Curtin University for his valuable advice in designing the TLC probe.

4.8 References

[1] Z. Zhang, D. Hinkson, M. Singer, H. Wang, S. Nesic, A mechanistic model of top-of-the-line corrosion, Corrosion. 63 (2007) 1051–1062.

[2] J.R. Piccardino, M. Stuvik, Y. Gunaltun, T. Pornthep, Internal inspection of wet gas lines subject to top of line corrosion, CORROSION/2004, Paper No. 04354, NACE, Houston, Texas, 2004.

[3] Y. Gunaltun, S. Punpruk, M. Thammachart, P. Tanaprasertsong, Worst case top of the line corrosion: cold spot corrosion, CORROSION/2010, Paper No. 10097, NACE, Houston, Texas, 2010.

[4] M. Joosten, D. Owens, A. Hobbins, H. Sun, M. Achour, D. Lanktree, Top-of-line corrosion – a field failure, EUROCORR/2010, Paper No. 9524, Gubkin Russian State University of Oil and Gas, Moscow, Russia, 2010.

[5] Y. Gunaltun, U. Kaewpradap, M. Singer, S. Nesic, S. Punpruk, M. Thammachart, Progress in the prediction of top of the line corrosion and challenges to predict orrosion rates measured in gas pipelines, CORROSION/2010, Paper No.10093, NACE, Houston, Texas, 2010.

[6] F. Vitse, S. Nesic, Y. Gunaltun, D.L. de Torreben, P. Duchet-Suchaux, Mechanistic model for the prediction of top-of-the-line corrosion risk, Corrosion. 59 (2003) 1075–1084.

[7] M.M. Islam, T. Pojtanabuntoeng, R. Gubner, Condensation corrosion of carbon steel at low to moderate surface temperature and iron carbonate precipitation kinetics, Corros. Sci. 111 (2016) 139–150.

[8] M. Singer, A. Camacho, B. Brown, S. Nesic, Sour top-of-the-line corrosion in the presence of acetic acid, Corrosion. 67 (2011) 85003–16.

[9] M. Singer, J. Al-Khamis, S. Nesic, Experimental study of sour top-of-the-line corrosion using a novel experimental setup, Corrosion. 69 (2013) 624–638.

[10] T. Pojtanabuntoeng, M. Singer, S. Nesic, Top-of-the-line corrosion in the presence of hydrocarbon co-condensation in flowing condition, CORROSION/2012, Paper No. C2012-0001534, NACE, Houston, Texas, 2012.

[11] B. Bavarian, J. Zhang, L. Reiner, B. Miksic, FNACE, Comparison of the corrosion protection effectiveness of vapor corrosion inhibitor and nitrogen blanketing system, CORROSION/2015, Paper No.5450, NACE, Houston, Texas, 2015.

[12] I. Jevremović, V. Mišković-Stanković, M. Achour, M. Singer, S. Nesic, Evaluation of a novel top-of-the-line corrosion (TLC) mitigation method in a

large scale flow loop, CORROSION/2013, Paper No. 2321, NACE, Houston, Texas, 2013.

[13] B. Bavarian, Y. Ikder, B. Samimi, L. Reiner, B. Miksic, FNACE, Comparison of the corrosion protection effectiveness of vapor corrosion inhibitors and dry air system, CORROSION/2015, Paper No.5449, NACE, Houston, Texas, 2015.

[14] I. Jevremović, M. Singer, M. Achour, V. Mišković-Stanković, S. Nesic, Evaluation of a novel top-of-the-line corrosion (TLC) mitigation method in a large-scale flow loop, Corrosion. 71 (2015) 389–397.

[15] J.J. Wylde, M. Reid, A. Kirkpatrick, N. Obeyesekere, D. Glasgow, When to batch and when not to batch : An overview of integrity management and batch corrosion inhibitor testing methods and application strategies, SPE Int. Symp. Oilf. Chem., Society of Petroleum Engineers, Woodlands, Texas, 2013: pp. 1–12.

[16] M. Singer, Study and modeling of the localized nature of top of the line corrosion, PhD desertation, Ohio University, Ohio, USA, 2013.

[17] S. Ramachandran, V. Jovancicevic, P. Rodgers, I. Ahmed, M. Al-Waranbi, A new top-of-the-line corrosion inhibitor to mitigate carbon dioxide corrosion in wet gas systems, CORROSION/2013, Paper No. 2274, NACE, Houston, Texas, 2013.

[18] M. Oehler, S. Bailey, R. Gubner, M. Gough, Testing of generic volatile inhibitor compounds in different top-of-the-line corrosion laboratory test methods, CORROSION/2012,Paper No. 1483, NACE, Houston, Texas, 2012.

[19] F. Ajayi, S. Lyon, Efficiency of volatile corrosion inhibitors in wet gas pipelines, CORROSION/2014, Paper No. 4236, NACE, Texas, 2014.

[20] ASTM G1 − 03, Standard practice for preparing , cleaning , and evaluating corrosion test, in: Annu. B. ASTM Stand., vol. 03.02, ASTM International, 2011.

[21] S. Guo, F. Farelas, M. Singer, A glycol/water co-condensation model to investigate the influence of monoethylene glycol on top-of-the-line corrosion,

Corrosion. 73 (2017) 742–755.

[22] J.L. Crolet, N. Thevenot, S. Nesic, Role of conductive corrosion products in the protectiveness of corrosion layers, Corrosion. 54 (1998) 194–203.

[23] J.L. Mora-Mendoza, S. Turgoose, Fe_3C influence on the corrosion rate of mild steel in aqueous CO_2 systems under turbulent flow conditions, Corros. Sci. 44 (2002) 1223–1246.

[24] R.W. Bosch, Electrochemical frequency modulation: a new electrochemical technique for online corrosion monitoring, Corrosion. 57 (2001) 60–70.

[25] S.S. Abdel-Rehim, K.F. Khaled, N.S. Abd-Elshafi, Electrochemical frequency modulation as a new technique for monitoring corrosion inhibition of iron in acid media by new thiourea derivative, Electrochim. Acta. 51 (2006) 3269–3277.

[26] L. Han, S. Song, A measurement system based on electrochemical frequency modulation technique for monitoring the early corrosion of mild steel in seawater, Corros. Sci. 50 (2008) 1551–1557.

[27] S. Nesic, J. Postlethwaite, and S. Olsen, Corrosion 52 (1996): p. 280.

[28] S. Nesic, and K.L.J. Lee, Corrosion 59 (2003): p. 616.

[29] E. Gulbrandsen, K. Bilkova, Solution chemistry effects on corrosion of carbon steels in presence of CO_2 and acetic acid, CORROSION/2006, Paper No. 06364, NACE, Houston, Texas, 2006.

[30] M. Javidi, M. Khodaparast, Inhibitive performance of monoethylene glycol on CO_2 corrosion of API 5L X52 steel, J. Mater. Eng. Perform. 24 (2015) 1417–1427.

[31] Z.Q. Bai, C.F. Chen, M.X. Lu, J.B. Li, Analysis of EIS characteristics of CO_2 corrosion of well tube steels with corrosion scales, Appl. Surf. Sci. 252 (2006) 7578–7584.

[32] Y. Chen, L. Zhang, H. Qin, L. Xu, M. Lu, Effects of temperature on CO_2 top of line corrosion of pipeline steel, CORROSION/2011, Paper No. 11327, NACE, Houston, Texas, 2011.

[33] S. Nesic, M. Nordsveen, R. Nyborg, A. Stangeland, A mechanistic model for

CO_2 corrosion with protective iron carbonate films, CORROSION/2001, Paper No. 1040, NACE, Houston, Texas, 2001.

[34] S. Nesic, Key issues related to modelling of internal corrosion of oil and gas pipelines - A review, Corros. Sci. 49 (2007) 4308–4338.

[35] G. Gusmano, P. Labella, G. Montesperelli, Study of the inhibition mechanism of imidazolines by electrochemical impedance spectroscopy, Corrosion. 62 (2006) 576–583.

[36] F. Farelas, A. Ramirez, Carbon dioxide corrosion inhibition of carbon steels through bis-imidazoline and imidazoline compounds studied by EIS, Int. J. Electrochem. Sci. 5 (2010) 797–814.

[37] F. Farelas, M. Galicia, B. Brown, S. Nesic, H. Castaneda, Evolution of dissolution processes at the interface of carbon steel corroding in a CO_2 environment studied by EIS, Corros. Sci. 52 (2010) 509–517.

[38] G.A. Zhang, Y.F. Cheng, On the fundamentals of electrochemical corrosion of X65 steel in CO_2-containing formation water in the presence of acetic acid in petroleum production, Corros. Sci. 51 (2009) 87–94.

[39] P. Altoé, G. Pimenta, C.F. Moulin, S.L. Díaz, O.R. Mattos, Evaluation of oilfield corrosion inhibitors in CO_2 containing media: A kinetic study, Electrochim. Acta. 41 (1996) 1165–1172.

[40] D. Harrington and P. Driessche, Electrochim. Acta, 56 (2011): p. 8005.

4.9 Appendix

Validation of TLC probe under immersion condition: Comparison of 3-electrode vs 2-electrode arrangements

Immersion tests were conducted to compare the performance of the TLC probe in 3-electrode and 2-electrode system. A small modification of the TLC probe shown in Figure 4.1 was done to accommodate the immersion test. The top portion of the working electrode and counter electrode part of the probe along with electrical joint was sealed with epoxy resin to isolate the probe from the contact with the solution

except the part where condensation took place. The part to be exposed with the solution was prepared for immersion test using same procedure used for TLC experiment.

The TLC probe was placed in a 1 L-glass cell equipped with a thermocouple for controlling the liquid temperature, CO_2 inlet and outlet. The electrolyte solution was 0.1% NaCl saturated with CO_2. The pH of the test solution was adjusted to 5.5 using 0.1 M $NaHCO_3$ solution, similar to pH of the condensed liquid [7] and the temperature was maintained at 30 °C. The 2-electrode cell setup was similar to TLC experiment. In case of 3-electrode cell setup, the reference electrode was connected to Ag/AgCl reference electrode where the outer surface of the TLC probe was used as a counter electrode. The electrochemical tests conducted were similar to those applied in the TLC experiments.

Figure 4.16 shows superimposed Nyquist plots obtained from both arrangements implying that the 2-electrode system provided nearly identical results to those obtained from the 3-electrode system. Further, when fitted the data with electrochemical equivalent circuit as shown in Figure 4.12, comparable values of charge transfer resistance (R_{CT}) were found in the both system as shown in Table 4.3. It has been reported previously that 2-electrode system was considered better for impedance measurement in absence and presence of corrosion inhibitor in CO_2 condition [39]. The polarization resistances (R_P) obtained from LPR technique are normally identical in the 3-electrode and 2-electrode arrangement a shown in Table 3. These results point towards that the 2- electrode system can be used successfully for measuring R_P and $R_{CT,}$ particularly when the corrosion potential is not an important parameter to measure. Hence, this result gave confident in the design of the electrochemical probe developed for this work. It should be noted that both setups showed greater R_{ct} compared to R_p. Harrington and Driessche explained that this behavior could occur in a system where an inductor dominates the impedance [40]. Further investigation into the significance and physical meanings of an inductor on corrosion is required, which is true not only for TLC applications.

Further, EFM was carried out under immersion condition using the same TLC probe to understand the necessity of dividing the *B* value by 2 in case of diffusion mode of calculation as applied in TLC study. Table 4.4 shows the comparison of *B* value obtained from 3-electrode and 2-electrode systems under immersion condition at variable applied potential. *B* value was calculated under active mode and diffusion mode. In both arrangements, *B* value obtained by calculating in diffusion mode (without dividing by 2) shows reproducibility and consistency even with the change of perturbation potential compared to those obtained from active mode. However, diffusion mode of calculation overestimate the *B* values by nearly double of the value reported in the literature for CO_2 condition [29-31] for both 2- and 3-electrode systems. The *B* value under active mode was 15 mV which increased to 40 mV when calculated under diffusion mode in identical condition. This observation is consistent with literature. Han and Song reported the significant increase of *B* values and corrosion current density when changing the calculation from active mode to diffusion mode in 0.6 M NaCl solution in oxygenated condition [26]. Kus and Mansfeld reported similar observation but only when the selected frequency was too high and was still well within the capacitive region which was not the case in this study. Further analysis is required to fully understand this behaviour.

Table 4.3: Comparison of charge transfer resistance (R_{CT}) and polarization resistance (R_P) in 3-electrode and 2-electrode arrangement under immersion condition in 0.1% NaCl, pH 5.5 and 30 °C temperature. Standard deviation calculated from 3 measurement

Parameters	3-Electrode	2-Electrode
R_{CT}, ohm.cm^2	273 ± 3.60	273 ± 1.15
R_P, ohm.cm^2	231 ± 2.88	233 ± 1.53

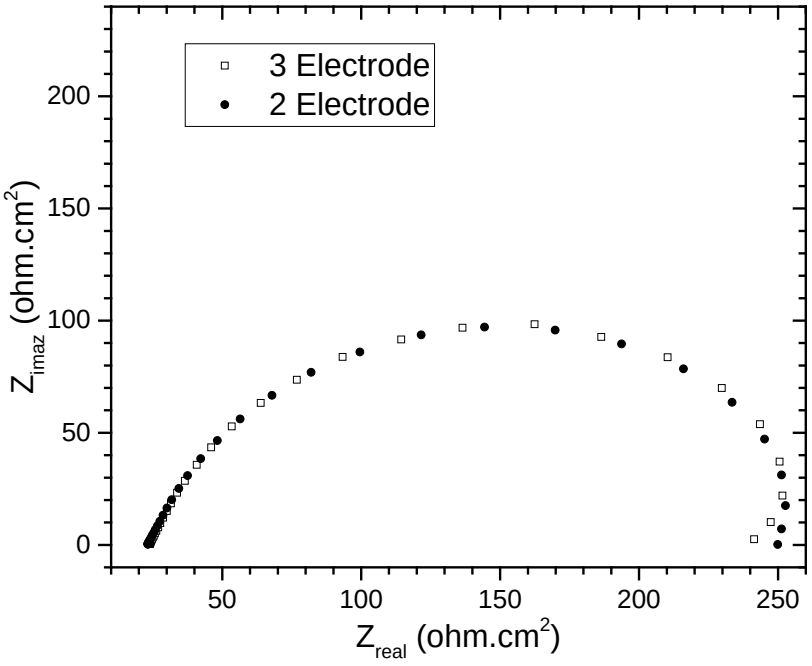

Figure 4.16: Comparison of Nyquist plot obtained from 3-electrode and 2-electrode cell setup under immersion condition in 0.1% NaCl, pH 5.5 and 30 °C temperature.

Table 4.4: Comparison of Stern-Geary constant (B) obtained from 3-electrode and 2-electrode cell arrangement under immersion condition in 0.1% NaCl, pH 5.5 and 30 °C temperature. Standard deviation calculated from 3 measurement

Base Frequency, Hz	Amplitude, mV	3-Electrode		2-Electrode	
		Active *B*, mV	Diffusion *B*, mV	Active *B*, mV	Diffusion *B*, mV
0.01	10	23 ± 0.29	39 ± 0.87	24 ± 0.29	35 ± 0.06
	7	19 ± 0.26	38 ± 0.54	19 ± 0.29	34 ± 0.08
	5	14 ± 1.14	37 ± 1.89	14 ± 1.22	34 ± 0.09

Chapter 5: Electrochemical investigation into the dynamic mechanism of CO_2 corrosion product film formation on the carbon steel under water condensation condition*

5.3 Abstract

This study presents a systematic investigation into corrosion behaviour of carbon steel exposed to continuous water condensation using a newly developed electrochemical setup. Corrosion rates and the $FeCO_3$ precipitation process under constant replenishing of condensed water were monitored using various electrochemical techniques. Electrochemical impedance spectroscopy (EIS), scanning electron microscopy, and confocal Raman spectroscopy indicated that $FeCO_3$ precipitation has three stages: active dissolution, formation of porous layer, and formation of protective layer consisting of inner (mixture of $FeCO_3$ and Fe_3C) and outer layer ($FeCO_3$). Corrosion rates increase with time during the active dissolution stage and start to decline when the porous layer forms. After the protective layer is established, corrosion rates reach the minimum values and become steady. EIS and linear polarisation resistance (LPR) techniques provides comparable corrosion rates with weight loss method.

Keywords: Carbon steel, EIS, polarization resistance, CO_2 corrosion, condensation.

5.4 Introduction

Carbon steel is widely used and is a cost effective material in multiphase pipelines for transportation of natural gas and condensate. During the transport of wet natural gas in stratified flow regime, water condensation can take place inside the upper portion of the pipeline due to the temperature gradient between process fluids and the outside environment. The condensed liquid contains dissolved CO_2, H_2S, and organic acids which is corrosive for the carbon steel pipeline. This phenomenon is sometime referred to as sweet top of the line corrosion (TLC) in a CO_2 dominating environment and in an absence of H_2S [1,2].

Iron carbonate ($FeCO_3$) is a predominant corrosion product in CO_2 corrosion of carbon steel [3,4]. It has been shown to provide a physical barrier between the electrolyte and

* The chapter is reproduced from 'M.M. Islam, T. Pojtanabuntoeng, R. Gubner, B. Kinsella, Electrochemical investigation into the dynamic mechanism of CO_2 corrosion product film formation on the carbon steel under water condensation condition, under review in Corrosion Science'.

the solid metallic surface which reduces the corrosion rate of carbon steel significantly [5]. For instance, pH stabilisation technique which is a widely adopted in wet gas pipelines promotes the formation of $FeCO_3$ by increasing solution pH. The efficiency of this technique relies on the integrity of the $FeCO_3$ [6]. The protectiveness of the iron carbonate layer depends on several environmental conditions, such as iron concentration [7,8], solution pH [9], temperature [7,9,10], partial pressure of CO_2 [11], droplet retention time [12], microstructure of the carbon steel [4,13], and exposure time [4].

The mechanism of $FeCO_3$ film formation and film growth in CO_2 environments under immersion conditions have been widely investigated. Hunnik et al. introduced the scaling tendency which is the ratio between the precipitation and iron dissolution to predict the protectiveness of the $FeCO_3$ scale formation [14]. According to Hunnik et al., the bulk scaling tendency of 0.5 is sufficient for such film to be protective [14].

Nesic et al. proposed a mechanistic model for the growth of $FeCO_3$ film on mild steel and anticipated that the precipitation kinetics is dependent on temperature and local species concentration [15]. Dugstad investigated the role of pH, temperature, and $FeCO_3$ supersaturation on the $FeCO_3$ film formation and reported that protective $FeCO_3$ formed at high temperature (> 60 °C) even with low supersaturation [16]. Conversely, porous and loosely adhered films formed at low temperature (< 40 °C) with high supersaturation [16].

Farelas et al. studied the evolution of the dissolution process of steel exposed to CO_2 environment electrochemically under turbulent flow condition. Based on EIS measurements, the study suggested three different stages of the interfacial process, namely: active adsorption state, active porous layer state and mixed porous layer [17]. Later, Gao et al. stated that $FeCO_3$ film is duplex in nature consisting of inner and outer layer and this duplex layer started to form after the critical point, where there is an abrupt increase of polarization resistance [18].

Dissolved CO_2 level was also shown to influence the mechanism of $FeCO_3$ formation. At super critical CO_2 conditions, Wei et al. found that an amorphous layer

preferentially formed on the steel surface and gradually evolved into the inner $FeCO_3$ scale. Once the inner layer was created, relatively porous $FeCO_3$ scale precipitated over the inner layer [19]. Conversely, at low CO_2 partial pressure, dense outer $FeCO_3$ scale formed first followed by the formation of thick porous inner layer which drastically reduced the uniform corrosion rates [19]. The study found better protectiveness of the outer corrosion product scale formed at 1 MPa and inner corrosion product formed at 9.5 MPa and vice versa.

The formation of $FeCO_3$ inside the inner wall of gas transportation pipelines under condensation condition in CO_2 environment is also reported in the literature [20-22]. Crystals with sharp edge and dense layer were found in the area covered by the water droplet [23]. The kinetics of $FeCO_3$ film formation was shown to be governed by temperature and condensation rates [12,24]. High temperature and low condensation rate lead to the formation of a very dense and protective $FeCO_3$ layer due to high level of super saturation.

A recent study found that the $FeCO_3$ formation under condensation condition differs from that under immersion condition because of the constant replenishment of fresh water from the condensation process [12]. Due to lack of appropriate monitoring technique, an *in-situ* $FeCO_3$ formation mechanism on the steel surface in the presence of CO_2 under water condensation conditions has not been investigated.

It is certain that electrochemistry is a useful and insightful method for studying corrosion and the resulting corrosion product formation. These methods have been used to determine the formation and kinetic parameters of corrosion product films and also to estimate the corrosion rate during the entire corrosion process [18,25-27]. However, implementation of electrochemical methods under water condensation condition has been challenging due to the limited quantity of electrolyte. In our previous study, we used a novel electrochemical method for continuous monitoring of corrosion rates under water condensation condition in the absence of $FeCO_3$ film [28].

In this present study, we have explored the real-time film formation mechanism of $FeCO_3$ on the steel surface under condensing water condition by analysing EIS data,

corrosion rate, supersaturation, scaling tendency and finally by cross sectional analysis using scanning electron microscopy (SEM), energy dispersive X-ray spectroscopy (EDS) and confocal Raman spectroscopy.

5.5 Experimental

The experimental setup for this study is shown in Figure 5.1 and the detailed procedure was outlined previously [12,28]. Two mm diameter carbon steel (UNS G10300) rod was used as a working electrode. It was inserted into a 3 mm hole created in the centre of a 20 mm diameter carbon steel rod. Both were electrically insulated from each other by coating with epoxy as shown in Figure 5.1a. Details of the TLC probe construction has been described previously [28]. The larger diameter rod was used as a counter electrode to form a two electrode system. The TLC probe was wet ground with silicon carbide paper to 1200 grit, cleaned with water, ethanol and dried with nitrogen. The dried probe was weighed with an analytical balance and subsequently was inserted into a polyethylene terephthalate (PET) lid so that the polished portion faced downward to the corrosive environment and the remaining part remained above the lid (Figure 5.1b). A copper tube was coiled around the upper portion of the probe through which cooling liquid was circulated to maintain the surface temperature. The lid was mounted onto a 2 L glass cell along with the arrangement of temperature probes for measuring gas temperature and surface temperature, thermocouple for controlling bulk liquid temperature, CO_2 inlet, and a condensed liquid collection cup creating an air-tight environment (Figure 5.1c). Prior to conducting an experiment, the complete assembly was deoxygenated by continuously sparging with high purity CO_2 gas (99.99%) for 10 min.

One thousand four hundred mL of high purity water (18.2 MΩ.cm), pre-sparged in a separate container with high purity CO_2 overnight and pre-heated to a predefined temperature, was transferred to the TLC cell using a peristaltic pump to avoid oxygen contamination. The desired gas temperature and surface temperature were achieved by controlling the bulk liquid temperature and the cooling water temperature,

respectively. In this study, gas temperature and surface temperature were maintained at 55 °C and 45 °C, respectively.

The condensed water, dropping into the condensate collector cup placed directly beneath the sample, was transferred immediately into the condensate reservoir at room temperature to avoid any re-evaporation. The liquid was then collected periodically from the reservoir to determine its mass, pH, and ferrous ion concentration. The *in-situ* corrosion rate was determined from electrochemical measurements and concentration of dissolved iron (Fe^{2+}) presenting in the condensed liquid at a certain exposure period [12]. After finishing the experiment, corrosion product was removed using Clarke solution and corrosion rate was calculated from weight loss of the TLC probe [12,29].

The electrochemical measurements were carried out in the 2 electrode arrangement as outlined previously [28]. Measurements were performed with a Gamry Instrument Potentiostat/Galvanostat/ZRA (Reference 600). Echem Analyst Software was used for fitting the data. Three electrochemical techniques were performed. Electrochemical frequency modulation (EFM) was conducted at two frequencies of 0.02 Hz and 0.05 Hz. Stern-Geary constant (B) and corrosion rate were calculated using the diffusion mode of Echem Analyst Software. Linear polarization resistance (LPR) was conducted within ±5 mV with respect to open circuit potential (OCP) at a scan rate of 10 mV/min. Electrochemical impedance spectroscopy (EIS) was carried out from 10 kHz to 0.1 Hz with an amplitude of 5 mV peak-to-peak using AC signals at OCP.

Experiments were duplicated to gain confidence in the reproducibility. Furthermore, one specimen was used for corrosion product characterization and subsequent weight loss whereas in the second experiment it was used for cross-sectional analysis. The cross-sectioned sample was prepared by embedding the specimen in a cold mount epoxy resin, cutting it using a diamond blade, and finally polishing to 1 µm with diamond paste. The corrosion product on the surface and cross-section was analysed using field emission scanning electron microscopy (FE-SEM) accompanied with energy dispersive X-ray spectroscopy (EDS). The corrosion product was also

characterised with confocal Raman spectroscopy at an excitation energy of 532 nm laser at ×100 magnification.

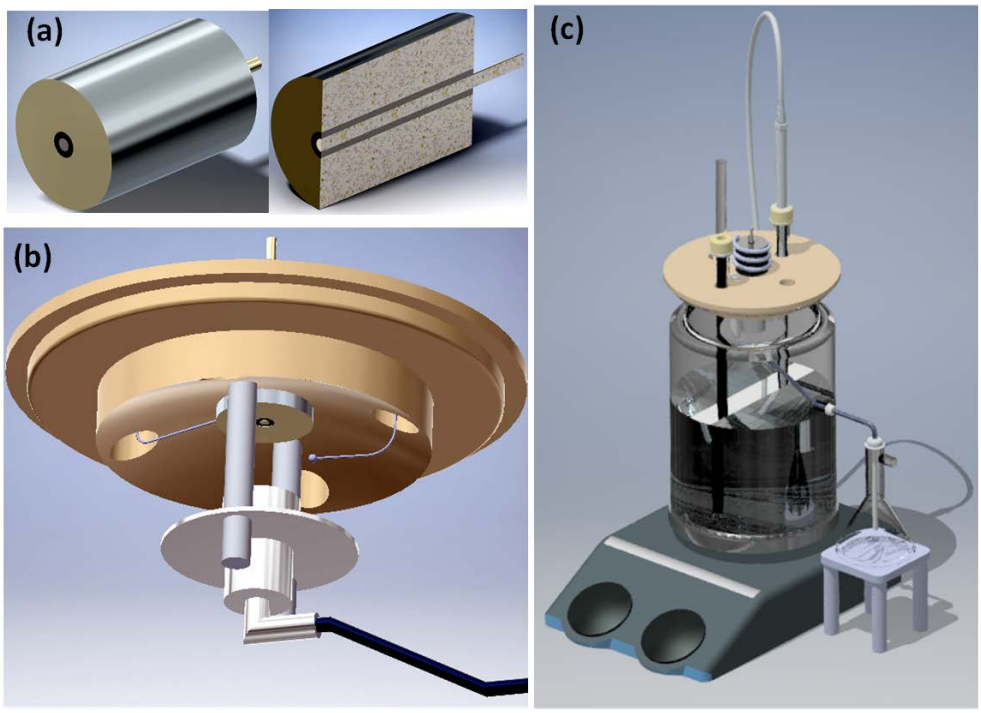

Figure 5.1: The schematic drawing showing an experimental setup for studying top-of-the-line corrosion (TLC); a) TLC probe, b) lid fitted with TLC probe, gas and surface temperature probe, and condensed liquid collection cup, and c) a complete test assembly.

5.6 Results and discussion

5.6.1 Top of the line corrosion rates

Figure 5.2 presents the *in-situ* TLC rates of carbon steel under condensation condition obtained from Fe^{2+} concentrations in the condensed liquid, electrochemical techniques of EIS, LPR and EFM performed on the steel electrode. Error bars denote the standard deviation of at least duplicate measurements. The *in-situ* corrosion rates obtained from measuring Fe^{2+} concentrations in the condensed liquid increases during the first 5 days of exposure. Afterwards, it decreases slowly until 13 days of exposure before it reaches steady values for the remaining of the experiments (i.e. 4 days).

Corrosion rates from EFM were calculated using the same approach as described earlier [28] and were found to overestimate the corrosion rate in relation to the other techniques. The higher corrosion rates from EFM is associated with the larger value of the Stern-Geary constant (*B*) obtained using this technique. Compared to our previous study [28], EFM was found to be an effective technique for determining the *B* value and corrosion rate of carbon steel under water condensation condition. This discrepancy could arise from the presence of a protective $FeCO_3$ layer found in this study which was not present in the previous investigation. It has been shown that the frequency related processes such as double-layer charging and inductive behaviour due to adsorption of intermediate species can influence the results of EFM [30]. The subsequent section on EIS will demonstrate that there is an increase in double layer capacitance and phase shift, associated with the formation of $FeCO_3$. An increase in double layer capacitance increases the capacitive current, and consequently influences the Faradaic current response [30]. Additionally, the phase shift causes the capacitive behaviour to move to a lower frequency range. As a result, the pre-selected frequency of 0.02 Hz to 0.05 Hz are no longer suitable and results in the corrosion rate being overestimated [31]. Selecting a lower base EFM frequency, to compensate for the phase shift, would prolong the measurement time and be impractical in following the changes in corrosion rate associated with the constant replenishment of condensed water.

Therefore, to calculate the corrosion rate from the EIS and LPR techniques, a *B* value of 13 mV obtained from literature for CO_2 corrosion [7,32,33] was used instead of using the *B* obtained from EFM. Corrosion rates obtained from EIS and LPR technique slightly differ from each other but the trends are similar. For instance, corrosion rates rise over the first 6 days and then remain steady with minor fluctuation for next 3 days. Afterwards, it gradually declines until the 13^{th} day where it became relatively constant or decreased more slowly. However, relatively lower corrosion rates are obtained up to 13 days from Fe^{2+} measurements compared to those from LPR and EIS. Because fraction of Fe^{2+} ions were accumulated in the surface as corrosion products and were not available in the condensed liquid. After 13 days of exposure, LPR corrosion rates

are lower compared to EIS and Fe^{2+} measurement because of the additional resistance introduced by the corrosion product scale.

Figure 5.3 compares the integrated corrosion rate obtained from weight loss with the average corrosion rates obtained from the data presented in Figure 5.2. The integrated corrosion rate from the weight loss measurement compares well with EIS, LPR and Fe^{2+} measurements indicating that *B* value used in LPR and EIS methods is reasonable. However, as previously discussed the, corrosion rates obtained from EFM resulted in an overestimation of the corrosion rates. It has similarly been reported by other authors using EFM investigating corrosion of carbon steel in aerated 0.5 N NaCl [31] indicating that EFM needs to be used with caution particularly under condition where protective or semi-protective scales such as iron oxide or $FeCO_3$ may form.

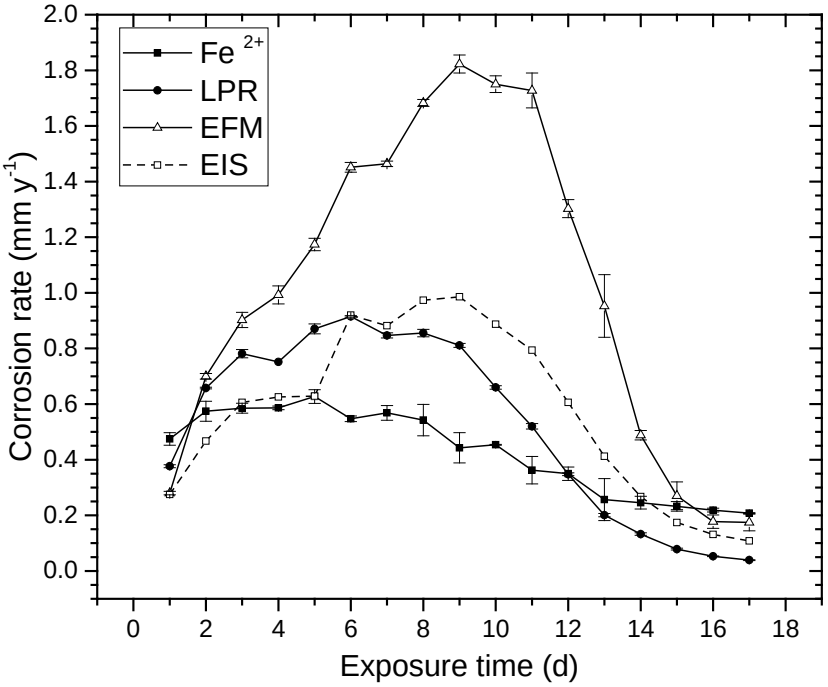

Figure 5.2: In-situ top-of-the-line corrosion rates with respect to time obtained from measurement of ferrous ion (Fe^{2+}) concentration, liner polarisation resistance (LPR), electrochemical impedance spectroscopy (EIS) and electrochemical frequency modulation (EFM) techniques at 55 °C gas temperature and 45 °C surface temperature.

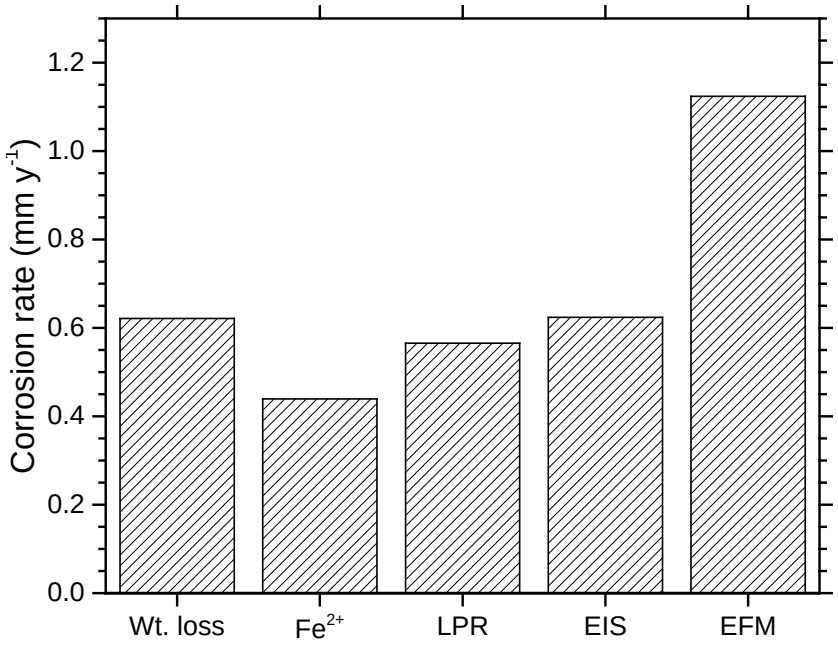

Figure 5.3: Comparison of integrated corrosion rates obtained from different methods at 55 °C gas temperature and 45 °C surface temperature

5.6.2 $FeCO_3$ super saturation of condensed liquid and scaling tendency

Supersaturation of the condensed liquid and scaling tendency under condensing condition was calculated based on the approach discussed previously according to the Equations (5.1) and (5.2) [12]:

$$S_S = \frac{C_{Fe^{2+}} C_{CO_3^{2-}}}{K_{sp}} \tag{5.1}$$

$$S_T = \frac{R_{CLA}}{R_{corr}} \tag{5.2}$$

where S_S is the $FeCO_3$ supersaturation, dimensionless; $C_{Fe^{2+}}$ is ferrous ion concentration in the condensed liquid, kmol m^{-3}; K_{sp} is the $FeCO_3$ solubility constant, (kmol m^{-3})$^{-2}$; S_T is the scaling tendency, dimensionless; R_{CLA} is the corrosion layer accumulation rate, kmol m^{-2} s^{-1} and R_{corr} is the rate of dissolution of metal measured in the condensed liquid, kmol m^{-3} s^{-1}. R_{CLA} was calculated from S_S under water condensing conditions based on the approach described previously [12].

Figure 5.4 shows the variation of supersaturation of $FeCO_3$ and scaling tendency throughout the experimental period. Both curves exhibits an identical pattern and are correlated to the Fe^{2+} concentration in the condensed liquid in a given condition. Initially, the supersaturation is around 52, which steeply increases to about 84 on the 4^{th} day of exposure because of the higher concentration of Fe^{2+} from the corrosion process. Afterwards, it decreases gradually down to 10 after 14 days of exposure as corrosion rates decreased. After 16 days of exposure, it remained nearly constant to around 4. Similarly, scaling tendency rises from 0.45 to around 0.6 during first 4 days. From 5 to 8 days, it declines slightly, but the value remains above 0.5. After that, it decreases gradually to reach to below 0.1 at the end of the experiment.

The variation of supersaturation and scaling tendency with time will be discussed further in the subsequent section to explain the formation of $FeCO_3$ at different stages of the corrosion process.

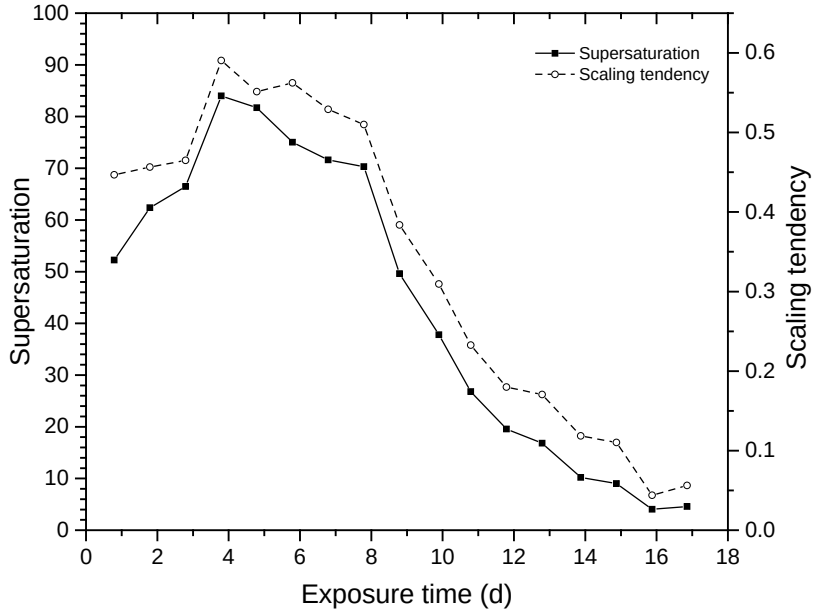

Figure 5.4: $FeCO_3$ supersaturation of the condensed liquid and scaling tendency of corrosion product film with respect to time.

5.6.3 Surface characterization and cross sectional analysis of the corrosion product

Figure 5.5 represents the SEM images of surface and cross section of the corrosion products obtained at 6, 10 and 17 days of exposure. The left hand side is the SEM image taken from the top view of the surface while the right hand side depicts the cross sectional images from a duplicate experiment.

After 6 days of exposure, $FeCO_3$ partially formed on the surface according to the back scattered SEM image shown in Figure 5.5a. The bright areas indicates the bare steel surface and the grey portion is the area covered with $FeCO_3$. The phenomena is clearer in the cross sectional image where voids consisting of lamellar cementite are visible between the porous corrosion product layer and base metal. It appears that crystals started to precipitate preferentially above the lamellar cementite and grew with time.

After 10 days of exposure, the surface is covered with $FeCO_3$ crystals in most part as shown in Figure 5.5b. Yet, the layer is still porous as $FeCO_3$ is partially absent. The corresponding cross sectional image shows signs of localised corrosion attack which suggests that corrosive solution can enter through the pores (Figure 5.5b). However, corrosion rate steeply decreased during this period since most of the surface was covered with $FeCO_3$ scale. It is also worthwhile emphasising that the Fe^{2+} and electrochemical measurements can only estimate uniform corrosion rates.

After 17 days of exposure, the surface is completely covered with dense crystals of $FeCO_3$ as shown in Figure 5.5c. The cross section shows a thick corrosion product layer consisting of outer and inner layer (indicated by a dashed line), which potentially depicts the original surface of the metal sample. Underneath that line, the corrosion product/bare steel interface is uneven which could developed from the aggregation of multiple localised attack. This indicates that the localised corrosion previously seen in Figure 5.5b is only the initiation or transition to uniform corrosion.

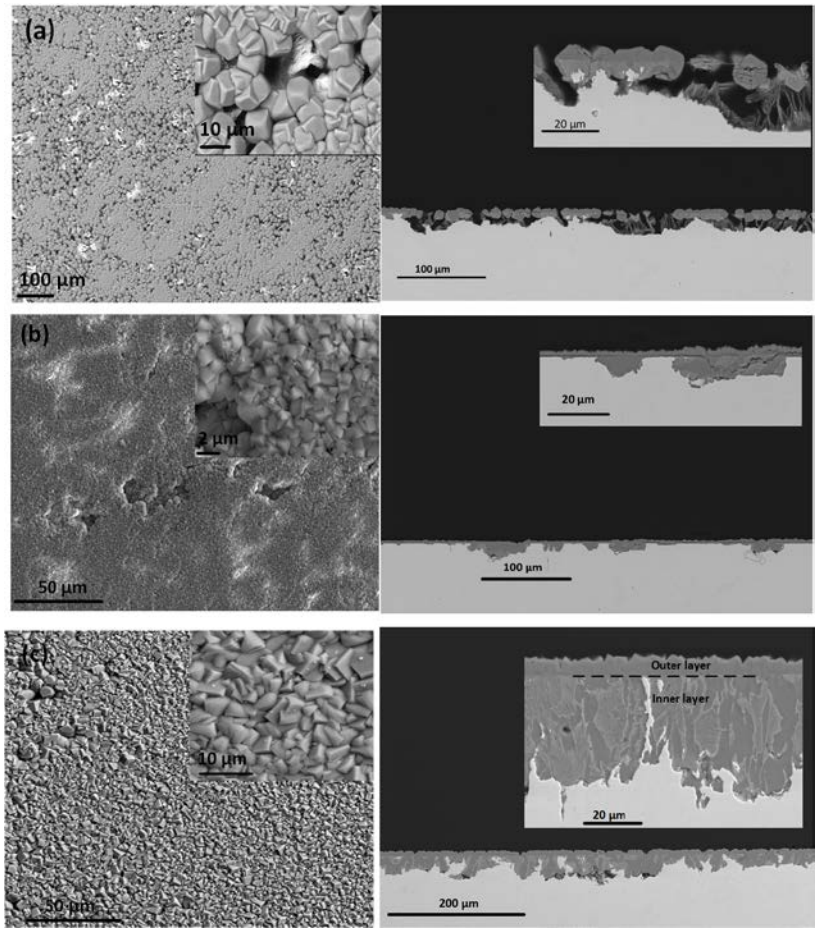

Figure 5.5: SEM-BSD images of corrosion product of surface (left row) and cross section (right row) after; a) 6 days exposure, b) 10 days exposure, and c) 17 days exposure.

Figure 5.6 shows SEM image and EDS spectra of both inner and outer layers of the cross section of the corrosion product after 17 days exposure. It is evident from the SEM backscattered image that the inner layer has mixed phases whereas the outer layer has homogeneous composition. Nonetheless, EDS only demonstrates the presence of Fe, C and O in both layers corresponding to $FeCO_3$ as typically seen in CO_2 corrosion. EDS could not distinguish the difference in the nature of corrosion product particularly at the inner layer where mixed phases are apparent.

Confocal Raman identified the lamellar type structure found in the inner layer to be Fe_3C. The result is shown in Figure 5.7. Two intense peaks at 1087 cm^{-1} and 287 cm^{-1} in Figure 5.7a are typical signature of $FeCO_3$ [12,34]. On the other hand, there are

areas with significant amount of Fe_3C present, as seen in the broad Fe_3C peak visible at 1322-1376 cm^{-1} and 1560-1600 cm^{-1} [35,36]. Raman mapping reveals that the bright area having lamellar structure in the optical micrograph (Figure 5.7b) corresponds well to areas depicted in red (Figure 5.7c1 and 5.7c2) indicating the presence of Fe_3C. This confirms that the outer layer is $FeCO_3$ and the thick inner layer consists of $FeCO_3$ integrated in a lamellar Fe_3C matrix. Other investigators also support the formation of duplex $FeCO_3$ layer where Fe_3C was present in the inner layer in CO_2 environment [8,18]. It appears that corrosion rate reaches steadily low values once the duplex layer is formed.

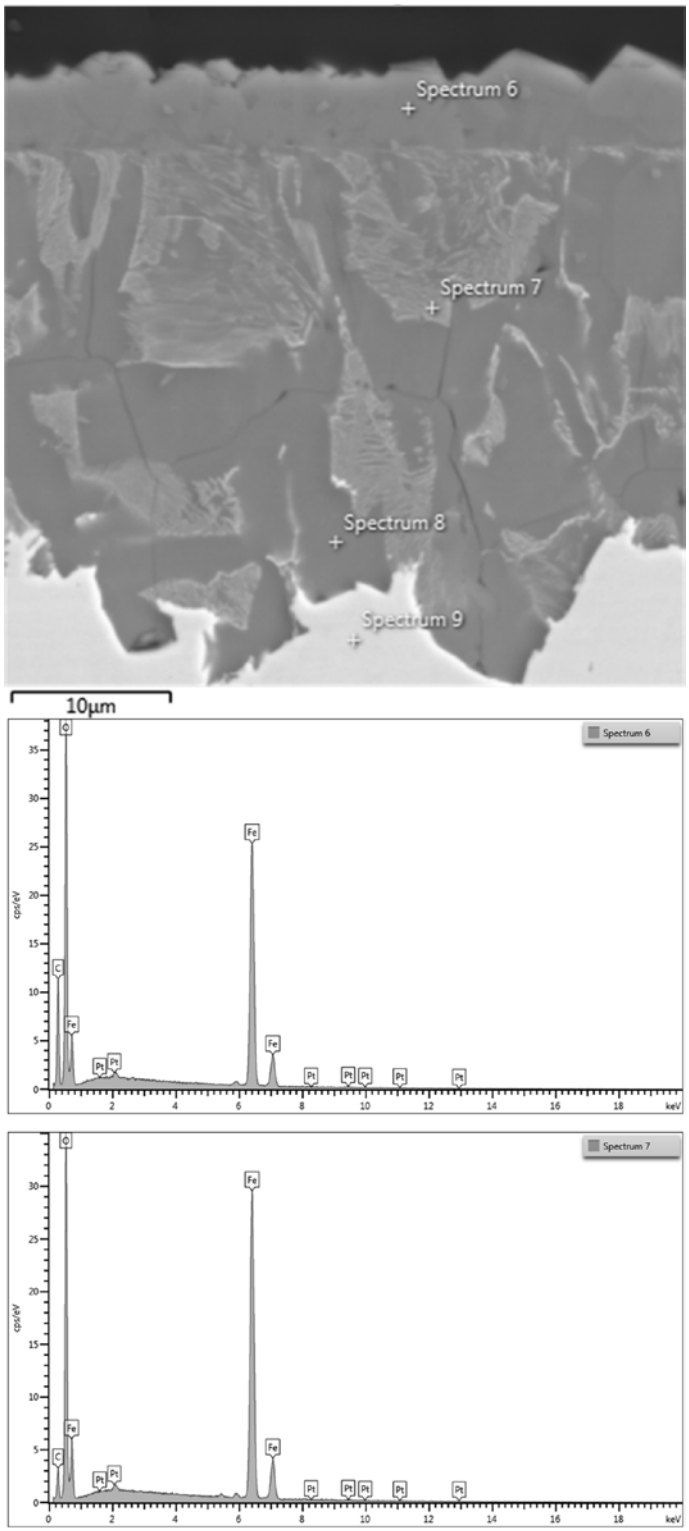

Figure 5.6: SEM-BSD image and EDS spectrum of cross section of corrosion product after 17 days of exposure.

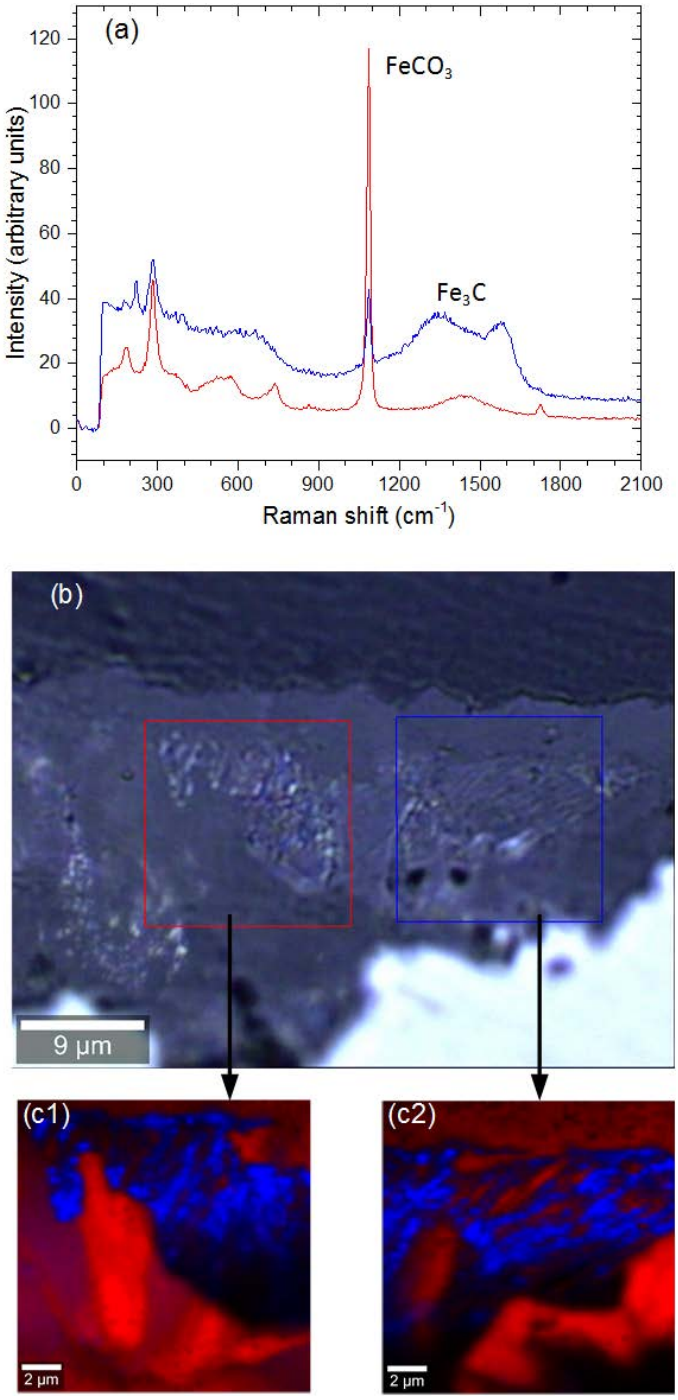

Figure 5.7: Confocal Raman analysis of corrosion product film formed after 17 days of exposure; a) spectra, b) optical images showing areas for analysis, and c) Raman mapping showing areas with distinct composition. Red represents $FeCO_3$ and blue represents areas containing Fe_3C.

5.6.4 $FeCO_3$ formation mechanism under water condensing condition - electrochemical impedance spectroscopy (EIS) study

EIS is a powerful technique to study the mechanism of the metal/electrolyte interfacial processes [37-39]. During the corrosion study, EIS was continuously recorded which also demonstrated three different patterns corresponding to the trend shown by the Fe^{2+} concentration and electrochemical corrosion rate measurements. Based on impedance signatures and corrosion rates, three different stages can be categorised which are similar to those reported under total immersion conditions; namely active dissolution, formation of porous layer and formation of protective layer [17].

5.6.4.1 Active dissolution

Figure 5.8 shows the Nyquist and Bode plots for the first 5 days of exposure under the condensing water condition. The Nyquist plots were (Figure 8a) composed of a capacitive semicircle and an inductive loop. A decrease in the diameter of capacitive semicircles with exposure time indicates that the charge transfer process of cathodic reactions was promoted [17,18].

Figure 5.8b shows the Bode impedance and phase angle representations of the EIS spectra during the first 5 days. A decrease in impedance values at the low frequency region of the Bode plot with time denotes the reduction in charge transfer resistance during this period. The phase angle representation shows characteristic of the charge transfer process [17]. No sign of $FeCO_3$ film formation is identified from the phase angle representation since the current and voltage are in phase at high frequency region ($>10^3$ Hz).

The interfacial phenomena occurred during the first 5 days exposure is characterised by equivalent circuit (EC) presented in Figure 5.9. This type of EC was typically employed to describe the interfacial process in CO_2 corrosion [17]. R_S is the solution resistance, Q_{DL} is the constant phase element (CPE) representing the double layer capacitance, R_{CT} is the charge transfer resistance, R_L is the inductive resistance and L is the inductance. The CPE was used instead of pure double layer capacitance to take

into account the electrode surface heterogeneities and therefore to improve the fitting. The impedance of CPE is expressed as shown in Equation (5.3) [40-43]:

$$Z_{CPE} = [Q(j\omega)^n]^{-1} \tag{5.3}$$

where Z_{CPE} is the impedance of CPE in ohm cm^2, Q is the proportionality factor of CPE in ohm^{-1} s^n cm^{-1}, ω is the sine wave modulation angular frequency equivalent to $2\pi f$ in rad. s^{-1}, $j^2 = -1$ is the imaginary number, and n is an empirical exponent ($0 \leq n \leq 1$) which indicates the deviation from the ideal capacitive behaviour.

The corresponding values of the equivalent circuit elements (fitting results) are listed in Table 5.1 and shown as solid lines in Figure 5.8. The double layer capacitance (C_{DL}) given in Table 5.1 is calculated from CPE parameters according to the Equation (5.4) [44]:

$$C_{\mathrm{DL}} = Q^{1/n}(R_s^{-1} + R_{CT}^{-1})^{(n-1)/n} \tag{5.4}$$

where C_{DL} is the capacitance in F cm^{-2}, R_S is the solution resistance in ohm cm^2 and R_{CT} is the charge transfer resistance parallel to capacitor in ohm cm^2.

According to Table 5.1, charge transfer resistance decreases from 587 ohm cm^2 to 240 ohm cm^2 at the 5th day of exposure indicating active dissolution of the iron from the metal surface. During this period, capacitance of double layer also increases from 131 to 957 µF cm^{-2} which is associated with the increase of the active surface area where the cathodic reaction takes place [4,13]. Value of L and R_L remains nearly constant from the 2nd day of exposure indicating that the surface was saturated by the adsorbed species.

Ferrite and pearlite are the main components of carbon steel where pearlite consists of ferrite and lamellar cementite (Fe_3C) [5,18]. Preferential dissolution of ferrite occurs leaving lamellar Fe_3C, which is more noble, on the surface [13,18]. Fe_3C being an electronic conductor acts as a cathode where the hydrogen reduction takes place creating a galvanic coupling effect causing faster dissolution of the ferrite phase [12,17,45]. This explains the decrease in the charge transfer resistance and the ensuing

increase in corrosion rates over the first 5 days. Moreover, Fe_3C provides the larger surface area for cathodic hydrogen evolution reaction which increases the capacitance of the double layer [17,46,47].

The results also exhibit induction loops at low frequency (Figure 5.8a). The existence of a low frequency induction loop has been related to the adsorption of intermediate species at the steel surface; i.e. $FeOH_{ads}$, which is proposed to participate in the active iron dissolution process according to Equation (5.5) to (5.7) [17,46,48,49].

$$Fe + H_2O \leftrightarrow FeOH_{ads} + H^+ + e^- \quad (5.5)$$

$$FeOH_{ads} \rightarrow FeOH^+_{sol} + e^- \quad (5.6)$$

$$FeOH^+_{sol} + H^+ \leftrightarrow Fe^{2+}_{sol} + H_2O \quad (5.7)$$

Therefore, during the first 5 days exposure, the steel surface was subjected to a continuous dissolution forming lamellar Fe_3C on the surface where adsorption of intermediate species occurs.

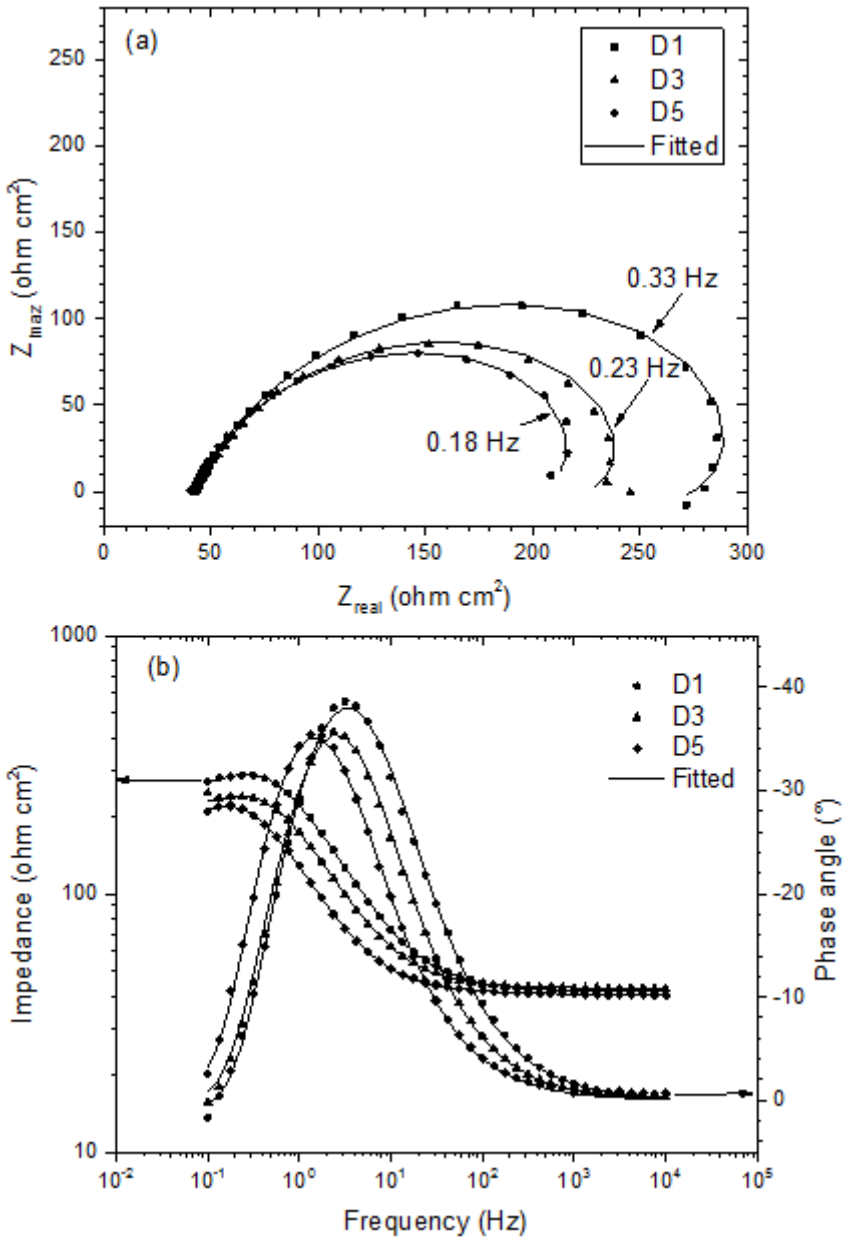

Figure 5.8: (a) Nyquist and (b) Bode representations of carbon steel corroding under condensing condition in CO_2 environment during the first 5 days.

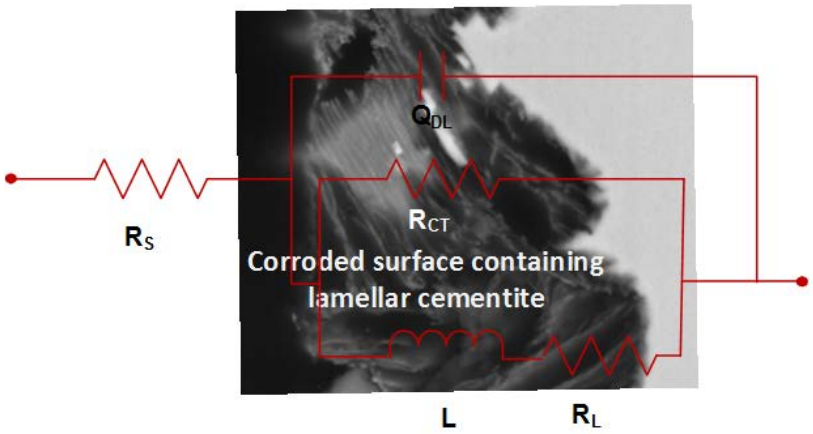

Figure 5.9: Equivalent circuit used to fit the EIS data during1-5 days, superimposed on the cross-section of corrode steel; R_S is solution resistance, R_{CT} is charge transfer resistance, Q_{DL} is constant phase element presenting double layer capacitance, L is inductance and R_L is resistance of inductance.

Table 5.1: Values of electrical elements extracted from EIS spectra from day 1-5 shown in Figure 5.8 using the equivalent circuit shown in Figure 5.9.

Day	R_S, ohm cm^2	R_{CT}, ohm cm^2	L, H cm^2	R_L, ohm cm^2	C_{DL}, µF cm^{-2}	Chi-square × 10^4
1	38	587	1493	2062	131	7.18
2	42	323	649	719	325	9.13
3	43	249	653	658	525	1.83
4	39	241	629	584	760	6.17
5	41	240	652	532	957	7.46

5.6.4.2 Formation of porous layer

Figure 5.10 presents the EIS curves obtained during 6-13 days exposure. After 5 days exposure, the inductive loop disappears and a second semicircle becomes evident at high frequency as shown in the Nyquist plot (Figure 5.10a). The semicircle at lower frequency is attributed to the electrochemical process of corrosion whereas the one at high frequency is often associated with a film formation process either by inhibitor [50] or corrosion product [19] or coating [51]. In this study, the semicircle in the high frequency range initially has small magnitude and subsequently enlarges with time.

Therefore, it can be stipulated that a layer of corrosion product started to form on the surface after 5 days exposure. The existence of a second high frequency time constant is also apparent in the phase curves shown in Figure 5.10c. The high frequency phase angle which was close to zero in the early stage (1-5 days) started to deviate after 5 days of exposure. Zero phase angle corresponds to an in-phase component and, at high frequency, it represents a solution resistance. Such deviation emphasizes the formation of a corrosion product layer that has capacitive behaviour.

It has been stated earlier that the preferential dissolution of ferrite occurs while lamellar Fe_3C remains on the steel surface resulting in an enhanced iron dissolution process. Consequently, higher values of supersaturation and scaling tendency were found during the first 5 days exposure as shown in Figure 5.4. This favours the precipitation of $FeCO_3$ as shown in Figure 5.5a resulting in a second semicircle in the Nyquist plot (Figure 5.10a). When the precipitation starts, it reduces the active sites of metal dissolution and consequently corrosion rates.

EIS curves during 6-13 days exposure are fitted with the EC shown in Figure 5.11. The EC is superimposed on the cross section of specimen obtained after 6 days of immersion. In addition to R_{CT} and C_{DL}, the resistance and capacitance of the porous layers denoted R_{PO} and C_{PO}, respectively, were introduced. The data fitted with the circuit are presented in Table 5.2.

As shown in Table 5.2, R_S increases with time due to the reduction in Fe^{2+} concentration in the condensed liquid. R_{CT} varies slightly until 9 days of exposure and afterwards increases steeply. This implies that the $FeCO_3$ film formed during this period was highly porous in nature since the full coverage was not attained (Figure 5.5) and provided minimum corrosion protection until day 9 of exposure. During this time, corrosive solution continues to enter through the pores and corrodes the steel surface. R_{PO} increased gradually while C_{PO} decreased steeply. It has been shown that capacitance has an inverse proportion to thickness [44,51]. Therefore, the results in this study suggest there is a gradual increase of the thickness of the porous layers with time.

During this period, the porous layer grew by continuous precipitation of $FeCO_3$ from the droplet. Fe^{2+} liberated from the steel surface reacts with carbonate ions in the condensed water forming $FeCO_3$ causing the porous layer to thicken. In other words, the corrosion product layer grew due to homogeneous precipitation of $FeCO_3$. This is apparent when comparing Figure 5.5a and Figure 5.5b.

The inner part of the porous layer closer to the steel surface appears to comprise of lamellar Fe_3C and voids filled with condensed water (Figure 5.5a). It is unknown whether this trapped solution has the same water chemistry as that in the condensed water. It is, however, reasonable to envisage that the presence of the porous outer layer can inhibit the outward diffusion of ferrous ions to some extent. This in turn increases the supersaturation level and the tendency of $FeCO_3$ precipitation within the void. The reduction in porosity in conjunction with the growth in $FeCO_3$ thickness results in the decline in C_{PO}. The decrease in active corrosion areas also leads to the lower double layer capacitance (C_{DL}).

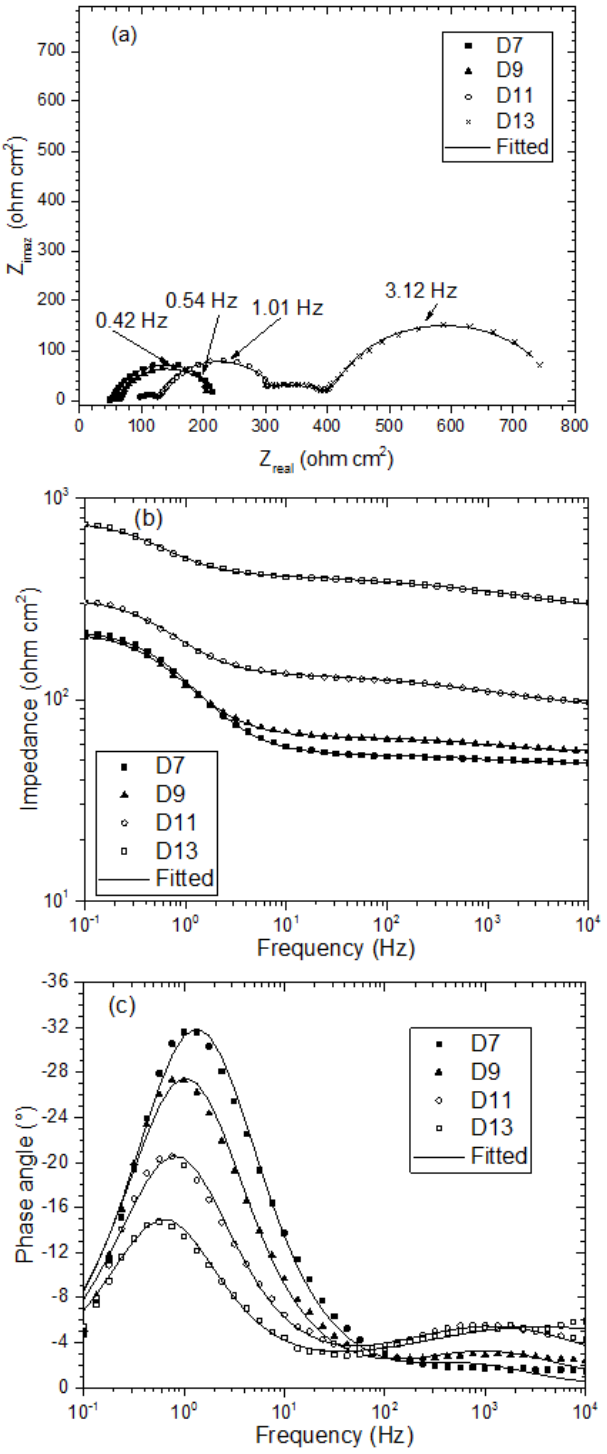

Figure 5.10: Impedance results for 6-13 days exposure under condensing condition in CO_2 environment: (a) Nyquist and (b and c) Bode representations.

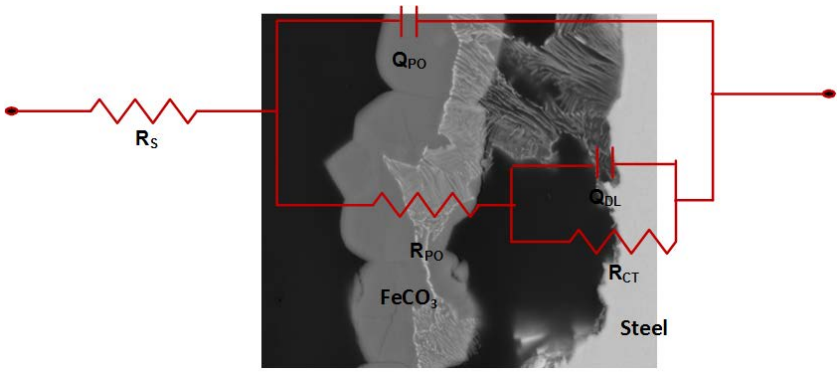

Figure 5.11: Equivalent circuit used to fit the EIS data during days 6-13 superimposed on an SEM image; R_S is solution resistance, R_{CT} is charge transfer resistance, R_{PO} is resistance of porous layer, Q_{DL} and Q_{PO} are the constant phase element representing double layer capacitance and capacitance of porous layer, respectively.

Table 5.2: Values of electrical elements extracted from EIS spectra from day 6-13 shown in Figure 5.10 using the equivalent circuit shown in Figure 5.11 that represents the formation of porous phase.

Day	R_S, ohm cm^2	R_{CT}, ohm cm^2	R_{PO}, ohm cm^2	C_{DL}, µF cm^{-2}	C_{PO}, µF cm^{-2}	Chi-square × 10^4
6	42	164	4.01	1074	251.44	7.31
7	49	171	4.83	1166	48.94	4.79
8	52	155	8.60	1376	16.08	4.02
9	55	153	11.15	1578	14.34	3.63
10	75	170	25.66	1535	5.22	2.11
11	88	190	46.49	1387	3.10	1.64
12	132	249	85.20	1202	1.53	1.21
13	237	366	189.50	844	0.19	9.42

5.6.4.3 Formation of protective layer

After 14 days, there is a shift in EIS patterns suggesting the onset of different interfacial processes. Figure 5.12 shows the EIS curves during the period from 14 -17 days. Nyquist plots in Figure 5.12a shows two semicircles similar to Figure 5.10a but with larger magnitude at the high frequency range.

The EIS data collected during 14 to 17 days were fitted to the EC shown in Figure 5.13 which proposes that the corrosion product consists of 2 layers; i.e. outer (mainly $FeCO_3$) and inner (combination of $FeCO_3$ and Fe_3C) layers. Additional resistances, R_{IN} and R_{OUT} (resistance of inner and outer layer, respectively) and capacitances Q_{IN} and Q_{OUT} (constant phase elements presenting the capacitance of inner and outer layer, respectively) are introduced in addition to R_{CT} and C_{DL} of the conventional Randle's circuit. The EC shown in Figure 5.13 is superimposed on the cross sectional image of the corrosion product obtained after 17 days exposure to demonstrate what each parameter physically represents. A similar EC has been proposed when duplex layer of corrosion product forms on the metal surface in CO_2 environments [18,19].

Table 5.3 lists the numerical values of the elements making up the EC shown in Figure 5.13. Solution resistance, R_S, despite a small variation, remains reasonably steady, which is in good agreement with the reasonably constant Fe^{2+} concentration produced by corrosion in the condensed liquid.

R_{IN} increases at a much greater extent than R_{OUT} does, potentially indicating the thicker inner layer compared to the outer layer. A relatively higher value of R_{IN} compared to R_{OUT} has also been reported previously [18,19]. Interestingly, the capacitance of inner and outer layer does not differ significantly probably because both layers consist predominantly of $FeCO_3$.

The magnitude of the semicircle at low frequency continues to increase with time indicating a continuing increase of R_{CT} (Table 5.3). As $FeCO_3$ continues to precipitates and is incorporated within the porous structure of Fe_3C, the charge transfer process is obstructed. As a results, the inner $FeCO_3$ increases its protectiveness. The active sites for corrosion also decrease resulting in the decrease of double layer capacitance, C_{DL} [4].

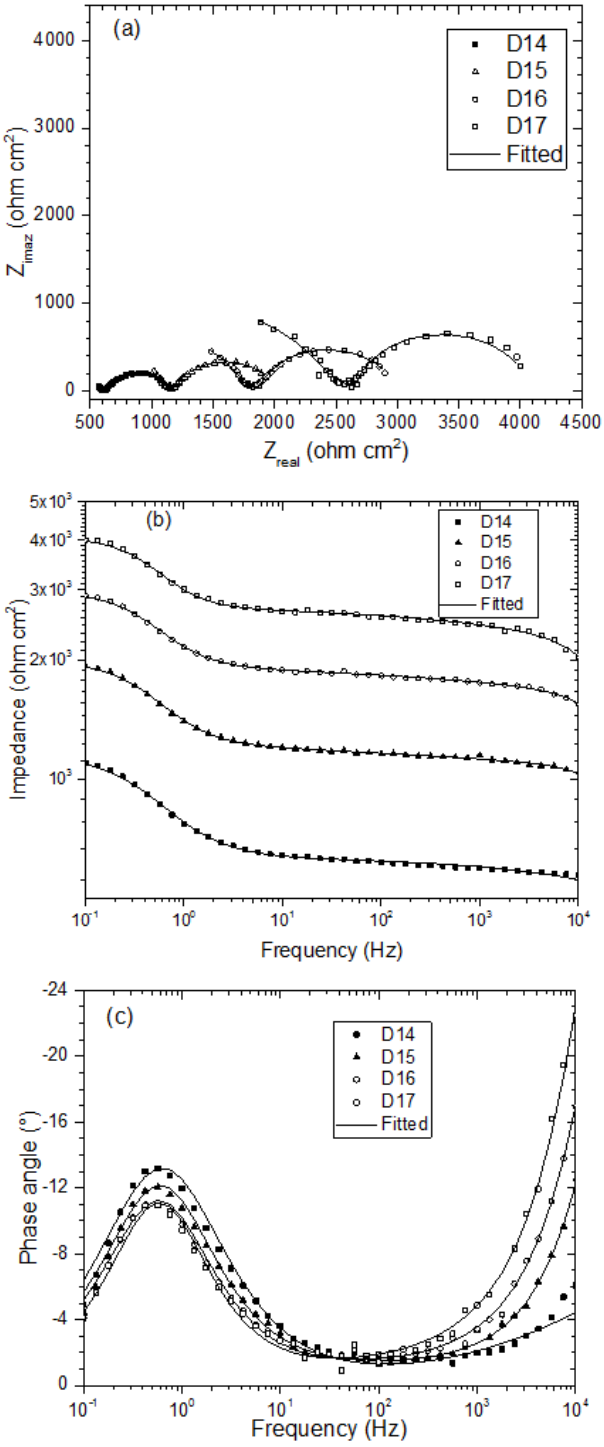

Figure 5.12: Impedance results for 14-17 days of exposure under condensing condition in CO_2 environment: (a) Nyquist and (b and c) Bode representations.

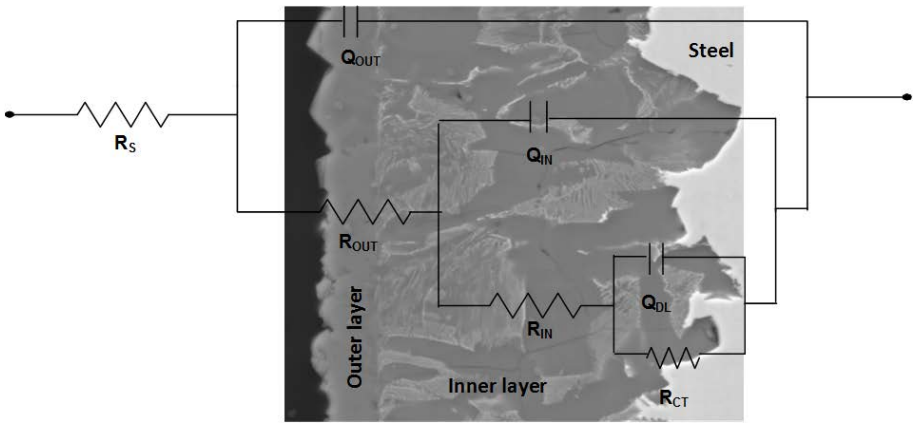

Figure 5.13: Equivalent circuit used to fit the EIS data during 14-17 days; R_S is solution resistance, R_{CT} is charge transfer resistance, R_{IN} is resistance of inner layer, R_{OUT} is resistance of outer layer, Q_{DL}, Q_{IN} and Q_{OUT} are constant phase element presenting double layer capacitance, capacitance of inner layer, and capacitance of outer layer, respectively.

Table 5.3: Values of electrical elements extracted from EIS spectra from day 14-17 shown in Figure 5.12 using the equivalent circuit shown in Figure 5.13 that represents the formation of protective film.

Day	R_S, ohm cm^2	R_{CT}, ohm cm^2	R_{IN}, ohm cm^2	R_{OUT}, ohm cm^2	C_{DL}, µF cm^{-2}	$C_{IN,}$ $10^3 \times$ µF cm^{-2}	$C_{OUT,}$ $10^4 \times$ µF cm^{-2}	Chi-square $\times 10^4$
14	269	564	324.4	44.2	533	9.12	1.21	1.64
15	197	867	822.4	272.7	339	8.13	0.30	6.19
16	264	1148	1281.0	436.1	263	1.04	0.33	5.62
17	297	1403	1443.0	986.3	222	0.18	0.35	1.60

5.7 Conclusions

An *in-situ* corrosion monitoring technique for carbon steel under condensing condition was developed and used to elucidate the interfacial phenomena associated with the corrosion process and $FeCO_3$ precipitation. The important outcomes of this study are outlined below.

- The newly designed electrochemical probe successfully enables different stages of CO_2 corrosion rates and mechanisms for carbon steel under condensation conditions to be monitored *in-situ.*
- The use of EIS in conjunction with cross-sectional analysis of the corrosion product films explains the interfacial phenomena associated with the process; i.e. iron dissolution and $FeCO_3$ precipitation.
- The mechanism of CO_2 corrosion product film formation, under the conditions evaluated in this study, involved 3 stages: i.) active state when corrosion rates increased for the first 5 days due to the galvanic coupling effect of iron carbide with ferrite, ii.) formation of a porous layer when corrosion rates start to decline between 6-13 days exposure, and iii.) formation of a protective $FeCO_3$ layer when corrosion rates become stable and reached minimum values after 13 days exposure.
- The inner layer of corrosion product consists of Fe_3C and $FeCO_3$ as characterized by confocal Raman spectroscopy while the outer layer consisted of mainly $FeCO_3$.

Acknowledgement

The authors would like to acknowledge the Microscopy & Microanalysis Facility (MMF), Curtin University for the access of SEM and EDS and Dr. Thomas Becker, Department of Chemistry, Curtin University for helping with analysing Raman data. The work was supported by International Postgraduate Research Scholarship (IPRS) provided by Curtin University.

5.8 References

[1] D. Hinkson, Z. Zhang, M. Singer, S. Nesic, Chemical composition and corrosiveness of the condensate in top-of-the-line corrosion, Corrosion. 66 (2010) 045002–045008.

[2] Z. Zhang, D. Hinkson, M. Singer, H. Wang, S. Nesic, A mechanistic model of top-of-the-line corrosion, Corrosion. 63 (2007) 1051–1062.

[3] B.R. Linter, G.T. Burstein, Reactions of pipeline steels in carbon dioxide solutions, Corros. Sci. 41 (1999) 117–139.

[4] D.A. López, S.N. Simison, S.R. de Sánchez, The influence of steel microstructure on CO_2 corrosion. EIS studies on the inhibition efficiency of benzimidazole, Electrochim. Acta. 48 (2003) 845–854.

[5] J.B. Sun, G.A. Zhang, W. Liu, M.X. Lu, The formation mechanism of corrosion scale and electrochemical characteristic of low alloy steel in carbon dioxide-saturated solution, Corros. Sci. 57 (2012) 131–138.

[6] Thunyaluk Pojtanabuntoeng, Brian Kinsella, Hoda Ehsani, James McKechnie, Assessment of corrosion control by pH neutralisation in the presence of glycol at low temperature, Corros. Sci. (2017).

[7] S. Nesic, Key issues related to modelling of internal corrosion of oil and gas pipelines - A review, Corros. Sci. 49 (2007) 4308–4338.

[8] M. Rogowska, J. Gudme, A. Rubin, K. Pantleon, R. Ambat, Effect of Fe ion concentration on corrosion of carbon steel in CO_2 environment, Corros. Eng. J. 51 (2016) 25–36.

[9] A.S. Yaro, K.R. Abdul-Khalik, A.A. Khadom, Effect of CO_2 corrosion behavior of mild steel in oilfield produced water, J. Loss Prev. Process Ind. 38 (2015) 24–38.

[10] W. Sun, S. Nesic, R.C. Woollam, The effect of temperature and ionic strength on iron carbonate ($FeCO_3$) solubility limit, Corros. Sci. 51 (2009) 1273–1276.

[11] S. Nesic, W. Sun, Corrosion in acid gas solutions, in: T.J.A. Richardson (Ed.), Shreir's Corros., Oxford, Elsevier, 2010: pp. 1270–1298.

[12] M.M. Islam, T. Pojtanabuntoeng, R. Gubner, Condensation corrosion of carbon steel at low to moderate surface temperature and iron carbonate precipitation kinetics, Corros. Sci. 111 (2016) 139–150.

[13] J.L. Mora-Mendoza, S. Turgoose, Fe_3C influence on the corrosion rate of mild steel in aqueous CO_2 systems under turbulent flow conditions, Corros. Sci. 44 (2002) 1223–1246.

[14] E.W.J. van Hunnik, B.F.M. Pots, E.L.J.A. Hendriksen, The formation of protective $FeCO_3$ corrosion product layer in CO_2 corrosion, CORROSION/1996, Paper No. 6, NACE, Houston, Texas, 1996.

[15] S. Nesic, K.L.J. Lee, A mechanistic model for carbon dioxide corrosion of mild steel in the presence of protective iron carbonate films - Part 3: Film growth model, Corrosion. 59 (2003) 616–628.

[16] A. Dugstad, Mechanism of protective film formation during CO_2 corrosion of carbon steel, CORROSION/98, Paper No. 31, NACE, Houston, Texas, 1998.

[17] F. Farelas, M. Galicia, B. Brown, S. Nesic, H. Castaneda, Evolution of dissolution processes at the interface of carbon steel corroding in a CO_2 environment studied by EIS, Corros. Sci. 52 (2010) 509–517.

[18] M. Gao, X. Pang, K. Gao, The growth mechanism of CO_2 corrosion product films, Corros. Sci. 53 (2011) 557–568.

[19] L. Wei, X. Pang, C. Liu, K. Gao, Formation mechanism and protective property of corrosion product scale on X70 steel under supercritical CO_2 environment, Corros. Sci. 100 (2015) 404–420.

[20] S. Guo, F. Farelas, M. Singer, A glycol/water co-condensation model to investigate the influence of monoethylene glycol on top-of-the-line corrosion, Corrosion. 73 (2017) 742–755.

[21] T. Pojtanabuntoeng, M. Singer, S. Nesic, Top-of-the-line corrosion in the presence of hydrocarbon co-condensation in flowing condition, CORROSION/2012, Paper No. C2012-0001534, NACE, Houston, Texas, 2012.

[22] F. Vitse, S. Nesic, Y. Gunaltun, D.L. de Torreben, P. Duchet-Suchaux, Mechanistic model for the prediction of top-of-the-line corrosion risk, Corrosion. 59 (2003) 1075–1084.

[23] M. Singer, Study and modeling of the localized nature of top of the line corrosion, PhD desertation, Ohio University, Ohio, USA, 2013.

[24] M. Singer, D. Hinkson, Z. Zhang, H. Wang, S. Nesic, CO_2 top of the line corrosion in presence of acetic acid: A parametric study, Corrosion. 69 (2013) 719–735.

[25] P. Altoé, G. Pimenta, C.F. Moulin, S.L. Díaz, O.R. Mattos, Evaluation of oilfield corrosion inhibitors in CO_2 containing media: A kinetic study, Electrochim. Acta. 41 (1996) 1165–1172.

[26] M. Pourbaix, Applications of electrochemistry in corrosion science and in practice, Corros. Sci. 14 (1974) 25–82.

[27] B. Kinsella, Y.J. Tan, S. Bailey, Electrochemical impedance spectroscopy and surface characteriztion techniques to study carbon dioxide corrosion product scales, Corrosion. 54 (1998) 835.

[28] M.M. Islam, R. Gubner, T. Pojtanabuntoeng, Development of an electrochemical method to study top-of-the-line corrosion, CORROSION/2017, Paper no. 9106, NACE, Houston, Texas 2017.

[29] ASTM G1 − 03, Standard practice for preparing , cleaning , and evaluating corrosion test, in: Annu. B. ASTM Stand., vol. 03.02, ASTM International, 2011.

[30] R.W. Bosch, W.F. Bogaerts, Instantaneous corrosion rate measurement with

small-amplitude potential intermodulaton techniques, Corros. Sci. 52 (1996) 204–212.

[31] E. Kuş, F. Mansfeld, An evaluation of the electrochemical frequency modulation (EFM) technique, Corros. Sci. 48 (2006) 965–979.

[32] S. Nesic, J. Postlethwaite, S. Olsen, An electrochemical model for prediction of corrosion of mild steel in aqueous carbon dioxide solutions, Corrosion. 52 (1996) 280–294.

[33] S. Nesic, M. Nordsveen, R. Nyborg, A. Stangeland, A mechanistic model for carbon dioxide corrosion of mild steel in the presence of protective iron carbonate films - part 2: a numerical experiment, Corrosion. 59 (2003) 489–497.

[34] M. Hanesch, Raman spectroscopy of iron oxides and (oxy)hydroxides at low laser power and possible applications in environmental magnetic studies, Geophys. J. Int. 177 (2009) 941–948.

[35] C.T. Lee, M.S. Odziemkowski, D.W. Shoesmith, An in situ Raman-electrochemical investigation of carbon steel corrosion in Na_2CO_3/$NaHCO_3$, Na_2SO_4, and NaCl solutions, J. Electrochem. Soc. 153 (2006) B33–B41.

[36] X.X. Bi, B. Ganguly, G.P. Huffman, F.E. Huggins, M. Endo, P.C. Eklund, Nanocrystalline α–Fe, Fe_3C, and Fe_7C_3 produced by CO_2 laser pyrolysis, J. Mater. Res. 8 (1993) 1666–1674.

[37] F. Mansfeld, Electrochemical impedance spectroscopy (EIS) as a new tool for investigating methods of corrosion protection, Electrochim. Acta. 35 (1990) 1533–1544.

[38] K. Juttner, Electrochemical impedance spectroscopy (EIS) of corrosion processes on inhomogeneous surfaces, Electrochim. Acta. 35 (1990) 1501–1508.

[39] V.A. Alves, C.M.A. Brett, Characterisation of passive films formed on mild

steels in bicarbonate solution by EIS, Electrochim. Acta. 47 (2002) 2081–2091.

[40] A. Popova, M. Christov, A. Vasilev, Inhibitive properties of quaternary ammonium bromides of N-containing heterocycles on acid mild steel corrosion. Part II: EIS results, Corros. Sci. 49 (2007) 3290–3302.

[41] C.H. Hsu, F. Mansfeld, Technical note : Concerning the conversion of the constant phase element parameter Y_o into a capacitance, Corrosion. 57 (2001) 747–748.

[42] F. Bentiss, M. Outirite, M. Traisnel, H. Vezin, M. Lagrenée, B. Hammouti, Improvement of corrosion resistance of carbon steel in hydrochloric acid medium by 3 , 6-bis (3-pyridyl) pyridazine, Int. J. Electrochem. Sci. 7 (2012) 1699–1723.

[43] F.F. Eliyan, E.S. Mahdi, A. Alfantazi, Electrochemical evaluation of the corrosion behaviour of API-X100 pipeline steel in aerated bicarbonate solutions, Corros. Sci. 58 (2012) 181–191.

[44] B. Hirschorn, M.E. Orazem, B. Tribollet, V. Vivier, I. Frateur, M. Musiani, Determination of effective capacitance and film thickness from constant-phase-element parameters, Electrochim. Acta. 55 (2010) 6218–6227.

[45] J.L. Crolet, N. Thevenot, S. Nesic, Role of conductive corrosion products in the protectiveness of corrosion layers, Corrosion. 54 (1998) 194–203.

[46] F. Farelas, A. Ramirez, Carbon dioxide corrosion inhibition of carbon steels through bis-imidazoline and imidazoline compounds studied by EIS, Int. J. Electrochem. Sci. 5 (2010) 797–814.

[47] P. Li, T.C. Tan, J.Y. Lee, Impedance spectra of the anodic dissolution of mild steel in sulfuric acid, Corros. Sci. 38 (1996) 1935–1955.

[48] G.A. Zhang, Y.F. Cheng, On the fundamentals of electrochemical corrosion of X65 steel in CO_2-containing formation water in the presence of acetic acid

in petroleum production, Corros. Sci. 51 (2009) 87–94.

[49] S. Nesic, N. Thevenot, J.-L. Crolet, D.M. Drazic, Electrochemical properties of iron dissolution in the presence of CO_2 - Basic revisited, CORROSION/96, Paper No. 3, NACE, Houston, Texas, 1996.

[50] Y.J. Tan, S. Bailey, B. Kinsella, An investigation of the formation and destruction of corrosion inhibitor films using electrochemical impedance spectroscopy (EIS), Corros. Sci. 38 (1996) 1545–1561.

[51] Y. Zuo, R. Pang, W. Li, J.P. Xiong, Y.M. Tang, The evaluation of coating performance by the variations of phase angles in middle and high frequency domains of EIS, Corros. Sci. 50 (2008) 3322–3328.

[52] R. Álvarez-Bustamante, G. Negrón-Silva, M. Abreu-Quijano, H. Herrera-Hernández, M. Romero-Romo, a. Cuán, et al., Electrochemical study of 2-mercaptoimidazole as a novel corrosion inhibitor for steels, Electrochim. Acta. 54 (2009) 5393–5399.

Appendix I: Are condensation rate and corrosion rates proportional in TLC?*

I.1 Abstract

An investigation has been conducted to distinguish the influence of main parameters such as surface temperature, gas temperature and condensation rate on top-of-the-line corrosion (TLC) using a new experimental setup. Experiments were carried out at atmospheric pressure and under stagnant fluid conditions at the bottom of the vessel. A small flow of water vapour saturated with high purity CO_2 was purged through the cell to maintain anoxic conditions. The surface temperature was controlled to 15 °C, 30 °C, and 45 °C whereas the gas temperature was varied between 40 °C and 55 °C. Corrosion rates were determined by weight loss and iron concentration measurement.

The results demonstrate that the surface temperature is the main parameter controlling two primary processes that determine TLC severity; i.e. iron dissolution and the iron carbonate precipitation. At low surface temperature (approx. 15 °C), TLC rates remained relatively constant regardless of the water condensation rate, possibly due to slow kinetics of iron dissolution process. With increasing surface temperature, TLC rates increased up to 30 °C in spite of decreasing condensation rates. However, condensation rates came to play role at higher surface temperature (approximately 45 °C) when iron carbonate precipitated on the surface.

Keywords: surface temperature, gas temperature, water condensation, iron carbonate

I.2 Introduction

Top-of- the-line corrosion (TLC) may be regarded as the corrosion inside the upper portion (between 10 o'clock and 2 o'clock position) of steel pipelines caused by the droplets of water saturated with corrosive constituents [1,2]. In wet gas transportation pipelines, the inside gas temperature is higher than the outside environment resulting in water condensation at the top-of-the-line (TOL). The corrosive constituents such as carbon dioxide (CO_2), hydrogen sulphide (H_2S) are dissolved in condensed water and organic acids, mainly acetic acid (HAc) co-condense. As a result, condensed liquid is

* This chapter is reproduced from 'M.M. Islam, R. Gubner, T. Pojtanabuntoeng, Are corrosion rates and condensation rates proportional in TLC?, CORSYM-2015, NACE International and Gateway India Section, Paper No. 3, 2015'.

acidic and corrosive to the steel surface [3]. Depending on the corrosive constituents, TLC can be sub-divided as 'sweet' corrosion occurring at CO_2 dominated environment and 'sour' corrosion taking place at H_2S containing environment [4]. It has been reported that sweet TLC takes place in different mechanism and is more serious compared to sour condition [5]. The present TLC study focuses on sweet condition.

TLC rates under sweet conditions depend mostly on water condensation rate, wet gas temperature, pipe wall temperature, gas velocity, partial pressure of CO_2, flow regime and organic acid content [6-10]. Among all, the first three parameters are interrelated with each other and it is a challenge to distinguish the importance of each parameter. Most TLC studies focused on either the effect of condensation rate or gas temperature [10-13]. For example, Chen et al. demonstrated that TLC rate was increased with the gas and liquid film temperature within the range between 40 °C to 80 °C [11]. Similarly, an empirical sweet TLC rate calculation model has been developed based on wet gas temperature, partial pressure of CO_2, and condensation rate eliminating the effect of surface temperature [10]. Nevertheless, the recently published advanced mechanistic model of TLC also only considers gas temperature, CO_2 partial pressure, gas velocity, condensation rate, and acetic acid concentration [2,12]. The surface temperature was not taken into consideration for the model. Likewise, TLC rates were also studied at different condensation rates ranging from 0.001-1 ml $m^{-2}s^{-1}$ [6,14,15]. Literature concluded that TLC rates and condensation rates are proportional. However, the behavior of TLC at low surface temperatures and high condensation rates is not well defined in the literature. At low surface temperatures, electrochemical reactions are supposed to be kinetically slow. Hence, it is an unresolved question whether the proportional relationship will remain applicable or not at these conditions. Therefore, the present study aims at differentiating the influence of surface temperature, gas temperature and condensation rate on sweet TLC.

I.3 Experimental

I.3.4 Preparation of sample

A carbon steel rod with a diameter of 20 mm was cut into samples of 16 mm in length. After an initial polishing with 600 grit silicon carbide paper followed by cleaning with water and ethanol, the samples were electro-coated with an organic lacquer (Powercron 6000 CX) leaving one circular surface exposed for experiments. Afterwards, the samples were again polished with silicon carbide paper to 1200 grit. After a subsequent cleaning with DI water and ethanol, the samples were kept in an oven before weighing with an analytical balance (0.1 mg).

I.3.5 Cell set up

The TLC cell set-up used in this study is depicted in Figure I.1 and the procedure was discussed previously [16]. A TLC lid assembled with samples, cooling chamber, CO_2 inlet and outlet, thermocouple, and condensed liquid collecting cup, surface temperature and gas temperature probe was placed onto a two-litre glass cell creating an air-tight environment. The whole assembly was placed on a hotplate and high purity (99.99 %) CO_2 gas was sparged for 10 minutes to eliminate the oxygen in the vessel. The cooling chamber was connected to a water bath to maintain the desired surface temperature.

1400 ml of high purity water (18.2 MΩ.cm), pre-sparged with CO_2 overnight and preheated to a predefined temperature in a separate container, was transferred to the TLC cell using a peristaltic pump. As the vapour temperature and surface temperature reached to the desired value, the experiment started. The condensed liquid, dropped into a precipitation cup placed directly beneath the sample, was collected periodically to determine weight, pH, and ferrous ion concentration. The condensation rate was calculated based on known time, collected weight and surface area of the sample. The *in-situ* corrosion rate was calculated based on iron concentration dissolved in the condensed liquid for a certain exposure time.

I.3.6 Sample characterization

At the end of the experiment, the sample was removed from the lid, rinsed with ethanol and dried with nitrogen gas (99.99 %) before examining the surface with Scanning Electron Microscopy (SEM). Afterwards, corrosion products were removed following ASTM G1-03 using the Clark solution (1000 mL of hydrochloric acid, 20 g of antimony trioxide and 50 g of stannous chloride) and the corrosion rate was calculated from weight loss.

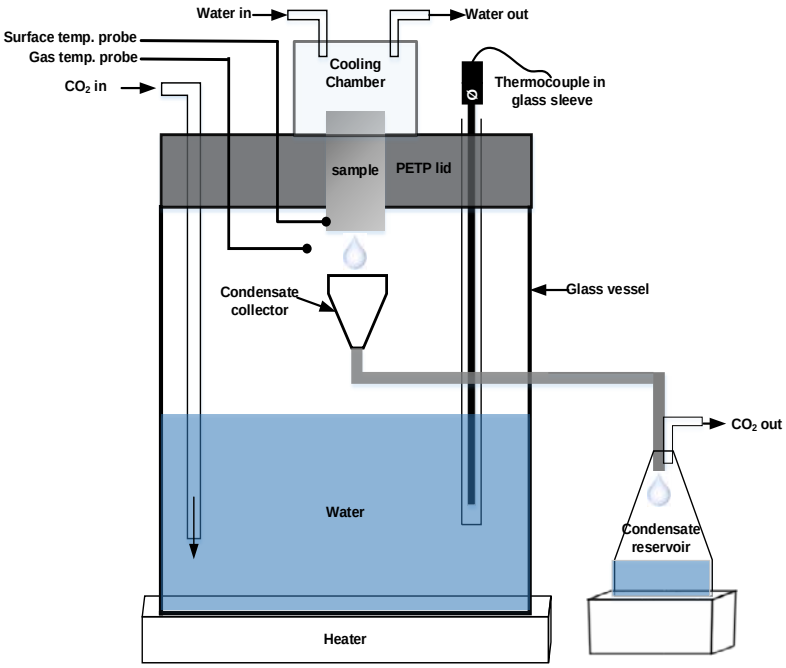

Figure I.1: Schematic representation of top-of-the-line corrosion (TLC) setup; modified from Ref.[16].

I.4 Results and discussion

I.4.4 TLC rates at 55 °C gas temperature and different surface temperatures

Figure I.2 presents the influence on surface temperature on the TLC rates and condensation rates at 55 °C gas temperature. The histogram shows the TLC rates and the line diagram represents the condensation rates. A non-linear relationship between

TLC rates with surface temperature was found. TLC rates at 15 °C surface temperature were lower compare to the TLC at 30 °C. As surface temperature increased from 15 to 30 °C, corrosion rates became almost double despite the slight decrease in condensation rate from 1.55 g $m^{-2}s^{-1}$ to 1.20 g $m^{-2}s^{-1}$. Further increase in surface temperature up to 45 °C reduced the corrosion rate by almost 50% and the condensation rate to 0.43 g $m^{-2}s^{-1}$.

The results discussed above can be explained by two phenomena; i.e. iron dissolution process and super saturation of iron carbonate. At 15 and 30 °C surface temperature and 55 °C gas temperature, the condensation rates were 1.55 and 1.2 g $m^{-2}s^{-1}$respectively (Figure I.2). These high condensation rates do not allow the surface to be saturated with iron carbonate. SEM indicates no iron carbonate crystal formation at these conditions (Figure I.3a and b). In this case, iron dissolution process mainly governed by the surface temperature becomes the key factor to determine the corrosion rate [16]. Consequently, increasing the surface temperature from 15 to 30 °C enhances the iron dissolution process kinetically. Therefore, corrosion rates increase though condensation rates are reduced within this range of surface temperature.

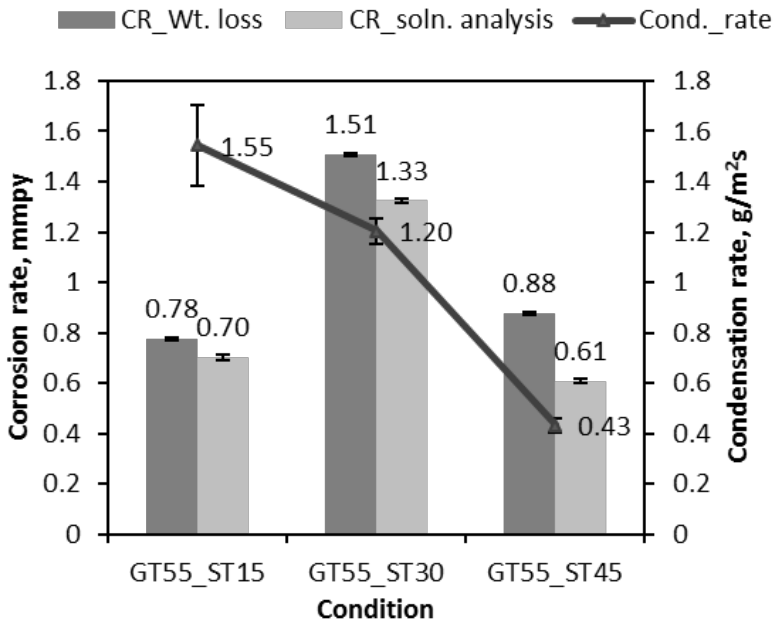

Figure I.2: Effect of surface temperature (ST) on the top-of-the-line corrosion (TLC) at 55 °C gas temperature (GT).

A further increase of surface temperature up to 45 °C, the condensation rate decreased to 0.43 g $m^{-2}s^{-1}$ due to the decrease in temperature gradient between surface temperature and gas temperature (55 °C). A different phenomenon was observed in this condition. As condensation rate decreased, the system was allowed to reach super saturation to form iron carbonate precipitation. Increasing the surface temperature also favoured the kinetics of iron carbonate precipitation [16]. This is confirmed by SEM showing that the surface is fully covered with iron carbonate crystals (Figure I.3c). The above phenomena explain the reason of the reduction of corrosion rate at 45 °C surface temperature.

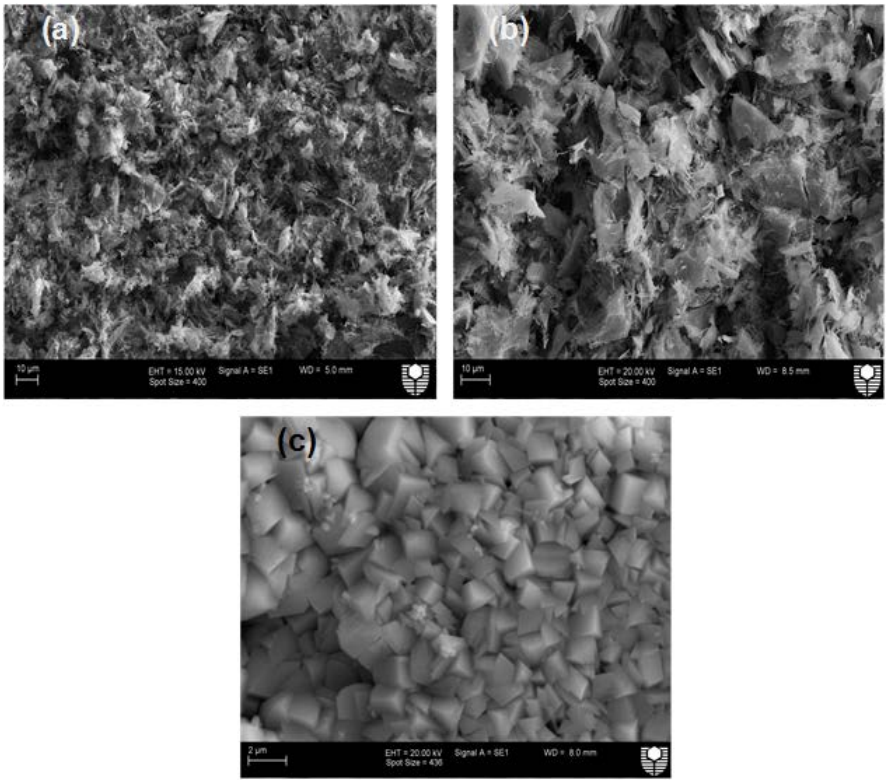

Figure I.3: SEM of samples after corrosion tests at 55 °C gas temperature and different surface temperature; (a) 15 °C surface temperature, (b) 30 °C surface temperature and, (c) 45 °C surface temperature; modified from Ref.[16].

I.4.5 TLC rates at 15 ℃ surface temperature and different gas temperatures

Figure I.4 (a) describes the TLC rates with time at different gas temperatures (40 °C and 55 °C) while the surface temperature was maintained at 15 °C. It was observed that the corrosion rates obtained by iron concentration measurement increase linearly with time throughout the entire experiment at both gas temperatures. TLC rates at 55 °C gas temperature are slightly higher than the TLC at 40 °C, but their increasing patterns are linear. Figure I.4 (b) compares average corrosion rates obtained from weight loss and iron concentration measurements along with the average condensation rates from the two experiments. A minor influence of condensation rates on TLC rates were identified while comparing the TLC rates with condensation rate at 15 °C surface temperatures. At 15 °C surface temperature, increase of gas temperature from 40 to

55 °C increased the condensation rate from 0.63 to 1.54 g/m^{2}s. Nonetheless, only minor changes in corrosion rates were observed.

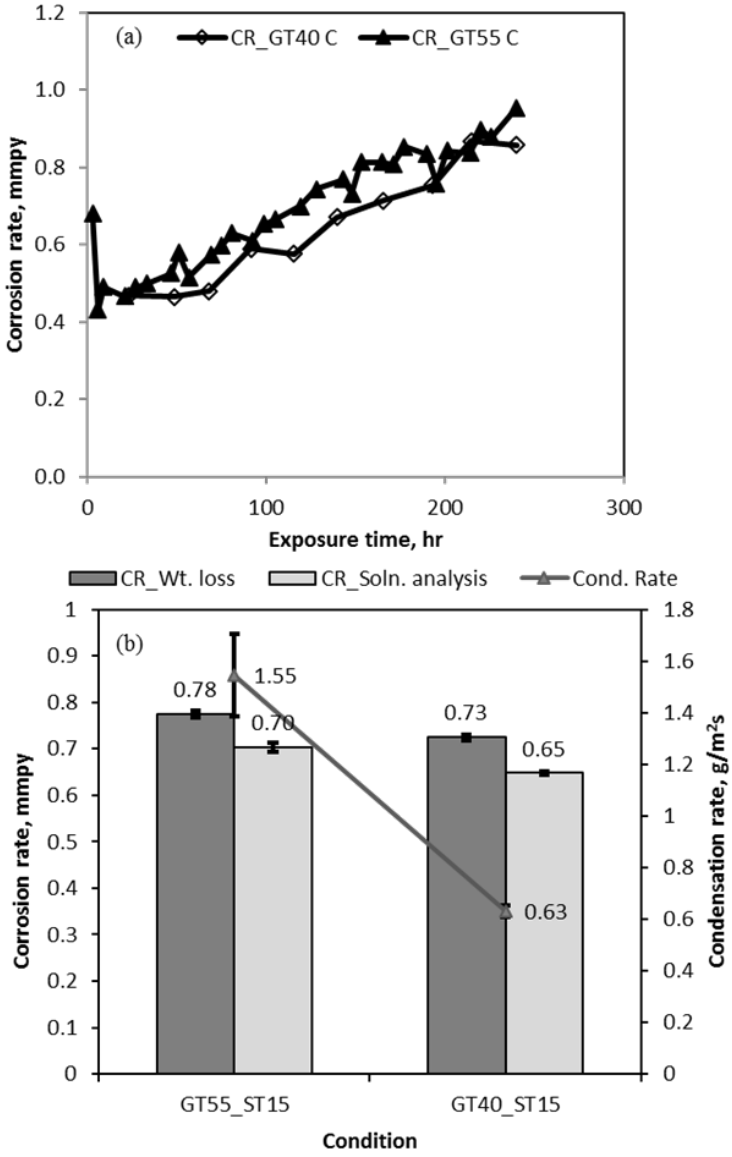

Figure I.4: Effect of gas temperature (GT) on top-of-the-line corrosion (TLC) at 15 °C surface temperature (ST).

These results can be explained by the fact that at 15 °C surface temperature, the driving force for electrochemical corrosion is significantly low. As a result, surface temperature becomes the rate determining step for the corrosion process. In addition, the negative temperature coefficient of $FeCO_3$ solubility in water facilitates the dissolution of $FeCO_3$ in the condensing liquid at low temperatures [17]. Hence, the formation of iron carbonate film becomes thermodynamically and kinetically unfavorable. It can be concluded that increasing condensation rates do not necessarily influence TLC rates, particularly at low surface temperature. In other words, TLC is not always proportional to the condensation rate.

I.5 Conclusions

The results have shown that surface temperature is the main parameter governing TLC severity. At low surface temperatures, TLC rates do not follow the proportional relationship with condensation rate due to the slow kinetics of iron dissolution process. Increasing the surface temperature has both negative and positive effects as it enhances the iron dissolution process and the iron carbonate precipitation. As a result, corrosion rate increases with surface temperature up to 30 °C and then decreases as the protection by iron carbonate becomes more dominant.

Acknowledgements

The authors would like to acknowledge the Microscopy & Microanalysis Facility (MMF), Curtin University for the access of SEM and EDS. One of us (M.M.I.) thanks the Curtin university for International Postgraduate Research Scholarship (IPRS). We would also like to thank NACE Founding Malaysia Section to provide a scholaship to attend the confernce and to present this paper.

I.6 References

[1] M. Singer, A. Camacho, B. Brown, S. Nesic, Sour top-of-the-line corrosion in the presence of acetic acid, Corrosion. 67 (2011) 85003–16.

[2] Z. Zhang, D. Hinkson, M. Singer, H. Wang, S. Nesic, A mechanistic model of top-of-the-line corrosion, Corrosion. 63 (2007) 1051–1062.

[3] F. Vitse, S. Nesic, Y. Gunaltun, D.L. de Torreben, P. Duchet-Suchaux, Mechanistic model for the prediction of top-of-the-line corrosion risk, Corrosion. 59 (2003) 1075–1084.

[4] M. Singer, A. Camacho, B. Brown, S. Nesic, Sour top-of-the-line corrosion in the presence of acetic acid, CORROSION/2010, Paper No. 10100, NACE, Houston, Texas, 2010.

[5] M. Bonis, Form sweet to sour TLC: what's different?, 2nd Int. TLC Conf., Bangkok, PTTEP, 2009.

[6] R.A. Ojifinni, C. Li, A parametric study of sweet top-of-line corrosion in wet gas pipelines, CORROSION/2011, Paper No. 11331, NACE, Houston, Texas, 2011.

[7] S. Asher, W. Sun, R. Ojifinni, J. Pacheco, C. Li, J. Nelson, et al., Top of the line corrosion prediction in wet gas pipelines, CORROSION/2012, Paper No. C2012-0001303, NACE, Houston, Texas, 2012.

[8] M. Singer, J. Al-Khamis, S. Nesic, Experimental study of sour top-of-the-line corrosion using a novel experimental setup, Corrosion. 69 (2013) 624–638.

[9] G. Svenningsen, R. Nyborg, Modeling of top of line corrosion with organic acid and glycol, CORROSION/2014, Paper No. 4057, NACE, Houston, Texas, 2014.

[10] R. Nyborg, A. Dugstad, Top of line corrosion and water condensation rates in wet gas pipelines, CORROSION/2007, Paper No. 07555, NACE, Houston, Texas, 2007.

[11] Y. Chen, L. Zhang, H. Qin, L. Xu, M. Lu, Effects of temperature on CO_2 top of line corrosion of pipeline steel, CORROSION/2011, Paper No. 11327, NACE, Houston, Texas, 2011.

[12] Z. Zhang, D. Hinkson, M. Singer, H. Wang, S. Nesic, A mechanistic model of top of the line corrosion, CORROSION/2007, Paper No. 07556, NACE,

Houston, Texas, 2007.

[13] F. Vitse, S. Nesic, Y. Gunaltun, D.L. de Torreben, P. Duchet-Suchaux, Mechanistic model for the prediction of top-of-theline corrosion risk, CORROSION/2003, Paper No. 03633, NACE, Houston, Texas, 2003.

[14] G. Svenningsen, F. Martin, N. Rolf, H. Fukagawa, I. Kurniawan, Top of line corrosion with high CO_2 and organic acid, CORROSION/2013, Paper No. 2591, NACE, Houston, Texas, 2013.

[15] M. Singer, D. Hinkson, Z. Zhang, H. Wang, S. Nesic, CO_2 top of the line corrosion in presence of acetic acid: A parametric study, Corrosion. 69 (2013) 719–735.

[16] M.M. Islam, T. Pojtanabuntoeng, R. Gubner, Condensation corrosion of carbon steel at low to moderate surface temperature and iron carbonate precipitation kinetics, Corros. Sci. 111 (2016) 139–150.

[17] H. Qin, L. Xu, W. Chang, M. Lu, L. Zhang, Top of the line corrosion under low temperature and high condensation rate conditions, CORROSION/2011, Paper No. 11328, NACE, Houston, Texas, 2011.

Appendix II: Electrochemical investigation into the influence of monoethylene glycol on CO_2 corrosion in presence of acetic acid*

II.1 Abstract

This study is aimed to i) determine the dissociation constant (pK_a) of acetic acid (HAc) in monoethylene glycol (MEG), and ii) investigate the influences of MEG on CO_2 corrosion of carbon steel in presence of HAc. This study reveals that MEG impedes the dissociation of HAc, hence increases the pK_a constant. The predicted concentration of undissociated HAc is increased in presence of MEG at pH 5 and above. MEG also hinders the galvanic effect of ferrite and cementite by adsorbing on the active sites and reduce the corrosion rate. The inhibition efficiency of MEG is strongly dependent on its concentration. HAc is found to aggravate the corrosion of carbon steel but its activity considerably reduces with increasing MEG concentration.

Keywords: Monoethylene glycol, dissociation constant, CO_2 corrosion, acetic acid.

II.2 Introduction

In remote subsea production of oil and natural gas, transportation of multiphase fluids through pipelines from offshore platforms to onshore platforms or storage area can be challenging. Water in the presence of carbon dioxide (CO_2), organic acids and hydrogen sulphide (H_2S) causes corrosion in the interior of the pipelines [1-3]. Typical concentrations of organic acids that can be encountered in the pipeline range somewhere between being 100 – 3000 ppm [4]. Acetic acid (HAc) is the dominant species among other organic acids and is usually accounted for 50% to 90% of the total [5,6]. The pK_a of HAc (4.76 at 25 °C) is stronger than that of the carbonic acid (6.3 at 25 °C) [6]. Controversial effects of HAc on carbon steel corrosion in CO_2 condition were reported in the literature. Some studies reported increased corrosivity in the presence of HAc [6-12], whereas others reported that HAc works as a mild corrosion inhibitor especially at room temperature by shifting the anodic potential to positive direction [13.14]. However, when HAc co-condenses with water at the top-of-the-line (TOL), it always aggravates the top-of-the-line corrosion (TLC) [4,15].

* This chapter is reproduced from 'M.M. Islam, R. Gubner, T. Pojtanabuntoeng, Electrochemical investigation into the influence of monoethylene glycol on CO_2 corrosion in presence of acetic acid, manuscript in preparation'.

In addition to corrosion, the presence of water and small hydrocarbon molecules can form an ice-like substance called “hydrate” which may block the pipelines and reduce the line capacities [16]. Monoethylene glycol (MEG) has been widely used to inhibit hydrate formation due to its low toxicity and recycling capability [17-19]. MEG is also reported to possess a corrosion inhibition property [20-25]. This could be another reason that MEG is a preferred choice over other hydrate inhibitors. Typical concentrations of MEG encountered in the pipeline can vary greatly; e.g. 80 to 90 wt.% at the beginning of pipelines to 35-50 wt.% after it is diluted with condensed and/or produced water [26].

It was reported that MEG adsorbs at the steel surface and thus keeps corrosive species such as water and CO_2 derivatives away resulting in the reduction of corrosion rate [21,27,28]. However, the adsorption did not seem to be via chemisorption [29]. MEG also affects physico-chemical properties of water presenting in the pipeline; e.g. density, viscosity, CO_2 solubility, and solution conductivity [27,30]. Moreover, MEG decreases the iron solubility and slow down the kinetics of $FeCO_3$ precipitation [26,31].

Since MEG and HAc are present in a large number of the wet gas transportation pipelines, their combined effect towards pipeline corrosion is of importance. It was recently reported that the undissociated HAc is not significantly electroactive to take part in its direct reduction. Therefore, the main cathodic reaction is the H^+ reduction which is called buffering effect [6,32]. In this case, the extent of corrosivity of HAc depends on its dissociation constant (pK_a), which in turn relied on the temperature, solvent property and ionic strength of the solution [33-37]. Therefore, it is expected that MEG could alter the pK_a of HAc in the similar manner as other organic solvents. However, the pK_a values of HAc in the presence of MEG has, to the best of our knowledge, not been reported previously.

Therefore, the present investigation aimed to determine the dissociation constant of HAc in the presence of MEG and to examine the influences of MEG on carbon steel corrosion in presence of HAc.

II.3 Experimental

II.3.4 Determination of pK_a of HAc in MEG solution

The dissociation constant of HAc in MEG solutions was determined by titration method. The titrant, 0.3M of NaOH which was calibrated against the standard 0.1M potassium hydrogen phthalate, was filled in a graduated burette. The analytes were 0.03M HAc in 0%, 30%, 50% and 80% (wt.%) MEG solution. A glass vessel filled with an aliquot of analyte was placed on a hotplate and was fitted with a pH probe, a thermocouple and a magnetic stirrer. After the analyte reached the test temperature (30 °C, 50 °C and 80 °C), the titrant was added slowly into the vessel and corresponding and steady pH was recorded. The process was repeated until the equivalence point of the titration, which was identified by the sharp change of pH, was attained. Each experiment was repeated three times and standard deviation was below 5%. The measured pH was compensated to minimize the effect of mixed solvent [38]. The dissociation constant of HAc (K_a) in MEG solutions was then obtained based on Equation (II.1) [39]. K_a is a slope of a linear relationship between $[\mathrm{H}^+]\,V_B$ vs $(V_E - V_B)$. Then pK_a was calculated from the negative logarithm of K_a.

$$[\mathrm{H}^+]\,V_B = K_a(V_E - V_B) \qquad \text{(II.1)}$$

where V_E and V_B are the volume of titrant added at an equivalent point and at any point, respectively, K_a is the acid dissociation constant and $[\mathrm{H}^+]$ is the concentration of hydrogen ion with respect to any given measurements.

II.3.5 Corrosion study of 1030 carbon steel in MEG and HAc solutions

Carbon steel specimens having the chemical composition of C 0.30%; Mn 0.75%; Si 0.25%; P 0.04%; S 0.04% with the balance iron were used in this investigation. The test specimens were machined to 6.3 mm in diameter and 10 mm in length. The specimens were soldered and casted in epoxy resin leaving approximately 0.32 cm^2 exposed to test solutions. After a successive wet grinding with silicon carbide paper

up to 1200 grit, the samples were rinsed with deionised water (DI) (resistance 18.2 MΩ cm), degreased with ethanol, and then dried with nitrogen.

The solutions were 30, 50, and 90 wt.% MEG in DI water with 3 wt.% NaCl. In experiments with HAc, a concentration of HAc was maintained at 1000 ppm. The solution was saturated with CO_2 prior and was maintained during the experiment and temperature was kept at 30 °C. The pH of MEG containing solutions was measured following the procedure of Sandengen et al.[38] and maintained at 4 using either 0.1M $NaHCO_3$ or 0.1M HCl.

Electrochemical tests were conducted using Gamry Reference 600 potentiostat-galvanostat in a three-electrode arrangement where Ag/AgCl (3M KCl) and platinum coated titanium mesh electrode acted as reference and counter electrodes, respectively. Open circuit potential (OCP) of the specimens was monitored for 1 h to stabilize. Then, linear polarization resistance was measured for 24 h at a scan rate of 10 mV/min within ±10 mV with respect to OCP. Afterwards, electrochemical impedance spectroscopy (EIS) was carried out in the frequency range of 10,000-0.01 Hz and with an AC potential amplitude of 10 mV applied. Finally, potentiodynamic polarization test was performed from +250 to -250 mV with respect to OCP at a scan rate of 10 mV/min. All the data were analysed using Gamry Echem Analyst software (Version 6.25).

II.4 Results and discussion

II.4.4 Dissociation constant (pK_a) of HAc

The pK_a of HAc in different MEG solutions at different temperatures is presented in Figure II.1. It can be seen that the pK_a of HAc increases with MEG concentration indicating that MEG impedes the dissociation of HAc. This is true for all 3 temperatures tested. Samini and Kenndler found a higher value of pK_a of HAc in non-aqueous solvent compared to water and explained that 'solvent effect' and 'medium effect' played key roles in changing the pK_a. The 'solvent effect' is the change in property of the system resulting from solvent composition whereas the 'medium effect' is change in solute behaviour with respect to different solvent [34]. When MEG

is added to the water, the properties of the solution change; such as viscosity, solution conductivity, pH, polarity, etc. This is referred to as 'solvent effect'. In the same line, the properties of HAc are also changed in MEG containing solutions, such as, dielectric constant, entropy of ionization and heat of ionization which is referred to as the 'medium effect'.

As a consequence of an increase in the *pKa*, water chemistry and speciation of corrosive species in MEG containing solutions may deviate from those of water. As shown in Figure II.2, in acidic conditions up to pH 4, most of the HAc would remain in an un-dissociated state, both in water and MEG solutions. Therefore, at pH 4 or below, the change in pK_a due to the presence of MEG does not affect overall concentration of HAc. Nonetheless, as pH increases towards neutral and alkali region, significantly higher concentration of the un-dissociated HAc in MEG containing solution are expected. A higher concentration of HAc may co-condense and consequently accelerate TLC severity as HAc is volatile and the condensed water has low buffering capacity. On the contrary, the change in un-dissociated HAc concentration may or may not affect the corrosion behaviour under the bottom of the line condition as recent research has challenged the existence of the direct reduction of HAc [6,32].

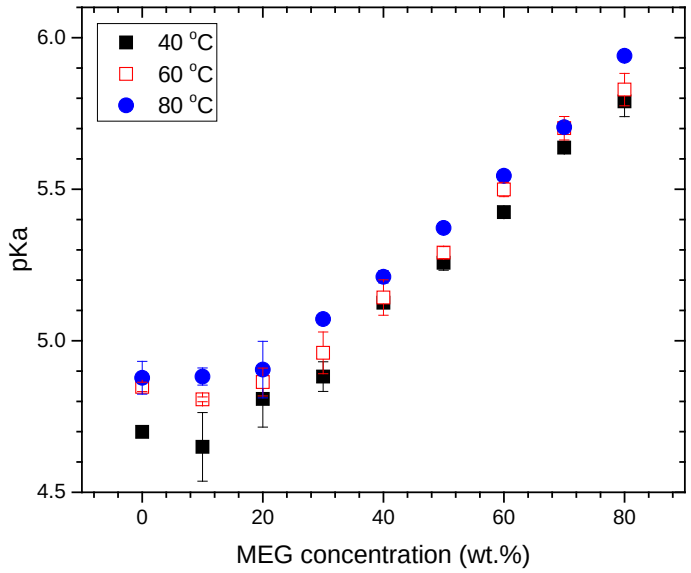

Figure II.1: The variation in dissociation constant of HAc in the presence of MEG at varying temperatures.

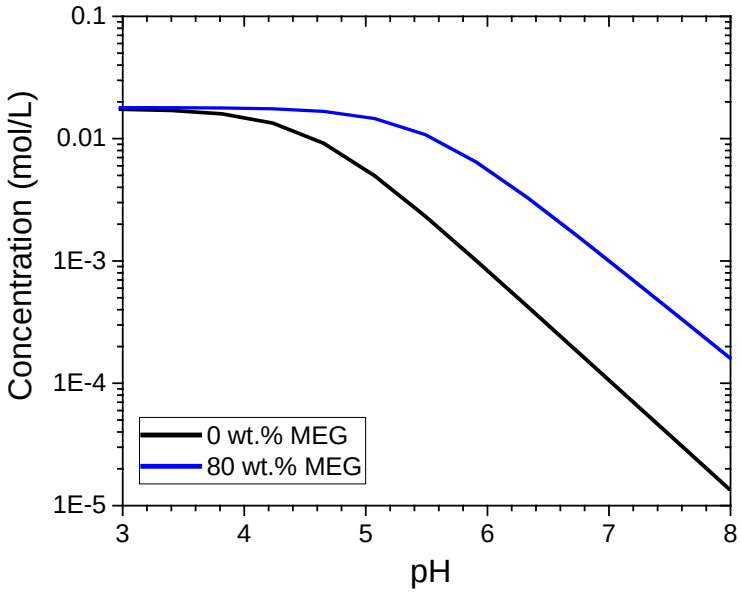

Figure II.2: Predicted concentration of undissociated HAc as a function of pH at 0% and 80% MEG.

II.4.5 Polarization studies

II.4.5.1 Potentiodynamic polarization

Potentiodynamic polarization experiments were conducted to gain an understanding of the corrosion mechanism associated with MEG in the absence and presence of HAc by observing corrosion potential, Tafel slopes and the nature of anodic and cathodic curves. Figure II.3 and Figure II.4 present the polarization curves of carbon steel immersed in solutions of different MEG concentrations in the absence and presence of 1000 ppm HAc, respectively.

In the absence of HAc (as shown in Figure II.3), both the anodic and cathodic current density decrease with increasing MEG content indicating an inhibitive performance of MEG. Corrosion potential shifts towards the anodic direction with increasing MEG contents suggesting MEG blocks the active sites. Further, the anodic branches particularly for those in the presence of MEG exhibit an inflection at approximately 150 mV positive to OCP, which is absent in MEG-free solutions. The inflection in the anodic curve has been denoted as desorption potential, E_d, at which surface film converted from a stable to an unstable state [40,41]. The E_d shifts towards the noble direction with increasing MEG concentration (approximately -0.6 V at 30 % MEG to -0.45 V for 90 % MEG) indicating an enhanced tendency of MEG adsorption as the concentration increases. That E_d only is present in the presence of MEG can be considered as evidence of MEG adsorption onto the metal surface.

Almost a similar behaviour of the polarization curve is observed when experiments were conducted in the presence of 1000 ppm acetic at different MEG concentrations, as shown in Figure II.4: Both the anodic and cathodic current density decrease and corrosion potential shifts toward the noble direction with increasing MEG concentration.

To distinguish the interrelationship of HAc and MEG on corrosion of carbon steel, polarisation curves were rearranged as shown in Figure II.5. In the absence of MEG, 1000 ppm of HAc results in an increased cathodic current density but the anodic

current density is reduced. The corrosion current density also increases in the presence of HAc. This indicates that HAc aggravates the carbon steel corrosion by accelerating the cathodic reaction. A peak, similar to E_d, is found in the anodic polarisation curve in the presence of HAc and without MEG. This indicates that undissociated HAc might also adsorb onto the surface. However, in the presence of 90 % MEG, the shape of the anodic curve is almost the same with or without HAc but the cathodic current density slightly increases in the presence HAc. This might indicate that the surface is saturated with MEG and, therefore, further adsorption by HAc is not possible. Therefore, the influence of HAc on carbon steel corrosion reduces drastically at 90% MEG solution.

Polarisation parameters were extracted from the curves shown in Figure II.3 and Figure II.4. Because the cathodic branches exhibit mass transfer controlled behaviour, only the anodic polarization curves were considered for Stern-Geary constant (*B*) as shown in Equation (II.2) [42].

$$B = \frac{b_a}{2.303} \tag{II.2}$$

where *B* is the Stern-Geary constant, V and b_a is the anodic Tafel slope, V.

Table II.1 illustrates the polarization parameters in the absence and the presence of HAc. *B* remained nearly 17-18 at all concentrations of MEG with or without HAc present. Though current density and corrosion rates decreased with MEG content, they exhibit relatively higher values in the presence of HAc indicating that HAc aggravates the corrosivity of the medium in spite of maintaining the constant pH. The inhibition efficiency of MEG shown in Table II.1 was calculated according to the following equation:

$$\eta\% = \frac{i^{\circ}_{\mathrm{corr}} - i_{\mathrm{corr}}}{i^{\circ}_{\mathrm{corr}}} \times 100 \tag{II.3}$$

where $i_{\mathrm{corr}}^{\circ}$ and i_{corr} are the corrosion current density in the absence and the presence of MEG, respectively.

Overall, the inhibition efficiency of MEG strongly relies on its concentration. At lower concentration (30%), MEG exhibits remarkably low efficiency in the presence of HAc (η = 43%) compared to its absence (η = 69%). However, when concentration exceeds 50%, the inhibition efficiency of MEG in the absence and in the presence of HAc is nearly same. This phenomena indicates that the corrosivity of HAc is significantly reduced when the concentration of MEG increases to 50% and above.

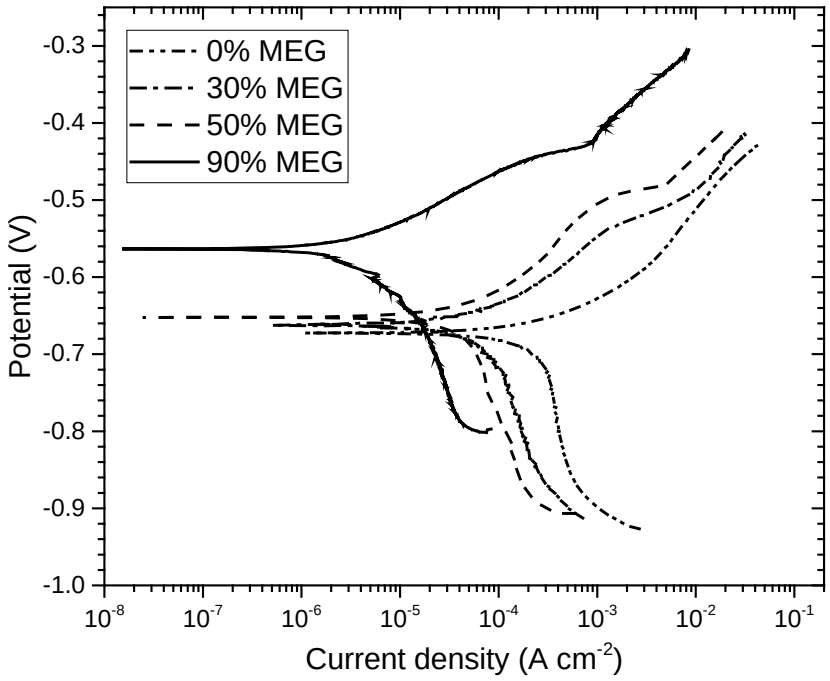

Figure II.3: Potentiodynamic polarization curves of carbon steel in different MEG contents in 3% NaCl solution saturated with CO_2 at 30 °C and pH 4.

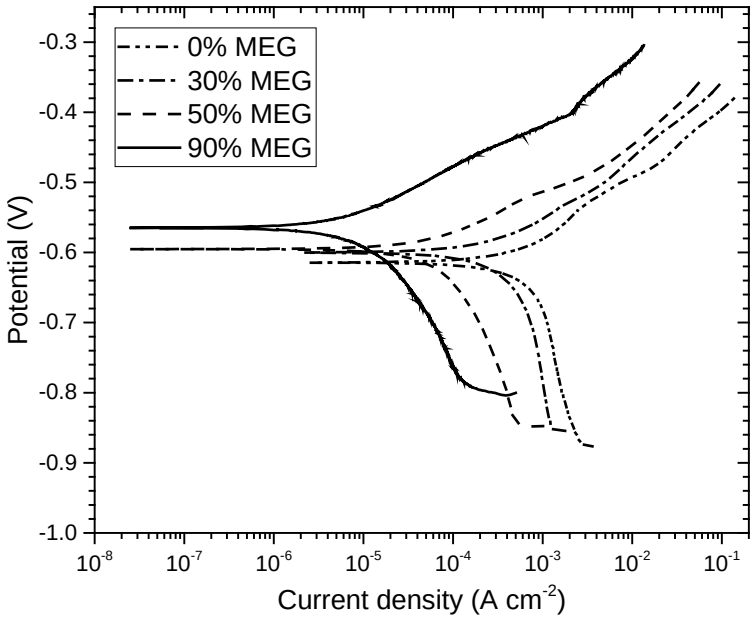

Figure II.4: Potentiodynamic polarization curves of carbon steel in different MEG content in 3% NaCl and 1000 ppm HAc solution saturated with CO_2 at 30 °C and pH 4.

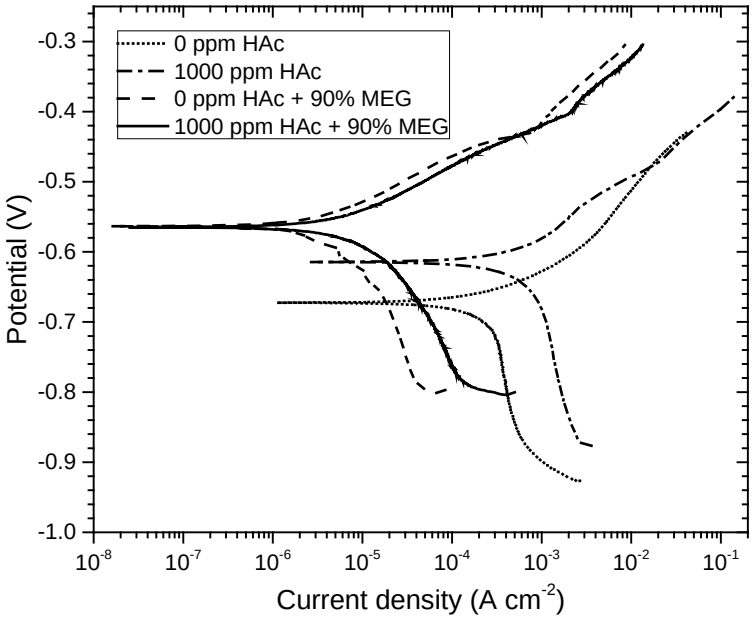

Figure II.5: Comparison of polarization curves of carbon steel in absence and presence of 1000 ppm acetic acid (HAc) and 90 wt.% MEG in 3% NaCl solution saturated with CO_2 at 30 °C and pH 4.

Table II.1: Polarization parameters and the corresponding inhibition efficiency of MEG in CO_2 saturated solution containing 3% NaCl at 30 °C and pH 4.

% of MEG	In the absence of HAc				In the presence of 1000 ppm HAc			
	i_{corr} µA cm^{-2}	B, mV	CR. mm y^{-1}	η, %	i_{corr} µA cm^{-2}	B, mV	CR. mm y^{-1}	η, %
0	130	16.1	1.51		294	18.12	3.41	
30	40	18.6	0.46	69	169	17.56	1.96	43
50	28	18.12	0.32	79	40	16.58	0.46	86
90	3	18.3	0.04	98	5	18.49	0.06	98

II.4.5.2 Linear polarization

Linear polarization was conducted to monitor the corrosion rate continuously after the stabilization of the OCP for 24 h to get a complete understanding on inhibition efficiency of MEG. Corrosion rate was calculated from the polarisation resistance using the *B* obtained from Table II.1 in each condition according to Equations (II.4) and (II.5) [43]:

$$i_{corr} = 10^6 \times \frac{B}{R_p} \tag{II.4}$$

$$CR = 3.27 \times 10^3 \frac{i_{corr}\,\mathrm{EW}}{\rho} \tag{II.5}$$

where i_{corr} is the corrosion current density in µA cm^{-2}, R_p is the polarisation resistance in ohm cm^2, *CR* is the corrosion rate in mm y^{-1}, EW is the equivalent weight of the corroding species which is 27.92 g and ρ is the density of the corroding material which is 7.87 g cm^{-3}.

Figure II.6 represents the corrosion rate in different MEG concentrations up to 24 h of immersion in the absence HAc. Corrosion rates gradually increased throughout the entire period in the absence of MEG. During this stage, selective dissolution of ferrite

occurs leaving lamellar cementite on the surface [1,44,45]. Cementite, being an electronic conductor, creates galvanic coupling with ferrite [46]. As a consequence, corrosion rates increase. However, when MEG is introduced in the system, corrosion rates do not increase with immersion time suggesting that MEG blocks either the cementite phase, or ferrite phase, or both, and suppresses the galvanic effect.

Figure II.7 presents the corrosion rates with time in the presence of 1000 ppm HAc and at different MEG concentrations. With the exception of 30% MEG, similar trends of corrosion rates are found when compared with Figure II.6. At 30% MEG, corrosion rates show an upward trend in the presence of HAc (Figure II.7) which is opposite in the absence of HAc (Figure II.6). That is why, inhibition efficiency of 30% MEG reported in Table 1 in the presence of HAc is drastically low.

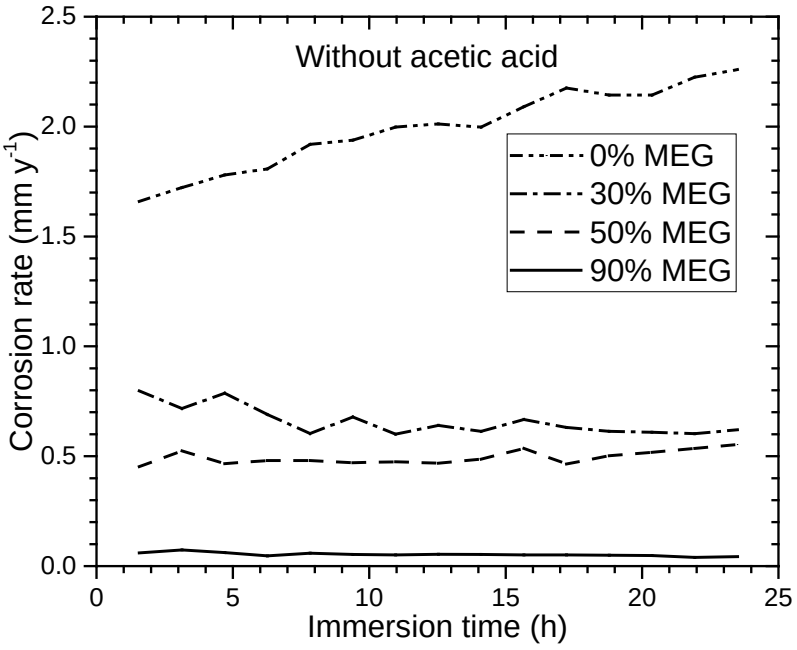

Figure II.6: Effect of MEG on corrosion of carbon steel for 24 h in 3% NaCl at 30 °C and pH 4. Corrosion rate was calculated from polarization resistance using the corresponding B values shown in Table II.1.

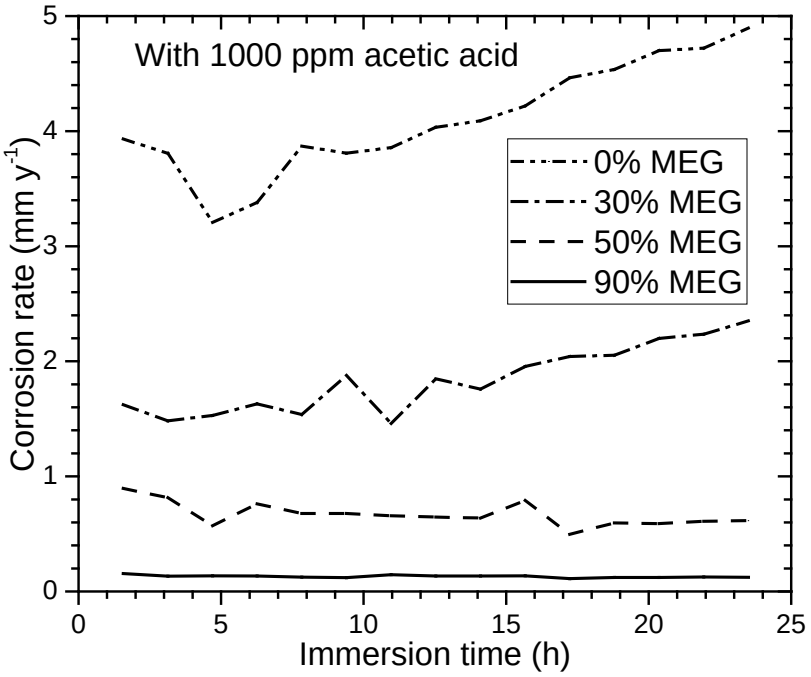

Figure II.7: Effect of MEG on corrosion of carbon steel in presence of 1000 ppm acetic acid for 24 h in 3% NaCl at 30 °C and pH 4. Corrosion rate was calculated from polarization resistance using the corresponding B values shown in Table II.1.

II.4.6 Electrochemical impedance spectroscopy (EIS) study

EIS is a powerful technique to investigate the corrosion phenomena as it provides information of reactions occurring at the metal-electrolyte interface by fitting the data with an appropriate equivalent circuit (EC). Figure II.8 represents both the Nyquist and Bode plots at different MEG contents in the absence of HAc after 24 h of immersion. The inset in Figure II.8a shows the full range of the curves. It is apparent that the Nyquist curves of 0 wt.% MEG consists of a depressed semicircle followed by an inductive loop at low frequency regions. The semicircle refers to the time constant of charge transfer and double-layer capacitance whereas the inductive loop originated due to the relaxation process of the adsorbed species at the electrode surface [47].

However, in the presence of MEG, the inductive loop is absent within the frequency range selected for this study which may suggest that interfacial processes have been modified. The diameter of the semicircle increases with increasing MEG

concentrations indicating an inhibition of charge transfer process. The phase angle presentation shown in Figure II.8c indicates that the characteristics frequency decreases and maximum phase angle increases with MEG content.

The Nyquist, Bode impedance and phase angle representations in the presence of HAc at different MEG contents after 24 h of immersion are shown in Figure II.9a, II.9b and II.9c, respectively. In the presence of HAc but without MEG, Nyquist curve shows two time constant as shown in Figure II.9a (inset). The presence of two time constants are also confirmed from the corresponding phase curves in Figure II.9c demonstrating the formation of a corrosion product layer or other adsorbed species that has capacitive behaviour at the surface. This layer does not provide corrosion protection since corrosion rate increased with time. However, when MEG was added in the HAc solution, the nature of the EIS curve changed, suggesting a change in the interfacial process because of the adsorption of MEG.

The equivalent circuit (EC), shown in Figure II.10a, was used to fit the EIS data of 0% MEG without HAc whereas all other data were fit with EC as shown in Figure II.10b. The fitting curves are shown with solid lines in Figure II.8 and II.9 and the corresponding fitting parameters are shown in Table II.2. R_S decreases whereas R_{CT} increases with increasing MEG content in the absence and the presence of 1000 ppm HAc. However, the value of R_{CT} in the absence of HAc is higher compared to that in its presence in all MEG concentrations indicating relatively higher corrosion rates in the presence of HAc. The results are in good agreement with LPR and potentiondynamic experiments. Similarly, the capacitance of the double layer decreases with increasing MEG concentrations in the absence and the presence of HAc. The decrease in capacitance is caused by replacing high dielectric water molecule from the surface by relatively lower dielectric MEG molecules [48]. Therefore, the decrease in double layer capacitance is another indication of an adsorption of MEG on the surface [28].

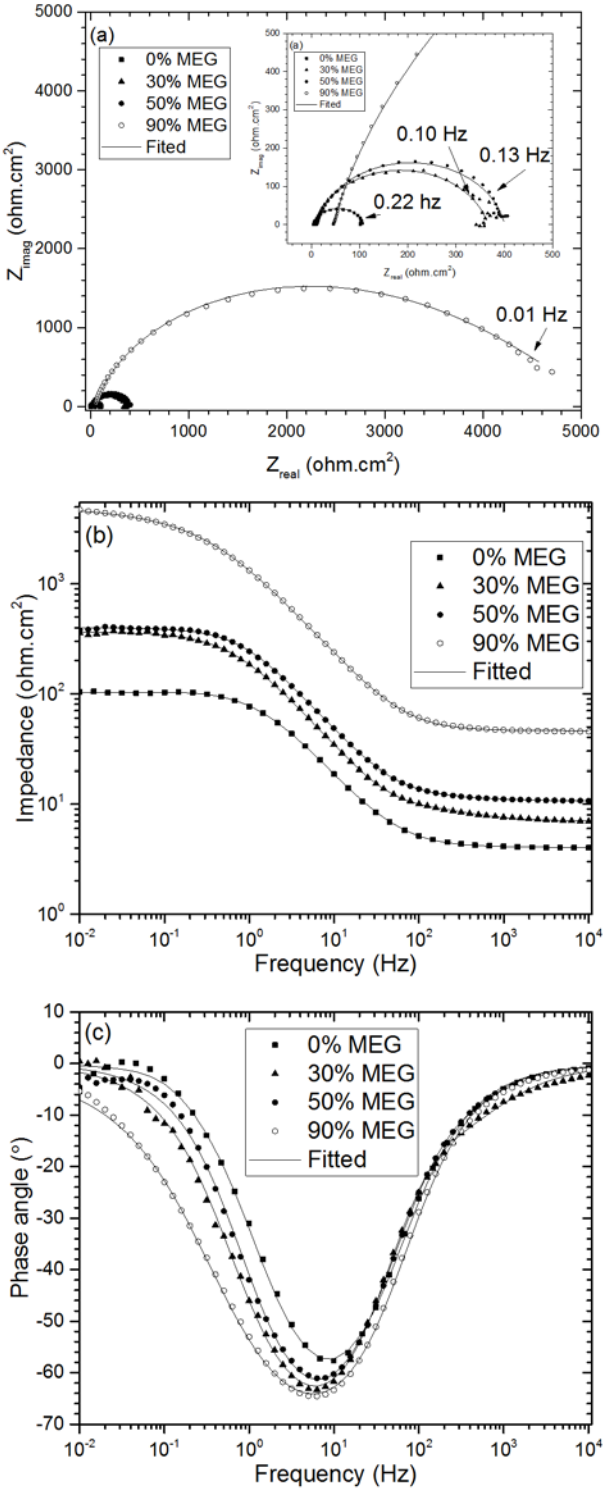

Figure II.8: Comparison of EIS curves in different MEG content in 3% NaCl at 30 °C temperature and pH 4 a) Nyquist plots and b) & c) Bode plots.

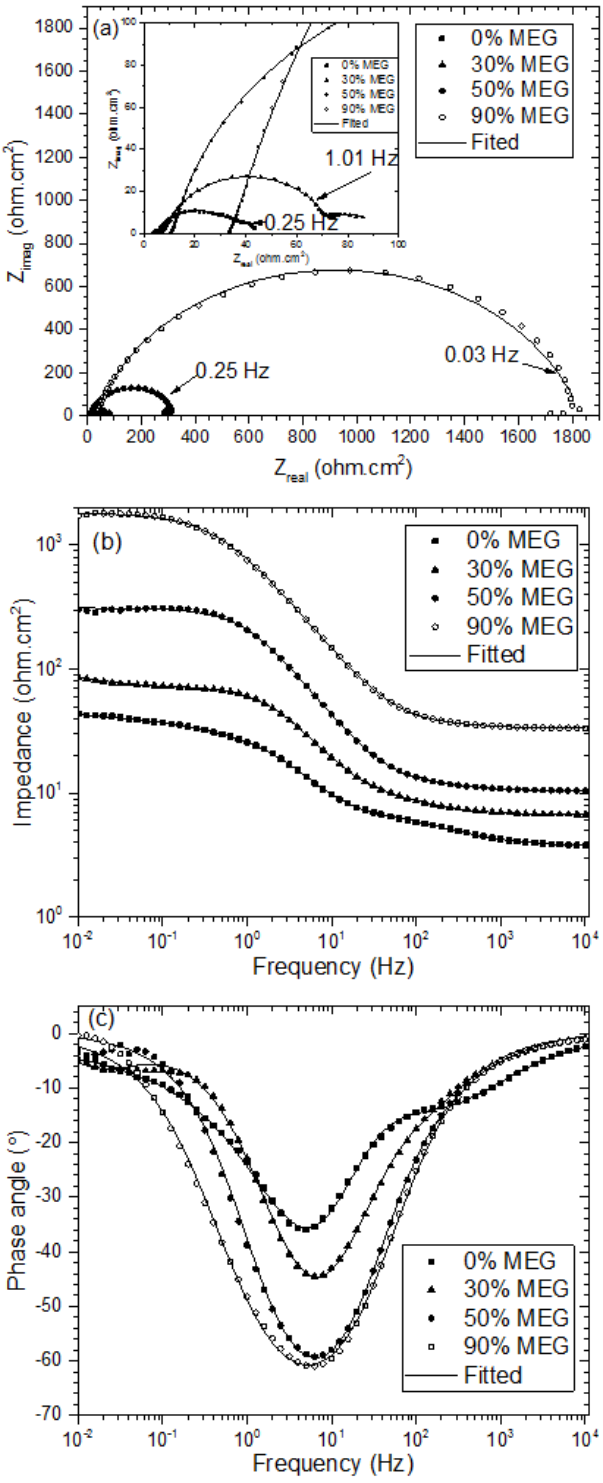

Figure II.9: Comparison of EIS curves in different MEG content in presence of 1000 ppm HAc in 3% NaCl at 30 °C and pH 4 a) Nyquist plots and b) & c) Bode plots.

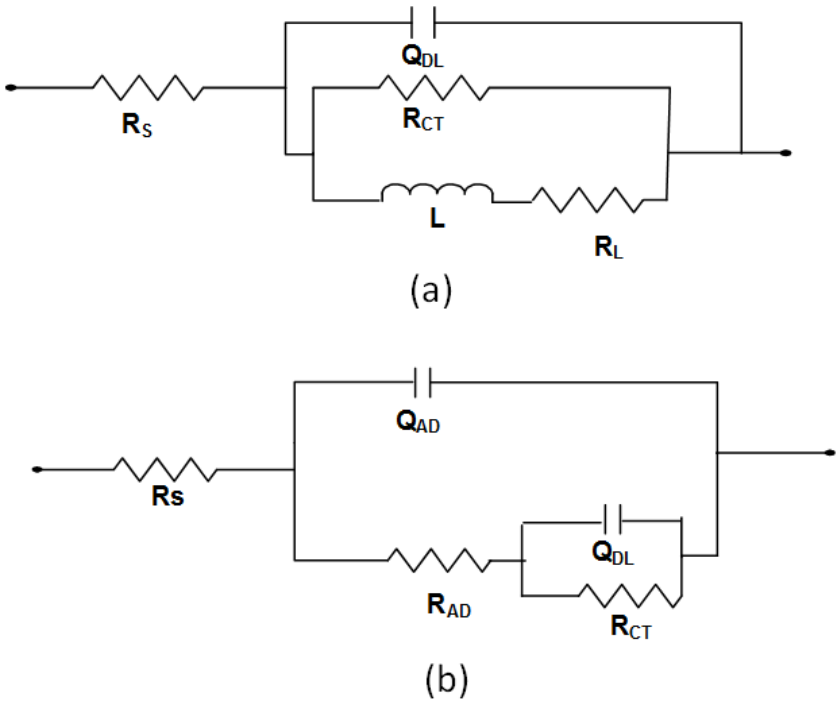

Figure II.10: Equivalent circuit to fit the EIS data; R_S is the solution resistance, R_{CT} is the of charge transfer resistance, L is the inductance, R_L is the resistance of the inductor, R_{AD} is the resistance of adsorbed layer, Q_{DL} and Q_{AD} are the constant phase element presenting the double layer capacitance and capacitance of the adsorbed layer respectively.

Table II.2: Comparison of EIS parameters in absence and in presence of HAc at different MEG content at 30 °C and pH 4.

% of MEG	In the absence of HAc			In the presence of HAc		
	R_S ohm cm^2	R_{CT} ohm cm^2	C_{DL} µF cm^{-2}	R_S ohm cm^2	R_{CT} ohm cm^2	C_{DL} µF cm^{-2}
0	4	104	1182	4	33	1143
30	7	353	185	7	58	331
50	11	385	156	10	294	208
90	46	5250	33	34	1796	188

II.5 Conclusions

- The dissociation constant of HAc increases with MEG concentration and temperature.
- MEG inhibits the corrosion of carbon steel by adsorbing and subsequently blocking the active sites. It also hinders the galvanic effect between ferrite and cementite phase. However, inhibition efficiency of MEG has strong dependency on its concentration.
- HAc aggravates the CO_2 corrosion of carbon steel. However, its activity decreases significantly with increasing MEG concentration.
- EIS also indicates the adsorption of MEG on the surface. Double layer capacitance decreases with increasing MEG content indicating that MEG replaces water molecules at the surface and occupies the area itself, thus suppress the availability of species susceptible for the reduction reaction.

II.6 References

[1] M.M. Islam, T. Pojtanabuntoeng, R. Gubner, Condensation corrosion of carbon steel at low to moderate surface temperature and iron carbonate precipitation kinetics, Corros. Sci. 111 (2016) 139–150.

[2] C. de Waard, U. Lotz, D.E. Milliams, Predictive model for CO_2 corrosion engineering in wet natural gas pipelines, Corrosion. 47 (1991) 976–985.

[3] S. Peng, Z. Zeng, An experimental study on the internal corrosion of a subsea multiphase pipeline, Petroleum. 1 (2015) 75–81.

[4] Y.M. Gunaltun, D. Larrey, Correlation of cases of top of line corrosion with calculated water condensation rates, CORROSION/2000, Paper No.00071, NACE, Houston, Texas, 200.

[5] P.C. Okafor, S. Nesic, Effect of acetic acid on CO_2 corrosion of carbon steel in vapor-water two-phase horizontal flow, Chem. Eng. Commun. 194 (2007) 141–157.

[6] T. Tran, B. Brown, S. Nesic, B. Tribollet, Investigation of the electrochemical mechanisms for acetic acid corrosion of mild steel, Corrosion. 70 (2013) 223–229.

[7] G.A. Zhang, Y.F. Cheng, Corrosion of X65 steel in CO_2-saturated oilfield formation water in the absence and presence of acetic acid, Corros. Sci. 51 (2009) 1589–1595.

[8] J. Amri, E. Gulbrandsen, R.P. Nogueira, The effect of acetic acid on the pit propagation in CO_2 corrosion of carbon steel, Electrochem. Commun. 10 (2008) 200–203.

[9] S.D. Zhu, A.Q. Fu, J. Miao, Z.F. Yin, G.S. Zhou, J.F. Wei, Corrosion of N80 carbon steel in oil field formation water containing CO_2 in the absence and presence of acetic acid, Corros. Sci. 53 (2011) 3156–3165.

[10] Z. Jia, X. Li, C. Du, Z. Liu, J. Gao, Effect of acetic acid on CO_2 corrosion of 3Cr low-alloy steel, Mater. Chem. Phys. 132 (2011) 258–263.

[11] G.A. Zhang, Y.F. Cheng, On the fundamentals of electrochemical corrosion of X65 steel in CO_2-containing formation water in the presence of acetic acid in petroleum production, Corros. Sci. 51 (2009) 87–94.

[12] M.H. Nazari, S.R. Allahkaram, The effect of acetic acid on the CO_2 corrosion of grade X70 steel, Mater. Des. 31 (2010) 4290–4295.

[13] E. Gulbrandsen, K. Bilkova, Solution chemistry effects on corrosion of carbon steels in presence of CO_2 and acetic acid, CORROSION/2006, Paper No. 06364, NACE, Houston, Texas, 2006.

[14] J.L. Crolet, N. Thevenot, A. Dugstad, Role of free acetic acid on the CO_2 corrosion of steels, CORROSION/99, Paper No. 24, NACE, Houston, Texas, 1999.

[15] D. Hinkson, Z. Zhang, M. Singer, S. Nesic, Chemical composition and corrosiveness of the condensate in top-of-the-line corrosion, Corrosion. 66 (2010) 045002–045008.

[16] M. Wu, S. Wang, H. Liu, A study on inhibitors for the prevention of hydrate formation in gas transmission pipeline, J. Nat. Gas Chem. 16 (2007) 81–85.

[17] F. Ning, L. Zhang, Y. Tu, G. Jiang, M. Shi, Gas-hydrate formation, agglomeration and inhibition in oil-based drilling fluids for deep-water drilling, J. Nat. Gas Chem. 19 (2010) 234–240.

[18] B.A. Stefl, S.F. Bosen, Buffering and inhibition of glycol in gas dehydration applications: an alternative to amines, Corrosion. 53 (1997) 163–168.

[19] K. AlHarooni, A. Barifcani, D. Pack, R. Gubner, V. Ghodkay, Inhibition effects of thermally degraded MEG on hydrate formation for gas systems, J. Pet. Sci. Eng. 135 (2015) 608–617.

[20] M. Javidi, M. Khodaparast, Inhibitive performance of monoethylene glycol on CO_2 corrosion of API 5L X52 steel, J. Mater. Eng. Perform. 24 (2015) 1417–1427.

[21] T. Pojtanabuntoeng, M. Salasi, R. Gubner, The influence of mono ethylene glycol on CO_2 corrosion of carbon steel at elevated temperature (80-120 °C), CORROSION/2014, Paper No. 4176, NACE, Houston,Texas, 2014.

[22] J. Kvarekvål, A. Pedersen, An electrochemical study of corrosion inhibition of carbon steel in sour glycol solutions, CORROSION/2013, Paper No. 2447, NACE , Houston, Texas, 2013.

[23] A. Sherik, A. Lewis, A. Rasheed, A. Jabran, Effect of triethylene glycol on corrosion of carbon steel in H_2S, CO_2 and O_2 environments, CORROSION/2010, Paper No. 10188, NACE, Houston, Texas, 2010.

[24] E. Samiento-Bustos, J.G. González-Rodriguez, J. Uruchurtu, V.M. Salinas-Bravo, Corrosion behavior of iron-based alloys in the LiBr+ethylene glycol+H_2O mixture, Corros. Sci. 51 (2009) 1107–1114.

[25] S. Guo, F. Farelas, M. Singer, Effect of monoethylene glycol on sweet top of the line corrosion, CORROSION/2016, Paper No. 7891, NACE, Houston, Texas, 2016.

[26] G. Svenningsen, R. Nyborg, Modeling of top of line corrosion with organic acid and glycol, CORROSION/2014, Paper No. 4057, NACE, Texas, 2014.

[27] E. Gulbrandsen, J. Morard, Why does glycol inhibit CO_2 corrosion?, CORROSION/98, Paper No. 98221, NACE, Houston, Texas, 1998.

[28] T. Pojtanabuntoeng, B. Kinsella, H. Ehsani, J. McKechnie, Assessment of corrosion control by pH neutralisation in the presence of glycol at low temperature, Corros. Sci. (2017).

[29] I. Ivonye, C. Wang, X. Hu, A. Neville, Corrosion study of carbon steel in the presence of monoethylene glycol (MEG) and corrosion inhibitors in acid, CORROSION/2013, Paper No. 2349, NACE, Houston, Texas, 2013.

[30] H. Lu, A. Kan, M. Tomson, Effects of monoethylene glycol on carbonate equilibrium and calcite solubility in gas/monoethylene glycol/nacl/water mixed systems, SPE J. (2010) 714–725.

[31] E. Flaten, G. Watterud, J.-P. Andreassen, M. Seiersten, Precipitation of iron and calcium carbonate in pipelines at varying meg contents, SPE Int. Oilf. Scale Conf/2008, Society of Petroleum Engineers, Aberdeen, UK, 2008.

[32] A. Kahyarian, B. Brown, S. Nesic, Mechanism of cathodic reactions in acetic acid corrosion of iron and mild steel, Corrosion. 72 (2016) 1539–1546.

[33] J. Reijenga, A. van Hoof, A. van Loon, B. Teunissen, Development of methods for the determination of pKa values, Anal. Chem. Insights. 8 (2013) 53–71.

[34] K. Sarmini, E. Kenndler, Ionization constants of weak acids and bases in organic solvents, J. Biochem. 38 (1999) 123–137.

[35] E.J. Cohn, F.F. Heyroth, M.F. Menkin, V. 50, E.J. Cohn, F.F. Heyroth, et al., The dissociation constant of acetic acid and the solutions' activity coefficients of the ions in certain acetate, J. Am. Chem. Soc. 50 (1928) 696–714.

[36] Y.A. Fadeeva, L.P. Safonova, Dissociation constant of acetic acid in (n,n-

dimethylformamide + water) mixtures at the temperature 298.15 K, J. Solut. Chem. 40 (2011) 980–988.

[37] P.M. Shanbhag, R.C. Bates, Dissociation constants of acetic acid and protonated tris(hydroxymethyl)-aminomethane in 80 mass% 2-methoxyethanol/20 mass % water in the range 10 to 50°, Bull. Des Sociétés Chim. Belges. 90 (2010) 1–7.

[38] K. Sandengen, B. Kaasa, T. Østvold, pH measurements in monoethylene glycol (MEG) + water solutions, Ind. Eng. Chem. Res. 46 (2007) 4734–4739.

[39] G. Gran, Determination of the equivalence point in potentiometric titrations. Part II, Analyst. 77 (1952) 661–671.

[40] G. Gusmano, P. Labella, G. Montesperelli, Study of the inhibition mechanism of imidazolines by electrochemical impedance spectroscopy, Corrosion. 62 (2006) 576–583.

[41] F. Bentiss, M. Outirite, M. Traisnel, H. Vezin, M. Lagrenée, B. Hammouti, Improvement of corrosion resistance of carbon steel in hydrochloric acid medium by 3 , 6-bis (3-pyridyl) pyridazine, Int. J. Electrochem. Sci. 7 (2012) 1699–1723.

[42] ASTM G102 − 89, Standard practice for calculation of corrosion rates and related information from electrochemical measurements, in: Annu. B. ASTM Stand., ASTM International, 2010.

[43] ASTM G59-97, Standard test method for conducting potentiodynamic polarization resistance measurements, in: Annu. B. ASTM Stand., ASTM International, 2009.

[44] F. Farelas, M. Galicia, B. Brown, S. Nesic, H. Castaneda, Evolution of dissolution processes at the interface of carbon steel corroding in a CO_2 environment studied by EIS, Corros. Sci. 52 (2010) 509–517.

[45] J.L. Mora-Mendoza, S. Turgoose, Fe_3C influence on the corrosion rate of

mild steel in aqueous CO_2 systems under turbulent flow conditions, Corros. Sci. 44 (2002) 1223–1246.

[46] J.L. Crolet, N. Thevenot, S. Nesic, Role of conductive corrosion products in the protectiveness of corrosion layers, Corrosion. 54 (1998) 194–203.

[47] P. Li, T.C. Tan, J.Y. Lee, Impedance spectra of the anodic dissolution of mild steel in sulfuric acid, Corros. Sci. 38 (1996) 1935–1955.

[48] M.N. Khomami, I. Danaee, A.A. Attar, M. Peykari, Kinetic and thermodynamic studies of AISI 4130 steel alloy corrosion in ethylene glycol-water mixture in presence of inhibitors, Met. Mater. Int. 19 (2013) 453–464.

Bibliography

Abdel-Rehim, S.S., Khaled, K.F. & Abd-Elshafi, N.S., 2006. Electrochemical frequency modulation as a new technique for monitoring corrosion inhibition of iron in acid media by new thiourea derivative. *Electrochimica Acta*, 51(16), pp.3269–3277.

Ajayi, F. & Lyon, S., 2014. Efficiency of volatile corrosion inhibitors in wet gas pipelines. In *CORROSION 2014*. Houston, Texas: NACE International, Paper No. 4236.

AlHarooni, K. et al., 2015. Inhibition effects of thermally degraded MEG on hydrate formation for gas systems. *Journal of Petroleum Science and Engineering*, 135, pp.608–617.

Altoé, P. et al., 1996. Evaluation of oilfield corrosion inhibitors in CO_2 containing media: A kinetic study. *Electrochimica Acta*, 41(7–8), pp.1165–1172.

Álvarez-Bustamante, R. et al., 2009. Electrochemical study of 2-mercaptoimidazole as a novel corrosion inhibitor for steels. *Electrochimica Acta*, 54(23), pp.5393–5399.

Alves, V.A. & Brett, C.M.A., 2002. Characterisation of passive films formed on mild steels in bicarbonate solution by EIS. *Electrochimica Acta*, 47(13), pp.2081–2091.

Amri, J., Gulbrandsen, E. & Nogueira, R.P., 2008. The effect of acetic acid on the pit propagation in CO_2 corrosion of carbon steel. *Electrochemistry Communications*, 10(2), pp.200–203.

Asher, S. et al., 2012. Top of the line corrosion prediction in wet gas pipelines. In *CORROSION 2012*. Houston, Texas : NACE, Paper No. C2012-0001303.

ASTM G102 − 89, 2010. Standard practice for calculation of corrosion rates and related information from electrochemical measurements. In *Annual Book of ASTM Standard*, (Reapproved 2010). ASTM International..

ASTM G1 − 03, 2011. Standard practice for preparing , cleaning , and evaluating corrosion test. In *Annual Book of ASTM Standard*. ASTM International.

ASTM G59-97, 2009. Standard test method for conducting potentiodynamic

polarization resistance measurements. In *Annual Book of ASTM Standard*. ASTM International.

Bai, Z.Q. et al., 2006. Analysis of EIS characteristics of CO2 corrosion of well tube steels with corrosion scales. *Applied Surface Science*, 252(20), pp.7578–7584.

Bavarian, B., Zhang, J., et al., 2015. Comparison of the corrosion protection effectiveness of vapor corrosion inhibitor and nitrogen blanketing system. In *CORROSION 2015*. Houston, Texas: NACE, Paper No.5450.

Bavarian, B., Ikder, Y., et al., 2015. Comparison of the corrosion protection effectiveness of vapor corrosion inhibitors and dry air system. In *CORROSION 2015*. Houston, Texas: NACE. Paper No.5449.

Bentiss, F. et al., 2012. Improvement of corrosion resistance of carbon steel in hydrochloric acid medium by 3 , 6-bis (3-pyridyl) pyridazine. *International Journal of Electrochemical Science*, 7, pp.1699–1723.

Berntsen, T., Seiersten, M. & Hemmingsen, T., 2013. Effect of $FeCO_3$ Supersaturation and Carbide Exposure on the CO_2 Corrosion Rate of Carbon Steel. *Corrosion*, 69(6), pp.601–613.

Bi, X.-X. et al., 1993. Nanocrystalline α–Fe, Fe_3C, and Fe_7C_3 produced by CO_2 laser pyrolysis. *Journal of Materials Research*, 8(7), pp.1666–1674.

Bonis, M., 2009. Form Sweet to sour TLC: what's different? In *2nd International TLC Conference*. Bangkok, p. PTTEP, 2009.

Bosch, R.W., 2001. Electrochemical frequency modulation: a new electrochemical technique for online corrosion monitoring. *Corrosion*, 57(1), pp.60–70.

Bosch, R.W. & Bogaerts, W.F., 1996. Instantaneous corrosion rate measurement with small-amplitude potential intermodulaton techniques. *Corrosion Science*, 52(3), pp.204–212.

Cattanach, K., Ramachandran, S. & Jovancicevic, V., 2011. A new methodology for monitoring corrosion under sales gas conditions using the quartz crystal

microbalance. In *CORROSION 2011*. Houston, Texas: NACE, Paper No 11085.

Chen, Y. et al., 2011. Effects of temperature on CO_2 top of line corrosion of pipeline steel. In *CORROSION 2011*. Houston, Texas: NACE, Paper No. 11327.

Cohn, E.J. et al., 1928. The dissociation constant of acetic acid and the solutions' activity coefficients of the ions in certain acetate. *Journal of American Chemical society*, 50(3), pp.696–714.

Crolet, J.L., 1993. Protrctiveness of Corrosion Layers. In K. R. Trethewey & P. R. Roberge, eds. *Modelling Aqueous Corrosion From Individual Pits to System Management*. London: Kluwer Academic Publishers, pp. 1–28.

Crolet, J.L., Thevenot, N. & Dugstad, A., 1999. Role of free acetic acid on the CO_2 corrosion of steels. In *CORROSION 99*. Houston, Texas: NACE, Paper No. 24.

Crolet, J.L., Thevenot, N. & Nesic, S., 1998. Role of conductive corrosion products in the protectiveness of corrosion layers. *Corrosion*, 54(3), pp.194–203.

Dugstad, A., 1998. Mechanism of protective film formation during CO_2 corrosion of carbon steel. In *CORROSION 98*. Houston, Texas: NACE, Paper No. 31.

Dugstad, A., 2014. Top of line corrosion- impact of MEG and organic acid in the gas phase. In *CORROSION 2014*. Houston, Texas: NACE, Paper No. 4382.

Dugstad, A. & Dronen, P.-E., 1999. Efficient corrosion control of gas condensate pipelines by pH-stabilisation. In *CORROSION 99*. Houston, Texas: NACE, Paper No. 20.

Eliyan, F.F. & Alfantazi, A., 2014. On the theory of CO_2 corrosion reactions - investigating their interrelation with the corrosion products and API-X100 steel microstructure. *Corrosion Science*, 85, pp.380–393.

Eliyan, F.F., Mahdi, E.S. & Alfantazi, A., 2012. Electrochemical evaluation of the corrosion behaviour of API-X100 pipeline steel in aerated bicarbonate solutions. *Corrosion Science*, 58, pp.181–191.

Estavoyer, M., 1981. Corrosion problems at Lack sour gas field. In *H_2S corrosion in*

oil and gas production. Houston, Texas: NACE, p. 905.

Fadeeva, Y.A. & Safonova, L.P., 2011. Dissociation constant of acetic acid in (n,n-dimethylformamide + water) mixtures at the temperature 298.15 K. *Journal Solution Chemistry*, 40, pp.980–988.

Farelas, F. et al., 2010. Evolution of dissolution processes at the interface of carbon steel corroding in a CO_2 environment studied by EIS. *Corrosion Science*, 52(2), pp.509–517.

Farelas, F. & Ramirez, A., 2010. Carbon dioxide corrosion inhibition of carbon steels through bis-imidazoline and imidazoline compounds studied by EIS. *International Journal of Electrochemical Science*, 5, pp.797–814.

Flaten, E. et al., 2008. Precipitation of iron and calcium carbonate in pipelines at varying meg contents. In *Proceedings of SPE International Oilfield Scale Conference*. Aberdeen, UK: Society of Petroleum Engineers, pp. 1–9.

Fosbøl, P., Thomsen, K. & Stenby, E., 2009. Improving mechanistic CO_2 corrosion models. In *CORROSION 2009*. Houston, Texas: NACE, Paper No. 9561.

Gao, M., Pang, X. & Gao, K., 2011. The growth mechanism of CO_2 corrosion product films. *Corrosion Science*, 53(2), pp.557–568.

Gran, G., 1952. Determination of the equivalence point in potentiometric titrations. part 11. *Analyst*, 77, pp.661–671.

Gulbrandsen, E. & Bilkova, K., 2006. Solution chemistry effects on corrosion of carbon steels in presence of CO_2 and acetic acid. In *CORROSION 2006*. Houston, Texas: NACE, Paper No. 06364.

Gulbrandsen, E. & Bilkova, K., 2006. Solution chemistry effects on corrosion of carbon steels in presence of CO_2 and acetic acid. In *CORROSION 2006*. Houston, Texas: NACE, Paper No. 06364.

Gulbrandsen, E. & Morard, J., 1998. why does glycol inhibit CO_2 corrosion? In *CORROSION 98*. Houston, Texas: NACE, Paper No. 98221.

Gunaltun, Y., Kaewpradap, U., et al., 2010. Progress in the prediction of top of the line corrosion and challenges to predict orrosion rates measured in gas pipelines. In *CORROSION 2010*. Houston, Texas: NACE, Paper No. 10093.

Gunaltun, Y., Punpruk, S., et al., 2010. Worst case top of the line corrosion: cold spot corrosion. In *CORROSION 2010*. Houston, Texas: NACE, Paper No. 10097.

Gunaltun, Y. et al., 2010. Laboratory testing of volatile corrosion inhibitors. In *CORROSION 2010*. Houston, Texas: NACE, Paper No. 10095.

Gunaltun, Y. & Belghazi, A., 2001. Control of top of the line corrosion by chemical treatment. In *CORROSION 2001*. Houston, Texas: NACE, Paper No. 01033.

Gunaltun, Y.M. & Larrey, D., 2000. Correlation of cases of top of line corrosion with calculated water condensation rates. In *CORROSION 2000*. Houston, Texas: NACE, Paper No.00071.

Gunaltun, Y.M., Supriyatman, D. & Achmad, J., 1999. Top of line corrosion in multiphase gas lines. A case history. In *CORROSION 99*. NACE, Paper No. 36.

Guo, S. et al., 2012. Corrosion of alloy steels containing 2% chromium in CO_2 environments. *Corrosion Science*, 63, pp.246–258.

Guo, S., Farelas, F. & Singer, M., 2017. A glycol/water co-condensation model to investigate the influence of monoethylene glycol on top-of-the-line corrosion. *Corrosion*, 73(6), pp.742–755.

Guo, S., Farelas, F. & Singer, M., 2016. Effect of monoethylene glycol on sweet top of the line corrosion. In *CORROSION 2016*. Houston, Texas: NACE, Paper No. 7891.

Gusmano, G., Labella, P. & Montesperelli, G., 2006. Study of the inhibition mechanism of imidazolines by electrochemical impedance spectroscopy. *Corrosion*, 62(7), pp.576–583.

Han, J., Brown, B.N. & Nesic, S., 2010. Investigation of the galvanic mechanism for

localized carbon dioxide corrosion propagation using the artificial pit technique. *Corrosion*, 66(9), pp.95003–12.

Han, L. & Song, S., 2008. A measurement system based on electrochemical frequency modulation technique for monitoring the early corrosion of mild steel in seawater. *Corrosion Science*, 50(6), pp.1551–1557.

Hanesch, M., 2009. Raman spectroscopy of iron oxides and (oxy)hydroxides at low laser power and possible applications in environmental magnetic studies. *Geophysical Journal International*, 177(3), pp.941–948.

Hinkson, D. et al., 2008. A study of the chemical composition and corrosivity of the condensate in top of the line corrosion. In *CORROSION 2008*. Houston, Texas: NACE, Paper No. 08466.

Hinkson, D. et al., 2010. Chemical composition and corrosiveness of the condensate in top-of-the-line corrosion. *Corrosion*, 66(4), pp.045002–045008.

Hirschorn, B. et al., 2010. Determination of effective capacitance and film thickness from constant-phase-element parameters. *Electrochimica Acta*, 55(21), pp.6218–6227.

Hoda, E., 2013. *Influence of Monoethylene Glycol (MEG) on the corrosion inhibition of wet-gas flow lines*. Perth, Australia: Curtin University.

Hsu, C.H. & Mansfeld, F., 2001. Technical note : Concerning the conversion of the constant phase element parameter Y_0 into a capacitance. *Corrosion*, 57(9), pp.747–748.

Hunnik, E.W.J. van, Pots, B.F.M. & Hendriksen, E.L.J.A., 1996. The formation of protective $FeCO_3$ corrosion product layer in CO_2 corrosion. In *CORROSION 1996*. Houston, Texas: NACE, Paper No. 6.

Islam, M.M., Gubner, R. & Pojtanabuntoeng, T., 2017. Development of an electrochemical method to study top-of-the-line corrosion. In *CORROSION 2017*. Houston Texas: NACE, Paper No. 9106.

Islam, M.M., Pojtanabuntoeng, T. & Gubner, R., 2016. Condensation corrosion of carbon steel at low to moderate surface temperature and iron carbonate precipitation kinetics. *Corrosion Science*, 111, pp.139–150.

Ivonye, I. et al., 2013. Corrosion study of carbon steel in the presence of monoethylene glycol (MEG) and corrosion inhibitors in acid. In *CORROSION 2013*. Houston, Texas: NACE, Paper No. 2349.

Javidi, M. & Khodaparast, M., 2015. Inhibitive performance of monoethylene glycol on CO_2 corrosion of API 5L X52 steel. *Journal of Materials Engineering and Performance*, 24(4), pp.1417–1427.

Jevremovic, I. et al., 2012. A novel method to mitigate the top-of-the-line corrosion in wet gas pipelines by corrosion inhibitor within a foam matrix. *Corrosion*, 69(2), pp.186–192.

Jevremović, I. et al., 2015. Evaluation of a novel top-of-the-line corrosion (TLC) mitigation method in a large-scale flow loop. *Corrosion*, 71(3), pp.389–397.

Jevremović, I. et al., 2013. Evaluation of a novel top-of-the-line corrosion (TLC) mitigation method in a large scale flow loop. In *CORROSION 2013*. Houston, Texas: NACE, Paper No. 2321.

Jia, Z. et al., 2011. Effect of acetic acid on CO_2 corrosion of 3Cr low-alloy steel. *Materials Chemistry and Physics*, 132, pp.258–263.

John, D. et al., 2009. Top of the line corrosion control by chemical treatment. In *CORROSION 2009*. Houston, Texas: NACE, Paper No. 09286.

John R. Scully, Corrosion is a Global Issue. *Corrosion*. Available at: http://corrosionjournal.org/page/specialfeatures?code=nace-prem-site [Accessed July 19, 2017].

Johnson, M.L. & Tomson, M.B., 1991. Ferrous carbonate precipitation kinetics and its impact on CO_2 corrosion. In *CORROSION/91*. Houston, Texas: NACE, Paper No. 268.

Joosten, M. et al., 2010. Top-of-Line Corrosion – A Field Failure. In *EuroCorr 2010*. Moscow, Russia, 13-17 September 2010: Gubkin Russian State University of Oil and Gas, Paper No. 9524.

Juttner, K., 1990. Electrochemical impedance spectroscopy (EIS) of corrosion processes on inhomogeneous surfaces. *Electrochimica Acta*, 35(10), pp.1501–1508.

Kaewpradap, U., 2015. Top of the line corrosion field case. In *Top of the line corrosion conference 2015*. Jakarta, Indonesia: NACE, July 27-29, 2015.

Kahyarian, A., Brown, B. & Nesic, S., 2016. Mechanism of cathodic reactions in acetic acid corrosion of iron and mild steel. *Corrosion*, 72(12), pp.1539–1546.

Khomami, M.N. et al., 2013. Kinetic and thermodynamic studies of AISI 4130 steel alloy corrosion in ethylene glycol-water mixture in presence of inhibitors. *Metals and Materials International*, 19(3), pp.453–464.

Kinsella, B., Tan, Y.J. & Bailey, S., 1998. Electrochemical impedance spectroscopy and surface characteriztion techniques to study carbon dioxide corrosion product scales. *Corrosion*, 54(10), p.835.

Kuş, E. & Mansfeld, F., 2006. An evaluation of the electrochemical frequency modulation (EFM) technique. *Corrosion Science*, 48, pp.965–979.

Kvarekvål, J. & Pedersen, A., 2013. An electrochemical study of corrosion inhibition of carbon steel in sour glycol solutions. In *CORROSION 2013*. Houston, Texas: NACE, Paper No. 2447.

Lee, C.T., Odziemkowski, M.S. & Shoesmith, D.W., 2006. An in situ Raman-electrochemical investigation of carbon steel corrosion in Na_2CO_3/$NaHCO_3$, Na_2SO_4, and NaCl solutions. *Journal of the Electrochemical Society*, 153(2), pp.B33–B41.

Lehmann, M.N. et al., 2014. Corrosion inhibitor and oxygen scavenger for use as meg additives in the inhibition of wet gas pipelines. In *Offshore Technology*

Conference. Kuala Lumpur: pp. 1–20.

Li, P., Tan, T.C. & Lee, J.Y., 1996. Impedance spectra of the anodic dissolution of mild steel in sulfuric acid. *Corrosion Science*, 38(11), pp.1935–1955.

Linter, B.R. & Burstein, G.T., 1999. Reactions of pipeline steels in carbon dioxide solutions. *Corrosion Science*, 41(1), pp.117–139.

López, D.A., Simison, S.N. & de Sánchez, S.R., 2003. The influence of steel microstructure on CO_2 corrosion. EIS studies on the inhibition efficiency of benzimidazole. *Electrochimica Acta*, 48(7), pp.845–854.

Lu, H., Kan, A. & Tomson, M., 2010. Effects of monoethylene glycol on carbonate equilibrium and calcite solubility in gas/monoethylene glycol/NaCl/water mixed systems. *SPE Journal*, (September), pp.714–725.

Mansfeld, F., 1990. Electrochemical impedance spectroscopy (EIS) as a new tool for investigating methods of corrosion protection. *Electrochimica Acta*, 35(10), pp.1533–1544.

Mendez, C. et al., 2005. Effect of acetic acid, ph and meg on the CO_2 top of the line corrosion. In *CORROSION 2005*. Houston, Texas: NACE, Paper No. 05278.

Mora-Mendoza, J.L. & Turgoose, S., 2002. Fe_3C influence on the corrosion rate of mild steel in aqueous CO_2 systems under turbulent flow conditions. *Corrosion Science*, 44(6), pp.1223–1246.

Nazari, M.H. & Allahkaram, S.R., 2010. The effect of acetic acid on the CO_2 corrosion of grade X70 steel. *Materials & Design*, 31(9), pp.4290–4295.

Nesic, S. et al., 2001. A mechanistic model for CO_2 corrosion with protective iron carbonate films. In *CORROSION 2001*. Houston, Texas: NACE, Paper No. 1040.

Nesic, S. et al., 1996. Electrochemical properties of iron dissolution in the presence of CO_2 - Basic revisited. In *CORROSION 96*. Houston, Texas: NACE, Paper No 3.

Nesic, S., 2007. Key issues related to modelling of internal corrosion of oil and gas pipelines - A review. *Corrosion Science*, 49(12), pp.4308–4338.

Nesic, S. et al., 2003. A mechanistic model for carbon dioxide corrosion of mild steel in the presence of protective iron carbonate films - Part 2: A numerical experiment. *Corrosion*, 59(6), pp.489–497.

Nesic, S. & Lee, K.L.J., 2003. A mechanistic model for carbon dioxide corrosion of mild steel in the presence of protective iron carbonate films - Part 3: Film growth model. *Corrosion*, 59(7), pp.616–628.

Nesic, S., Postlethwaite, J. & Olsen, S., 1996. An electrochemical model for prediction of corrosion of mild steel in aqueous carbon dioxide solutions. *Corrosion*, 52(4), pp.280–294.

Nesic, S. & Sun, W., 2010. Corrosion in acid gas solutions. In T. J. A. Richardson, ed. *Shreir's Corrosion*. Elsevier, pp. 1270–1298.

Ning, F. et al., 2010. Gas-hydrate formation, agglomeration and inhibition in oil-based drilling fluids for deep-water drilling. *Journal of Natural Gas Chemistry*, 19(3), pp.234–240.

Nordsveen, M. et al., 2003. A mechanistic model for carbon dioxide corrosion of mild steel in the presence of protective iron carbonate films - Part 1: Theory and verification. *Corrosion*, 59(5), pp.443–456.

Nyborg, R., 1998. Initiation and growth of mesa corrosion altack during CO_2 corrosion of carbon steel. In *CORROSION 98*. Houston, Texas: NACE, Paper No. 48.

Nyborg, R. & Dugstad, A., 1998. Mesa corrosion altack in carbon steel and 0.5 % chromium steel. In *CORROSION 98*. Houston, Texas: NACE, Paper No. 29.

Nyborg, R. & Dugstad, A., 2007. Top of line corrosion and water condensation rates in wet gas pipelines. In *CORROSION 2007*. Houston, Texas: NACE, Paper No. 07555.

Oddo, J. & Tomson, M., 1982. Simplified calculation of $CaCO_3$ saturation at high temperatures and pressures in brine solutions. *Journal of Petroleum Technology*, 34(7), pp.1583–1590.

Oehler, M. et al., 2012. Testing of generic volatile inhibitor compounds in different top-of-the-line corrosion laboratory test methods. In *CORROSION 2012*. Houston, Texas: NACE, Paper No. 1483.

Oehler, M., 2012. *Top-of-the-line corrosion control by continuous chemical treatment*. Perth, Australia: Curtin University.

Ojifinni, R.A. & Li, C., 2011. A parametric study of sweet top-of-line corrosion in wet gas pipelines. In *CORROSION 2011*. Houston, Texas: NACE, Paper No. 11331.

Okafor, P.C. & Nesic, S., 2007. Effect of acetic acid on CO_2 corrosion of carbon steel in vapor-water two-phase horizontal flow. *Chemical Engineering Communications*, 194(2), pp.141–157.

Olsen, S. & Dugstad, A., 1991. Corrosion under dewing condition. In *CORROSION 91*. Houston, Texas: NACE, Paper No. 472.

Pedersen, K.S., Michelsen, M.L. & Fredheim, A.O., 1996. Phase equilibrium calculations for unprocessed well streams containing hydrate inhibitors. *Fluid phase equilibria*, 126(1), pp.13–28.

Peng, S. & Zeng, Z., 2015. An experimental study on the internal corrosion of a subsea multiphase pipeline. *Petroleum*, 1(1), pp.75–81.

Piccardino, J.R. et al., 2004. Internal inspection of wet gas lines subject to top of line corrosion. In *CORROSION 2004*. Houston, Texas: NACE, Paper No. 04354.

Pojtanabuntoeng, T. et al., 2017. Assessment of corrosion control by pH neutralisation in the presence of glycol at low temperature. *Corrosion Science*.

Pojtanabuntoeng, T., Salasi, M. & Gubner, R., 2014. The Influence of mono ethylene glycol on CO_2 corrosion of carbon steel at elevated temperature (80-120 ^oC). In

CORROSION 2014. Houston, Texas: NACE, Paper No. 4176.

Pojtanabuntoeng, T., Singer, M. & Nesic, S., 2012. Top-of-the-line corrosion in the presence of hydrocarbon co-condensation in flowing condition. In *CORROSION 2012*. Houston, Texas: NACE, Paper No. C2012-0001534.

Pojtanabuntoeng, T., Singer, M. & Nesic, S., 2011. Water/hydrocarbon co-condensation and the influence on top-of-the-line corrosion. In *CORROSION 2011*. Houston, Texas: NACE, Paper No. 11330.

Popova, A., Christov, M. & Vasilev, A., 2007. Inhibitive properties of quaternary ammonium bromides of N-containing heterocycles on acid mild steel corrosion. Part II: EIS results. *Corrosion Science*, 49(8), pp.3290–3302.

Pots, B.F.M. & Hendriksen, E.L.J.A., 2000. CO_2 corrosion under scaling conditions - the special case of top-of-line corrosion in wet gas pipelines. In *CORROSION 2000*. Houston, Texas: NACE, Paper No. 00031.

Pourbaix, M., 1974. Applications of electrochemistry in corrosion science and in practice. *Corrosion Science*, 14(1), pp.25–82.

Punpruk, S., Thammachart, M. & Gunaltun, Y., 2010. Field testing of volatile corrosion inhibitors and evaluation of batch treatment efficiency by cooled probe. In *CORROSION 2010*. Houston, Texas: NACE, Paper No. 100096.

Qin, H. et al., 2011. Top of the line corrosion under low temperature and high condensation rate conditions. In *CORROSION 2011*. Houston, Texas: NACE, Paper No. 11328.

Ramachandran, S. et al., 2013. A new top-of-the-line corrosion inhibitor to mitigate carbon dioxide corrosion in wet gas systems. In *CORROSION 2013*. Houston, Texas: NACE, Paper No. 2274.

Ramachandran, S. et al., 2006. Inhibition of acid gas corrosion in pipelines using glycol for hydrate inhibition. In *CORROSION 2006*. Houston, Texas: NACE, Paper No. 06447.

Reijenga, J. et al., 2013. Development of methods for the determination of pKa values. *Analytical Chemistry Insights*, 8(1), pp.53–71.

Rogowska, M. et al., 2016. Effect of Fe ion concentration on corrosion of carbon steel in CO_2 environment. *Corrosion EngineeringOnline) Journal*, 51(1), pp.25–36.

Samiento-Bustos, E. et al., 2009. Corrosion behavior of iron-based alloys in the LiBr+ethylene glycol+H_2O mixture. *Corrosion Science*, 51(5), pp.1107–1114.

Sandengen, K., Kaasa, B. & Østvold, T., 2007. pH measurements in monoethylene glycol (MEG) + water solutions. *Industrial & Engineering Chemistry Research*, 46(14), pp.4734–4739.

Sarmini, K. & Kenndler, E., 1999. Ionization constants of weak acids and bases in organic solvents. *Journal of Biochemistry*, 38, pp.123–137.

Shanbhag, P.M. & Bates, R.C., 2010. Dissociation constants of acetic acid and protonated tris(hydroxymethyl)-aminomethane in 80 mass% 2-methoxyethanol/20 mass % water in the range 10 to 50 °C. *Bulletin des Sociétés Chimiques Belges*, 90(1), pp.1–7.

Sherik, A. et al., 2010. Effect of triethylene glycol on corrosion of carbon steel in H_2S, CO_2 and O_2 environments. In *CORROSION 2010*. Houston, Texas: NACE, Paper No. 10188.

Singer, M. et al., 2013. CO_2 top of the line corrosion in presence of acetic acid: A parametric study. *Corrosion*, 69(7), pp.719–735.

Singer, M. et al., 2010. Sour top-of-the-line corrosion in the presence of acetic acid. In *CORROSION 2010*. Houston, Texas: NACE, Paper No. 10100.

Singer, M. et al., 2011. Sour top-of-the-line corrosion in the presence of acetic acid. *Corrosion*, 67(8), pp.85003–16.

Singer, M., 2013. *Study and Modeling of the Localized Nature of Top of the Line Corrosion*. Ohio, USA: Ohio University.

Singer, M., 2017. Study of the localized nature of top of the line corrosion in sweet environment. *Corrosion*, 73(8), pp.1030–1055.

Singer, M., Al-Khamis, J. & Nesic, S., 2013. Experimental study of sour top-of-the-line corrosion using a novel experimental setup. *Corrosion*, 69(6), pp.624–638.

Singer, M., Nesic, S. & Gunaltun, Y., 2004. Top of the line corrosion in presence of acetic acid and carbon dioxide. In *CORROSION 2004*. Houston, Texas: NACE, Paper No. 04377.

Stawicki, O. et al., 2010. Monitoring of top of line corrosion with eddy current technology combined with magnetic flux leakage method. In *CORROSION 2010*. Houston, Texas: NACE, Paper no. 10094.

Stefl, B.A. & Bosen, S.F., 1997. Buffering and inhibition of glycol in gas dehydration applications: an alternative to amines. *Corrosion*, 53(2), pp.163–168.

Sun, J.B. et al., 2012. The formation mechanism of corrosion scale and electrochemical characteristic of low alloy steel in carbon dioxide-saturated solution. *Corrosion Science*, 57, pp.131–138.

Sun, W. & Nesic, S., 2006. Basics revisited: kinetics of iron carbonate scale precipitation in CO_2 corrosion. In *CORROSION 2006*. Houston, Texas: NACE, Paper No.6365.

Sun, W. & Nesic, S., 2008. Kinetics of corrosion layer formation: Part 1 - Iron carbonate layers in carbon dioxide corrosion. *Corrosion*, 64(4), pp.334–346.

Sun, W., Nesic, S. & Woollam, R.C., 2009. The effect of temperature and ionic strength on iron carbonate ($FeCO_3$) solubility limit. *Corrosion Science*, 51, pp.1273–1276.

Sun, Y.H., Hong, T. & Jepson, W.P., 2001. Corrosion under wet gas conditions. In *CORROSION 2001*. Houston, Texas: NACE, Paper No. 1034.

Svenningsen, G. et al., 2013. Top of line corrosion with high CO_2 and organic acid.

In *CORROSION 2013*. Houston, Texas: NACE, Paper No. 2591.

Svenningsen, G. & Nyborg, R., 2014. Modeling of top of line corrosion with organic acid and glycol. In *CORROSION 2014*. Houston, Texas: NACE, Paper No. 4057.

Tan, Y.J., Bailey, S. & Kinsella, B., 1996. An investigation of the formation and destruction of corrosion inhibitor films using electrochemical impedance spectroscopy (EIS). *Corrosion Science*, 38(9), pp.1545–1561.

Thomson, G.W., 1946. The Antoine equation for vapor-pressure data. *Chemical reviews*, 38, pp.1–39.

Tran, T. et al., 2013. Investigation of the electrochemical mechanisms for acetic acid corrosion of mild steel. *Corrosion*, 70(3), pp.223–229.

Uhlig, H.H., 1948. *The corrosion handbook*, New York: John Willey and Sons Inc.

Uzelac, N.I. et al., 2004. New generation of ultrasonic in-line inspection tools. In *Corrosion 2004*. Houston, Texas: NACE, Paper no. 4162.

Villarreal, J., Laverde, D. & Fuentes, C., 2006. Carbon-steel corrosion in multiphase slug flow and CO_2. *Corrosion Science*, 48(9), pp.2363–2379.

Vitse, F. et al., 2003. Mechanistic model for the prediction of top-of-the-line corrosion risk. *Corrosion*, 59(12), pp.1075–1084.

Vitse, F. et al., 2003. Mechanistic model for the prediction of top-of-theline corrosion risk. In *CORROSION 2003*. Houston, Texas: NACE, Paper No. 03633.

Vitse, F., Alam, K. & Gunaltun, Y., 2002. Semi-empirical model for prediction of the top of the line corrosion risk. In *CORROSION 2002*. Houston, Texas: NACE, Paper No. 02245.

de Waard, C., Lotz, U. & Milliams, D.E., 1991. Predictive model for CO_2 corrosion engineering in wet natural gas pipelines. *Corrosion*, 47(12), pp.976–985.

Wei, L. et al., 2015. Formation mechanism and protective property of corrosion product scale on X70 steel under supercritical CO_2 environment. *Corrosion Science*, 100, pp.404–420.

Wu, M., Wang, S. & Liu, H., 2007. A study on inhibitors for the prevention of hydrate formation in gas transmission pipeline. *Journal of Natural Gas Chemistry*, 16(1), pp.81–85.

Wylde, J.J. et al., 2013. When to batch and when not to batch : an overview of integrity management and batch corrosion inhibitor testing methods and application strategies. In *SPE International Symposium on Oilfield Chemistry*. Woodlands, Texas: Society of Petroleum Engineers.

Yaakob, N., 2015. *Top of the Line Corrosion in CO_2/H_2S Environments.* Ohio, USA: Ohio University.

Yaro, A.S., Abdul-Khalik, K.R. & Khadom, A.A., 2015. Effect of CO_2 corrosion behavior of mild steel in oilfield produced water. *Journal of Loss Prevention in the Process Industries*, 38, pp.24–38.

Zhang, G.A. & Cheng, Y.F., 2009. Corrosion of X65 steel in CO_2-saturated oilfield formation water in the absence and presence of acetic acid. *Corrosion Science*, 51(8), pp.1589–1595.

Zhang, G.A. & Cheng, Y.F., 2009. On the fundamentals of electrochemical corrosion of X65 steel in CO_2-containing formation water in the presence of acetic acid in petroleum production. *Corrosion Science*, 51(1), pp.87–94.

Zhang, Y. et al., 2012. Discussion of the CO_2 corrosion mechanism between low partial pressure and supercritical condition. *Corrosion Science*, 59, pp.186–197.

Zhang, Z. et al., 2007a. A mechanistic model of top-of-the-line corrosion. *Corrosion*, 63(11), pp.1051–1062.

Zhang, Z. et al., 2007b. A mechanistic model of top of the line corrosion. In *CORROSION 2007*. Houston, Texas: NACE, Paper No. 07556.

Zhu, S.D. et al., 2011. Corrosion of N80 carbon steel in oil field formation water containing CO_2 in the absence and presence of acetic acid. *Corrosion Science*, 53(10), pp.3156–3165.

Zuo, Y. et al., 2008. The evaluation of coating performance by the variations of phase angles in middle and high frequency domains of EIS. *Corrosion Science*, 50(12), pp.3322–3328.

Appendix III: Copyright statements

The following pages contain documents stating:

The rights granted by Elsevier to reproduce the published materials that form **Chapter 2** of this thesis

The rights granted by NACE International to reproduce the published materials that form **Chapter 4** of this thesis

ELSEVIER LICENSE
TERMS AND CONDITIONS

Aug 26, 2017

This Agreement between Mr. Md Mayeedul Islam ("You") and Elsevier ("Elsevier") consists of your license details and the terms and conditions provided by Elsevier and Copyright Clearance Center.

License Number	4166241285780
License date	Aug 11, 2017
Licensed Content Publisher	Elsevier
Licensed Content Publication	Corrosion Science
Licensed Content Title	Condensation corrosion of carbon steel at low to moderate surface temperature and iron carbonate precipitation kinetics
Licensed Content Author	Md Mayeedul Islam,Thunyaluk Pojtanabuntoeng,Rolf Gubner
Licensed Content Date	Oct 1, 2016
Licensed Content Volume	111
Licensed Content Issue	n/a
Licensed Content Pages	12
Start Page	139
End Page	150
Type of Use	reuse in a thesis/dissertation
Portion	full article
Format	both print and electronic
Are you the author of this Elsevier article?	Yes
Will you be translating?	No
Title of your thesis/dissertation	An investigation on the top-of-the-line corrosion using novel methods
Expected completion date	Sep 2017
Estimated size (number of pages)	200
Requestor Location	Mr. Md Mayeedul Islam Building 614 5 De Laeter Way Bentley, WA 6102 Australia Attn: Mr. Md Mayeedul Islam
Total	0.00 AUD
Terms and Conditions	

INTRODUCTION

1. The publisher for this copyrighted material is Elsevier. By clicking "accept" in connection with completing this licensing transaction, you agree that the following terms and conditions apply to this transaction (along with the Billing and Payment terms and conditions established by Copyright Clearance Center, Inc. ("CCC"), at the time that you opened your Rightslink account and that are available at any time at http://myaccount.copyright.com).

GENERAL TERMS

2. Elsevier hereby grants you permission to reproduce the aforementioned material subject to the terms and conditions indicated.

3. Acknowledgement: If any part of the material to be used (for example, figures) has appeared in our publication with credit or acknowledgement to another source, permission must also be sought from that source. If such permission is not obtained then that material may not be included in your publication/copies. Suitable acknowledgement to the source must be made, either as a footnote or in a reference list at the end of your publication, as follows:
"Reprinted from Publication title, Vol /edition number, Author(s), Title of article / title of chapter, Pages No., Copyright (Year), with permission from Elsevier [OR APPLICABLE SOCIETY COPYRIGHT OWNER]." Also Lancet special credit - "Reprinted from The Lancet, Vol. number, Author(s), Title of article, Pages No., Copyright (Year), with permission from Elsevier."
4. Reproduction of this material is confined to the purpose and/or media for which permission is hereby given.
5. Altering/Modifying Material: Not Permitted. However figures and illustrations may be altered/adapted minimally to serve your work. Any other abbreviations, additions, deletions and/or any other alterations shall be made only with prior written authorization of Elsevier Ltd. (Please contact Elsevier at permissions@elsevier.com). No modifications can be made to any Lancet figures/tables and they must be reproduced in full.
6. If the permission fee for the requested use of our material is waived in this instance, please be advised that your future requests for Elsevier materials may attract a fee.
7. Reservation of Rights: Publisher reserves all rights not specifically granted in the combination of (i) the license details provided by you and accepted in the course of this licensing transaction, (ii) these terms and conditions and (iii) CCC's Billing and Payment terms and conditions.
8. License Contingent Upon Payment: While you may exercise the rights licensed immediately upon issuance of the license at the end of the licensing process for the transaction, provided that you have disclosed complete and accurate details of your proposed use, no license is finally effective unless and until full payment is received from you (either by publisher or by CCC) as provided in CCC's Billing and Payment terms and conditions. If full payment is not received on a timely basis, then any license preliminarily granted shall be deemed automatically revoked and shall be void as if never granted. Further, in the event that you breach any of these terms and conditions or any of CCC's Billing and Payment terms and conditions, the license is automatically revoked and shall be void as if never granted. Use of materials as described in a revoked license, as well as any use of the materials beyond the scope of an unrevoked license, may constitute copyright infringement and publisher reserves the right to take any and all action to protect its copyright in the materials.
9. Warranties: Publisher makes no representations or warranties with respect to the licensed material.
10. Indemnity: You hereby indemnify and agree to hold harmless publisher and CCC, and their respective officers, directors, employees and agents, from and against any and all claims arising out of your use of the licensed material other than as specifically authorized pursuant to this license.
11. No Transfer of License: This license is personal to you and may not be sublicensed, assigned, or transferred by you to any other person without publisher's written permission.
12. No Amendment Except in Writing: This license may not be amended except in a writing signed by both parties (or, in the case of publisher, by CCC on publisher's behalf).
13. Objection to Contrary Terms: Publisher hereby objects to any terms contained in any purchase order, acknowledgment, check endorsement or other writing prepared by you, which terms are inconsistent with these terms and conditions or CCC's Billing and Payment terms and conditions. These terms and conditions, together with CCC's Billing and Payment terms and conditions (which are incorporated herein), comprise the entire agreement between you and publisher (and CCC) concerning this licensing transaction. In the event of any conflict between your obligations established by these terms and conditions and those established by CCC's Billing and Payment terms and conditions, these terms and conditions shall control.
14. Revocation: Elsevier or Copyright Clearance Center may deny the permissions described in this License at their sole discretion, for any reason or no reason, with a full refund payable

to you. Notice of such denial will be made using the contact information provided by you. Failure to receive such notice will not alter or invalidate the denial. In no event will Elsevier or Copyright Clearance Center be responsible or liable for any costs, expenses or damage incurred by you as a result of a denial of your permission request, other than a refund of the amount(s) paid by you to Elsevier and/or Copyright Clearance Center for denied permissions.

LIMITED LICENSE

The following terms and conditions apply only to specific license types:

15. **Translation**: This permission is granted for non-exclusive world **English** rights only unless your license was granted for translation rights. If you licensed translation rights you may only translate this content into the languages you requested. A professional translator must perform all translations and reproduce the content word for word preserving the integrity of the article.

16. **Posting licensed content on any Website**: The following terms and conditions apply as follows: Licensing material from an Elsevier journal: All content posted to the web site must maintain the copyright information line on the bottom of each image; A hyper-text must be included to the Homepage of the journal from which you are licensing at http://www.sciencedirect.com/science/journal/xxxxx or the Elsevier homepage for books at http://www.elsevier.com; Central Storage: This license does not include permission for a scanned version of the material to be stored in a central repository such as that provided by Heron/XanEdu.

Licensing material from an Elsevier book: A hyper-text link must be included to the Elsevier homepage at http://www.elsevier.com . All content posted to the web site must maintain the copyright information line on the bottom of each image.

Posting licensed content on Electronic reserve: In addition to the above the following clauses are applicable: The web site must be password-protected and made available only to bona fide students registered on a relevant course. This permission is granted for 1 year only. You may obtain a new license for future website posting.

17. **For journal authors:** the following clauses are applicable in addition to the above:

Preprints:

A preprint is an author's own write-up of research results and analysis, it has not been peer-reviewed, nor has it had any other value added to it by a publisher (such as formatting, copyright, technical enhancement etc.).

Authors can share their preprints anywhere at any time. Preprints should not be added to or enhanced in any way in order to appear more like, or to substitute for, the final versions of articles however authors can update their preprints on arXiv or RePEc with their Accepted Author Manuscript (see below).

If accepted for publication, we encourage authors to link from the preprint to their formal publication via its DOI. Millions of researchers have access to the formal publications on ScienceDirect, and so links will help users to find, access, cite and use the best available version. Please note that Cell Press, The Lancet and some society-owned have different preprint policies. Information on these policies is available on the journal homepage.

Accepted Author Manuscripts: An accepted author manuscript is the manuscript of an article that has been accepted for publication and which typically includes author-incorporated changes suggested during submission, peer review and editor-author communications.

Authors can share their accepted author manuscript:

- immediately
  - via their non-commercial person homepage or blog
  - by updating a preprint in arXiv or RePEc with the accepted manuscript
  - via their research institute or institutional repository for internal institutional uses or as part of an invitation-only research collaboration work-group
  - directly by providing copies to their students or to research collaborators for their personal use
  - for private scholarly sharing as part of an invitation-only work group on commercial sites with which Elsevier has an agreement

- After the embargo period
  - via non-commercial hosting platforms such as their institutional repository
  - via commercial sites with which Elsevier has an agreement

In all cases accepted manuscripts should:

- link to the formal publication via its DOI
- bear a CC-BY-NC-ND license - this is easy to do
- if aggregated with other manuscripts, for example in a repository or other site, be shared in alignment with our hosting policy not be added to or enhanced in any way to appear more like, or to substitute for, the published journal article.

Published journal article (JPA): A published journal article (PJA) is the definitive final record of published research that appears or will appear in the journal and embodies all value-adding publishing activities including peer review co-ordination, copy-editing, formatting, (if relevant) pagination and online enrichment.
Policies for sharing publishing journal articles differ for subscription and gold open access articles:
Subscription Articles: If you are an author, please share a link to your article rather than the full-text. Millions of researchers have access to the formal publications on ScienceDirect, and so links will help your users to find, access, cite, and use the best available version.
Theses and dissertations which contain embedded PJAs as part of the formal submission can be posted publicly by the awarding institution with DOI links back to the formal publications on ScienceDirect.
If you are affiliated with a library that subscribes to ScienceDirect you have additional private sharing rights for others' research accessed under that agreement. This includes use for classroom teaching and internal training at the institution (including use in course packs and courseware programs), and inclusion of the article for grant funding purposes.
Gold Open Access Articles: May be shared according to the author-selected end-user license and should contain a CrossMark logo, the end user license, and a DOI link to the formal publication on ScienceDirect.
Please refer to Elsevier's posting policy for further information.
18. **For book authors** the following clauses are applicable in addition to the above:
Authors are permitted to place a brief summary of their work online only. You are not allowed to download and post the published electronic version of your chapter, nor may you scan the printed edition to create an electronic version. **Posting to a repository:** Authors are permitted to post a summary of their chapter only in their institution's repository.
19. **Thesis/Dissertation**: If your license is for use in a thesis/dissertation your thesis may be submitted to your institution in either print or electronic form. Should your thesis be published commercially, please reapply for permission. These requirements include permission for the Library and Archives of Canada to supply single copies, on demand, of the complete thesis and include permission for Proquest/UMI to supply single copies, on demand, of the complete thesis. Should your thesis be published commercially, please reapply for permission. Theses and dissertations which contain embedded PJAs as part of the formal submission can be posted publicly by the awarding institution with DOI links back to the formal publications on ScienceDirect.

Elsevier Open Access Terms and Conditions
You can publish open access with Elsevier in hundreds of open access journals or in nearly 2000 established subscription journals that support open access publishing. Permitted third party re-use of these open access articles is defined by the author's choice of Creative Commons user license. See our open access license policy for more information.
Terms & Conditions applicable to all Open Access articles published with Elsevier:
Any reuse of the article must not represent the author as endorsing the adaptation of the article nor should the article be modified in such a way as to damage the author's honour or reputation. If any changes have been made, such changes must be clearly indicated.
The author(s) must be appropriately credited and we ask that you include the end user license and a DOI link to the formal publication on ScienceDirect.

If any part of the material to be used (for example, figures) has appeared in our publication with credit or acknowledgement to another source it is the responsibility of the user to ensure their reuse complies with the terms and conditions determined by the rights holder.
Additional Terms & Conditions applicable to each Creative Commons user license:
CC BY: The CC-BY license allows users to copy, to create extracts, abstracts and new works from the Article, to alter and revise the Article and to make commercial use of the Article (including reuse and/or resale of the Article by commercial entities), provided the user gives appropriate credit (with a link to the formal publication through the relevant DOI), provides a link to the license, indicates if changes were made and the licensor is not represented as endorsing the use made of the work. The full details of the license are available at http://creativecommons.org/licenses/by/4.0.
CC BY NC SA: The CC BY-NC-SA license allows users to copy, to create extracts, abstracts and new works from the Article, to alter and revise the Article, provided this is not done for commercial purposes, and that the user gives appropriate credit (with a link to the formal publication through the relevant DOI), provides a link to the license, indicates if changes were made and the licensor is not represented as endorsing the use made of the work. Further, any new works must be made available on the same conditions. The full details of the license are available at http://creativecommons.org/licenses/by-nc-sa/4.0.
CC BY NC ND: The CC BY-NC-ND license allows users to copy and distribute the Article, provided this is not done for commercial purposes and further does not permit distribution of the Article if it is changed or edited in any way, and provided the user gives appropriate credit (with a link to the formal publication through the relevant DOI), provides a link to the license, and that the licensor is not represented as endorsing the use made of the work. The full details of the license are available at http://creativecommons.org/licenses/by-nc-nd/4.0.
Any commercial reuse of Open Access articles published with a CC BY NC SA or CC BY NC ND license requires permission from Elsevier and will be subject to a fee.
Commercial reuse includes:

- Associating advertising with the full text of the Article
- Charging fees for document delivery or access
- Article aggregation
- Systematic distribution via e-mail lists or share buttons

Posting or linking by commercial companies for use by customers of those companies.

20. **Other Conditions**:

v1.9

Questions? customercare@copyright.com or +1-855-239-3415 (toll free in the US) or +1-978-646-2777.

NACE International
15835 Park Ten Place
Houston, TX 77084
Tel: 281-228-6200
Fax: 281-228-6300

NACE INTERNATIONAL
The Worldwide Corrosion Authority

Permission to Reproduce Figures, Photos, and Tables from Copyrighted Works

Date: 08/08/2017

Name: Md Mayeedul Islam Title: Mr

Company ("Publisher"): Curtin University

Address: 5 De Laeter Way, Bentley, WA 6101, Australia

Tel: +61 8 9266 2063 Fax: +61 8 9266 7221

Email: m.islam26@postgrad.curtin.edu.au

Material to be Reproduced ("Work"): Please provide a complete description of the material involved. Include the following elements where applicable: publication name, issue date, page number, figure/photo/table number, paper number, conference name, etc.

Development of an electrochemical method to study top-of-the-line corrosion

CORROSION 2017 conference, Paper number 9106

Reproduction Method ("Publication Media"): Please provide a complete description of how and where the Work will be used. Include the following elements as applicable: publication name, issue, circulation, print run, web site address, conference name, presentation time and place, etc.

The complete article will be reproduced in PhD thesis

NACE International ("NACE") hereby grants to "Publisher" the right to publish the Work utilizing the Publication Media described above. The publication right granted herein is limited the specific Publication Media described above. To the extent the publication of the Work is to occur by an above-specified date, such as in a particular periodical or at a particular conference, the right granted herein shall automatically terminate upon the date of such occurrence, whether or not the Work is actually published. To the extent the Publication Media is a web site, the publication right is limited to publication at the specific web site URL identified above. Any right granted herein is a limited, non-transferable, non-exclusive right. No other rights in the Work are granted herein.

Publisher shall not edit or modify the Work except to meet the style and graphic requirements of the individual media involved.

The Publisher shall include the following notation with any publication of the Work:*

A. Conference Paper
Reproduced with permission from NACE International, Houston, TX. All rights reserved. Author(s), Paper NUMBER presented at CORROSION/YEAR, City, State. © NACE International FIRST YEAR OF PUBLICATION.

B. Journal Article
Reproduced with permission from NACE International, Houston, TX. All rights reserved. Author(s) name, Article title, Journal title, Vol. no., Issue no., and publication year. © NACE International FIRST YEAR OF PUBLICATION.

C. Magazine Article
Reproduced with permission from NACE International, Houston, TX. All rights reserved. Author(s) name, Article title, Magazine title, Vol. no., Issue no., and publication year. © NACE International FIRST YEAR OF PUBLICATION.

D. Standards
STANDARDS/TECHNICAL COMMITTEE REPORT NAME. © NACE International YEAR. All rights reserved by NACE. Reprinted with permission. NACE standards are revised periodically. Users are cautioned to obtain the latest edition; information in an outdated version of the standard may not be accurate.

* Modifications to Notations: Other reference wording can be used, but must be approved by NACE in writing *in advance*.

The Publisher shall include full bibliographic citations of or references to the original NACE source, where applicable.

Publisher shall obtain a copy of the original Work directly from NACE International and shall not utilize copies of the Work from other sources, including the author(s).

To the extent the Work is published on a web site as authorized herein, the Work shall be posted in a file format that does not allow the content of the Work to be easily copied from the Web Site or changed.

As between NACE and Publisher, Publisher acknowledges that NACE owns all rights in the Works.

Publisher shall not be entitled to any compensation for its efforts in promoting the Work.

THE WORK IS PROVIDED "AS IS." ALL EXPRESS OR IMPLIED COVENANTS, CONDITIONS, REPRESENTATIONS OR WARRANTIES, INCLUDING ANY IMPLIED WARRANTY OF MERCHANTABILITY OR FITNESS FOR A PARTICULAR PURPOSE OR CONDITIONS OF ACCURACY, COMPLETENESS OR QUALITY AND THOSE ARISING BY STATUTE OR OTHERWISE IN LAW, ARE HEREBY DISCLAIMED.

IN NO EVENT WILL NACE BE LIABLE FOR ANY DIRECT, INDIRECT, PUNITIVE, SPECIAL, INCIDENTAL OR CONSEQUENTIAL DAMAGES IN CONNECTION WITH OR RELATED TO THIS AGREEMENT (INCLUDING LOSS OF PROFITS, USE, DATA, OR OTHER ECONOMIC ADVANTAGE), HOWSOEVER ARISING.

This Agreement and the rights granted herein may be terminated immediately by NACE upon breach of this Agreement by Publisher. Unless earlier terminated, this Agreement and the rights granted herein will automatically terminate 6 months from the Date set forth above. If the Work has not been published within that time period, a new Agreement must be obtained.

Publisher may not, directly or indirectly, sell, assign, sublicense, lease, rent, distribute, or otherwise transfer this Agreement or any rights granted herein, without the prior written consent of NACE.

If any provision of this Agreement is found to be unenforceable, then this Agreement shall be deemed to be amended by modifying such provision to the extent necessary to make it legal and enforceable while preserving its intent. The remainder of this Agreement shall not be affected by such modification.

This Agreement does not create, and shall not be construed to create, any employer-employee, joint venture or partnership relationship between the parties. No officer, employee, agent, servant or independent contractor of either party shall at any time be deemed to be an employee, servant, agent or contractor of any other party for any purpose whatsoever.

This Agreement shall be governed by, and construed and enforced in accordance with, the laws of the State of Texas, without regard to the choice of law provisions of that State.

This Agreement shall only be effective if signed by authorized representatives of both parties. This Agreement constitutes the entire Agreement between the parties with respect to the subject matter of this Agreement. Any change, modification or waiver hereto must be in writing and signed by authorized representatives of both parties.

Other Terms & Conditions: _____

Publisher hereby requests permission to publish the Work described above and agrees to comply with all Terms and Conditions listed above.

Request submitted by:

Printed Name
Md Mayeedul Islam

Title
Mr

Signature
Md Mayeedul Islam

Date
08/08/2017

Request approved by NACE:

Printed Name
Daniela Freema

Printed Name
Daniela Freeman

Title
Audience Development Manager

Signature
daniela.freeman@nace.org

Date
8/15/2017

Request agreed to by:

Lead Author Printed Name
Md Mayeedul Islam

Lead Author Title
Mr

Lead Author Signature
Md Mayeedul Islam

Date
08/08/2017

Appendix IV: Written statements of co-authors

The written statements of co-authors about the contribution of the candidate on each publication that forming individual chapter of this thesis are given in the subsequent pages.

To whom it may concern,

I, Md Mayeedul Islam, as the first author of the publication entitled '***Condensation corrosion of carbon steel at low to moderate surface temperature and iron carbonate precipitation kinetics***' was primarily involved in planning and conducting the experiments, data analysis and interpretation of the findings and manuscript preparation.

First author signature

I, as a co-author, endorse that this level of contribution by the first author indicated above is appropriate.

Thunyaluk Pojtanabuntoeng	
Full name of co-author 1	**Signature of co-author 1**
Rolf Gubner	
Full name of co-author 2	**Signature of co-author 2**

To whom it may concern,

I, Md Mayeedul Islam, as the first author of the publication entitled '***Influence of monoethylene glycol on the condensation rate and corrosion rate of carbon steel under condensing condition***' was primarily involved in planning and conducting the experiments, data analysis and interpretation of the findings and manuscript preparation.

First author signature

I, as a co-author, endorse that this level of contribution by the first author indicated above is appropriate.

Thunyaluk Pojtanabuntoeng

Full name of co-author 1

Signature of co-author 1

Rolf Gubner

Full name of co-author 2

Signature of co-author 2

To whom it may concern,

I, Md Mayeedul Islam, as the first author of the publication entitled '***Development of an electrochemical method to study top-of-the-line corrosion***' was primarily involved in planning and conducting the experiments, data analysis and interpretation of the findings and manuscript preparation.

First author signature

I, as a co-author, endorse that this level of contribution by the first author indicated above is appropriate.

Thunyaluk Pojtanabuntoeng

Full name of co-author 1

Signature of co-author 1

Rolf Gubner

Full name of co-author 2

Signature of co-author 2

To whom it may concern,

I, Md Mayeedul Islam, as the first author of the publication entitled '***Electrochemical investigation into the dynamic mechanism of CO_2 corrosion product film formation on the carbon steel under water condensation condition'*** was primarily involved in planning and conducting the experiments, data analysis and interpretation of the findings and manuscript preparation.

First author signature

I, as a co-author, endorse that this level of contribution by the first author indicated above is appropriate.

Thunyaluk Pojtanabuntoeng	
Full name of co-author 1	**Signature of co-author 1**
Rolf Gubner	
Full name of co-author 2	**Signature of co-author 2**
Brian Kinsella	
Full name of co-author 3	**Signature of co-author 3**

To whom it may concern,

I, Md Mayeedul Islam, as the first author of the publication entitled '***Are corrosion rates and condensation rates proportional in TLC?***' was primarily involved in planning and conducting the experiments, data analysis and interpretation of the findings and manuscript preparation.

First author signature

I, as a co-author, endorse that this level of contribution by the first author indicated above is appropriate.

Thunyaluk Pojtanabuntoeng	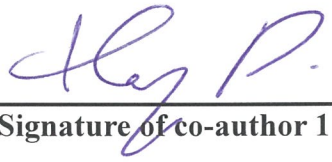
Full name of co-author 1	**Signature of co-author 1**
Rolf Gubner	
Full name of co-author 2	**Signature of co-author 2**

To whom it may concern,

I, Md Mayeedul Islam, as the first author of the publication entitled '***Electrochemical investigation into the influence of monoethylene glycol on CO_2 corrosion in presence of acetic acid***' was primarily involved in planning and conducting the experiments, data analysis and interpretation of the findings and manuscript preparation.

First author signature

I, as a co-author, endorse that this level of contribution by the first author indicated above is appropriate.

Thunyaluk Pojtanabuntoeng	
Full name of co-author 1	**Signature of co-author 1**
Rolf Gubner	
Full name of co-author 2	**Signature of co-author 2**